AXIAL LOAD TRANSFER MECHANISM OF ROCK BOLTS

A Thesis submitted by

Hadi Nourizadeh
BEng, MEng

For the award of

Doctor of philosophy

2023

THIS PAGE INTENTIONALLY LEFT BLANK

THIS PAGE INTENTIONALLY LEFT BLANK

ABSTRACT

Rock bolts are widely used in mining and geotechnical engineering. They can effectively improve the stability of rock mass, reducing the rock mass deformation, and resulting in improvements in safety, cost and time. Nonetheless, a comprehensive assessment of fully grouted rock bolts is necessary, particularly under diverse geotechnical scenarios. Gaps in knowledge persist concerning their behaviour at elevated temperatures, within triaxial confinement, and under varying encapsulation length, grout properties, and rock mass attributes. Furthermore, the impact of commonly employed protective plastic sheaths, used for protecting steel rock bolts against corrosion, on the axial behaviour of these bolts remains ambiguous in the existing literature. These aspects of reinforcement systems have been understudied, restricting practical implementation. This thesis undertakes both experimental and analytical investigations into the axial behaviour of fully grouted rock bolts. The first paper examines the mechanical, thermal, and bonding characteristics of commonly used anchoring Unsaturated Polyester Resins (UPR) under elevated temperatures, revealing significant impacts above 150°C. The second paper delves into pullout performance under triaxial testing, uncovering how non-uniform confining stress on cubic samples influences bearing capacity, bonding stiffness, and lateral deformation. The third paper delves into the factors affecting axial load transfer mechanisms in fully encapsulated rock bolts, investigating embedment length, bonding material characteristics, and host rock conditions. The study unveils that increasing embedment length enhances pullout capacity up to a critical length, beyond which ultimate strength and bond stress distribution stabilise. Notably, the shear modulus of bonding materials was found as the most influential factor in axial load transfer and bond stress distribution. Lastly, this study explores the axial behaviour of fully grouted protective sheathed rock bolts. The findings indicate the vulnerability of the grout-sheath interface amongst the other features, mainly if the encapsulation length falls short. The outcomes of this research significantly enhance our comprehension of the axial load transfer mechanism of fully grouted rock bolts across various conditions. Moreover, these findings hold practical value in guiding the design, modelling, manufacturing, and application of reinforcement systems within domains like mining, tunnelling, underground excavations, and slope stability.

CERTIFICATION OF THESIS

I, Hadi Nourizadeh, declare that the PhD Thesis entitled Axial Load Transfer Mechanism of Rock Bolts is not more than 100,000 words in length including quotes and exclusive of tables, figures, appendices, bibliography, references, and footnotes.

This Thesis is the work of Hadi Nourizadeh except where otherwise acknowledged, with the majority of the contribution to the papers presented as a Thesis by Publication undertaken by the student. The work is original and has not previously been submitted for any other award, except where acknowledged.

Date: 19/September/2023

Endorsed by:

Associate Professor Ali Mirzaghorbanali
Principal Supervisor

Professor Kevin McDougall
Associate Supervisor

Professor Naj Aziz
Associate Supervisor

Student and supervisors' signatures of endorsement are held at the University.

STATEMENT OF CONTRIBUTION

The articles produced from this study were a joint contribution of the authors. The details of the scientific contribution of each author are provided below:

Paper 1:

Nourizadeh, H., Mirzaghorbanali, A., McDougall, K., Jeewantha, LHJ., Craig, P., Motallebiyan, A., Jodeiri Shokri, B., Rastegarmanesh, A., Aziz, N. (2023). Characterisation of mechanical and bonding properties of anchoring resins under elevated temperature. International Journal of Rock Mechanic and Mining Sciences 2023;170:105506. (Impact Factor: 7.2; CiteScore:13)
https://doi.org/10.1016/j.ijrmms.2023.105506.

The overall contribution of Hadi Nourizadeh was 60% related to the conceptualisation, methodology, test design, data collection, critical review of related literature, analysis and interpretation of data, and drafting and revising the final submission. Ali Mirzaghorbanali, Kevin McDougall, Janitha Jeewantha, Peter Craig, Amin Motallebiyan, Behshad Jodeiri Shokri, Ashkan Rastegarmanesh, and Naj Aziz contributed to the methodology, structuring of the manuscript, formal analysis, methodology, resources, writing- review and editing.

Paper 2:

Nourizadeh, H., Mirzaghorbanali, A., Serati, M., Mahmoud, ME., McDougall, K., Aziz, N. (2023). Failure characterisation of fully grouted rock bolts under triaxial testing. International Journal of Rock Mechanic and Geotechnical Engineering; (Impact Factor: 7.3, CiteScore: 10.9)
https://doi.org/10.1016/j.jrmge.2023.08.013

The overall contribution of Hadi Nourizadeh was 65% related to the conceptualisation, methodology, test design, data collection, critical review of related literature, analysis and interpretation of data, and drafting and revising the final submission. Ali Mirzaghorbanali, Mehdi Serati, Mutaz El Mahmoud, Kevin McDougall and Naj Aziz contributed to the methodology, structuring of the manuscript, formal analysis, methodology, resources, writing- review and editing.

Paper 3:

Nourizadeh, H., Mirzaghorbanali, A., McDougall, Mitri, H., Craig, P., Rastegarmanesh, A., Aziz, N. (2023). Unveiling Axial Load Transfer Mechanism in Fully Encapsulated Rock Bolts. International Journal of Rock Mechanic and Rock Engineering; Under Review; (Impact Factor: 6.9; CiteScore: 11.4)

The overall contribution of Hadi Nourizadeh was 65% related to the conceptualisation, methodology, test design, data collection, critical review of related literature, analysis and interpretation of data, and drafting and revising the final submission. Ali Mirzaghorbanali, Kevin McDougall, Hani Mitri, Peter Craig, Ashkan Rastegarmanesh and Naj Aziz contributed to the methodology, structuring of the manuscript, methodology, resources, writing- review and editing.

Paper 4:

Nourizadeh, H., Mirzaghorbanali, A., McDougall, Aziz, N. (2023). Exploring the Axial Performance of Protective Sheathed Rock Bolts through Large-Scale Testing; Under preparation for submission.

The overall contribution of Hadi Nourizadeh was 65% related to the conceptualisation, methodology, test design, data collection, critical review of related literature, analysis and interpretation of data, and drafting and revising the final submission. Ali Mirzaghorbanali, Kevin McDougall, and Naj Aziz contributed to the methodology, structuring of the manuscript, methodology, resources, writing- review and editing.

ACKNOWLEDGEMENTS

In this pivotal moment, I extend my heartfelt appreciation to those who have been instrumental in the realisation of this thesis.

First, I sincerely thank my principal supervisor, Associate Professor Ali Mirzaghorbanali. His dedication, contributions, and guidance have been the cornerstone of my academic journey. His mentorship has not only enriched my research but also shaped my intellectual growth. My gratitude extends to my esteemed co-supervisors, Professor Kevin McDougall and Professor Naj Aziz, whose expertise and guidance have been invaluable throughout my PhD thesis. Their insights, support, and collaborative spirit have propelled me forward. I extend my sincere thanks to Professor Peter Schubel, the former director of the Centre for Future Materials (CFM) and Professor Xuesen Zeng for their support during my PhD tenure. Their leadership has been a beacon of inspiration. Many thanks to GRS UniSQ for their support throughout my PhD journey and for providing essential financial assistance through the International Tuition Fee and Stipend Scholarships. I am deeply indebted to the UniSQ technical staff members who have been pivotal in this endeavour. Thanks to Mr. Nathan Strenzel and Mr. Oliver Kinder, the UniSQ workshop staff, for their technical advice and invaluable assistance in manufacturing the required materials and devices for my experiments. I am also grateful to Mr. Wayne Crowell, Mrs. Piumika Ariyadasa, Dr. Choman Salih, and Dr. Mazhar Peerzada for their indispensable help in conducting my experiments. My gratitude extends to Jennmar Australia, especially Dr. Peter Craig and Minova Australia, and Mr. Robert Hawker, for their guidance, advice, and provision of essential materials that were instrumental in the success of my experiments. To my friends and all who have contributed, whether through academic support, technical support, or personal assistance, I extend my heartfelt thanks. To my family, especially my mother, whose support and encouragement have been a driving force. I pay tribute to my father, whose absence is felt deeply and who cannot witness this achievement.

Last but certainly not least, my wife, Hoda, has been the unwavering pillar of strength throughout this journey, with her steadfast support, boundless love, and unwavering belief in me.

This accomplishment is the result of collective efforts, and I am profoundly grateful to each of you who has played a part in this journey.

TABLE OF CONTENTS

LIST OF TABLES

TABLE OF FIGURES

CHAPTER1: INTRODUCTION

1.1. Background and motivation

The stability of underground excavations is a primary concern for geotechnical and mining engineers seeking to improve workers' safety, reduce environmental issues, and avoid financial loss. Anchoring systems are commonly used for reinforcing and supporting ground and underground structures (Rastegarmanesh et al., 2023). These systems can be classified into three main categories: stranded steel tendons (cable bolts), deformed or threaded steel bars (rock bolts), and glass fibre-reinforced polymer bars (GFRP). Rock bolts are generally considered the most adaptable and efficient reinforcement system in complex ground conditions (Li, 2017). The response of rock bolts to excitation or disturbance depends on many factors, such as the type of bolt, bonding materials, bolt arrangement in the field, confining and environmental conditions, surrounding rock mass and the mode of the subjected force, which can be predominantly shear, axial, or flexural (Chen, 2014, Li et al., 2014, Li et al., 2019). However, the typical behaviour is likely a combination of all the forces above (He et al., 2017).

Rock bolts vary in terms of design and material, but the fully encapsulated rock bolt is the most widely used in practice. Fully encapsulated anchored rock bolts are typically inserted into a pre-drilled hole in the host media and filled with a structural bonding agent. The function of the bonding agent is to transfer the anchoring load from the bolt to the surrounding rock mass and vice versa. Once a rock bolt is installed in a borehole and grouted, it interacts with the grouting materials and the surrounding rock mass as soon as deformations occur in the rock mass. Due to displacements in the rock mass, the load is transferred from the unstable rock to the grouting materials, then to the bolt, and subsequently to the intact rocks. This complex interaction restrains rock movement along a discontinuity and controls rock deformation along the grouted length. When a grouted bolt is subjected to a tensile force, the induced axial stress in the rod is distributed across the bolt-grout interface, the grout, the grout-rock interface, and the rock. The load is transferred and redistributed between the bolt and the host rock by bond (shear) resistance in the grout resulting from adhesion and mechanical interlocking between the bolt-grout and the grout-rock (Signer, 1990). The uneven surfaces of the bolt and drill hole provide irregular contact at the bolt-grout and

grout-rock interfaces. When the bolt is subjected to a load, stress concentration occurs at these asperities and irregularities, and the bond strength comes into play in the form of interlocking.

There are two basic types of encapsulation materials: chemical and non-chemical. Cement-based materials, often called grout, are an example of non-chemical bonding agents and are not covered in this study. Unsaturated polyester resin (UPR), vinyl ester resin (VER), and epoxy resin are the most commonly used chemical bonding materials (Contrafatto and Cosenza, 2014). UPR-based bonding products are widely used in mine support and building strengthening projects due to their shorter cure time, good bonding strength, and low cost (Xue-gui et al., 2016). The degradation process of UPR and VER under different conditions, such as exposure to chemicals, microwave radiation, and high temperature, has been studied. It has been established that immersion in aggressive solvents and exposure to higher temperatures (e.g., 1000 °C) degrade and carbonise the matrix, while UV radiation causes additional cross-linking in the resins (Pączkowski et al., 2022). For anchor bonding applications, anchor resins can be distinguished by vial (two-component cartridge) and injection systems. The two-component cartridges typically consist of a tube of polyester film filled with polyester resins and a curing agent (catalyst), which is usually a peroxide like methyl ethyl ketone peroxide or benzoyl peroxide. A film barrier of polyester is used to prevent migration between the resin and the hardener. Inorganic fillers such as calcium carbonate ($CaCO_3$) and silica are usually added to the resin components to enhance the mechanical properties and minimise expenses. Several studies have been conducted to investigate the effect of filler content and particle sizes on the mechanical properties of polyester resins, and it has been reported that mechanical and bonding properties of resins can be enhanced by incorporating an optimum content of filler (Bagherzadeh et al., 2020; Devi et al., 1998; Rahman et al., 2016; Witt and Cizek, 1954).

The behaviour of resin-encapsulated anchors can be viewed from two perspectives: short-term properties including gelling time, setting time (early curing time), and early bonding strength, and long-term properties including bearing capacity against static and dynamic loads and resistance to harsh and corrosive environments, temperature, and fire. The chemical formulation of resins is a critical characteristic, along with other parameters such as host rock mass condition, level of in-situ stress, and mechanical and geometric specifications of the anchoring element, which

influence the performance of rock bolting systems. The curing of thermosetting resins is an exothermic and time-dependent chemical reaction that occurs once the components (resin and curing agent) are mixed. Gelation is an important factor achieved when the chemical reaction proceeds sufficiently such that the mixture achieves a flexible but non-flowing three-dimensional high molecular structure. The gel time, early and full curing time, and viscosity of the product influence the suitability of chemically anchored rock bolts for particular applications (Fu et al., 2019).

It has been shown that the mechanical properties of the bonding agent have a significant impact on the response of rock bolts. For example, Yokota et al., (2019) found that the interfacial shear stiffness is slightly lower for specimens prepared with low-strength mortar. Teymen and Kılıç, (2018) concluded that the bond strength of fully grouted rock bolts increases logarithmically with an increase in the shear strength of the grout. However, in the experimental studies conducted by Benmokrane et al., (2000) and McKay and Erki, (1993), a clear relation between grout strength and anchor performance was not observed. Benmokrane et al., (1995) indicated that an increase in the modulus of elasticity of grouts can result in higher radial stiffness at the bolt-grout interface and, therefore, improve bond strength. Feng et al., (2022) demonstrated that the use of steel particles can enhance the mechanical performance of bolting systems. Shi et al., (2022) conducted both experimental and numerical studies, affirming the beneficial impact of the compressive strength of grouts on the effectiveness of rock bolts. Liu et al., (2021) concluded that Basalt FRP bars anchored with resin with a higher elastic modulus have higher shear stiffness compared to the bars anchored with a lower elastic modulus. Pull-out tests conducted by Dudek and Kadela, (2016) on chemically bonded steel bars showed that the bearing capacity of the bars bonded by epoxy adhesive is slightly higher than those bonded using polyester resins. The results of various studies also show that mechanical characteristics of grout play a vital role in determining the bearing capacity of rock bolts and cable bolts (Benmokrane et al., 1995; Hyett et al., 1992; Teymen and Kılıç, 2018; Yokota et al., 2019).

Previous research studies have shown that anchoring resins' mechanical properties and load-bearing capacity depend on temperature. Wang et al., (2020) examined the effects of high temperature and low humidity on the mechanical properties of grouting materials in high-geothermal tunnels. They found that these factors have an adverse effect on cementitious grout. Jahani et al., (2022)

experimentally studied the influence of temperature on the mechanical properties of a structural adhesive and found that the mechanical properties decrease when the curing and post-curing temperature exceeds the glass transition temperature (T_g) of the adhesive. It has been shown that for temperatures below 60°C, the properties of chemical bonding agents are slightly affected. However, for temperatures above 60°C, there is a significant reduction in bonding properties. Laredo et al., (2012) measured the elastic modulus, flexural strength, and compressive strength of polymer mortars under different temperatures and concluded that the flexural and compressive strength decrease at elevated temperatures.

Two sets of data are essential to characterise the bonding behaviour of an encapsulated bolt in thermal environments: the temperature distribution along the encapsulation length and the relationship between induced bond stress and temperature. The temperature profile along the bonded length is a time-dependent factor, but the testing configuration and method also affect the temperature distribution profile. There is limited literature regarding the investigation of the effects of elevated temperature on the bonding properties of chemically bonded anchors in concrete structures, particularly in underground applications. The experimental procedures and standards developed for investigating the performance of reinforcing materials in concrete structures under elevated temperatures may not be suitable for underground applications because the conditions vary significantly. Temperature rises in underground spaces, such as tunnels and mines, can be due to fire, combustion, machine working, and geothermal heat. In concrete structures, the temperature elevation in the bond is closely dependent on the geometry of the concrete structure (Pinoteau et al., 2013). In underground structures, only the free end of the reinforcing element and the external fixtures are exposed to the ambient heat, regardless of the geometry of the opening (except in the presence of geothermal heat, which is transmitted from all directions). In determining the resistance to heat of rebars in concrete structures, the main thermal flux is usually subjected to the lateral sides of the concrete specimens (Al-mansouri et al., 2019; Amine et al., 2017). The European Organisation for Technical Assessment (EOTA) outlines that "The main thermal flux shall be oriented towards the lateral side of the concrete cylinder. The non-bonded part of the rebar shall not be directly exposed to the heat source" (European Assessment Document, 2020). Al-mansouri et al., (2019) and Lakhani and Hofmann, (2017) observed a large difference in the temperature variation along the

encapsulation depth for the specimens where the bolt itself was exposed to heat compared to the specimens where the bolt was insulated.

Rock mass characteristics can also heavily influence the critical failure mechanism, failure location, and bond stiffness in the design of rock bolt systems (Hazrati et al., 2020; Salcher and Bertuzzi, 2018). The high quality of the host rock not only assures that failure will not occur in the rock, but it may also enhance the performance of the system (Moosavi et al., 2005). The axial slip of deformed bars generates radial dilation, which is inhibited or restricted by the normal stiffness of the rock mass. Hyett et al., (1992) indicate that dilation is suppressed in higher radial stiffness. Shear-off failure occurs at the bolt-grout contact, leading to greater load-bearing capacity. In contrast, in lower radial stiffness, the propagation of radial cracks through the grout annulus is predictable, resulting in a decrease in radial stress at the bolt-grout interface and, thus an instantaneous reduction in the bond resistance to pull-out. Yilmaz et al., (2013) conducted pullout tests on chemical anchors embedded in weak concrete, indicating the positive contribution of the concrete strength to the bond strength. On the contrary, Cao et al., (2014) reported the insignificance of the host rock uniaxial compressive strength (UCS) ranging from 30-136 MPa on the pullout capacity of rock bolts.

In-situ stress has a crucial role in the failure mode of an excavation (Li, 2017). Conversely, external confining stress can enhance the performance of rock bolts (Blanco et al., 2013). Therefore, it is essential to carefully consider the effect of *in-situ* stresses on the behaviour of rock bolts for their design. Hyett et al., (1995) conducted a series of pull-out tests using modified Hoek cells under constant confining pressures. The experiment results indicated that the bond strength increases with confining pressure. Thenevin et al., (2017) conducted several pull-out tests with emphasis on the influence of confinement pressure. They performed the pull-out test under constant radial stiffness and constant radial load using a triaxial cell with a confining pressure of up to 15 MP. The results were consistent with the past investigations, demonstrating that an increase in confining pressure leads to a higher peak bond strength. Kang et al., (2020) pointed out that, in practice, rock bolts are typically subjected to complex loading conditions rather than a simple pull-out load, significantly affecting their behaviour. Apart from experimental studies, analytical and numerical models have also been developed to investigate the effect of confining stress on the axial behaviour of rock bolts. Li et al., (2021) developed an analytical model based on the Modified

Continuously Yielding Criterion to analyse the performance of rock bolts under constant confining pressure. However, this model is only suitable for uniform constant confining pressure and cannot be applied to other boundary conditions. Similarly, the failure models developed by Blanco et al., (2013), Chen et al., (2020a) and Ho et al., (2019a) also assume uniform confining stress conditions.

Various types of failure can occur in response to axial bolt loads, and the type, magnitude, and direction of the distributed stress, along with the material properties of the components, dictate the main failure mode of the system. The encapsulation length determines whether a failure occurs in the bolt or another component. If the encapsulation length is sufficient to transfer all the load, then the bolt itself will fail once the applied load exceeds the ultimate capacity of the bolt. Alternatively, if the encapsulation length is insufficient, then localised failure takes place where the induced stresses exceed the material strength (either grout or rock). In the cross-sectional view, analytical solutions indicate that the induced bond stress is maximum at the bolt-grout interface and decreases exponentially with distance from the interface (Tepfers, 1979). Therefore, it is reasonable to assume that if the surrounding rock is relatively strong and bonding with the grout-rock, then the interface is sufficient to withstand localised stresses. Then failure occurs at the bolt-grout interface. This failure mode has often been reported as the main failure in the literature, although fractures, partial failure, and deformation in other parts have been observed to occur simultaneously. When debonding at the bolt-grout interface occurs, the deformation of the other parts can usually be neglected (Antino et al., 2016). In this case, the axial behaviour of the rock bolt can be effectively studied by examining the stress distribution along the bolt-grout interface. Pullout tests are commonly conducted to evaluate the axial behaviour and anchorage capacity of grouted rock bolts. Studies have shown that the evolution of stresses along the encapsulation length is non-uniform, and that the stresses decrease with distance from the loading point. Initially, the peak bond stress is captured near the loading end, but it decreases once debonding occurs and shifts incrementally towards the free end. Farmer, (1975) investigated the axial behaviour of fully grouted rock bolts and developed a theoretical model showing that the bond stress attenuates exponentially from the loading point to the far end of the bolt. The proposed theory was comparable to experimental results at lower anchor loads. Li and Stillborg, (2000) introduced a bond model for fully grouted rock bolts that illustrates how the bond stress develops from the loading end to the

free end. The proposed model consists of four main parts including a fully decoupled part where the bond stress is zero, a partially decoupled part with constant residual bond strength, a linear softening part that reaches the peak strength, and finally, a compatible deformation part where the bond stress decreases exponentially towards the free end of the bolt. The latter stage can be matched with the elastic stage introduced in other models. Benmokrane et al., (1995) assumed an average distribution of bond stress along the anchored length and expressed a trilinear debonding model between the induced bond stress and global slip based on experimental investigations. Afterwards, numerous trilinear bond-slip models were proposed including those by Yue et al., (2022), Martín et al., (2011), Cai et al., (2004), Ren et al., (2010), Chen et al., (2020b), Ma et al., (2013), and Zhou et al., (2010). Instrumented rock bolts using electric sensors, such as resistive strain gauges and fibre optics, have also been effectively used to measure axial strain along the anchored length to estimate the load. This information can be used to quantify the induced bond stress along the encapsulation length (Chen et al., 2020b; Farmer, 1975; Freeman, 1978; Huang et al., 2013; Singer et al., 1997; Teymen and Kılıç, 2018; Vlachopoulos et al., 2018; Zhang et al., 2006). Several factors including rock bolt geometry, bolt surface configuration, mechanical characteristics of the bolt, grout, and host rock, boundary conditions, anchorage length, drilling quality and drillhole diameter, annulus thickness, and installation and grouting quality affect the axial behaviour and bearing capacity of grouted bolts. Some of these factors can be engineered to improve the system's performance. Thus, a proper understanding of the combined effects of these factors is essential for practical rock bolting design.

Steel reinforcing elements are vulnerable to corrosion in their natural surroundings due to a thermo-electro-chemical process between cathodic and anodic areas. These regions can develop around voids or cracks that extend through the grout to the reinforcement. The void functions as an anode, where steel oxidation occurs, resulting in electron loss. These electrons are absorbed by cathodic regions on either side of the void. The steel acts as a conductor between these areas, with pore fluid acting as an electrolyte. Corrosion reduces the steel's cross-sectional area, increasing stress until the anode's electrons are depleted, potentially causing failure. Aziz et al., (2014) conducted a study on the long-term exposure of full-size bolts to a corrosive environment. The results show a reduction of up to 12.80% in the cross-sectional area of the bolts observed during the investigation.

Different types of corrosion affect rock bolts, encompassing crevice corrosion, pitting corrosion, stress corrosion cracking (SCC), and organic corrosion (Chen et al., 2021; Wu et al., 2019). Pitting corrosion, in particular, causes a big challenge, given its propensity to diminish the cross-sectional area of the bolt. This corrosion phenomenon not only compromises the structural integrity of the rock bolt but also poses significant obstacles to its overall performance and longevity.

Cementitious grouts using Portland cement are highly alkaline (pH 12-13). However, hardened cementitious grout reacts with carbon dioxide, leading to carbonation that reduces pH and initiates corrosion, particularly if the oxide film on the steel's surface is compromised. Additionally, hardened grout is prone to chloride penetration, reaching depths of over 50 mm and initiating corrosion. Pre-tensioned or heavily loaded elements are especially risky, as stress amplifies due to reduced cross-sectional area, accelerating corrosion through stress corrosion. Nitrates, hydrogen, and hydrogen sulphide are known stress corrosion contributors.

To protect steel reinforcing elements, various methods are available including painting, galvanising, epoxy coating, combination coating, sheathing, and combination sheathing. The sheathing is notably effective, particularly when slip is needed over a specific interface length, common when decoupling a "free length" for pre-tensioning. This involves encasing the reinforcing element in a flexible outer sheath (often High-Density Poly-Ethylene (HDPE)) filled with grouts. Engineering practice has proven its efficacy for corrosion protection, as it provides needed stiffness and controlled displacements through internal anchors. Nonetheless, the impact of sheathing on rock bolt axial performance requires further study.

This thesis presents a qualitative and quantitative discussion on the axial performance of full-encapsulated rock bolts under different conditions. Firstly, the mechanical and thermal characteristics and behaviour of commonly used anchoring UP resins were investigated. Additionally, the bearing performance of encapsulated rock bolts was investigated under elevated temperatures in simulated underground heating conditions. The interrelationship between the bearing capacity of rock bolts under ambient and elevated temperature conditions and the thermo-mechanical characteristics of the anchoring materials was then examined, and the relevant failure patterns were analysed. As previously stated, the conventional testing procedure developed for evaluating the effects of high temperatures on the performance of anchoring materials in concrete structures is not suitable for underground structures.

To address this incompatibility, a new testing set-up was designed to mimic the conditions of these environments. Secondly, to understand the effect of confining stresses in non-uniform conditions ($\sigma_2 \neq \sigma_3$), rock-bolted cubic samples were tested under triaxial stress conditions. Understanding the impact of confining stresses on rock bolt behaviour by simulating actual *in-situ* conditions can effectively inform the design and construction of more efficient and reliable rock support systems, leading to safer and more efficient underground excavations. The interaction between confining stresses and the principal stress ratio ($k=\sigma_2/\sigma_3$) and interfacial bond strength was also investigated. Thirdly, an all-encompassing laboratory study delved into the pullout performance of fully grouted rock bolts, guided by the intent of addressing four pivotal inquiries pertaining to the axial load transfer mechanism of rock bolting: How does the embedment length influence the distribution of bond stress and consequent system failure? To what extent does the choice of bonding material impact the distribution of bond stress? What correlation exists between peak bond resistance and the type of bonding material employed? How do the inherent properties of the host rock contribute to the distribution of bond stress and eventual failure mechanisms of the bolts? Lastly, this thesis investigated a facet that had been astonishingly disregarded within the literature: the effect of a protective plastic sheath on the axial performance of fully grouted rock bolts. This negligence has been rectified through comprehensive experimental research. The insights garnered from this endeavour substantially augment our comprehension of the axial load transfer mechanisms intrinsic to rock bolts. These insights, in turn, hold profound implications for the optimisation of their design, the finesse of their manufacturing processes, the precision of their modelling techniques, and, ultimately, their seamless integration into ground control systems.

1.2. Objectives

This doctoral thesis comprehensively explores the axial load transfer mechanisms and performance of fully grouted rock bolts across diverse geotechnical scenarios. The primary goal is to unravel the behaviour of these structural components within varying geological contexts. In the quest for this main goal, the research is carefully organised to include the following specific goals, each adding to a comprehensive understanding of the subject matter:

1. To understand the mechanical characteristics and behaviour of different types of encapsulation materials including resin-based agents and cementitious-based grouts.

2. To understand the thermal characteristics of resin-based encapsulation agents and the effect of elevated temperatures on the pullout performance of rock bolts.
3. To investigate the relationship between the mechanical characteristics of the encapsulation materials and the pullout behaviour of rock bolts.
4. To determine the effect of confining stresses on the axial load transfer mechanism of fully grouted rock bolts through true-triaxial testing techniques.
5. To evaluate the combined effect of encapsulation length, grouting mechanical characteristics and rock mass conditions on the axial performance of rock bolts.
6. To examine the axial behaviour of protective sheathed rock bolts with a focus on determining the effect of plastic sheath on the axial load transfer mechanism and failure modes of rock bolts.

1.3. Thesis organisation

This thesis is organised into seven chapters, outlined as follows:

- **Chapter 1**: Introduction

This introductory chapter lays the groundwork by providing the context and motivation for the research conducted within this thesis.

- **Chapter 2**: Literature Review

Chapter 2 offers an extensive literature review, presenting the latest advancements in the field and outlining the gaps in existing research.

- **Chapter 3**: Characterisation of mechanical and bonding properties of anchoring resins under elevated temperature

The third chapter, a technical exposition, presents experimental study exploring the thermal, mechanical, and bonding characteristics of unsaturated polyester resins. This chapter distinctly addresses the initial gap identified in Chapter 2.

- **Chapter 4**: Failure characterisation of fully grouted rock bolts under triaxial testing

Chapter 4 represents another technical segment, where the influence of confining stresses on the pullout capacity and performance of fully grouted rock bolts is investigated under true-triaxial testing conditions. This segment effectively fills the significant gap identified in the literature.

- **Chapter 5**: Unveiling Axial Load Transfer Mechanism in Fully Encapsulated Rock Bolts

The fifth chapter investigates the combined impact of encapsulation length,

grout and rock mass mechanical properties on axial load transfer mechanisms and bond stress distribution along the encapsulation length. This segment fulfil another research gap outlined in Chapter 2.

- **Chapter 6**: Exploring the Axial Performance of Protective Sheathed Rock Bolts through Large-Scale Testing

The sixth technical chapter centres on the extensive testing campaign that investigates the axial performance and behaviour of fully grouted protective sheath rock bolts. This chapter aims to technically cover an additional gap in the existing literature, as explicated in Chapter 2.

- **Chapter 7**: Conclusion and Future Outlook

Concluding the thesis, Chapter 7 provides a comprehensive summary of the main findings and contributions. Additionally, offers recommendations for future studies.

Based on the research conducted in this thesis, four journal articles have been published or are currently under review in high-ranked international journals ranked within the first quartile. Additionally, numerous papers and posters have been published and presented at national and international conferences, detailed in Appendix A.

1.4. Summary

Rock bolts play a pivotal role in mining and geotechnical engineering, enhancing rock mass stability, diminishing deformations, and reducing support costs and time. However, there exists a necessity to conduct comprehensive evaluations of fully grouted rock bolt performance under diverse geotechnical scenarios. Specifically, there is a gap in understanding their behaviour under elevated temperatures, within triaxial confinement, and under the combined influence of encapsulation length, grout properties, and rock mass attributes. Additionally, the demand for sheathed rock bolts in corrosive environments necessitates an exploration into their axial performance. These understudied aspects of reinforcement systems can limit their practical implementation and adaptation. To address these gaps, this thesis undertakes both experimental and analytical investigations into the axial behaviour of fully grouted rock bolts. This includes considering various encapsulation materials and techniques. The focus surrounds modes of bond stress distribution, axial load transfer mechanisms, system failure patterns, and the complex interactions among factors influencing the capacity and performance of these rock bolts. These investigations conclude in four technical chapters. The outcomes of this thesis enrich the overall comprehension of

rock bolt axial behaviour, offering valuable insights for designing and selecting rock bolts across diverse engineering applications. Furthermore, this information can substantially contribute to the assessment and improvement of existing analytical solutions for rock bolt design.

CHAPTER 2: LITERATURE REVIEW

2.1. Introduction

Rock bolts are crucial elements in geotechnical engineering that play a significant role in stabilising rock masses and preventing potential rockfall and rock burst hazards. These innovative devices are designed to reinforce and support rock structures by effectively transferring load and stress within the rock mass. The invention and usage of rock bolts have revolutionised the field of rock mechanics and have become indispensable in various industries including mining, tunnelling, construction, and slope stabilisation. The concept of using rock bolts originated from the need to address the inherent instability and unpredictable behaviour of rock formations. In the early days, miners and engineers faced numerous challenges while excavating underground mines or constructing tunnels through rocky terrain. They encountered issues such as rockfalls, collapsing tunnels, and instabilities that posed significant risks to workers and project integrity. To tackle these challenges, the invention of rock bolts emerged as a ground-breaking solution. The exact origins of rock bolts are difficult to trace, as their development and implementation evolved over time through experimentation and engineering advancements. However, their usage gained prominence in the mid-20th century, especially in mining operations.

Rock bolts are typically long, threaded steel rods that are inserted into pre-drilled holes in the rock mass. The holes are usually drilled using specialised machinery or handheld tools, depending on the scale of the project. The rods are then anchored in place using various techniques, such as mechanical anchoring, grouting, or a combination of both. Once installed, rock bolts provide reinforcement by creating a load-bearing system within the rock mass. They effectively redistribute stresses, enhance the overall stability of the rock structure, and mitigate potential rockfall hazards. By anchoring the rock mass to more stable zones or structures, rock bolts increase the structural integrity and prevent the movement and displacement of rocks.

Over the years, rock bolt technology has advanced significantly, with the development of various types and designs to suit different geological conditions and project requirements. Some common rock bolts include mechanical rock bolts, expansion shell anchors, resin bolts, and grouted bolts. Each type has advantages and is selected based on factors such as rock type, load requirements, and installation

conditions. The invention and widespread usage of rock bolts have significantly contributed to the safety and efficiency of rock engineering projects. They have facilitated the construction of underground mines, tunnels, and infrastructure in challenging geological conditions. Rock bolts continue to evolve, with ongoing research and development focusing on enhancing their performance, durability, and ease of installation.

2.2. Ground control systems

Ground control is the science of studying, examining, and controlling the deformation occurring in rock strata/mass in response to excavations. Ground support systems which have been used for many years both in surface, near surface and deep excavations, are generally natural and artificial techniques and systems employed to limit the undesired rock mass displacement/deformation. Over time, many ground-supporting products have been developed to improve the stability of the rocks. However, it is beneficial to distinguish between elements and techniques contributing to ‘supporting’ the rock mass and those that contribute to ‘reinforcing’ rock mass. Therefore, herein two definitions are introduced:

Support is the application of techniques and devices to provide reactive forces to the surface of excavations. The support systems include timber, shotcrete, mesh, steel and concrete sets and liners. The support systems can be divided into three categories: point support systems, strip support systems and areal support systems (Galvin, 2016).

Reinforcement refers to the devices and techniques that improve the rock mass properties from within the rock mass. The reinforcement systems include rock bolts, cable bolts and ground anchors (Galvin, 2016).

Both support and reinforcement techniques may be **passive** or **active**. In the passive case, displacement in the rock mass is required to create a reactive force to resist further movement. While in the active mode, the measure provides already pre-load to the rock mass. Thus, it interacts with the rock mass immediately after installation. In general, it is true to say that **support systems** are used to resist rock mass displacement while **reinforcement systems** are utilised to strengthen rock mass leading to displacement prevention and restriction (Galvin, 2016).

In terms of the time of installing the supporting/reinforcing measure, three definitions can be introduced including **primary support** describing the measures applied during or immediately after excavation, **secondary support** referring to the

measure applied sometime after excavation and **tertiary support** referring to the additional support and reinforcement measures installed subsequent to the installation of secondary support.

2.3. Support systems

2.3.1. Standing support

Standing support refers to devices and techniques designed and installed between the roof and floor of excavation to provide restriction against potential convergence. These systems principally include wooden, steel and hydraulic props, timber and cementitious chocks, and rock pillars (Figure 2.1).

Figure 2.1. Standing support systems wooden props (tope-left), hydraulic props (top-right), CAN© cementitious chocks (bottom-left) and timber chocks (bottom-right) (Galvin, 2016)

2.3.2. Steel arches and sets

Steel arches and sets have been significantly substituted by rock bolts and cable bolts in modern mining practices. Yet, circumstances may arise where anchoring the reinforcing element becomes impractical or when substantial load transfer is not feasible through these elements. More importantly, if there is a need to distribute the dead load to the excavation surroundings, steel arches can be a viable solution to meet these specific demands (Figure 2.2).

Figure 2.2. Steel arch support

2.3.3. Shotcrete

Shotcrete is a method of applying sprayed concrete onto surfaces to stabilise and reinforce excavations. It involves pneumatically projecting a mixture of cement, aggregates, and water onto the surface using a nozzle. Shotcrete provides immediate support and can conform to irregular surfaces. It is commonly used in tunnelling, mining, and slope stabilisation projects (Figure 2.3).

2.3.4. Steel mesh

Steel mesh, also known as wire mesh or wire netting, is used in conjunction with shotcrete or as a standalone ground support system. It consists of interwoven steel wires, forming a mesh pattern. Steel mesh provides tensile strength and confinement to the shotcrete or surrounding rock mass, enhancing stability and preventing rockfall (Figure 2.4).

Figure 2.3. Shotcrete support system

Figure 2.4. Mesh support system

2.4. Reinforcement systems

Reinforcement systems refer to any materials including bar, tube, and wire strands embedded and anchored within the rock mass surrounding the excavation. The reinforcement systems are generally associated with boreholes drilled in the surrounding medium. The most used reinforcement systems are:

- Steel and fibreglass rock bolts
- Cable bolts
- Split steel tubes
- Expandable steel shells

However, split steel tubes and expandable shells are usually considered in rock bolts. Reinforcement systems can be classified into one of the three categories listed in Table 1.

Table 1. Classification of reinforcement systems.

Reinforcement support classification	Nature of instability	Typical Length
Rock bolts	Surface	0-3 m
Cable bolts	Near surface	3-15 m
Ground Anchors	Deep seated	10-30 m

Rock bolts are usually a bar inserted into a borehole in a rock mass to strengthen the stability of the excavation. Rock bolts are manufactured using different materials, e.g., steel, fibreglass, carbon fibre, etc. Steel rock bolts are manufactured with a typical diameter of 22 mm deformed rod and are usually 1.2-2.2 m long for mining applications. Rock bolts can be anchored in the hole by different techniques and materials, which will be discussed later in this chapter. On the other hand, cable

bolts are the evolution of rock bolts and comprise a number of wires 6-7 mm in diameter stranded together, usually around a core. Cable bolts usually offer higher tensile capacity compared to rock bolts (600 kN vs. 300 kN). Cable bolts are flexible due to their structure making them applicable in longer holes (≈8m), while the typical rock bolts have a length of 2.1 m. Cable bolts are generally used in suspension applications by which large beams or blocks are pinned to above competent strata layers (Windsor, 1997).

As shown in Figure 2.5, cable bolts are installed in a hole pre-drilled into the rock mass and embedded in place using a pumpable bonding agent, i.e., cementitious grout or resin. The bonding agent is pumped through a central hole located on the free end of the cable bolt allowing it to fill the hole top to down. Using the barrel and wedge assembly along with a shell anchor or fast-set resin at the top of the hole allows for pretension in the reinforcement system.

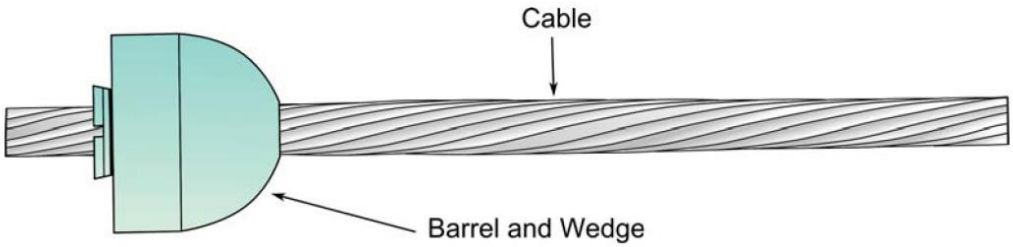

Figure 2.5 Cable bolt assembly (Vandermaat, 2014)

2.5. The origins of rock bolts: a historical perspective

The exact origins of rock bolts remain unclear, but their usage is believed to have begun in the late 19th century. However, the utilisation of steel materials for underground support dates back even further to the late 18th century. The earliest documented evidence of rock bolts in their modern form can be traced back to a patent submitted by Stephan, Frohlich, and Klupfel in 1913 (Kömürlü and Kesimal, 2016). In terms of the application of steel anchors, a publication from 1919 highlights the importance of replacing timbering with iron anchors in the Konigshutte coalfield in Upper Silesia, which was part of Germany at that time (Kovari, 2003). This publication verifies that the section supported by the bolts remained intact during a four-year testing period, in contrast to the timber-supported section that collapsed due to timber rotting. In a subsequent development, Keeley, (1934) documented a support concept employed in the McIntyre mine in Canada (Figure 2.6). This concept involved the application of a 3-meter-long expansion anchor to stabilise a hoist chamber. Weigel, (1943) authored the first publication containing relevant technical information on

anchoring bolts, providing an overview of its successful global applications. In a related study, Beyl, (1945) investigated the impact of anchors on ground deformation by measuring the magnitude of convergence in underground spaces. Notably, the literature highlights a remarkable surge in the adoption of rock bolts in American coal mines between 1943 and 1950 (Conway, 1948; Thomas et al., 1948), indicating a significant and rapid growth in their usage. A similar interest in employing rock bolts was also observed in Europe after 1950.

Statistical data from 1948 to 1950 vividly illustrates the rapid success of steel anchors in the United States, with a staggering 1,400 km of mine tunnels supported using these anchors (Forbes, 1950). Subsequently, starting from the 1950s, there was a notable increase in the number of publications encompassing laboratory and field research, textbooks, technical notes, and standardisation relating to anchors. The initial implementation of systematic anchoring bolts in tunnelling was documented in the construction of the Keyhole Dam in Wyoming, United States, in 1950 (Grundy, 1951). Pierce, (1953) reported that out of the total 42 km of the Delaware Water Supply Aqueduct project in New York, a substantial 19.5 km of the roof was systematically supported by rock bolts (Figure 2.7). Talobre, (1957) proposed an engineering model in which the radially arranged bolting pattern and the effective area was discussed.

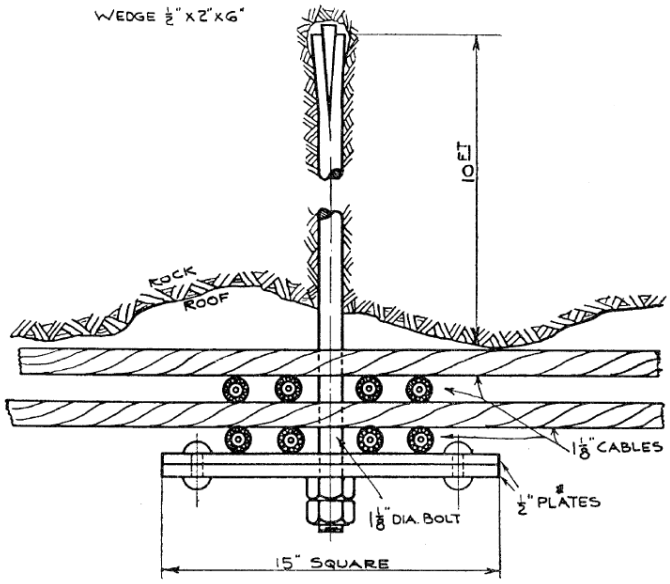

Figure 2.6. The rock bolt used in McIntyre mine in Canada (Keeley, 1934)

The information above highlights the increasing effectiveness of rock bolts as the primary supporting systems in various engineering fields including civil, mining, and geotechnical engineering. This recognition has been steadily growing since the

mid-20th century. Subsequently, significant advancements have been achieved in the design and materials used for these systems. The evolution of rock bolt design has been driven by the need to address the diverse challenges encountered in different engineering applications. Engineers and researchers have explored various factors to optimise the performance of rock bolt systems. Additionally, advancements in materials technology have played a vital role in the development of rock bolts. Steel has been widely used due to its strength and reliability. Alternative materials including composites and synthetic fibres, have also gained attention for their advantages, such as high strength-to-weight ratio and resistance to corrosion.

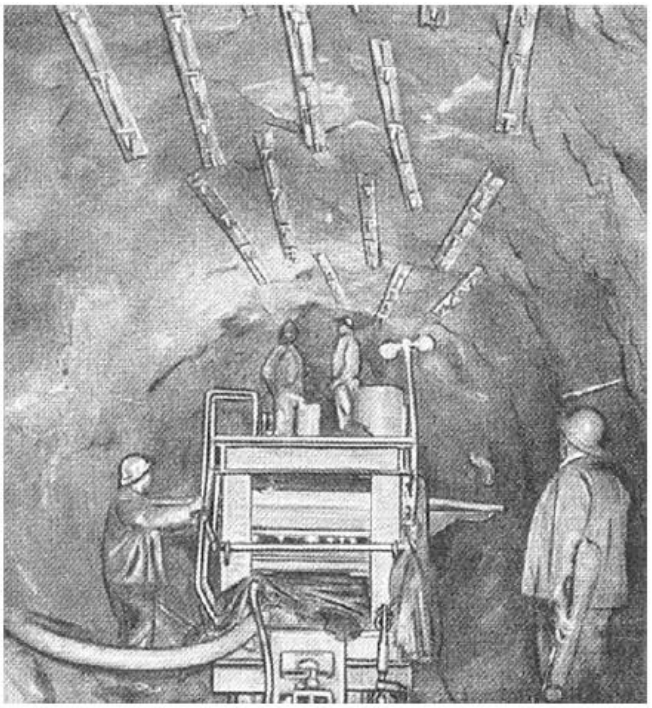

Figure 2.7. Rock bolts installation in the roof of Delaware Water Supply Aqueduct (Pierce, 1953)

2.6. History of the application of rock bolts in Australia

Australia adopted rock bolts for ground control in the late 1940s, following their introduction from the United States. In the Snowy Mountain Hydroelectric Scheme, which is regarded as one of the greatest engineering projects of the 20th century, rock bolts were incorporated as crucial elements in the tunnelling design for structural support. The Snowy Mountains Scheme was crucial in pioneering rock bolting and its advancements in Australia, employing it extensively for tunnel excavations and slope stability (Brown, 2002). Before the advent of rock bolts, timber props were the primary method of roof support in Australian underground mines (Gardener, 1971). Rock bolts revolutionised ground control in underground mines, significantly enhancing safety

and productivity in the mining industry. Elrington Colliery in New South Wales implemented the first experimental rock bolts in Australian coal mines in 1949 (Gardener, 1971). These early rock bolts had dimensions of 23 mm in diameter and 2200 mm in length and were used to supplement existing timber supports. The rock bolts were secured in place using a slot and wedge assembly installed with a pneumatic stopper and tightened with a nut, but they lacked significant pre-tensioning. The successful experiment led BHP to commence rock bolt manufacturing at their Port Kembla steelworks (Scotford, 1960). Eventually, a dedicated facility was constructed in Newcastle in 1961 to manufacture rock bolts, further affirming their success (Rataj and Yearby, 1999).

2.7. Classification of rock bolts

There is no unique definition for rock bolts, however, it is generally defined as a bar installed and fastened in a borehole drilled in rock with the aim of strengthening underground opening and slope stability (Blanco et al., 2013). Rock bolting systems can be classified based on various criteria, which may vary slightly depending on the context and specific application including the anchoring mechanism, type of encapsulation material, mechanical behaviour of the rod, material and shape of the rod, system reinforcement mode, and application. Among these criteria, the anchoring mechanism has been the most referenced factor in the classification of rock bolts. The anchoring mechanism refers to the method by which the rock bolt achieves its load-carrying capacity and provides stability to the surrounding rock mass. Table 2 presents the available rock bolts based on the different classification criteria. It is important to note that the classification of rock bolts may not be mutually exclusive, and different criteria can overlap. The selection of rock bolts for a particular project depends on various factors including geological conditions, load requirements, and engineering design considerations. The choice of anchoring mechanism is crucial as it directly affects the effectiveness and reliability of the rock bolt in providing support. Three main types of anchoring mechanisms are commonly employed: mechanical anchorage, bonded anchorage, and hybrid anchorage. These will be further elaborated upon in the subsequent sections.

2.8. The function of rock bolts

The *in-situ* stress redistribution weakens and fractures the rock mass surrounding an underground excavation. The primary objective of reinforcing with rock bolts is to enhance the strength of jointed rocks, prevent strata separation and control

the deformation after post-failure, enabling it to support itself (Bieniawski, 1984). The effectiveness of rock bolts is influenced by factors such as the type of rock bolt, anchorage system, lithology of the strata, and other geological and geotechnical conditions. Consequently, numerous theories have been proposed to explain the mechanisms behind rock bolting in ground support. The bolt system functions through one or a combination of three fundamental mechanisms: suspension, beam building, and keying (Luo et al., 1998), as described below.

2.8.1. Suspension

When excavating an opening, the laminated immediate roof often detaches from the main strata. According to the suspension theory, the immediate roof of the excavation is weaker compared to the upper layer, resulting in this scenario. In such cases, rock bolts are employed to secure the immediate roof to the self-supporting main roof by transferring the weight load of the strata between face plates and anchors to the main roof. Figure 2.21 illustrates the suspended weak roof strata connected to the competent strata. It is necessary for the bolts to have sufficient length to anchor into the stable rock and possess adequate tensile strength to uphold the weight of the rock.

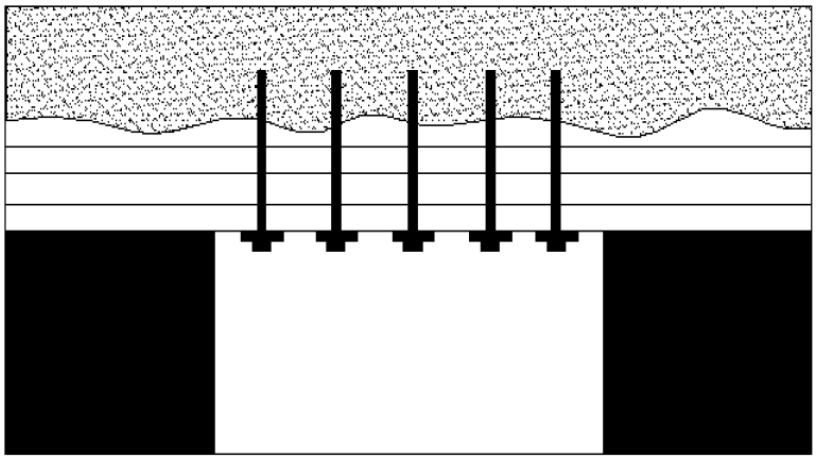

Figure 2.8. Suspension of the strata using rock bolts (Karabin and Debevec, 1977)

2.8.2. Beam building

In situations where the competent strata are inaccessible for regular roof bolts in terms of length or absent altogether, rock bolts can still be utilised to connect thin and feeble individual layers, forming a unified "beam". The internal rock bolts inserted through these weak layers serve the purpose of directly resisting shear forces generated by horizontal movements between the rock beds. Additionally, they contribute to increased friction between the layers by applying a perpendicular normal

force to the bedding plane (Luo, 1998). Figure 2.22 provides a visual depiction illustrating the primary role of rock bolts in beam building.

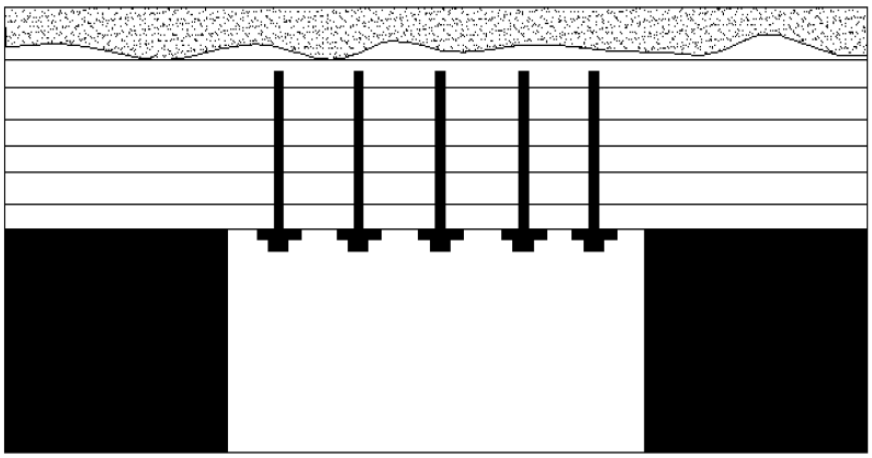

Figure 2.9. Beam building using rock bolts (Karabin and Debevec, 1977)

2.8.3. Strata keying

In the case of extensively fragmented and jagged roof layers, using rock bolts can enhance the frictional grip along rock joints, fissures, and vulnerable surfaces, as illustrated in Figure 2.23. By installing rock bolts, the occurrence of slippage and detachment between rock fractures can be avoided or reduced. The tension applied to the bolts significantly influences the keying effect, effectively securing and interlocking the fractured rock mass.

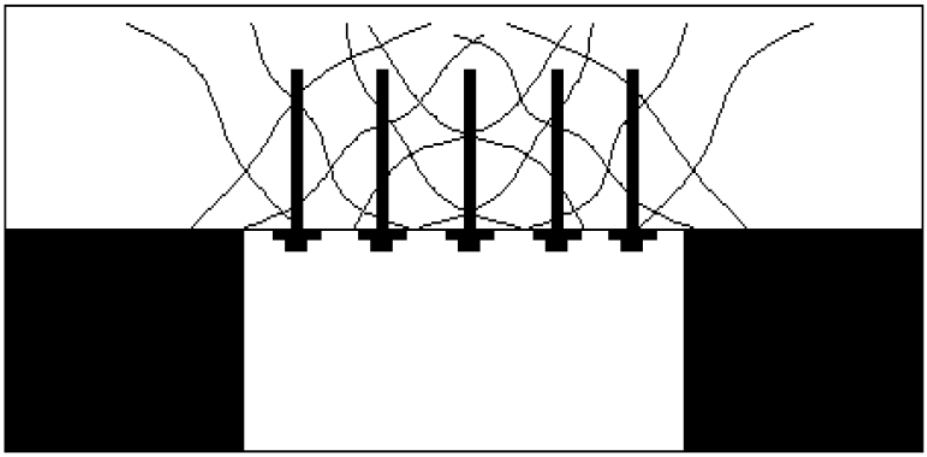

Figure 2.10. Keying of fragmented roof strata (Karabin and Debevec, 1977)

2.9. Mechanically anchored rock bolts

Mechanically anchored rock bolts are a type of rock bolt commonly used in geotechnical engineering and mining applications. Unlike the bonded anchorage rock bolts, mechanically anchored rock bolts achieve their load-carrying capacity through mechanical devices integrated into their design. The main purpose of mechanically anchored rock bolts is to provide immediate and reliable support in rock masses where

grouting may not be practical or necessary or where the desired level of support cannot be achieved through bonding alone. These bolts are particularly useful in challenging geological conditions or when time is a critical factor in the installation process. The anchorage mechanism of mechanically anchored rock bolts typically involves the use of expansion shells, wedges, or other mechanical devices. These devices are strategically placed along the length of the bolt and rely on frictional resistance or wedging action to secure the bolt within the drilled hole. By applying tension to the bolt, the mechanical devices expand or wedge against the rock, creating a secure and stable anchorage. The following examples are the most common types of mechanically anchored rock bolts:

Table 2. Classification of the rock bolts using different methods.

Classification criteria	Rock bolt type	Sub-classification
Anchoring mechanism	End (point) Anchored Bolts	
	Friction Anchored Bolts	
	Bonded Bolts	
	Hybrid anchored Bolts	
Mechanical behaviour of rod	Rigid	
	Ductile	
	Energy absorbing	
Material and shape of the rod	Steel Rebars	Mild Steel Bars
		Deformed Steel Bars
		High-Strength Deformed Bars
	Polymer Composite Rock Bolts	Fibre Glass Reinforced Polymer
Corrosion Protective Bolts	Steel Bolts	Galvanised Rebar
		Epoxy-Coated Rebar
		Stainless Steel Rebar
		Double Corrosion Rock Bolts
	Polymer Composite Rock Bolts	
Type of encapsulation material	Chemical-based bonding materials	Unsaturated Polymer Resin (UPR)
		Vinyl Ester Resin (VER)
		Epoxy Resin
	Non-chemical-based bonding materials	Cementitious Grouts
System reinforcement mode	Active Rock Bolts	
	Passive Rock Bolts	
Application	Temporary Rock Bolts	
	Permanent Rock Bolts	
Installation	Conventional Rock Bolts	
	Self-drilling Rock Bolts	

2.9.1. Split set anchors

The Split Set bolts were initially developed by (Scott, 1983). As shown in Figure 2.8, the system consists of a slotted tube made of high-strength steel and a face plate. Installation involves inserting it into a slightly smaller hole, and the spring force generated by compressing the C-shaped tube creates frictional anchorage along the entire length of the hole. Due to its quick and easy installation, the system has

gained worldwide acceptance among miners. It is particularly valuable in environments with mild rock bursts because it is designed to slip instead of rupture. As the demand for the Split Set bolts does not exceed their capacity, the system functions effectively and can be considered for various mining applications. However, it is rarely utilised in civil engineering projects. One of the main challenges associated with Split Set bolts is corrosion, as it is difficult to protect the outer surface of the dowel. While galvanising the tube helps to reduce corrosion, it is not a foolproof solution for long-term applications in aggressive environments. Sandvik Australia has designed and developed friction bolts that incorporate a bar and wedge arrangement at the bolt's top end, as shown in Figure 2.9. These specialised bolts are intended to be fully driven into the hole, and once in place, the nut at the bottom is rotated. This rotational action activates a set of wedges, effectively securing the top end of the bolt firmly in the rock.

Figure 2.11. Conventional Split-Set anchors including the plate (left) and bolt (right) (Jennmar Australia, 2017)

Figure 2.12. D47 MDX Sandvik Bolt (Sandvik, 2016)

2.9.2. Swellex anchors

Swellex anchors (dowel) are composed of a steel tube, e.g., 42 mm in diameter, which is folded during manufacturing to form a 25-28 mm diameter unit that can be installed in a hole with 32-39 mm diameter (Figure 2.10). The dowel is actively anchored and provides resistance by blasting high-pressure water, e.g., 30 MPa, by which the folded tube is inflated and makes contact with the wall of the borehole. Stillborg, (1994) performed pull tests on dowels with high tensile strength and enhanced ductility properties that were installed across a simulated joint. The results unveiled that when the joint opens, it generates a stress concentration on the section of the dowel that traverses the joint. This initiates a progressive reduction in the dowel's diameter at the joint, leading to continuous debonding of the system. However, owing to the ductile characteristic of the steel, the system was capable of undergoing debonding at a consistent load at the joint until failure occurred at 140 mm of

displacement, thereby facilitating enhanced energy absorption.

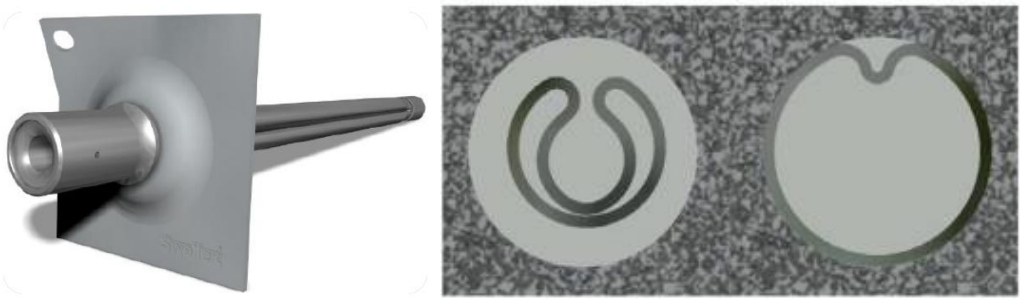

Figure 2.13. Swellex bolt and its application
(Jennmar Australia, 2017; Minova, 2019)

2.9.3. Expanding rock bolts

Expanding rock bolts are composed of a threaded rod at one end and segments or sections that can expand radially when the bolt is under tension (Figure 2.11). The other end is either forged or threaded to accommodate a nut. The expansion of these segments against the rock creates a gripping effect and establishes secure anchorage. It is essential to always install this type of anchor with a surface plate since it is specifically designed to be mechanically tightened for tensioning purposes. Each type of expansion shell anchor has its unique design and characteristics, offering varying levels of load capacity, adaptability to different rock conditions, and ease of installation. The appropriate expansion shell anchor selection depends on factors such as rock strength, joint spacing, anticipated loads, and project requirements.

Figure 2.14. Expansion shell anchors; whole system (top) and expansion shell (bottom) (Jennmar Australia, 2017; Minova, 2019)

2.10. Bonded rock bolts

Bonded rock bolts, also known as grouted rock bolts, are widely used in geotechnical engineering and mining industries to provide stability and reinforcement to rock masses. These bolts consist of a steel bar or strand that is installed into a borehole drilled into the rock, and the annulus between the bolt and the surrounding rock is filled with a bonding material. Hence, the entire bolt length can provide

resistance against any movement (Figure 2.12). The anchorage mechanism of this type of rock bolt is achieved by bond resistance (stress) between the components, i.e., bolt, grout, and surrounding rocks. Grouting is a crucial step in the installation of bonded rock bolts. The grout material, typically a cementitious or resin-based compound, fills the annular gap between the bolt and the rock, creating a strong bond between the two. The grout material should possess suitable properties such as high strength, low shrinkage, good adhesion to both the bolt and the rock surface, and resistance to environmental factors such as moisture or chemical degradation. The installation process involves drilling a hole into the rock mass at a predetermined depth and diameter. The hole is then thoroughly cleaned to remove any loose debris or contaminants that could hinder the bonding process. The rock bolt is inserted into the hole, ensuring proper alignment and contact with the surrounding rock surface. Finally, the grout material (cementitious grout or plumbable resin) is pumped into the annulus under pressure, displacing any remaining air or water and filling the void completely. When utilising resin capsules, which are commonly available in a two-component capsule format, the capsules are inserted into the drill hole, and the bolt is pushed into the capsule and rotated to ensure thorough mixing and adequate hardening of the mastic and catalyst components (Figure 2.13-top). This process facilitates the chemical reaction that transforms the resin into a durable and robust adhesive, reinforcing the rock formation. Once the resin components are mixed properly, the rotation is stopped, and the bolt is held in place for the specified set time. Once the required hardening is achieved, the bolt is torqued to the pre-determined torque in accordance with the approved ground control plan. When utilising cementitious grouts or pumpable resins for bonding, there are three techniques available for filling the annulus area including filling the drill hole before inserting the bolt (Figure 2.13-bottom), pumping the grout or resin through the designated grout hole positioned at the centre of the bolt (Figure 2.13-middle), and pumping the grout through the specified hole located on the grouting dome, where the installation of a steel or plastic sleeve along the bolt is necessary.

Figure 2.15. Conventional bonded (grouted) rock bolts (Jennmar Australia, 2017)

2.11. Hybrid anchored rock bolts

Hybrid anchored rock bolts combine multiple anchoring techniques, incorporating both the expanding shell and bonding mechanisms. These versatile rock bolts can be utilised as either a temporary or long-term ground control system. For instance, Figure 2.14 shows a rock bolt incorporating an expansion shell and grouting technique for installation—this arrangement, known as CT Bolt, was introduced in the early 1990s. The system consists of a threaded rod at both the top and bottom ends, with an expanding segment and a dome securely attached. The expanding shell provides immediate point anchorage while grouting the entire length of the bolt ensures comprehensive resistance against the applied load. The corrosion-protective polyethylene sleeve, or sheath, is affixed to the grouting dome to maintain proper alignment. Once the bolt is tightened and the expansion shell is activated, grout is injected into the bolt through the strategically positioned hole on the grouting dome. Hybrid anchored rock bolts offer the advantage of combining immediate point anchorage and full-length resistance, providing enhanced stability and support.

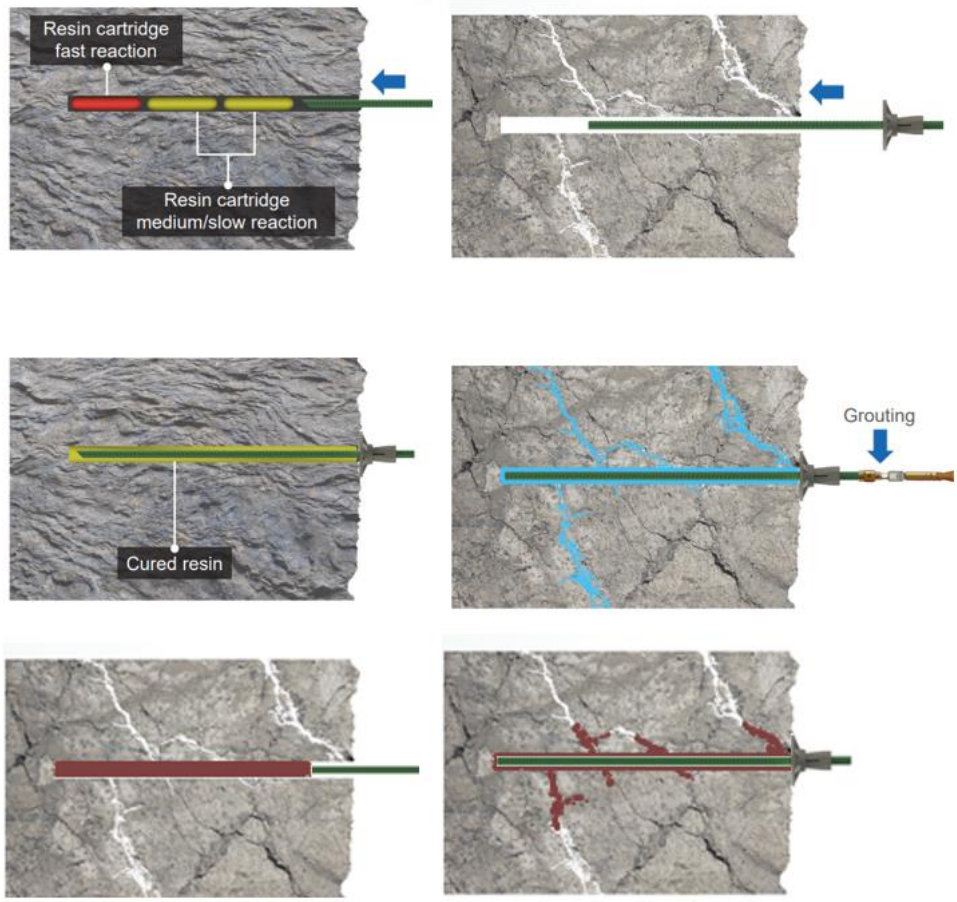

Figure 2.16. Different techniques to bond the rock bolts in the drill holes including resin capsules (top), grout-resin pumping after installation (middle), grout pumping before installation (bottom)

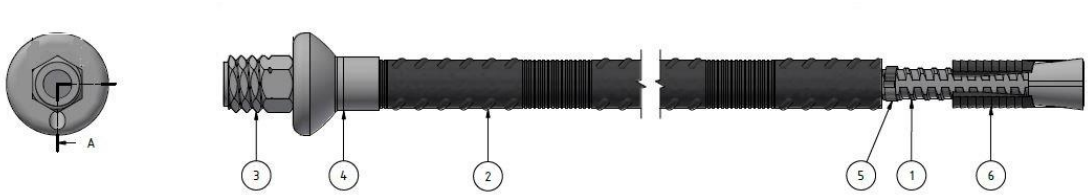

Figure 2.17. CT Bolt, which includes the expansion shell and also grouting technique; (1) thread bar, (2) HDPE protective sheath, (3) nut (4) grout bell, (5) bolt clip and (6) expansion shell (DSI Australia, 2018)

2.12. Engineered rock bolts

Self-drilling rock bolts are specialised anchoring systems designed to provide reinforcement and stability in rock and soil formations. These bolts are unique because they can be installed in a single operation, eliminating the need for pre-drilling or separate drilling equipment. The installation procedure for self-drilling rock bolts involves the use of a drilling rig or similar equipment that combines drilling and grouting functionalities. The bolt is equipped with a hollow core and an integrated drill bit at the front, as shown in Figure 2.15. As the bolt is rotated and pushed into the ground, the drill bit cuts through the rock or soil, creating a hole while simultaneously removing debris through the hollow core. Once the desired depth is reached, grout is injected through the hollow core under high pressure, filling the annular gap between the bolt and the surrounding ground. This grouting process enhances bonding and load transfer between the bolt and the formation, providing increased stability and support. Self-drilling rock bolts are commonly employed in applications such as tunnelling, slope stabilisation, mining, and ground reinforcement. Their efficient installation procedure and ability to combine drilling and grouting functions make them a preferred choice in situations where quick and reliable anchoring is required.

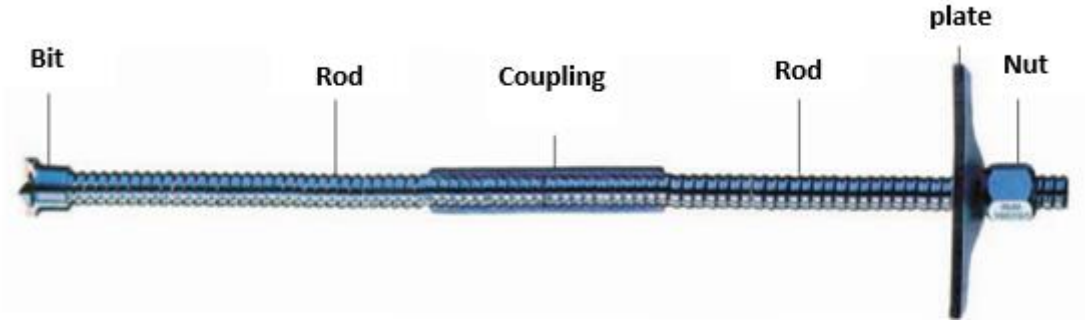

Figure 2.18. Self-drilling rock bolt (Atlas Copco, 2008)

2.13. Bonding materials

Different types of bonding materials are used in rock bolting to ensure effective anchorage and reinforcement. Two commonly employed categories are non-chemical

and chemical. Cementitious grouts are popular for rock bolting applications categorised in non-chemical bonding materials. These materials are composed of cement and additives, which are usually incorporated to increase mechanical characteristics and workability. Cementitious grouts offer robust bonding properties and can be pumped into the annular gap between the bolt and the surrounding rock. They harden over time, providing long-term strength and durability. Cementitious grouts are commonly used in applications requiring high load-bearing capacity, such as tunnelling and ground support for underground excavations. Figure 2.16 illustrates some cementitious grouts that are widely used in the Australian market. Stratabinder HS boasts low viscosity for optimal penetration into strata, coupled with a high early strength of 30 MPa achieved within 24 hours. The slow-set variation, Stratabinder HS Slow Set, provides a flexible option that remains workable for several hours. Conbex HES is a rapid-strength-gain grout (reaching up to 60 MPa within 24 hours) designed to minimise the risk of strata slippage. Its thixotropic properties make it well-suited for use in badly broken ground. Jennmar Bottom-up 100 grout (BU100) delivers an impressive strength of 100 MPa, ideal for cable bolting. This grout features a unique expansion system designed to counteract potential shrinkage. Stabilcem T, produced by MAPEI, is a pre-blended thixotropic mortar with controlled shrinkage specifically formulated for anchoring applications.

Figure 2.19. The commonly used cementitious grouts in rock bolting and cable bolting in Australia (Jennmar Australia, 2017; MAPEI, 2020; Minova, 2019)

Chemical bonding materials including unsaturated polyester resin (UPR), vinyl ester resin (VER), and epoxy resin, are other types of bonding materials used in rock bolting. They are available in two main forms: pumpable resins and two-component resin capsules. Pumpable resins also known as double-component resins, are mixed before pumping into the hole using a specific mixer. These resins typically consist of a base resin and a catalyst with various additives, providing good adhesion and load transfer. They cure to a solid state, ensuring reliable anchorage and support. Figure

2.17 depicts one of the commonly utilised pumpable anchoring resins in Australian underground coal mining. CarboThix™ is a thixotropic and rapidly curing silicate resin developed specifically for the installation of rock bolts in strata and for consolidation injection in disrupted strata.

Figure 2.20. Carbothix pumpable resins (Minova, 2019)

Resin capsules are also commonly used in rock bolting as a convenient and efficient method for introducing resin into boreholes, particularly in underground mines. They consist of a cylindrical container typically made of plastic or foil, filled with pre-measured quantities of resin and hardening agent (Figure 2.18). The capsule is designed to rupture and mix the components when subjected to pressure or impact during the installation of the bolt. The installation process of resin capsules, as seen in Figure 2.18, involves placing the capsule into the borehole, usually with the aid of a capsule insertion tool. Once the capsule is properly positioned, a mechanical or manual force is applied to break the capsule, initiating the mixing of resin and hardening agent by rotating the bolt with the prescribed rotation speed and time. The rupture of the capsule allows the resin to flow and fill the annular space between the bolt and the surrounding rock, ensuring bonding and anchorage.

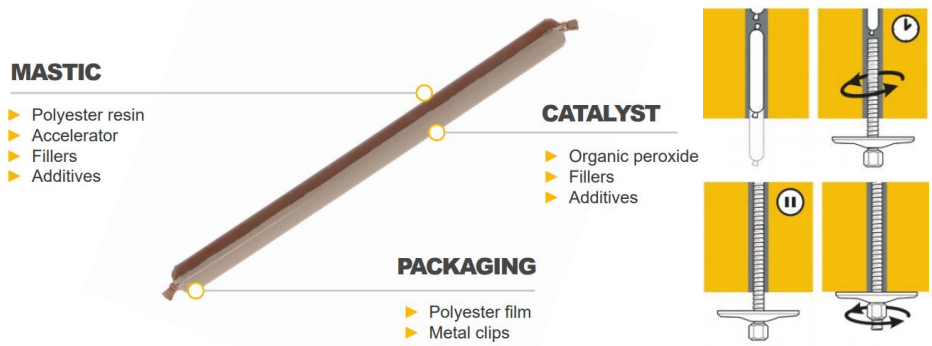

Figure 2.21. Two-component resins (left) and process of using resin cartridge for encapsulation of rock bolts (right)(Atlas Copco, 2008)

Resin capsules offer several advantages in rock bolting applications. First, they provide a convenient and controlled method for introducing resin into boreholes,

reducing the potential for mixing errors. The pre-measured quantities of resin and hardening agents ensure accurate mixing ratios, promoting reliable curing and bonding properties. The capsules also simplify the installation process, eliminating the need for separate mixing and injection equipment. This can save time and labour during installation. Furthermore, resin capsules are designed to provide rapid curing times, allowing for quick setting and load transfer. This is particularly beneficial in scenarios where immediate anchorage and support are required. The capsules are available in various sizes and configurations to accommodate different borehole diameters and project specifications. Proper mixing of resin capsules has been a concern for engineers, and various solutions have been proposed. Figure 2.19 displays a bolt specifically manufactured for use in underground mines. The design incorporates a distinctive paddle-shaped system to enhance the mixing of resin capsules and facilitate the shredding of the resin film. Achieving consistent and efficient mixing of the resin components yields higher strength, especially in large-diameter boreholes.

Figure 2.22. Engineered rock bolt with paddles for better mixing of resins

During rock bolt installation, resin capsules may bend, overlap, or pile up into the potential collapsed section of the borehole, resulting in weak resin mixing. Wang et al., (2022) developed synergistic components to mount on the conventional bolts to address the improper mixing of the resin capsules, as shown in Figure 2.20. The numerical and experimental analysis indicated that the developed synergistic components significantly enhanced the shredding of the film and mixing of the resin capsules resulting in effective encapsulation and greater bearing capacity.

Figure 2.23. Synergistic rock bolts for better mixing of resins (Wang et al., 2022)

2.14. Interaction between the rock bolting system components

A reinforcement system generally comprises four main components, as shown in Figure 2.24, namely:

- Rock

- Element
- Internal fixtures
- External fixtures

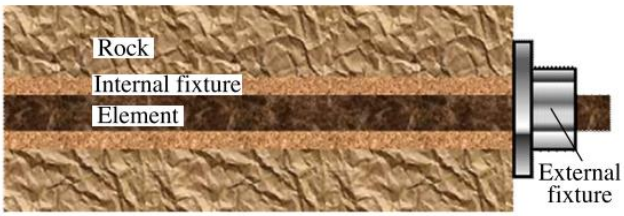

Figure 2.24. Generic reinforcement system (Cao et al., 2013a)

In fact, the surrounding rock mass is not a component of the reinforcing materials, however, the rock mass mechanical and geological properties directly affect the system's behaviour. To enhance structural integrity using a bolt, the reinforcing element pertains to the bolt itself, while the external fixture encompasses the face plate and nut. As for the internal fixture, it can take the form of a medium like cementitious grout or resin for encapsulating the bolt or a mechanical action such as friction at the bolt interface for frictionally coupled bolts, as discussed earlier. The internal fixture serves to establish a coupling condition at the interface. Displacements at the discontinuities typically exhibit greater magnitudes, resulting in more intricate load patterns, as depicted in Figure 2.25. In this figure, the displacements of the blocks are limited to translations only. However, block movements can also involve rotations in some instances, as shown in Figure 2.26, leading to more complex loadings.

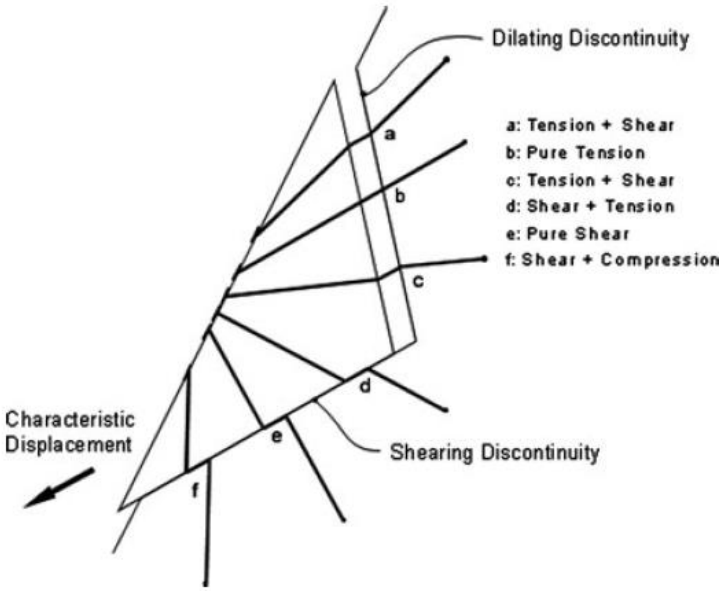

Figure 2.25. Loading of reinforcement system due to displacement of a block (Windsor, 1997)

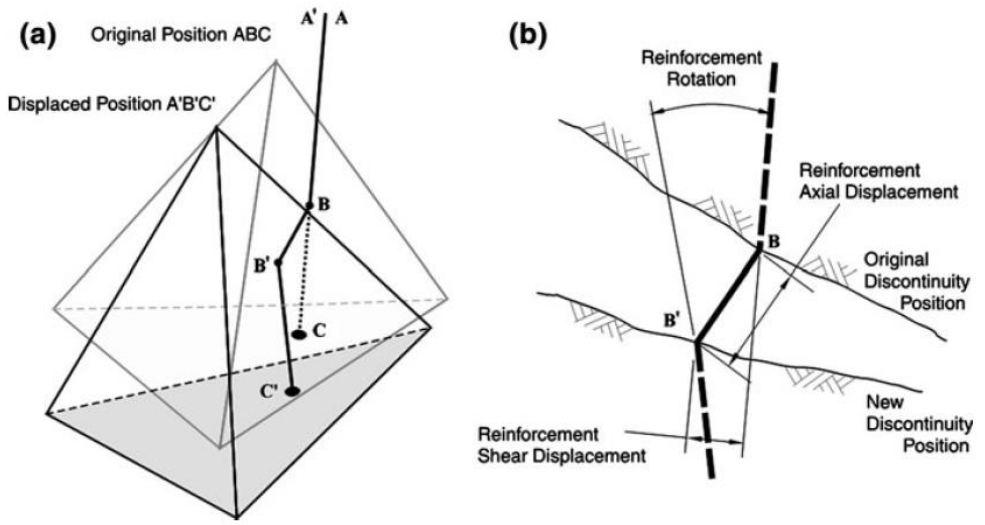

Figure 2.26. Loading of reinforcement system by rock block displacement and rotation (Thompson et al., 2012)

2.15. Rock bolts behaviour

Rock bolting systems generate forces as a response to rock mass movements or block displacement to control deformations and displacements at discontinuities. Geotechnical aspects of underground spaces and slope stability are usually associated with complex mechanical behaviour due to their specific structural and geological conditions as shown in Figure 2.25. Such an environment commonly consists of bedding planes and laminated strata where normal to shear displacements occur at multiple horizons. The primary purpose of bolt reinforcement is to reduce the movement of pre-existing fractures by applying pressure to the surfaces of these fractures. In certain situations, rock bolts can also prevent the development of additional fractures within unstable rock layers. Rock bolts installed across layers of bedded, jointed, or fractured rock have the capability to withstand both axial and shear deformations. Consequently, the function of fully grouted bolts can be categorised into three distinct types: firstly, providing axial resistance when rock bolts are subjected to tensile loads; secondly, shear resistance when bolts are placed across potential shear planes; and finally, combining both axial and shear resistance when bolts experience both pulling and shearing forces. Figure 2.27 illustrates two bolts in an underground space that yielded due to a combination of tension (causing joint opening) and shear forces at rock joints.

2.16. Failure modes of rock bolts in axial loading

The load transfer concept relies heavily on comprehending reinforcement system behaviour and its impact on excavation stability. This concept encompasses

three fundamental mechanisms: firstly, the transfer of load from an unstable zone to the reinforcing element due to rock movement; secondly, the transfer of load from the unstable region to a stable interior region through the element; and finally, the transfer of the load from the reinforcing element to the stable rock mass. The effectiveness of load transfer depends on various factors including the type and properties of the grout, the type and profile of the rock bolt, the hole and bolt diameter, anchorage length, rock material, confinement pressure, as well as over spinning and under spinning during installation procedures.

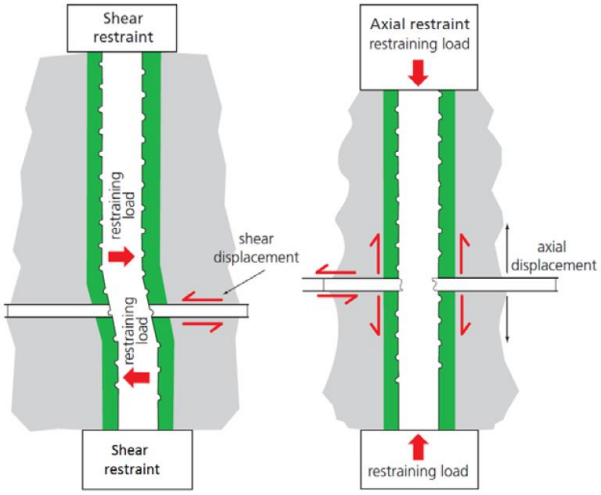

Figure 2.27. Behaviour of rock bolt in response to axial and shear forces (MINOVA et al., 2006)

The primary technique that a rock bolt resists against an axial load is the shear resistance generated at the anchorage interface. This shear resistance occurs at the shell-rock mass and bolt-rock mass interfaces in the case of point anchorage (a) and Swellex/Split set (c), respectively. However, in the case of bonded rock bolts (b), the induced shear resistance is formed at the bolt grout interface (Figure 2.28).

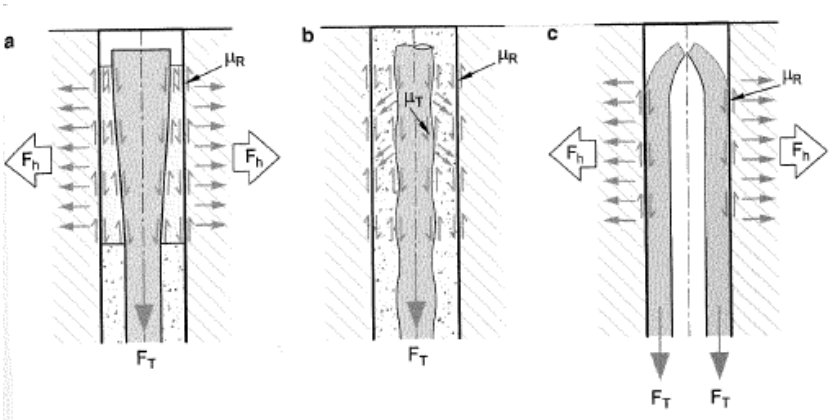

Figure 2.28. Response of different types of rock bolts to axial loads (Galvin, 2016)

In the case of fully grouted rock bolts, grout acts as a medium to transfer the

load from the rock to the reinforcing element. This force redistribution along the bolt results from movement in the rock mass, which transfers the load to the bolt through shear resistance in the grout (Figure 2.29).

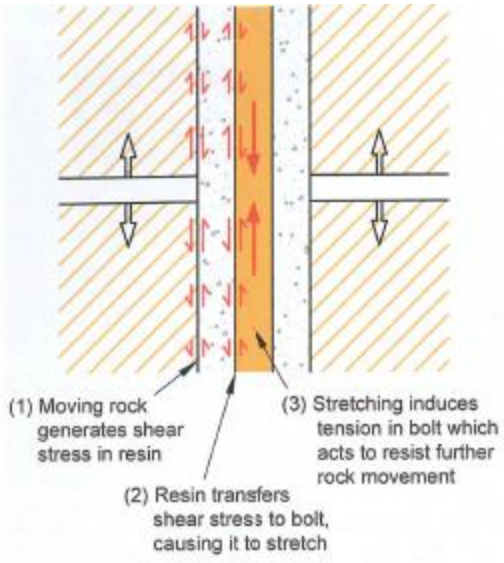

Figure 2.29. Load transfer concept in fully encapsulated rock bolts (Galvin, 2016)

Generally, the failure patterns of a bolting system define the ultimate load capacity of a rock bolt. Therefore, understanding the failure occurring in any reinforcement system is essential. Hutchinson and Diederichs, (1996) concluded that failure of rock bolt systems can occur in five modes, as shown in Figure 2.30 Mode A represents a breakage of the bolt shaft; this form of failure is rare because it requires the bond strength between the grout and bolt to be greater than the bolt's tensile strength. Many studies confirmed that the failure of fully grouted rock bolts occurs at the bolt-grout interface, as shown in mode B (Cao and Nemcik, 2012; Chen et al., 2020a; Hagan and Chen, 2014; Thenevin et al., 2017). This type of failure is due to the small contact area between the bolt and grout. However, if the rock strength is relatively weak or if the borehole diameter is relatively small, the rock-grout interface failure is more likely to occur as shown in mode D. Modes C and E depict failure at the grout-rock interface and surrounded rock, respectively (Cao and Nemcik, 2012; Hagan and Chen, 2014; Hutchinson and Diederichs, 1996).

2.17. Failure at the bolt-grout interface

The mechanic associated with a grouted reinforcing element subjected to axial loading is known as the bond mechanism. Bond is thought to be the shearing stress between the reinforcing element and the surrounding grout. In rock bolting, the bond may be described as the gripping effect of grout on the encapsulated length of a

deformed bar (Moosavi et al., 2005). This resistance can arise from adhesion and/or mechanical interlocking. Adhesion refers to the bonding between the grout, steel, and rock, while mechanical interlocking occurs when the grout fills irregularities between the bolt and the rock, creating a keying effect. Signer's research indicated the absence of adhesion between the grout and the bolt and between the grout and the rock interface (Signer, 1990). Aziz and Webb, (2003) also reported minimal adhesion between the bolt surface and the grout. In some studies, the adhesive component was disregarded due to its inability to mobilize sufficient frictional strength during certain conditions, as emphasised by Yazici and Kaiser, (1992). Each of these three components depends on the interaction between internal reaction forces of the whole system and the stress generated at the bolt-grout interface. The failure mode of bolt-grout interface as the dominant failure in rock bolting systems is related to the distribution of shear stress (magnitude and direction) and shear strength of grout. The mode of shear stress distribution is mostly associated with the bolt profile configuration as shown in Figure 2.31.

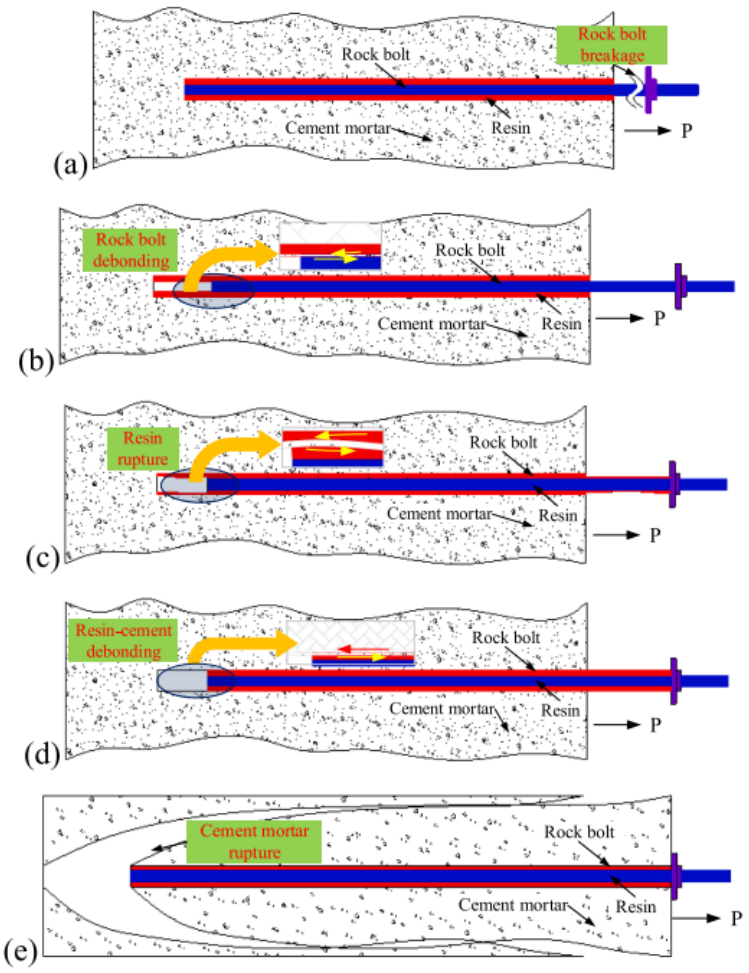

Figure 2.30. failure modes in fully grouted rock bolts (Chong et al., 2021)

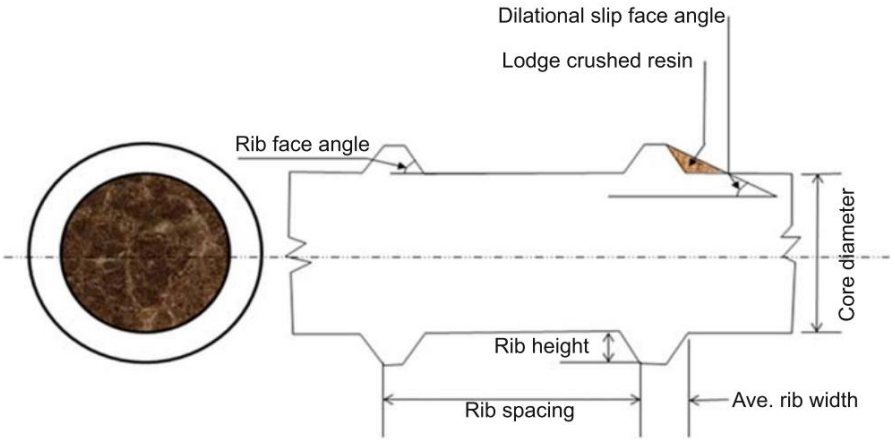

Figure 2.31. Bolt surface profile terminology (Wang et al., 2016)

Lutz, (1970) identified two fundamental failure modes for deformed reinforcing bars embedded in concrete cylinders subjected to axial loading. One is the radial splitting (dilation) of the grout medium, which can be initiated by the wedge action of the surface ribs, while the other is the interfacial shearing of the bar surface against the grout. Hyett et al. conducted a series of pullout tests in both laboratory and field settings to investigate the primary factors influencing the bond capacity of grouted cable bolts (Hyett et al., 1995, 1992). These tests specifically focused on 15.9 mm diameter 7-strand cable bolts that were grouted with type 10 Portland cement pastes. The study findings revealed that the bond capacity of cable bolts was primarily influenced by three key factors: cement properties, embedment length, and radial confinement. Notably, increasing the embedment length led to higher cable bolt capacity, although this relationship was not directly proportional. Additionally, higher capacities were observed when cable bolts were subjected to greater radial confinement. Radial splitting occurred due to the wedging action between the lugs of the cable and the concrete, resulting in outward pressure on the inside of the concrete annulus. This pressure was balanced by induced tensile circumferential stress within the annulus. However, if the tensile strength of the cement is surpassed, the circumferential stress reduces to zero, causing failure at the bolt-concrete interface (debonding failure). On the other hand, the shearing mechanism involved the crushing of concrete ahead of the ribs on the cable, allowing pullout along a cylindrical frictional surface. In conclusion, the study demonstrated that with an increase in radial confinement, the failure mechanism shifted from radial fracturing and lateral displacement of the grout annulus under low confinement to shearing of the cement flutes and pullout along a cylindrical frictional surface under high confinement.

Experimental studies conducted by Cao et al., (2014) and Nie et al., (2019) identified three main interfacial failure modes in rock bolting and cable bolting systems including the shear-off failure (the parallel shear failure), the dilational slip failure, the wedge slip and the combination of these failure mechanisms (Figure 2.32).

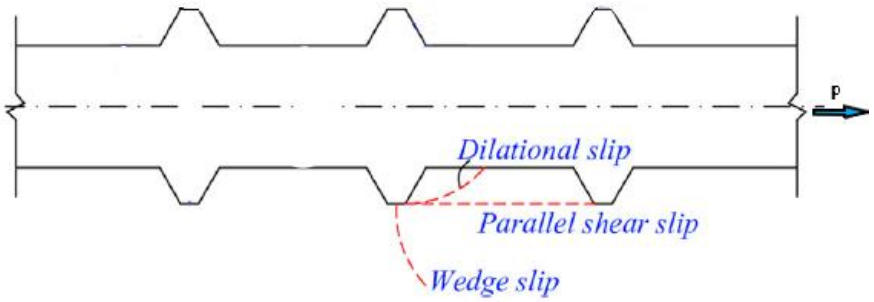

Figure 2.32. Failure modes at bolt-grout interface, after (Nie et al., 2019)

Tepfers, (1979) developed an analytical model to explain the distribution of tensile stress that leads to the formation of radial splitting cracks. During the pull-out process, the interface experiences significant stress concentrations, leading to the initiation and propagation of the debonding process along the reinforcing bar inside the specimen. Two types of cracks emerge from this process: cone-shaped cracks and longitudinal splitting cracks, both originating at the interface, as depicted in Figure 2.33. The specific crack patterns depend on the geometry and properties of the interface, as well as the surrounding concrete. Moreover, these crack patterns may not develop independently but interact through complex non-linear mechanisms. Tangential tensile stress is the primary cause of the splitting cracks. It was proposed that the radial components of the bond forces can be likened to a hydraulic pressure acting on a thick-walled concrete ring surrounding the reinforcing bar. The shear stress at the interface is distributed into the surrounding material through compression at a certain angle, and this is balanced by tensile stress rings in the concrete, as illustrated in Figure 2.34.

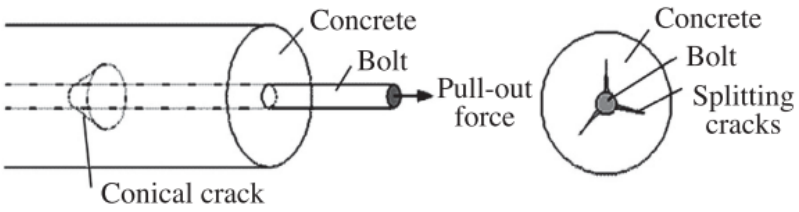

Figure 2.33. Concept of potential cracking in the embedded rebar in concrete (Tepfers, 1979)

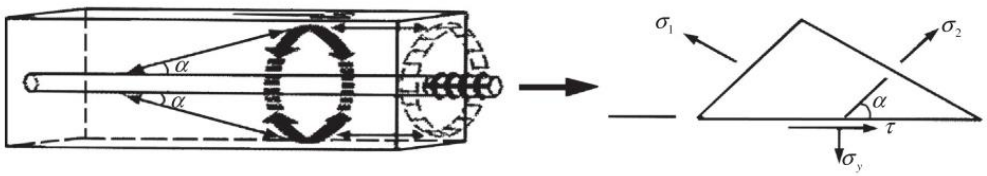

Figure 2.34. Balancing of the radial components of the bond stress against tensile stress rings (Tepfers, 1979)

The different stages of splitting failure during a pull test are summarised schematically in Figure 2.35 (Hyett et al., 1992). In the initial stage (stage 1), the response was mostly linear, but the experimental initial stiffness was significantly lower than what elastic solutions predicted. Hyett argued that this discrepancy was due to negligible adhesion between the cable and the cement. The reasons behind this negligible bond were identified as (1) the porous nature of the cement paste and (2) the bond being composed of isolated point contacts rather than continuous adhesion. As a result, the mechanical interlock and frictional resistance played a key role in the initial linear response during the pull test, although some partial adhesion might still be involved.

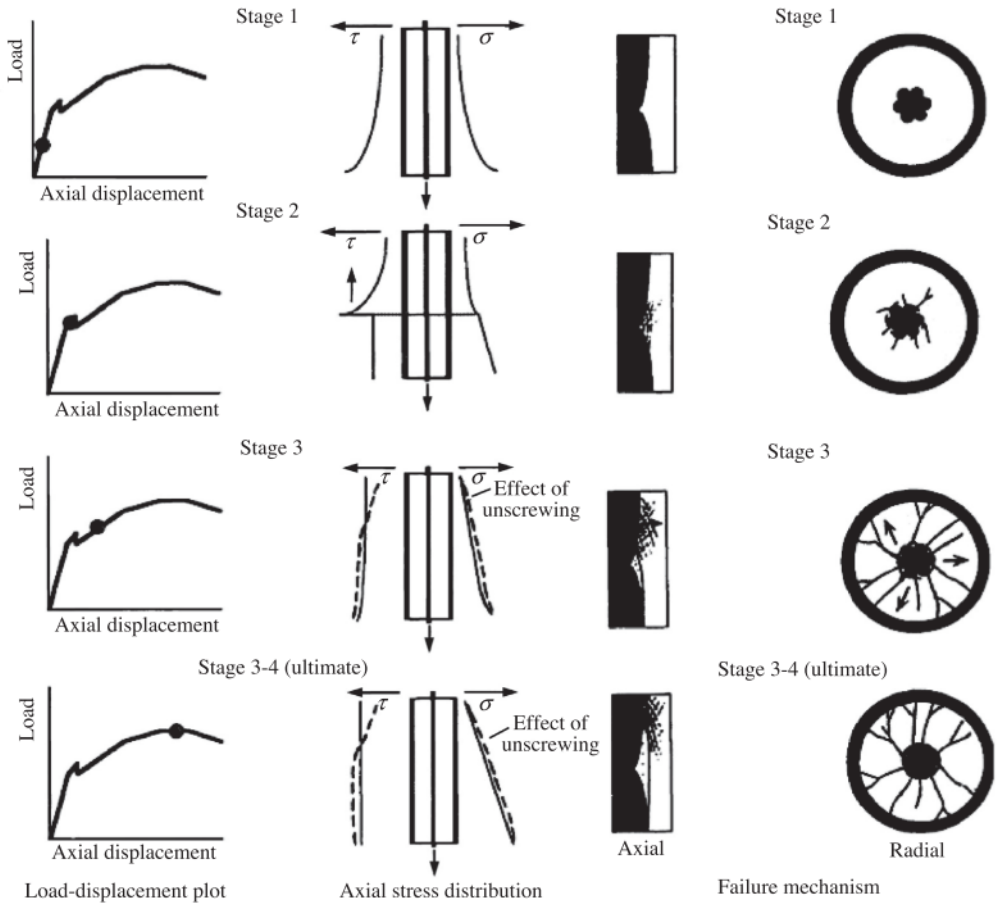

Figure 2.35. Radial cracks initiation and propagation due to splitting failure of a cable bolt (Hyett et al., 1992)

Moving on to stage 2, the failure mechanism became dependent on the radial confining pressure. The stress drop observed during this stage could be attributed to radial fracturing of the grout annulus and/or shear failure through the grout flutes. As the cable displacement increased further, the radial confining pressure was influenced by the potential for greater geometric mismatch between the cable and cement flutes. The ability of individual wedges, which now form the grout annulus, to be pushed aside was determined by the radial stiffness of the confining medium. When the radial stiffness was low, the favourable failure mechanism involved the lateral displacement of the wedges. However, when the radial stiffness was higher, dilation was suppressed, and failure was more likely to occur through the shear of the grout flutes and pullout along a cylindrical frictional surface.

Parallel shear failure is defined as a cylindrical failure that occurs in smooth bars and for very close-spacing ribbed bars (Figure 2.36). This failure has also been observed in short encapsulated laboratory pull-out tests when the confining material is stiff. In addition, Zhang et al., (2020) observed a new interfacial failure named sheared-crush in addition to the two other types of failure (Figure 2.37). The interfacial failure mechanism depends primarily on the mechanical properties of materials, the surface profile of bars and the level of confinement stress.

Figure 2.36. Shear-off failure at the bolt grout interface (Cao et al., 2014)

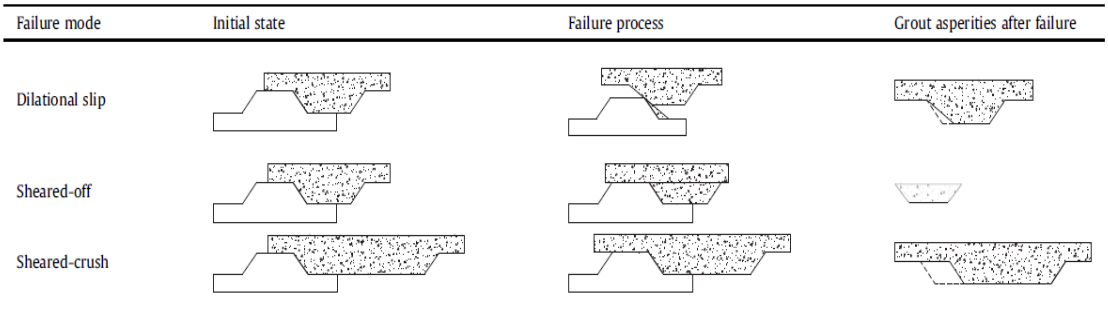

Figure 2.37. Schematic diagrams of failure modes at the bolt-grout interface (Zhang et al., 2020)

Figure 2.38 schematically illustrates each strength component's role in the bond-slip model. The frictional component can be associated with dilational slip, shear

failure of grout or rock mass, spiral displacement of the bolt and torsional unscrewing cable bolts (Hyett et al., 1995). Moosavi et al., (2005) pointed out that the frictional effect has the dominant effect on the system behaviour, especially after the onset of slip. Based on this argument, it was concluded that confining stress play a substantial role in load utilisation. Prior to the failure of the system (peak bond strength), the mechanical interlock deploys the bond capacity of the system. The mechanical interlock is mainly related to the mechanical properties of the grout materials, rock mass conditions, level of confining stress and bolt surface configuration including rib profile shape, rib height, rib face angle, angle of ribs wrap and rib spacing (Cao et al., 2013c; Cui et al., 2020).

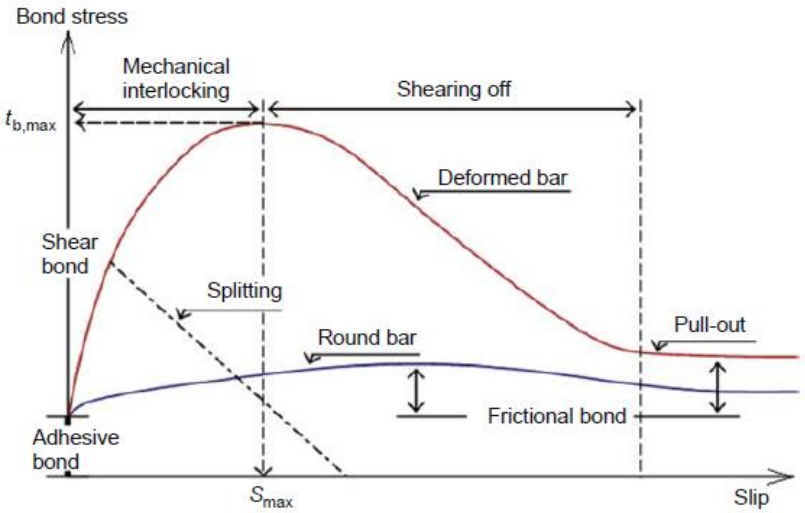

Figure 2.38. Bond-slip relationship (Hong and Park, 2012)

2.18. Factors influencing the performance of fully encapsulated rock bolts

The performance and load transfer mechanism of fully encapsulated rock bolts are generally governed by many factors, which can be classified into the following fundamental groups:

1) The mechanical, structural and geological properties of the surrounding rock mass and the boundary condition
2) The mechanical properties and thickness of gout
3) The mechanical properties, geometry and surface configuration of the bolt
4) Environmental factors such as temperature and groundwater

Other factors affect the performance of the fully grouted rock bolts, such as the installation procedure, the drill hole's cleanness, the drill hole, the moisture continent of the drill hole, the surface profile of the drill hole, the quality of grout pumping and grout mixing process.

2.18.1. Effects of rock mass and boundary conditions on rock bolts' performance

The strength of the rock mass where a bolt is installed generally dictates the critical failure mechanism and the failure place. For both soft and strong rocks, the critical failure mode is a shear failure, however, in soft rocks, the major failure occurs in the grout/rock interface and in strong rocks, the dominant failure can be seen in the grout/bolt interface. In addition to internal confinement, external confinement stress due to in-situ stress also influences the performance of the rock bolts. A relaxation in external confinement stress can result in a significant reduction in the anchorage capacity of rock bolts, especially at the grout-rock interface. However, very soft rocks behave differently as shear stress is almost uniformly distributed along the bolt length since the shear stress at the bolt-grout interface is interconnected to the axial load. Therefore, axial stress along the bolt decreases in a similar manner.

As mentioned above, the axial slip of deformed reinforcing elements generates radial dilation to some extent depending on the surface rightness geometry. This radial movement is inhibited or restricted by rock mass depending on its mechanical and structural characteristics, especially on normal stiffness. For hard rocks without effective joints, the radial movement (dilation) may generate radial confining stress resulting in a high bond capacity of the reinforcing element. However, soft rocks or intensively jointed and cracked hard rocks may not generate radial stress in response to the dilation. Figure 2.39 depicts the concepts around the reinforcement systems installed in the rock mass and the effect of confining pressures on the system.

As mentioned in the previous section, the performance of reinforcing elements can be evaluated via *in-situ* and/or laboratory tests. In laboratory tests, three modes of boundary conditions may be applied including constant normal stiffness (CNS), constant normal load (CNL), and neither CNS nor CNL. It should be noted that constant radial stiffness can better reflect the actual field conditions, compared to constant confining stress, because shear dilation is inhibited by surrounding rock mass, which subsequently increases interfacial normal load (Hyett et al., 1992; Shrivastava and Rao, 2018). Hyett et al., (1992) examined the effect of the radial stiffness on the axial and shear behaviour of cable bolts and concluded that higher boundary stiffness can lead to greater load-bearing capacity. For this purpose, they carried out split-pipe tests using PVC, aluminium, and steel pipes to investigate the influence of radial stiffness in different degrees on the bond capacity of grouted cable

bolts. It was stated that higher normal stiffness demonstrated higher bond capacities. It was also seen that the failure mechanism changed as the radial stiffness differs (Figure 2.40).

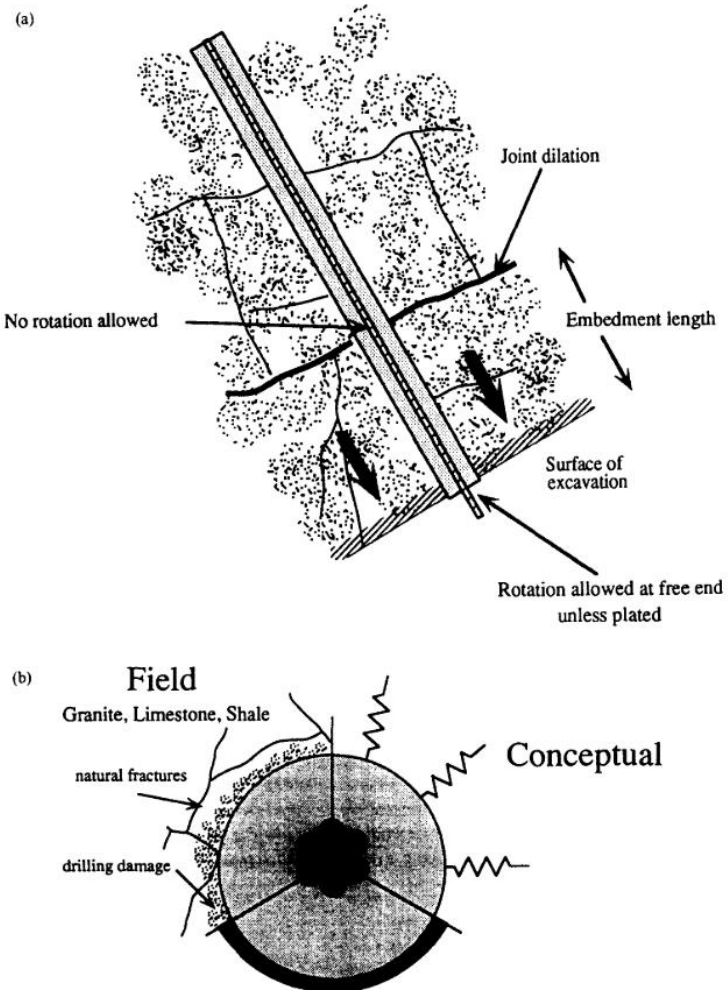

Figure 2.39. Key concepts in reinforcement system analysis, (a) the concept of forces subject to cable bolts, (b) the effect of boundary conditions (Hyett et al., 1992)

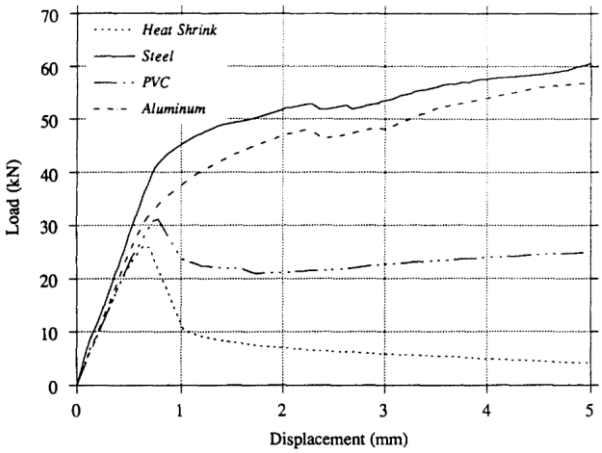

Figure 2.40. Effects of confining material on the axial performance of cable bolts (Hyett et al., 1992)

The authors used Eq. 1 to calculate the radial stiffness of the confining materials:

$$K_r = \frac{2E}{(1+\upsilon)}\left[\frac{d_0^2 - d_i^2}{d_i[(1-2\upsilon)d_i^2 + d_0^2]}\right] \quad (1)$$

where E, υ, d_i and d_0 are the elastic modulus, Poisson's ratio, internal diameter and external diameter of the confinement, respectively, as presented in Table 3.

Table 3. Properties of the confining materials used by Hyett et al., (1992).

	E (GPa)	υ	d_0 (mm)	d_i (mm)	K_r (MPa/mm)
Steel	200	0.25	60.13	49.30	1604.2
Al	72	0.25	60.45	49.02	599.5
PVC	3	0.32	60.61	47.50	3.7

Yilmaz et al., (2013) conducted pullout tests on chemical anchors embedded in weak concrete, indicating the positive contribution of the concrete strength to the bond strength. On the contrary, Cao et al., (2014) reported the insignificance of the host rock uniaxial compressive strength (UCS) ranging from 30-136 MPa on the pullout capacity of rock bolts. Che et al., 2020) conducted a DEM simulation on fully grouted rock bolts and showed that the width of the surrounding rock has a significant influence on the peak pullout strength of the rock bolts. It was concluded that with an increase in the rock width, the peak pullout strength first fluctuates and then increases gradually, however, in the samples with a width over 9.3 times of the grout thickness, the peak pullout strength is not affected (Figure 2.41).

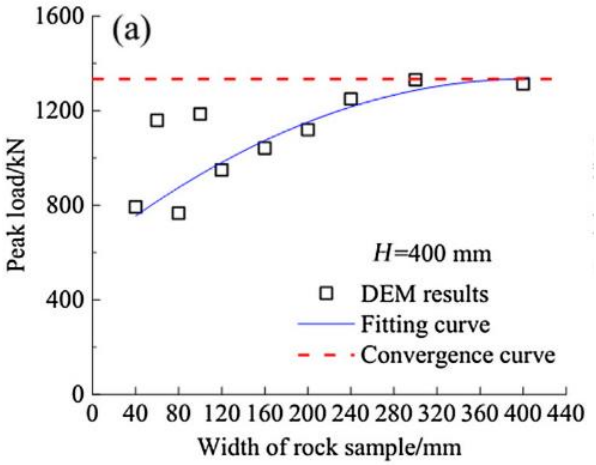

Figure 2.41. Peak pullout load versus sample width (Che et al., 2020)

Wee et al., (2016) investigated the bond-slip behaviour of rebar embedded in engineered cementitious composites (ECC) with compressive strength of 53.2 MPa and ready-mix concrete with a compressive strength of 31.8 MPa. Figure 2.42

illustrates the results of pullout tests on the samples with 65 mm encapsulation length in both ECC and Concrete. As seen, the peak load obtained in the ECC samples are higher than the ones in the concert samples. Figure 2.43 shows the force-slip relationships of the extended reinforcement. All the steel bars achieved their maximum strength. Throughout the pullout process, the surrounding ECC matrix remained intact. When comparing long reinforcement embedded in ECC with conventional concrete, similar yield, ultimate, and rupture forces were achieved. However, the associated slips of reinforcement in ECC were significantly smaller than those observed in concrete.

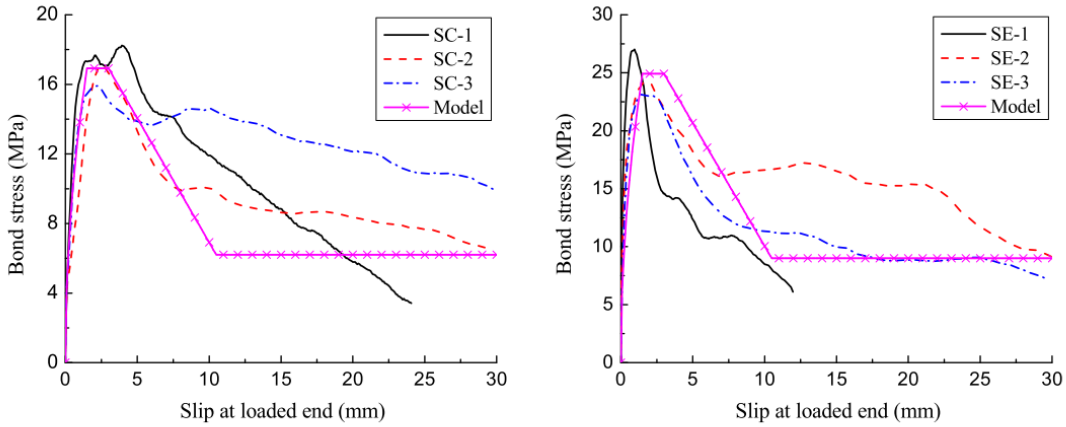

Figure 2.42. Force-slip curves for the short encapsulation (65 mm) in (a) concrete and (b) ECC (Wee et al., 2016)

Yi et al., (2023) investigated the effect of concrete compressive strength and rock mass integrity on the performance of anchored rock bolts using mortar. Rock mass integrity was calculated using the below equation:

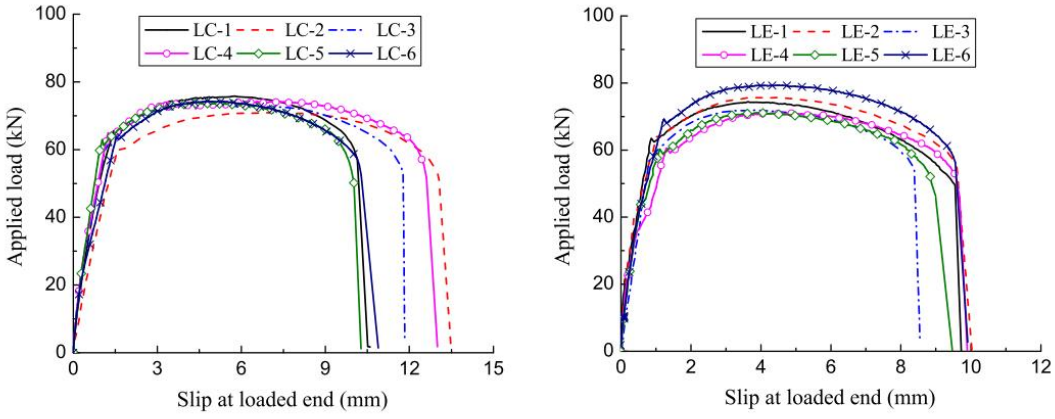

Figure 2.43. Force-slip curves for the long encapsulation (260 mm) in (a) concrete and (b) ECC (Wee et al., 2016)

$$K_v = (\frac{V_{pm}}{V_{pr}})^2 \quad (0 < K_v < 1) \tag{2}$$

where V_{pm} is the acoustic velocity of rock mass in Km/s and V_{pr} is the acoustic velocity of intact rock in Km/s. Higher K_v indicates a rock mass with higher quality and lower joint density.

The authors examined the performance of rock bolts under 15 different conditions including the compressive strength of concrete from 8.6 MPa to 45.3 MPa and rock mass integrity between 0.1 and 0.97 (Figure 2.44).

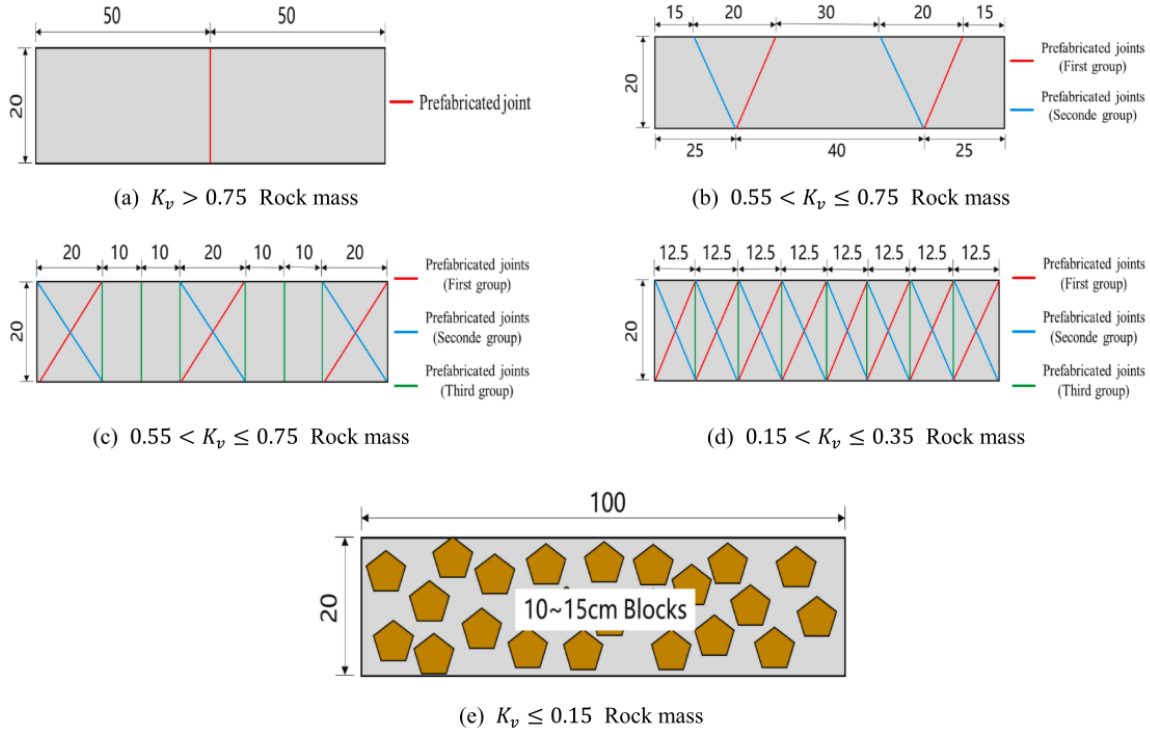

Figure 2.44. Rock mass simulation for obtaining different grades of rock mass integrity (K_v) (Yi et al., 2023)

The study investigated the failure mode of the specimens in both the entire system and at the bolt-grout interface. During the bolt pull-out process, the pull-out load is transferred from the mortar to the unstable rock blocks through shear stress. The failure modes of the joint rock are influenced by the rock mass integrity, with a higher occurrence of cracks near the pull-out end and fewer cracks further away.

The failure modes of the bolt-grout composite structure were mainly categorised based on the rock mass integrity (K_v):

- Structure failure (S1): Occurs when *Kv* > 0.75, leading to damage through longitudinal cracks and resulting in structure failure of the joint rock (Figure 2.45a).

- Joint surfaces failure (S2): Occurs when 0.55 < K_v ≤ 0.75, where the joints experience relative sliding during the pull-out load, causing stress concentration near the joints. This leads to rapid crack development around the prefabricated joints, resulting in joint surface failure (Figure 2.45c).
- Disintegrate failure (S3): When K_v ≤ 0.55, the joint development is extremely high, and the spacing between cracks is small. As a result, the cracks near the joint surfaces interconnect and penetrate, leading to disintegrate failure of the joint rock (Figure 2.45c).

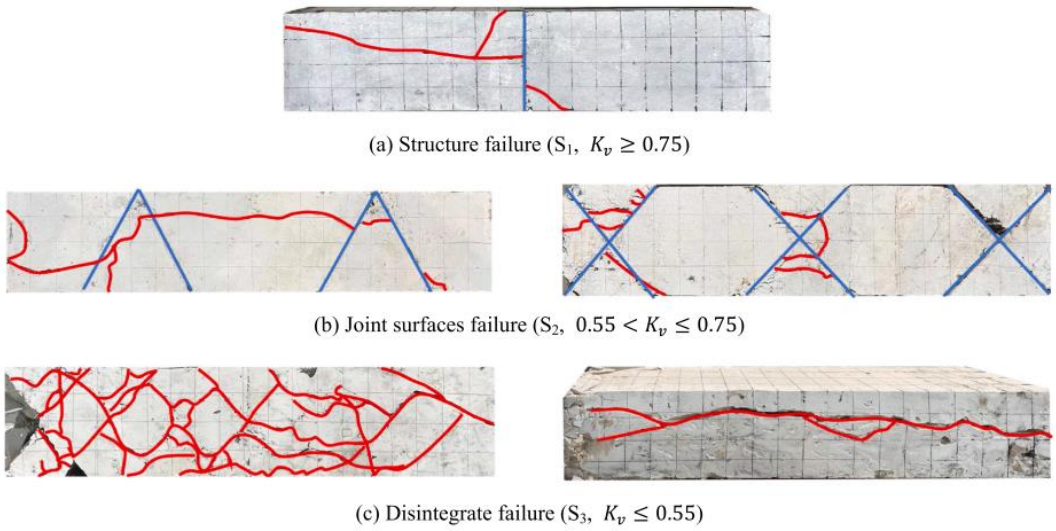

Figure 2.45. The failure mode of the specimens (Yi et al., 2023)

Figure 2.46 depicts the effects of testing conditions including the surrounding rock compressive strength and the rock mass integrity, on the pullout capacity of the encapsulated bolts. As seen, ultimate pullout load and displacement increase with the compressive strength and rock mass integrity.

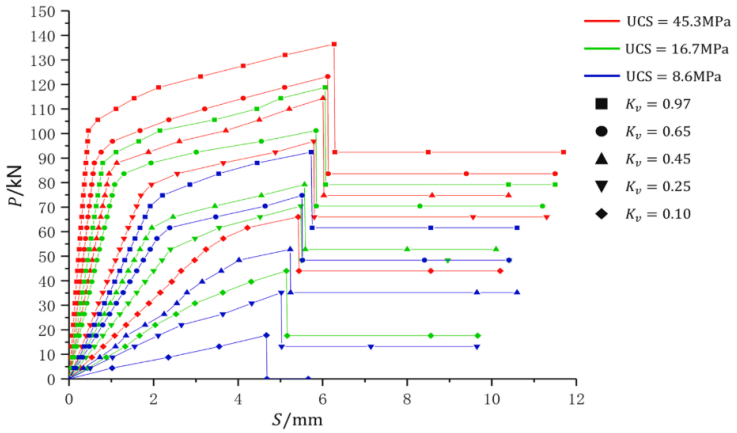

Figure 2.46. Load-displacement relation under different testing conditions (Yi et al., 2023)

Figure 2.47 illustrates the pullout test outcomes of bolts embedded in various rocks using a water-to-cement ratio of 0.4 grout and 250 mm of encapsulation length (Hyett et al., 1992). The cable bolt capacities were similar in granite and limestone, while lower results were observed in shale. Notably, the test results in limestone exhibited significantly higher consistency throughout the entire testing program compared to either shale or granite.

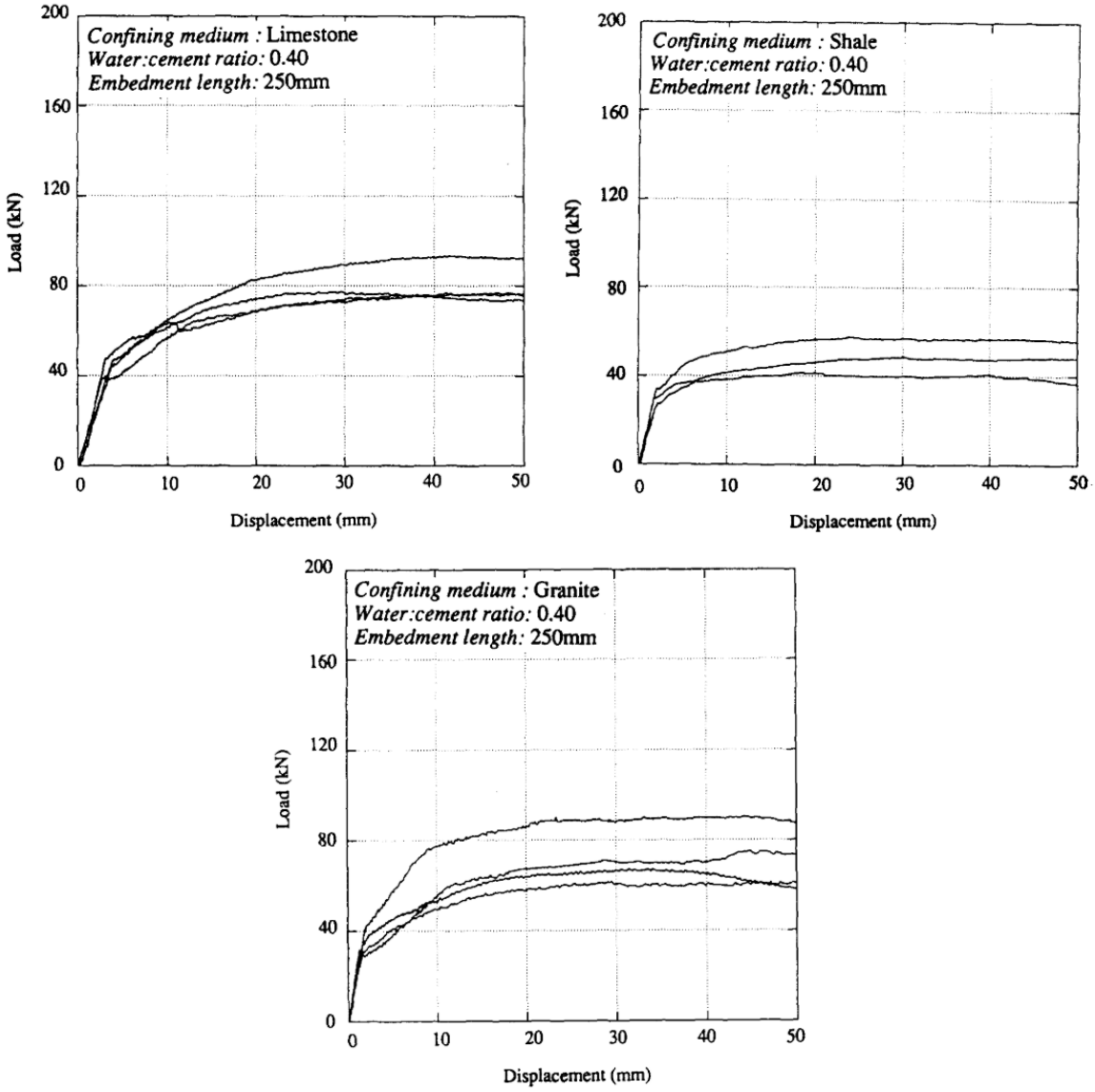

Figure 2.47. Results of field pullout test conducted on different rocks (Hyett et al., 1992)

Hyett et al., (1995) performed a number of pull-out tests in which the confining pressure was applied using a modified Hoek-Cell. Observations revealed that confining pressure significantly affects the ultimate bearing capacity of the system. Moosavi et al., (2005) designed a series of pull-out tests under constant radial confining pressure using a modified triaxial Hoek-Cell to qualify the effect of confining

pressure as a result of frictional-dilational interaction on the bond capacity. Cylindrical specimens were cast using Portland cement with embedment length of 100 and 150 mm. Bolts with different diameters including 22 and 28mm (ribbed bolts) were used. Also, the tests were designed for confining stress in the range 1.3-7.5 MPa. Visual investigation showed that for lower radial stress, cracks were fully developed on the outward surface of the specimens as shown in Figure 2.48. indicating dilational slip and failure mechanism. It was also illustrated that increase in confining pressure increases the bond strength and mobilised load capacity while radial dilation decreases (Figure 2.49).

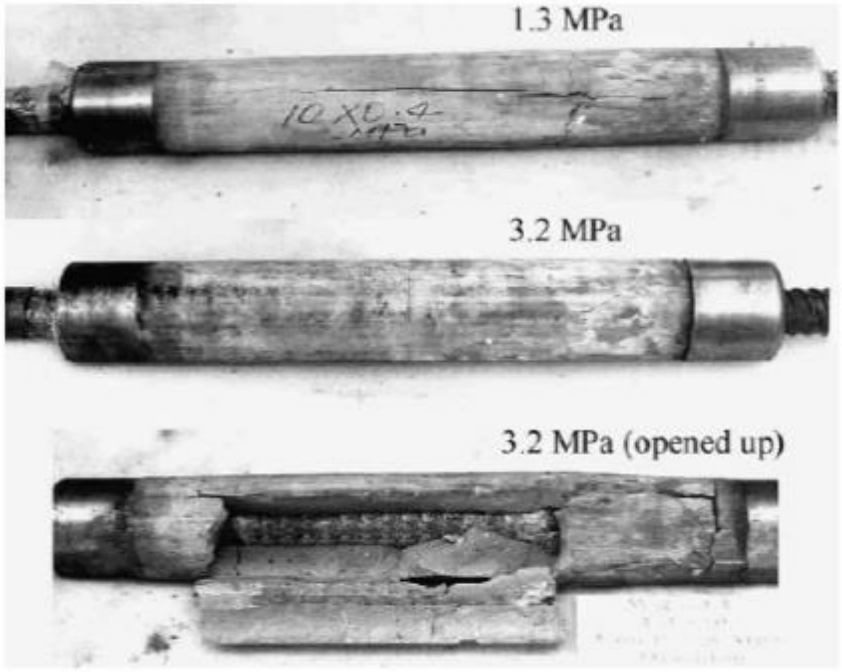

Figure 2.48. Samples condition after tests (Moosavi et al., 2005)

Martín et al., (2011) performed a series of pull-out tests campaign to examine the influence confining pressure. The results demonstrated that an increase in the confining pressure has a significant effect on the anchoring capacity. Also, it was observed that the radial fractures are much more significant in lower confining pressure. Nie et al., (2019) carried out a parametric study denoting that the highest bond and residual strength in bolting systems can be achieved at high confining pressures. Zhang et al., (2020)demonstrated that normal stress possesses a major effect on interface failure mode. For instance, it was shown that for a lower value of normal stress (0.5 MPa), dilational failure occurs. When normal stress reaches 2 MPa, shear-off failure was observed to be the dominant failure mode. In addition, in this moderate normal stress, the effect of rib spacing was effective. Once normal stress

increased to 6 MPa, shear-crush was also observed in addition to sheared-off failure.

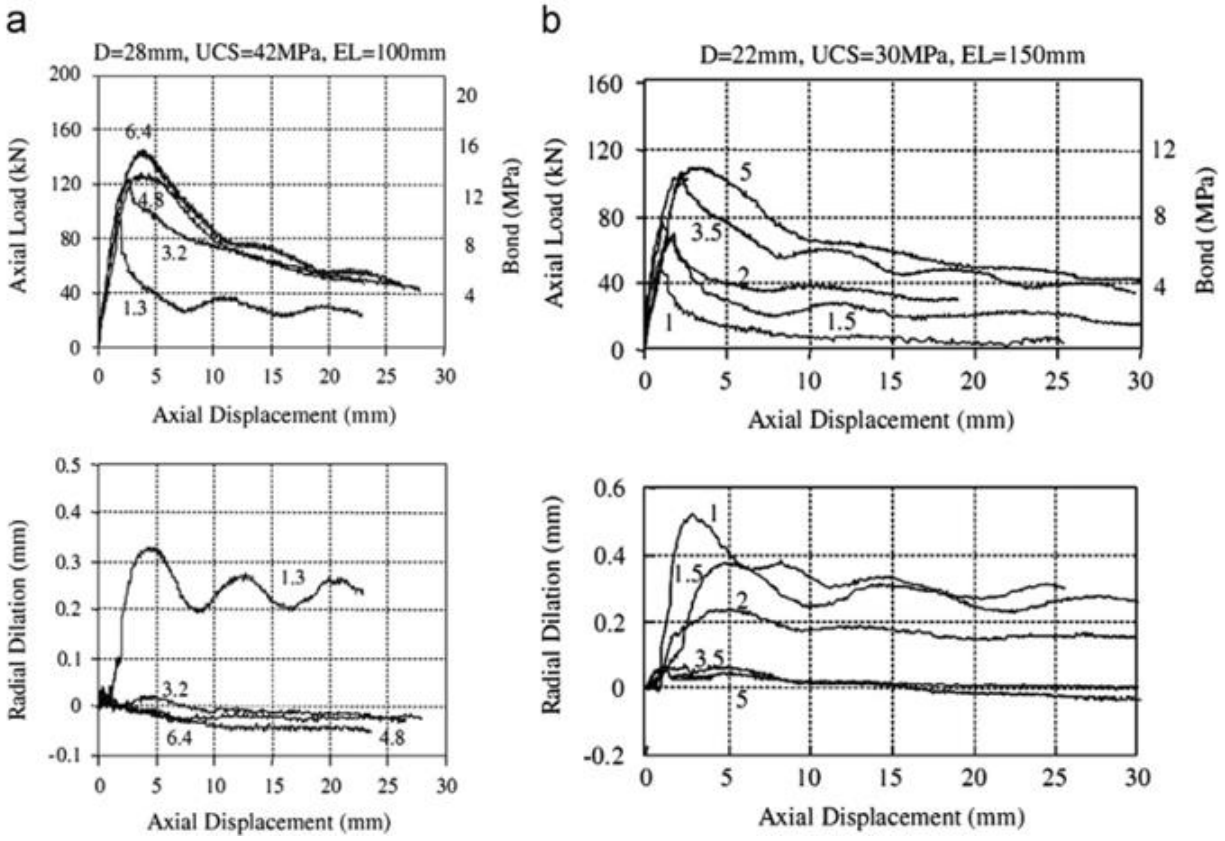

Figure 2.49. results of the pull-out test; D indicates the bolt diameter, UCS indicates the grout compressive strength, and EL is the encapsulation length (Moosavi et al., 2005)

Yokota et al., (2019) focused on examining how rock bolts interact with bond materials through laboratory shear tests and numerical simulations using Discontinuous Deformation Analysis (DDA). The researchers aimed to understand the supporting mechanism and the effects of rock bolting by analysing key parameters like ribs, rib angle, bond material strength, and confining pressure. Figure 2.50 shows the concept of the DDA simulation model developed for the investigation of the factors mentioned above. In terms of the bolt surface profile, two types of surfaces were applied in the experimental procedure including plane surfaces without ribs and ribbed surfaces with different angles (30°, 60° and 90°).

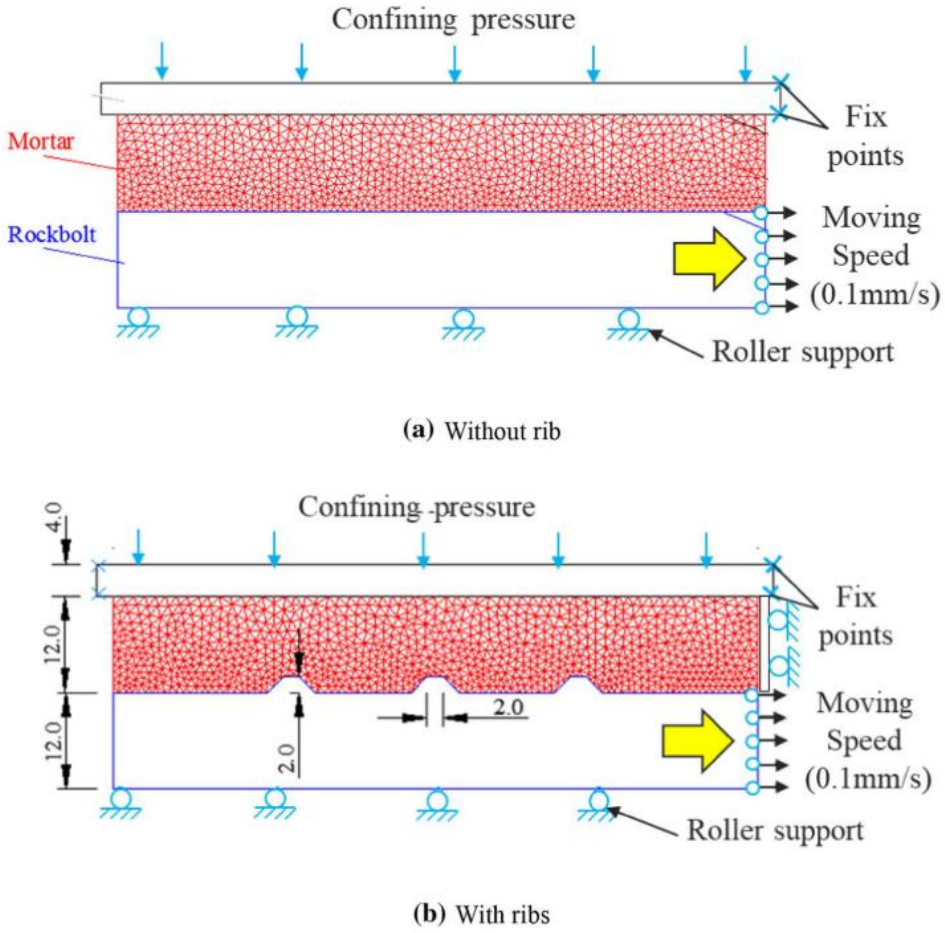

Figure 2.50. The DDA model developed to investigate the effect of rib angle, grout strength, and confining pressure on the behaviour of rock bolts (Yokota et al., 2019)

In the scenario of a rock bolt without ribs, increasing the confining pressure to 4 MPa resulted in a linear increase in shear stress until reaching peak strength, similar to the outcomes seen with a confining pressure of 2 MPa. Subsequently, the shear stress decreased to the residual value, mirroring the results obtained under 2 MPa confining pressure, as depicted in Figure 2.51a. Conversely, in the case of a rock bolt with ribs, the shear stiffness noticeably decreased as the shear stress approached peak strength. Additionally, the horizontal displacement significantly increased when the shear stress reached its residual value, as illustrated in Figure 2.51c. These observations may be attributed to the interlocking effect at the interface between the bolt rib and mortar, where the confining pressure considerably enhanced the mortar's resistance against the movement of each rock bolt rib both before and after reaching peak strength. Consequently, this led to an increased number of cracks in the mortar.

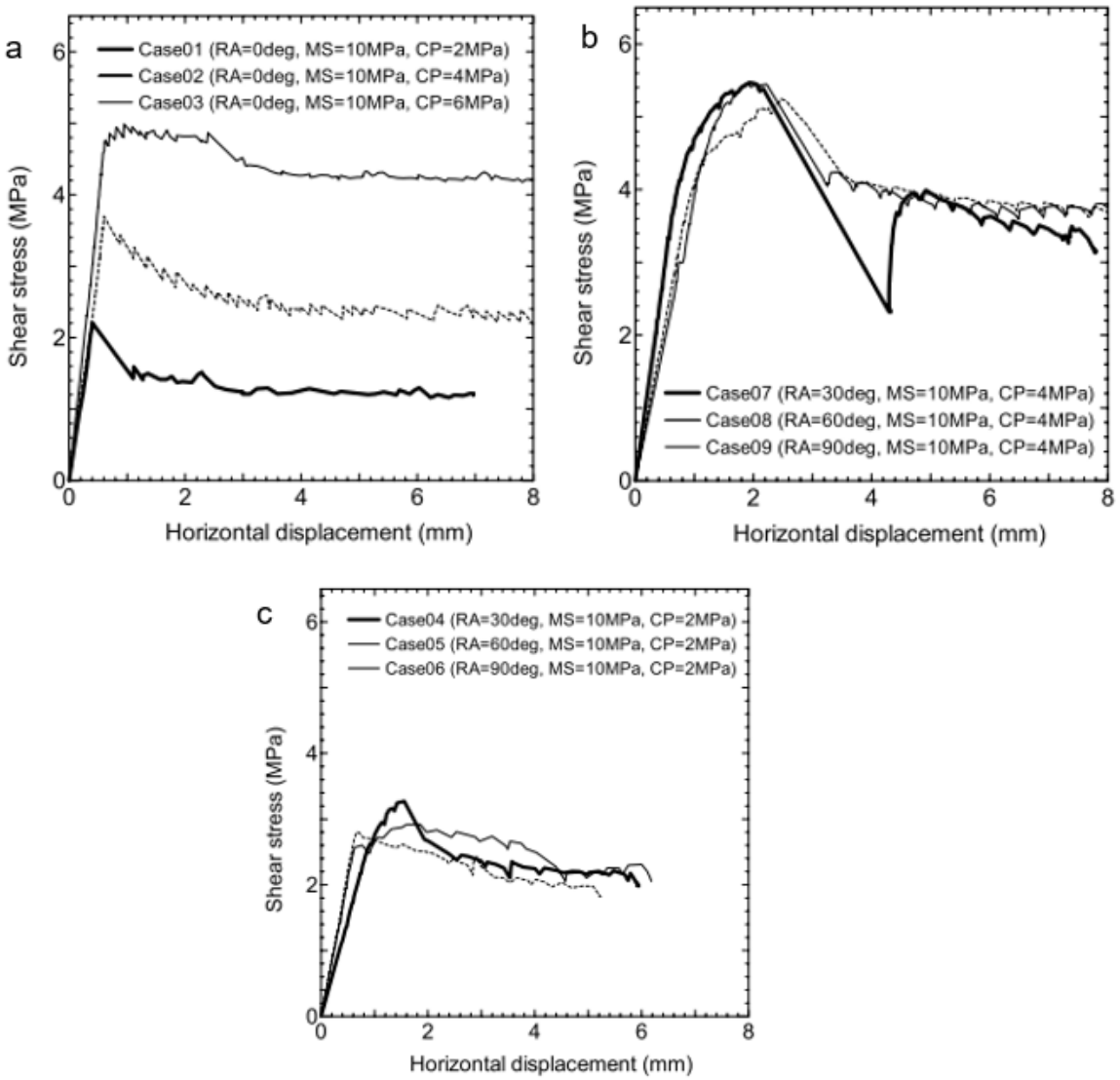

Figure 2.51. Results of laboratory shear test (Yokota et al., 2019)

Figure 2.52 summarises the results shown in Figures 2.51b and c and reveals that both peak and residual strength escalated with higher confining pressures.

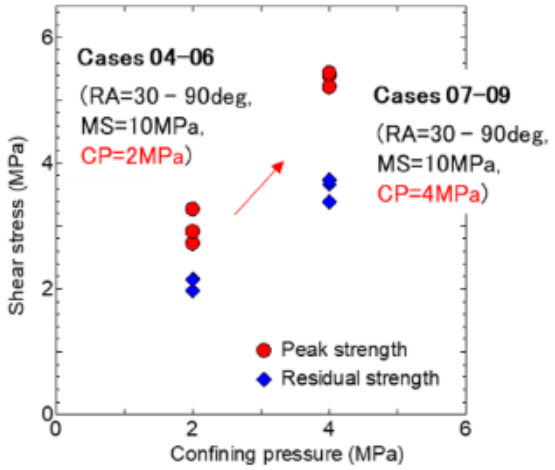

Figure 2.52. Summary of the effect of confining pressure derived from Figure 2.54 (Yokota et al., 2019)

2.18.2. Effects of grout characteristics on rock bolts performance

Grout acts as a medium to transfer the initiated stresses from the bolt to stable rock mass and the in-situ stress (lateral confining stress) from the surrounding rock to the bolt-grout interface. The bond strength of fully encapsulated rock bolts is basically frictional and depends on the shear characteristics of grout including cohesion and frictional angle, and also cohesion and interface roughness of bolt-grout and grout-rock interfaces. Up to now, a large number of experimental studies have been conducted to investigate the effects of grout properties on the efficiency of fully encapsulated rock bolts.

Hyett et al., (1995) performed a number of tests on fully grouted strand cable bolts, indicating the sensitivity of the bond strength to the grout properties. For instance, as the water-to-cement ratio (w/c) increased from 0.3 to 0.5, Young's modulus of grout and ultimate pull-out capacity decreased from 18.6 GPa to 9.3 GPa and 150 KN to 110 KN (under 10 MPa confinement), respectively. The results of various studies also show that Uniaxial Compressive Strength (UCS) and shear strength of grouts play vital roles in the determination of rock bolts and cable bolts bearing capacity (Benmokrane et al., 1995; Hyett et al., 1992; Li et al., 2012; Miller and Ward, 1998; Teymen and Kılıç, 2018; Zhang et al., 2020). Kılıc et al., (2003) conducted numerous pull-out tests on steel bars encapsulated in the basalt rock to study the effects of grout mechanical properties, w/c and curing time on the bearing capacity. In order to obtain grout with different mechanical properties, different mixtures using Portland cement, fly ash, and siliceous sand, along with different w/c and curing times prepared. The results revealed that an increase in the w/c ratios results in a decrease in the UCS of grout and ultimately a decrease in maximum pull-out load and bond strength. On the other hand, the bolt's performance improves with an increase in curing time. The summary of the results is presented in Table 4, where UCS_g, E_g and τ_g refer to the compressive strength of the grouts, elastic modulus and shear strength of the grout, respectively, while P_b, A_b and τ_b are the peak load, cross-section of the bolt and the induced bond strength at the blot-grout interface.

Figures 2.53 and 2.57 illustrate the relationship between the bond strength of the grouted bolts and the mechanical properties of the grout. As shown, an increase in the UCS, shear strength and elastic modulus causes an increase in the ultimate bond strength of the bolt in the logarithmic growth.

Table 4. Relationship between grout mechanical properties and bolt load capacity (Kilic et al., 2003).

Grout type	UCS_g (MPa)	E_g (GPa)	τ_g (MPa)	P_b (kN)	A_b (cm^2)	τ_b (MPa)	τ_b/τ_g
$w/c=0.40$[a]	5.30	1.15	2.04	16.53	84	1.94	0.95
$w/c=0.40$[b]	12.84	2.74	4.99	43.75	84	5.20	1.04
$w/c=0.40$[c]	17.74	2.96	6.22	55.28	84	6.63	1.07
$w/c=0.40$[d]	20.80	3.39	7.95	57.59	84	6.83	0.86
$w/c=0.40$[e]	22.94	3.79	9.17	59.84	84	7.14	0.78
10% sand[f]	31.60	6.22	6.73	55.45	83	6.73	1.00
10% fly ash[f]	30.58	4.89	7.34	58.15	83	6.32	0.86
5% fly ash[f]	33.33	5.25	8.05	56.01	83	6.73	0.84
White cement[f]	37.72	6.63	8.15	58.15	83	7.03	0.86
$w/c=0.40$[f]	32.01	7.40	10.30	75.26	102	7.34	0.71
$w/c=0.38$[f]	33.33	8.05	10.70	77.39	102	7.54	0.70
$w/c=0.36$[f]	38.94	9.12	11.30	78.99	102	7.75	0.68
$w/c=0.34$[f]	42.00	9.30	11.93	80.87	102	7.95	0.67

Curing time: [a]1 day; [b]3 days; [c]5 days; [d]7 days; [e]14 days; [f]21 days.

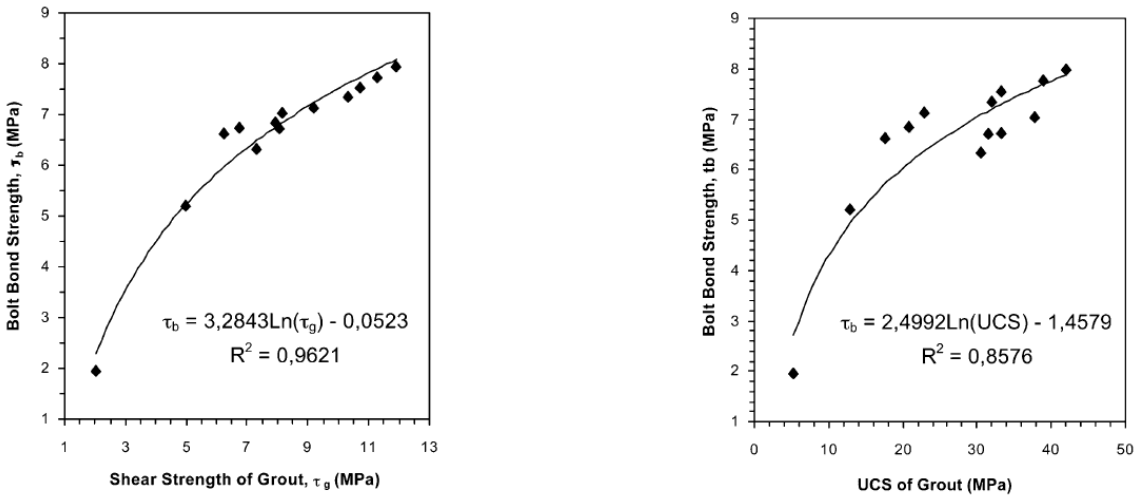

Figure 2.53. Relationship between grout mechanical properties and bond strength: (a) grout shear strength and (b) grout UCS (Kilic et al., 2003)

The authors also found a meaningful correlation between the curing time of the grout and the bearing capacity of the bolt as presented in Figure 2.55. As illustrated, 7 days of curing is the critical time for grouting until which bond and pullout load increases rapidly, however, after 7 days of curing time, the rate of increase reduces significantly.

Benmokrane et al., (1995) carried out a systematic experimental study on cable bolts and threaded bars with different configurations encapsulated using six different types of cement-based grouts. Tables 5 and 6 present the ingredients used in preparing the grouts and the mechanical characteristics of the grouts, respectively. The results of pullout tests on the specimen cured at the 3-day and 28-day marks are illustrated in Figure 2.56. As seen, there is a good correlation between the compressive strength and performance of the reinforcing materials. However, other

factors also impacted the performance, particularly the presence of aluminium powder, which caused the grout's expansion. The presence of the sand in G6, also significantly improves the pullout capacity of the reinforcing elements.

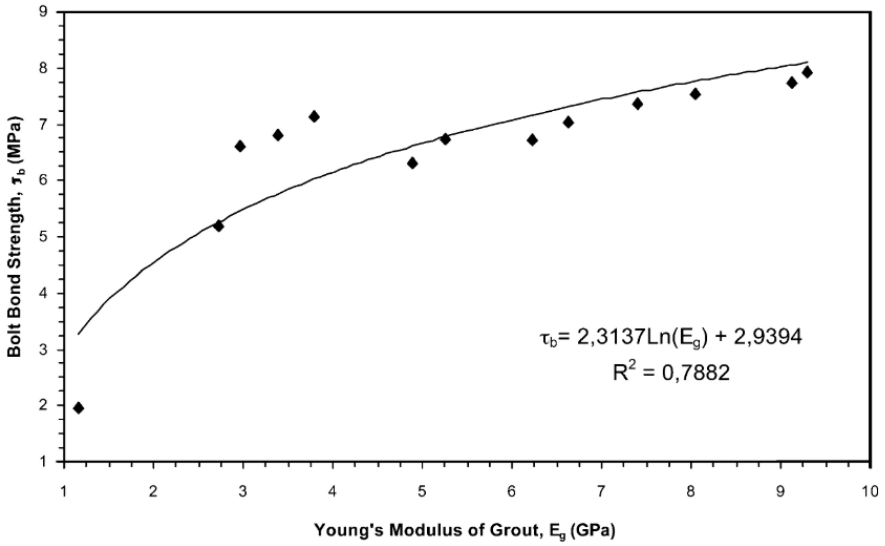

Figure 2.54. relation between the bolt bond strength and elastic modulus (Kilic et al., 2003)

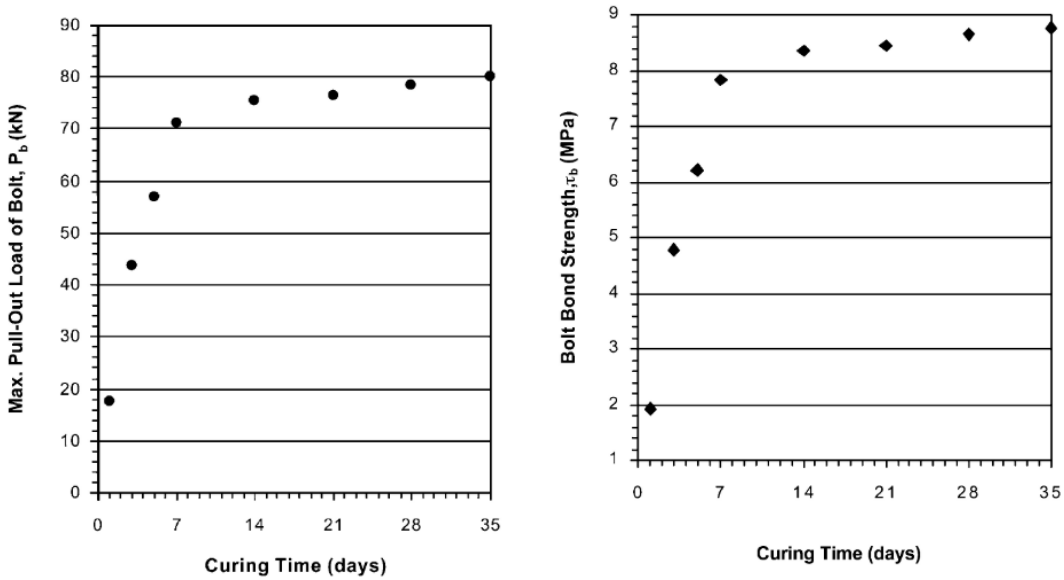

Figure 2.55. Relationship between curing time and the pullout characteristics of grouted bolt (Kilic et al., 2003)

Table 5. Composition of the grout (Benmokrane et al., 1995).

	G1	G2	G3	G4	G5	G6
Water	1	1	1	1	1	1
Portland Cement Type 10	2.2		2.22	2.02	1.66	2.22
Portland Cement Type 30		1.66				
Silica fumes				0.222		
Aluminium powder			1.55×10^{-4}			
Sand						0.95
Superplasticiser				0.057		
W/C ratio	0.45	0.6	0.45	0.45	0.6	0.45

Table 6. Mechanical properties of the grouts (Benmokrane et al., 1995).

	Compressive Strength (MPa)		Tensile Strength (MPa)		Modulus of elasticity (GPa)		Poisson's ratio	
	3 days	28 days	3 days	28 days	3 days	28 days	3 days	28 days
G1	26.6	52.6	2.8	3.8	11.1	14.8	0.12	0.14
G2	16.6	37.9	2.1	3.5	7.5	14.9	0.1	0.17
G3	21.4	40.3	1.9	3.7	6.8	12		0.17
G4	26.2	59.6	2.6	3.8	13.5	16.4	0.14	0.12
G5	19.2	34.6	1.8	3.4		8.8		
G6	29	51.8	3.2	4.3	15.4	17.9	0.1	0.15

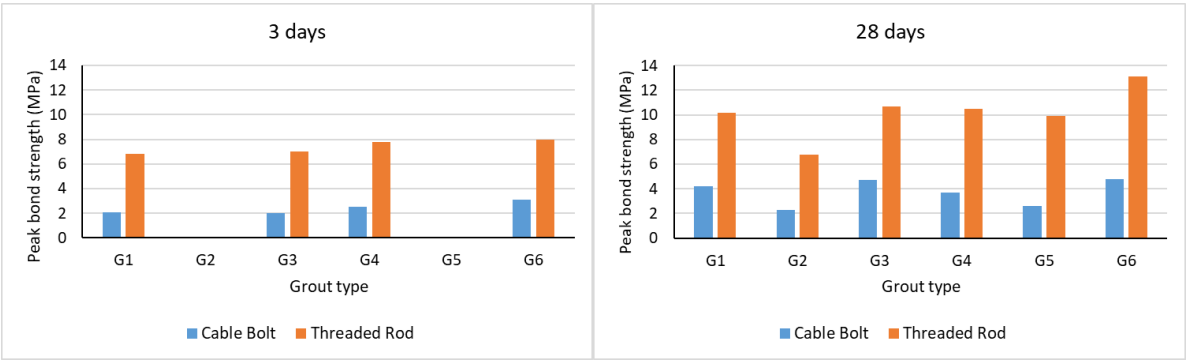

Figure 2.56. Peak bond strength of the tendons encapsulated by different types of grouts cured at 3 days (left) and 28 days (right); after Benmokrane et al., (1995).

Teymen and Kılıç, (2018) investigated the axial stress distribution of rock bolts by applying strain gauges. Bolts were installed in high-strength rock media grouted with mortar having different admixtures and w/c. It was concluded that the grout's mechanical characteristics affect shear and axial stress distributions and, consequently the ultimate bearing capacity Figure 2.57.

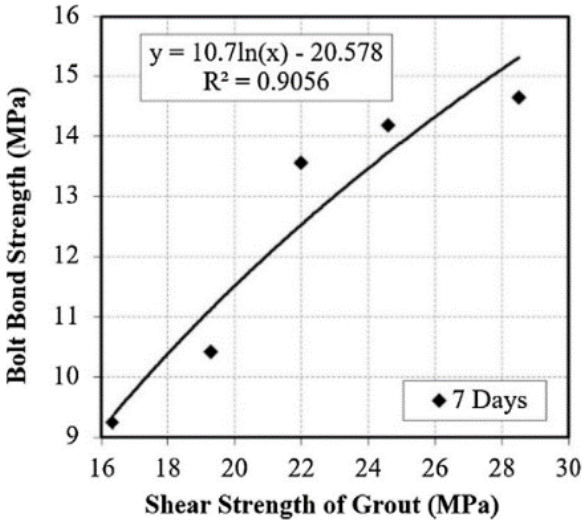

Figure 2.57. The relationship between grout shear strength and bond strength (Teymen and Kılıç, 2018)

Chang et al., (2017) conducted a number of tests indicating that grouts UCS influences the interface bond strength. The study demonstrated that when the

compressive strength of grout increases from 30 MPa to 60 Mpa, the interface bond strength increases from 3.8 to 11.5 Mpa (Figure 2.58).

Hyett et al., (1992) reported the effect of water-to-cement ratio (w/c) on the mechanical properties of Portland cement-based grouts. It is concluded that when the w/c ratios range from 0.7 to 0.35, there is a consistent increase in the UCS, tensile strength, and Young's modulus. The Poisson's ratio remains relatively constant within the range of 0.18 to 0.19. However, for water-to-cement ratios below 0.35, only Young's modulus continues to increase as expected (Figure 2.59a). In contrast, any discernible trend in the strength data is overshadowed by increased variability in both the UCS (Figure 2.59b) and the tensile strength (Figure 2.59c) results.

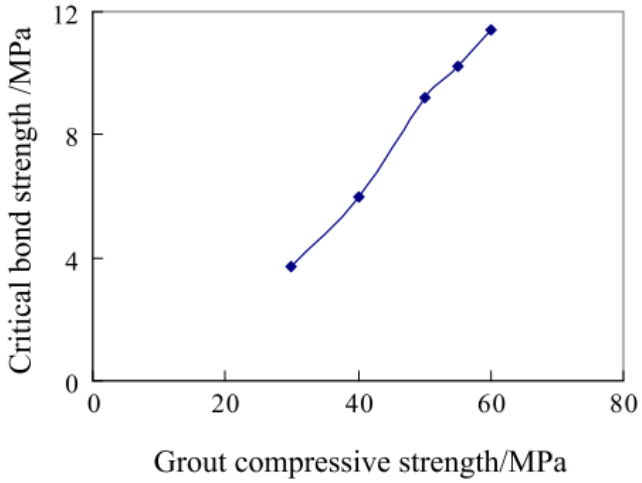

Figure 2.58. The relation between critical bond strength and grout compressive strength (Chang et al., 2017)

The experimental study conducted by Kılıc et al., (2003) also indicated the importance of the w/c in grouting materials. As indicated in Table 4, grout with higher w/c ratios demonstrates lower values in terms of UCS and shear strength, whereas grout with lower w/c ratios exhibits higher values in these properties. The optimal range appears to be between 0.34 and 0.40 for achieving favourable results. Although a w/c ratio of 0.34 yields the highest bond strength (Figure 2.60), it comes with a drawback (reduced pumpability), leading to difficulties during application. On the other hand, higher w/c ratios facilitate easier pumpability of grouting materials into the drilling hole. To achieve a plastic grout and thus better pumpability, bentonite clay can be incorporated at a maximum rate of 2% relative to the cement weight. Additionally, other additives may be used to expedite the setting time, enhance grout fluidity for injection with lower w/c, and promote expansion and pressurisation of the drill hole. However,

it is crucial to exercise caution and use the correct proportions of additives, as improper usage can lead to detrimental effects such as weakening and corrosion.

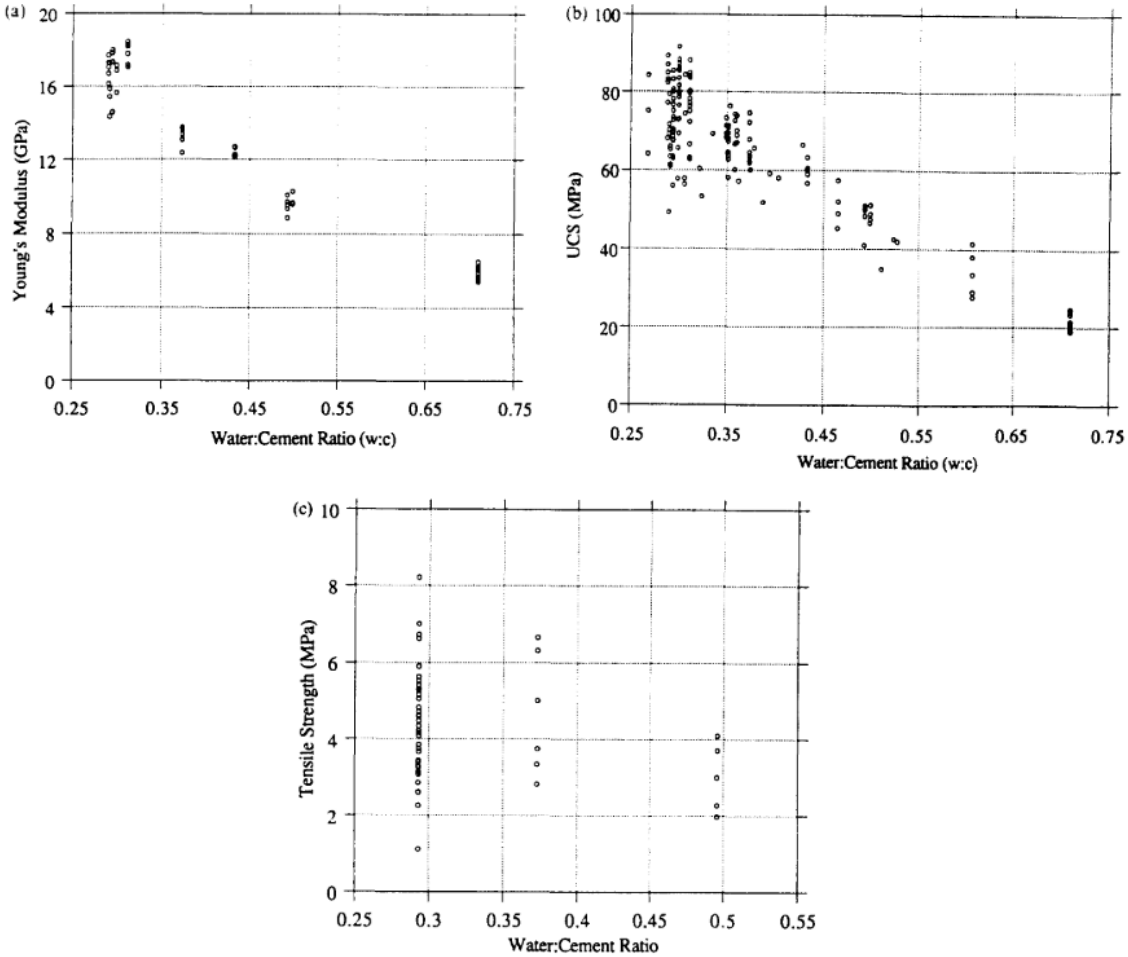

Figure 2.59. Mechanical characteristics of Portland cement in different w/c ratios paste at 28 days of curing (Hyett et al., 1992)

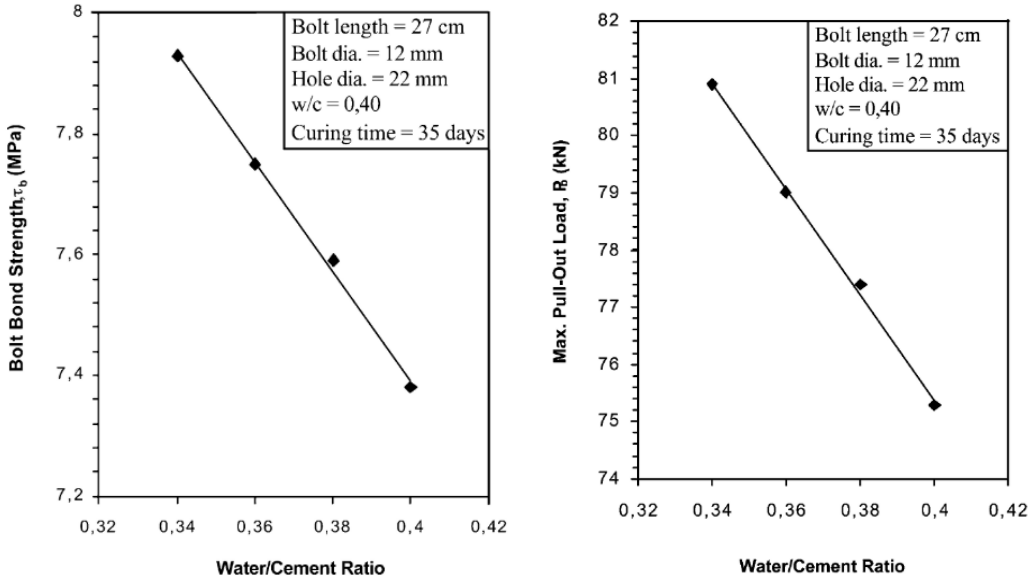

Figure 2.60. Effects of w/c on the pullout characteristics(Kilic et al., 2003)

Aziz et al., (2017) carried out a series of experiments on commercial grout products (Stratabinder HS and BU-100) to investigate the effects of w/c and curing time on grout mechanical properties (Table 7). The results show that an increase in the w/c from 28% to 42% causes a 43% reduction in the UCS of Stratabinder HS specimens (Figure 2.61). In this study, the effect of w/c is also noted on grout shear strength by conducting Punch shear tests (Figures 2.62 and 2.63).

Table 7. Mix properties used by (Aziz et al., 2017a).

	Strathabinder HS		BU-100	
Mix ID	Lit/bag	W/C (%)	Lit/bag	W/C (%)
1	5.6	0.28	3.6	0.18
2	6.4	0.32	4.4	0.22
A	7	0.35	6.5	0.25
3	7.6	0.38	5.6	0.28
4	8.4	0.42	6.4	0.32
5	9	0.42	7	0.35

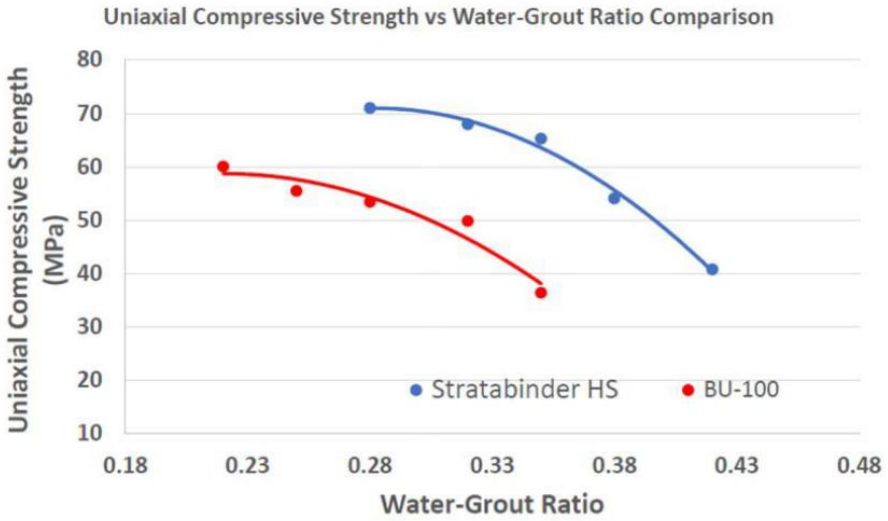

Figure 2.61. Effect of w/c ratio on the UCS of Strathabinder HS and BU100 grouts(Aziz et al., 2017a)

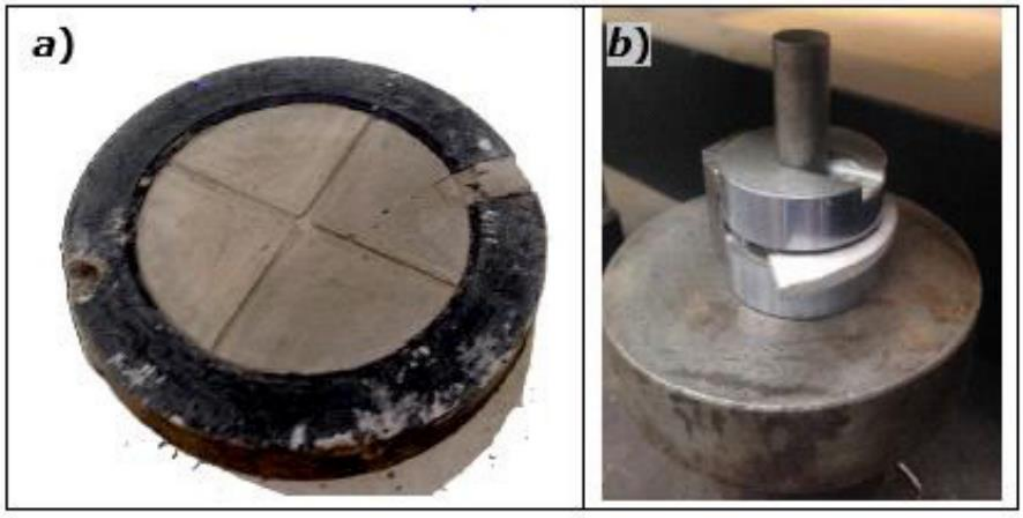

Figure 2.62. Punch shear specimen (a) and test (b) (Aziz et al., 2017a)

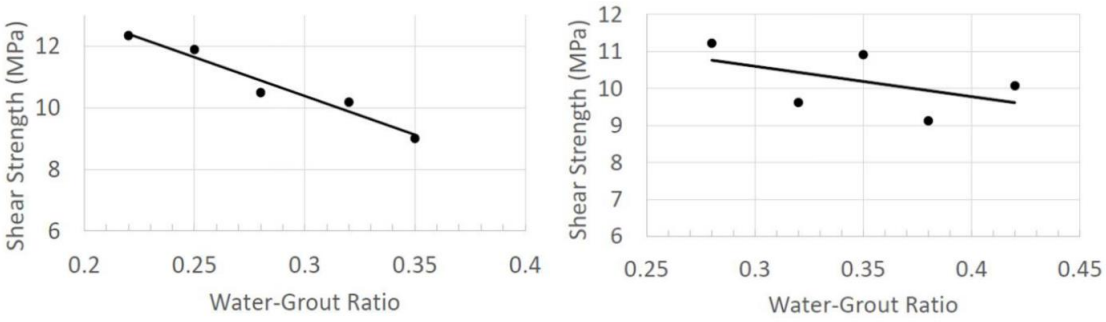

Figure 2.63. Effect of w/c ratio on the shear strength of Strathabinder HS and BU100 grouts (Aziz et al., 2017a)

Kim et al., (2019) evaluated the performance of fully encapsulated rock bolts using cementitious and resin grout. It was stated that the grouted bolts' ultimate bearing capacity is a function of water to grout ratio and curing time, as illustrated in Figures 2.64 and 2.65.

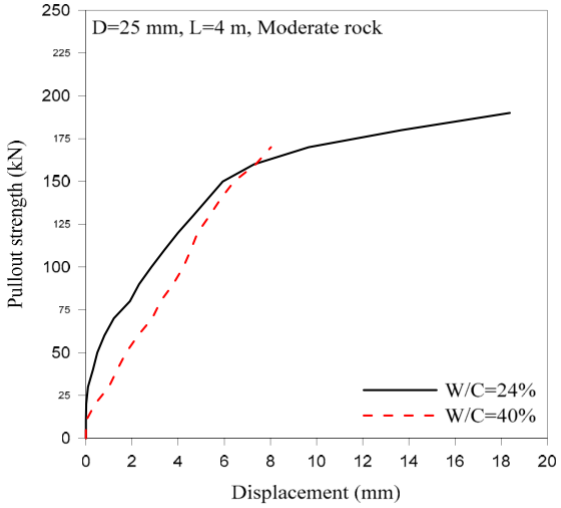

Figure 2.64. Effect of w/c ration on the pullout performance of rock bolts (Kim et al., 2019)

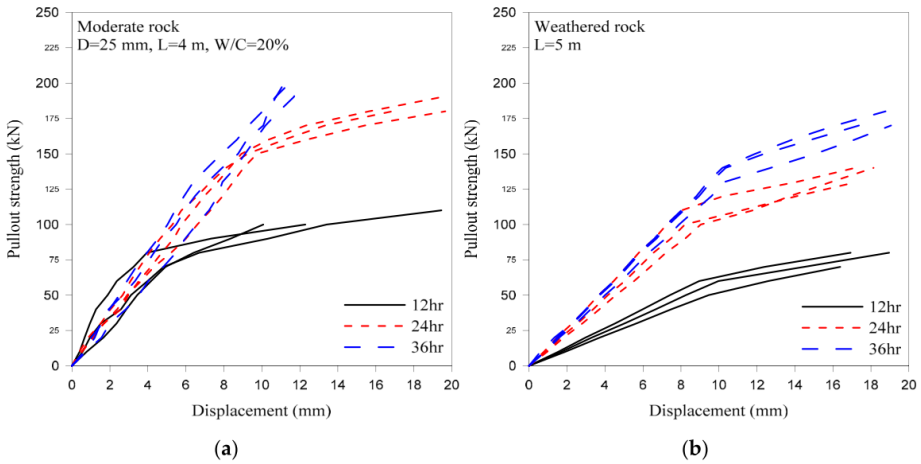

Figure 2.65. Effect of grout curing time on the pullout capacity of rock bolts; (a) moderate rock, and (b) weathered rock (Kim et al., 2019)

Li et al., (2016) illustrated that water to grout ratio is a crucial factor in the determination of critical length. For instance, for a sample with a w/c of 0.4, the critical embedment length was quantified as 32 mm. This length increases to 36 cm for w/c of 0.5. The experimental results also indicated a correlation between w/c and grout UCS, as shown in Figure 2.66.

Yokota et al., (2019) investigated the influence of grout strength on the reinforcing element behaviour by simplifying the bolting system to a joint system. The results of the tests demonstrated that as grout strength increases, the peak shear strength increases (Figure 2.67).

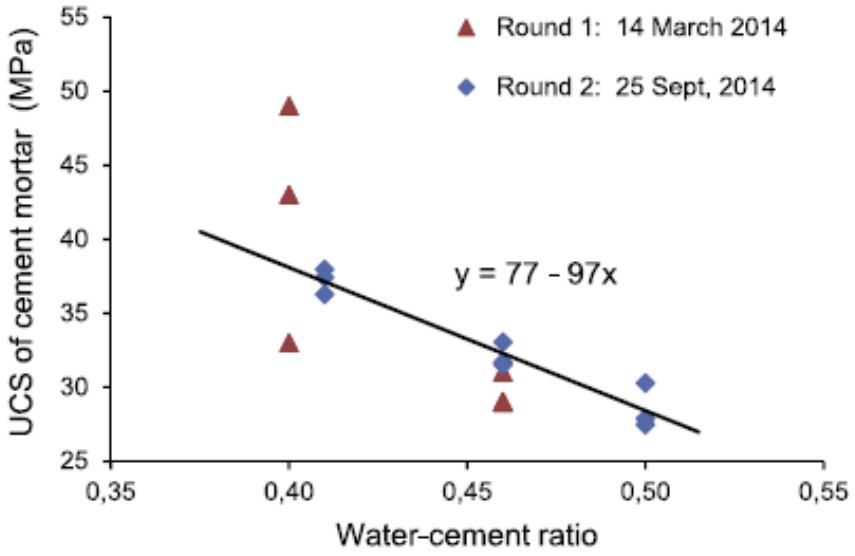

Figure 2.66. The relation between mortar UCS and w/c (Li et al., 2016)

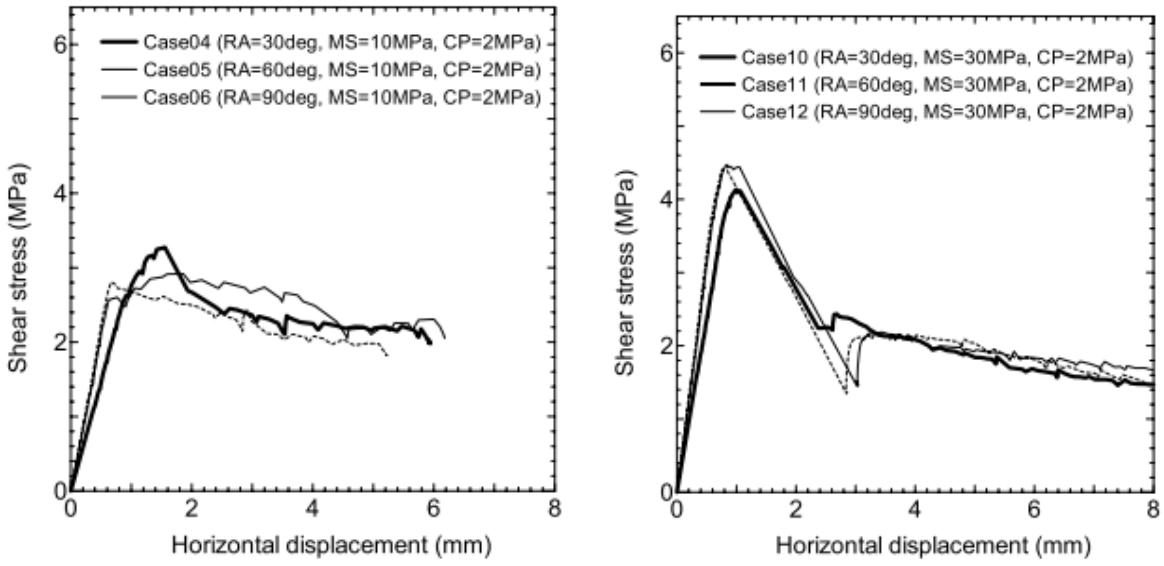

Figure 2.67. Effect of grout strength on the behaviour of rock bolts subjected to pullout force (rib angles from 30-90 degrees and with confining stress of 2 MPa) (Yokota et al., 2019)

Figure 2.68 (extracted from Figure 2.67) shows that the peak strength rises with higher mortar strength while the residual strength declines.

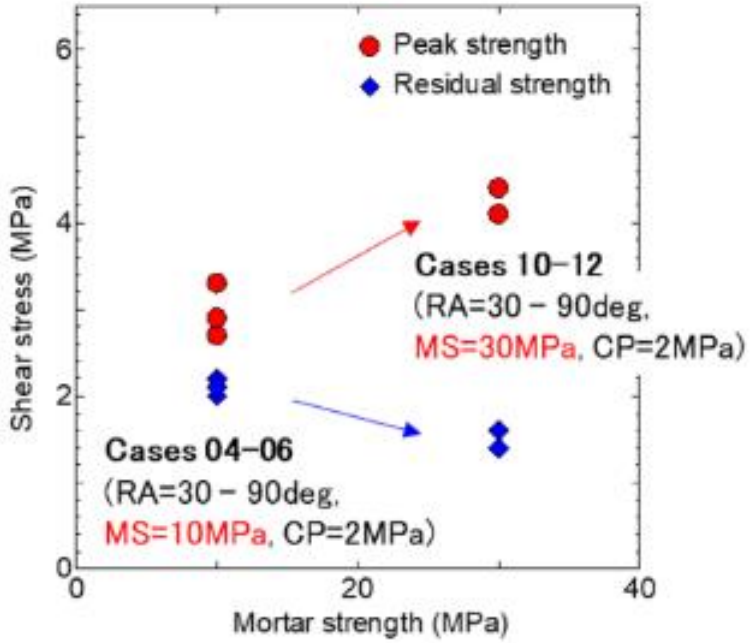

Figure 2.68. Summary of Figure 67(Yokota et al., 2019)

In terms of grout thickness, Bradly and Brown (2006) demonstrated by Eq. 3 that the annulus thickness of the grout has a reserve effect on the grout stiffness,

$$K_{bond} = \frac{2\pi G_e}{\ln\left(1 + \frac{2t}{d_b}\right)} \tag{3}$$

where K_{bond} is the grout stiffness, G_e is the shear modulus of the encapsulation medium, t is the grout annulus thickness, and d_b is the diameter of the bolt.

Several experimental and field studies have been carried out to find out the optimum annulus thickness showing that the value in the range of 2-7 mm has the best load transfer interaction. Fabjanczyk and Tarrant, (1992) reported that the optimum annulus thickness is the smallest, which can be used considering executive restrictions. In another research, Fuller 1994 concluded that cable bolts embedded in a 28 mm drill hole have a 40% higher peak pull-out load and a 30% higher pull-out stiffness than the ones installed in a 29 mm borehole. Aziz et al., (2006) demonstrated no noticeable difference in the performance of rock bolts with a nominal diameter ranging from 21.7 to 35 mm, however, the bearing capacity decreases above this range.

2.18.3. Effects of bolts geometry and surface profile configuration on rock bolts' performance

To date, numerous pullout tests have been carried out under constant radial stiffness and constant confinement stress conditions to determine the failure mechanism and the bond-slip behaviour of grouted rock bolts. The results demonstrated that the mechanical properties of the steel, along with the surface profile, diameter and length of bars, play effective roles in the shear behaviour of the bolt-grout interface. Splitting of grout never occurs for round bars. Thus it can be concluded that the geometry of surface ribs including rib height, rib width, rib angle and rib spacing shown in Figure 2.69, dominates the interfacial bond behaviour when deformed bars are subjected to axial loading (Tepfers, 1979). The surface profile defines the width of the shear zone and the angle of fractures at the encapsulation medium. Rib geometry also can effectively influence the mixing process of the two components of the resin cartridge.

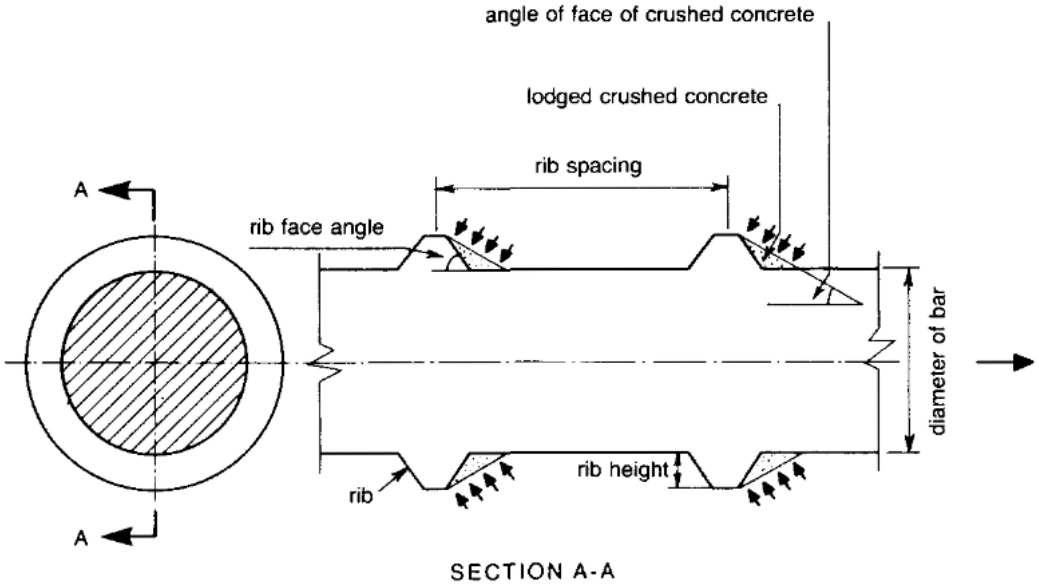

Figure 2.69. The geometry of a typical deformed bar and the mechanical interaction with concrete (Tepfers, 1979)

According to the test results conducted by Kılıc et al., (2002), it was demonstrated that an increase in the bolt diameter and bolt length results in a linear increase in the ultimate pull-out load. Murata and Kawai, (1984) conducted several splitting pullout tests to evaluate the bond strength of deformed bars with different rib face angles ranging from 15 to 90 degrees (Figure 2.70). The DDA numerical modelling conducted by Nie et al., (2019), under low confining stress, shows that maximum bond strength increases with an increase in the rib face angle from 30° to

90°, however, the effect of a rib face angle of less than 30° is not effective. It was also stated that rib spacing may influence bond stiffness as larger rib spacing can result in lower bond stiffness. Aziz and Webb, (2003) demonstrated that the bond strength of the bolting system increases with ribs spacing. Therefore, optimisation of the surface profile of the bars can effectively improve the performance of the fully grouted rock bolts. Aziz et al., (2006) conducted a comparative study to examine the performance of rock bolts in pullout and pushout tests. In this study, three types of common rock bolts used in Australian coal mining were employed. The results indicated that while the interfacial failure modes in both tests are similar, the bond strength of the bolt-grout interface in push test is greater than that of pullout test. Also, it was observed that the bond strength and axial load capacity increases with the rib height, rib spacing and the embedment length.

Cao et al., (2013b) conducted experimental and analytical studies in pull-pushout tests and concluded that the difference in the load capacity in pull-push tests can be the effect of Poisson's ratio as it relates to the steel bar, the properties of the failure surface and the radial stiffness of the boundary. Aziz et al., (2008) carried out two series of pushout and pullout tests on bolts in consonant radial stiffness with cylindrical steel sleeves of 115mm and 150mm in length. To evaluate the influence of surface profile on the ultimate axial load capacity, bolts with different rib heights and rib spacing were used, as shown in Figure 2.71. They reported that ultimate loading capacity increased with an increase in the rib spacing from 12.5mm to 37.5 mm, but it decreased when it further increased to 50 mm (Figure 2.72).

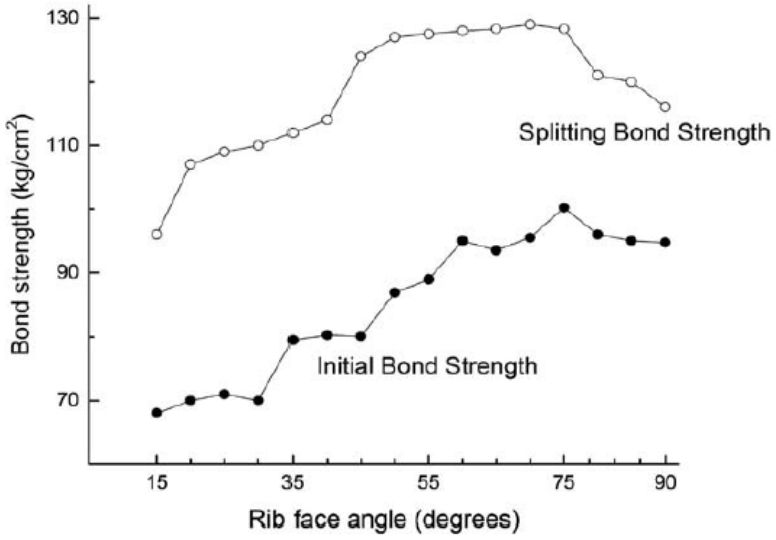

Figure 2.70. The effect of rib angle on bond strength (Murata and Kawai, 1984)

Bolt Type	T1	T2	T3	T2 Bolt Modified		
				G1	G2	G3
Profile Spacing (mm)	12.50	12.50	25.00	25.00	37.50	50.00
Profile Height (mm)	1.00	1.35	1.20	1.35	1.35	1.35
Average Profile Width (mm)	2.25	2.75	3.75	2.75	2.75	2.75
Profile Angle	22.5°	22.5°	22.5°	22.5°	22.5°	22.5°
Bolt Samples						

Figure 2.71. The surface profile specifications in the study (Aziz et al., 2008)

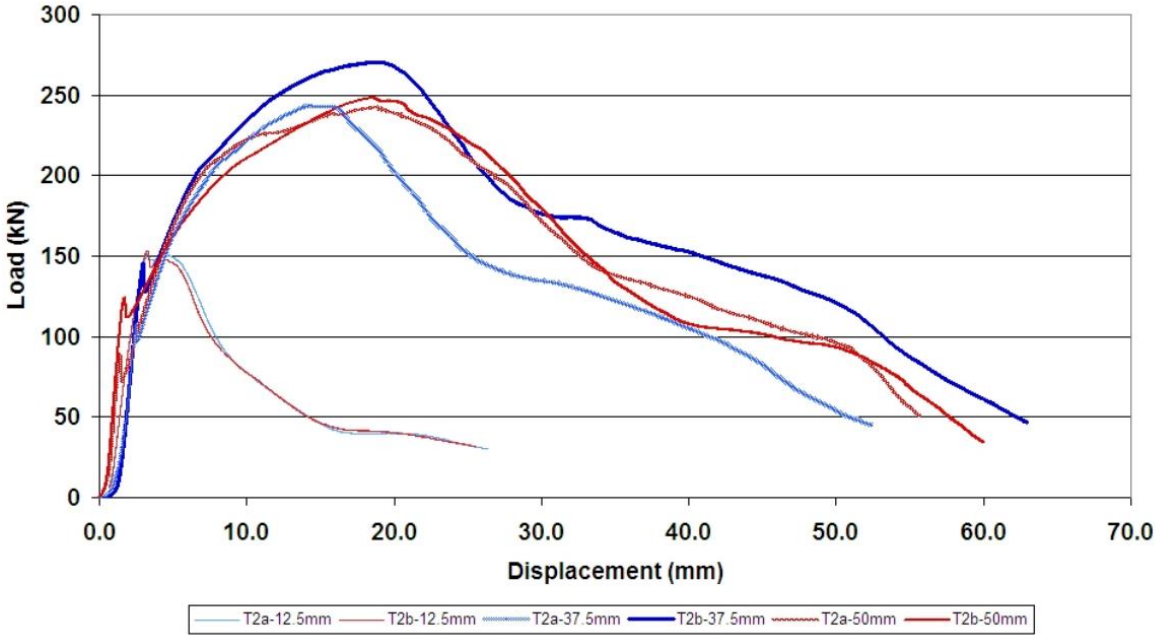

Figure 2.72. The effect of rib spacing on the load displacement curve (Aziz et al., 2008)

Ito et al., (2001) conducted pull-out tests by applying two deformed and twisted rock bolts and two plain strand and bulb strand cable bolts (Figure 2.73) and then attempted to visualise the failure patterns by X-ray CT scanner. The authors concluded that the failure mechanism is highly dependent on the type of reinforcing element, namely the shape ribs and lugs of the bolt. For example, the failure mode for the bolts with the twist shape lugs was spiral, however, for the strand cable bolts failure mode splitting mechanism.

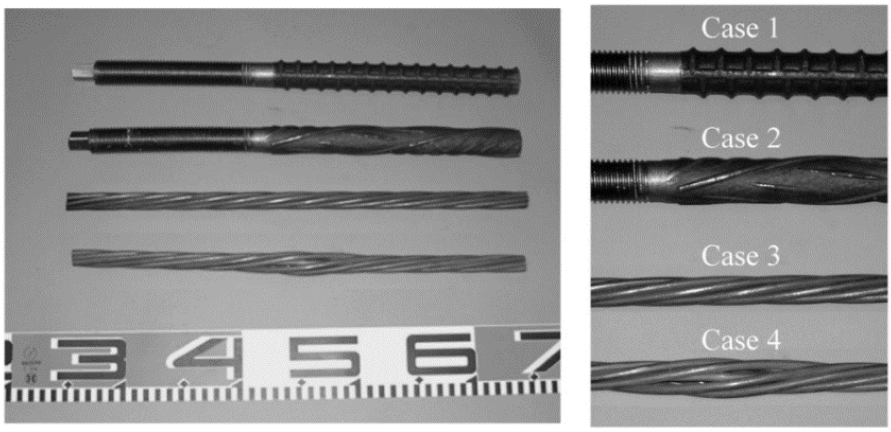

Figure 2.73. The cable bolts and rock bolts used in the study: the deformed bar (case 1), the twist bolt (case 2), the plain strand cable bolt (case 33) and the bulb strand cable bolt (case 4) (Ito et al., 2001).

Kilic et al., (2003) performed a direct pull-out test on rock bolts with different shapes of surface lugs including smooth surface bars, ribbed bars, single, double and triple conical lugged bars (Figures 2.74 and 2.75). The results of the experiments demonstrated that the strength of rock bolts is dependent on the surface profile, diameter and length of the bars. It was also concluded that decreasing in the angle of the conical lugs results in increasing the bearing capacity. As seen in Figure 2.76, rock bolts with triple conical lugs exhibit the best performance amongst the other arrangements, followed by rock bolts with double conical lugs. It was observed that the bond strength of the ribbed bolts is generally a result of the shearing strength of the grout (5.5 times greater than that of smooth bars), however, the bond strength of the conical shape bolts is the result of the combination of compressive and shearing strength of grout (27% greater than that of ribbed bars).

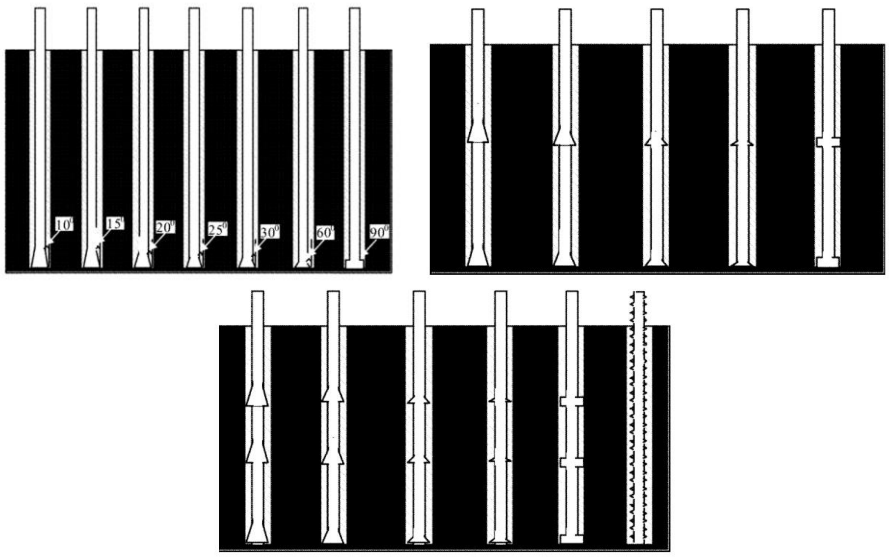

Figure 2.74. Schematic view of the lugged bolt (Kilic et al., 2003)

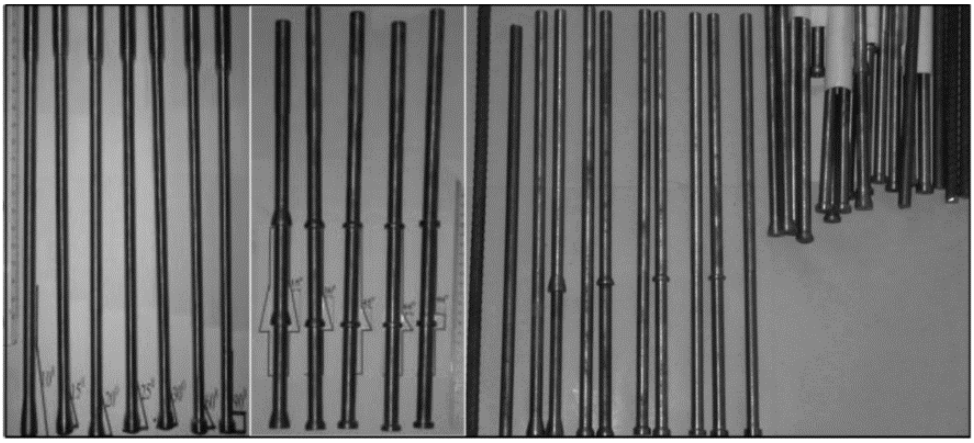

Figure 2.75. The bolt surface profile (Kilic et al., 2003)

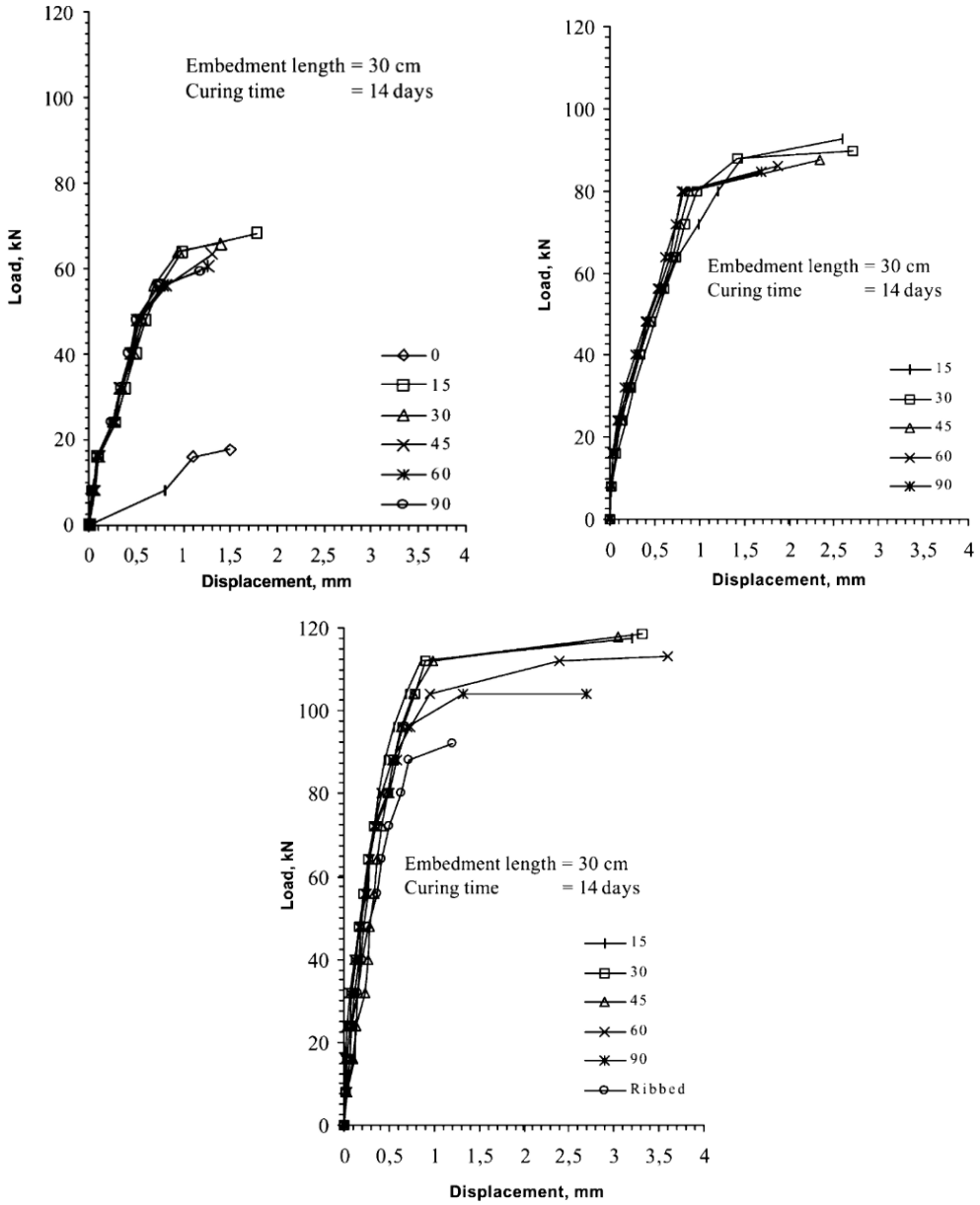

Figure 2.76. Load-displacement curves of bolts with different conical lugs arrangements (rib angles 0-90°) including single conical lugged bolts (left), double conical lugged bolts (middle), and triple conical lugged bolts (right) (Kilic et al., 2003)

Yokota et al., (2019) attempted to examine the influence of the bolt configuration including the presence or absence of ribs and rib angles, on the reinforcement mechanism by seeking the crack initiation and propagation. In this study rock bolting system was simplified as a typical joint in which the upper and lower sides were grout and steel, respectively (Figure 2.77). Experiment results revealed that rib angle has an insignificant influence on crack initiation and propagation and peak shear strength, however, as the rib angle decreases, the shear stiffness slightly increases (Figures 2.78 and 2.79).

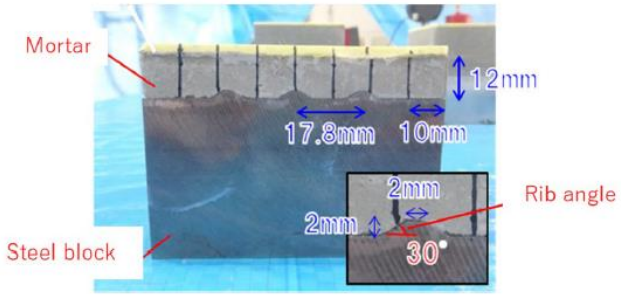

Figure 2.77. The prepared sample for the direct shear test (Yokota et al., 2019)

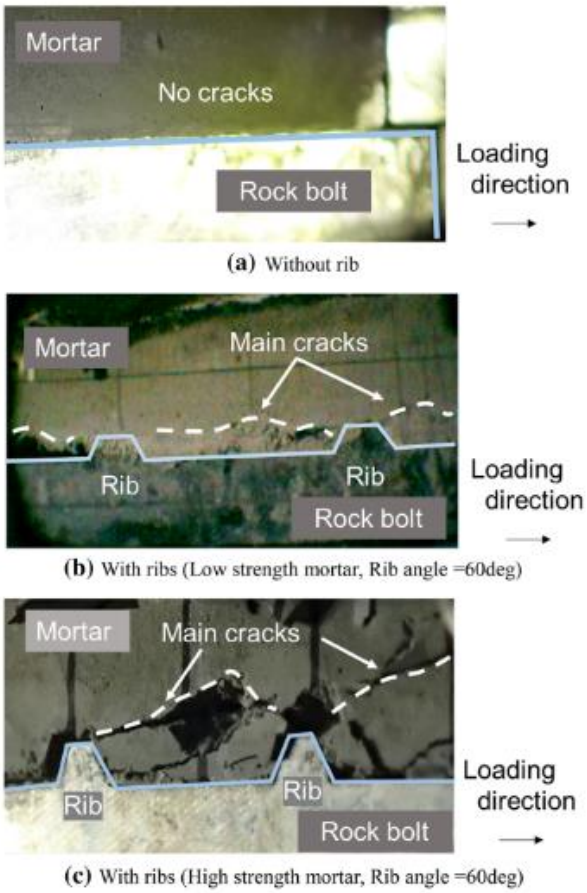

Figure 2.78. Visual investigation of the specimen after the test (Yokota et al., 2019)

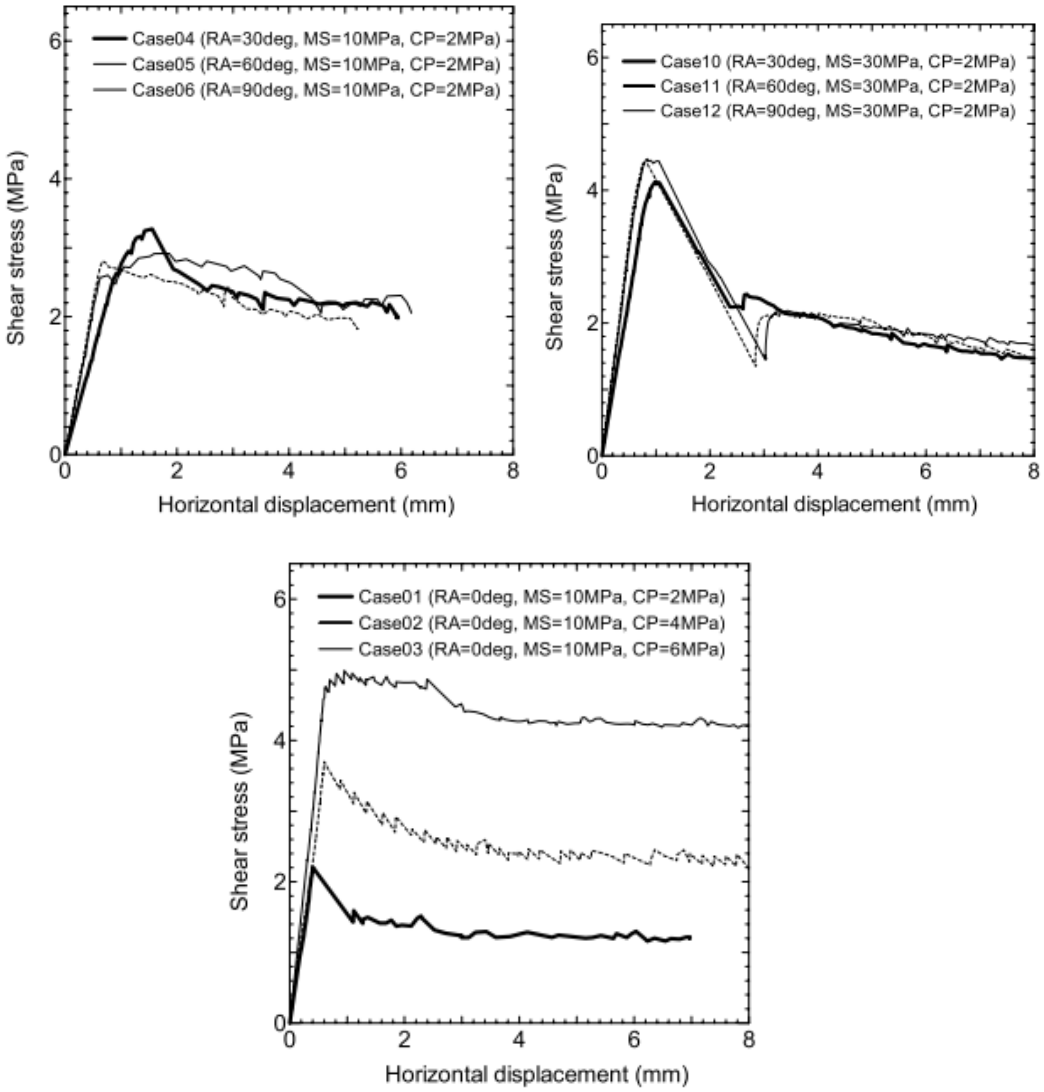

Figure 2.79. Effect of rib angle on the bond strength using a grout with UCS=30 MPa and confining stress of 2 MPa (Yokota et al., 2019)

Figure 2.80 presents a summary of the impact of mortar strength, as depicted in Figure 2.79. It is evident that an increase in rib angle from 0 to 30° enhances bolt performance, beyond which the capacity remains relatively unchanged.

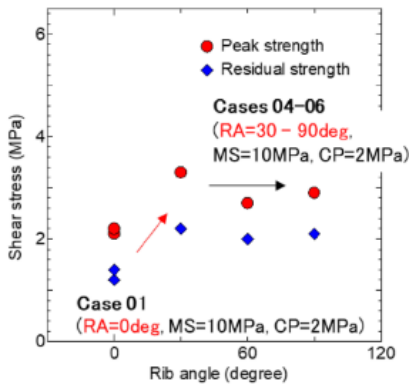

Figure 2.80. Summary of Figure 2.79 a and c (Yokota et al., 2019)

Cui et al., (2020) investigated the influence of bolt profiles including rib spacing, rib height and with/without ribs, on the interfacial shear response of rock bolts to a horizontal load using a direct shear test under high normal stiffness conditions. For this purpose, the bolt's surface profile was simulated on steel plates with different configurations, as shown in Figure 2.81. The test was conducted under both the CNL and CNS conditions for ribbed samples using a self-developed apparatus, however, for planar samples, only the CNL was performed. Figures 2.82 and 2.83 illustrate the influence of profile configuration under the CNL and CNS conditions, respectively. As shown, the effect of rib spacing is different under the CNL and CNS conditions. For example, under the CNL condition, the highest shear strength belongs to the specimen with 10mm rib spacing, while the peak shear strength under CNS conditions belongs to the specimen with 20mm rib spacing. On the other hand, in terms of rib height, its effect on the shear behaviour of the bolt-grout interface is similar under both conditions. As can be seen, the highest bond strength is attained when the rib height is 20mm. Compression of test results in direct shear under the CNS tests with the study conducted by (Aziz et al., 2008) reveals good agreement although there is a discrepancy in the optimal rib spacing.

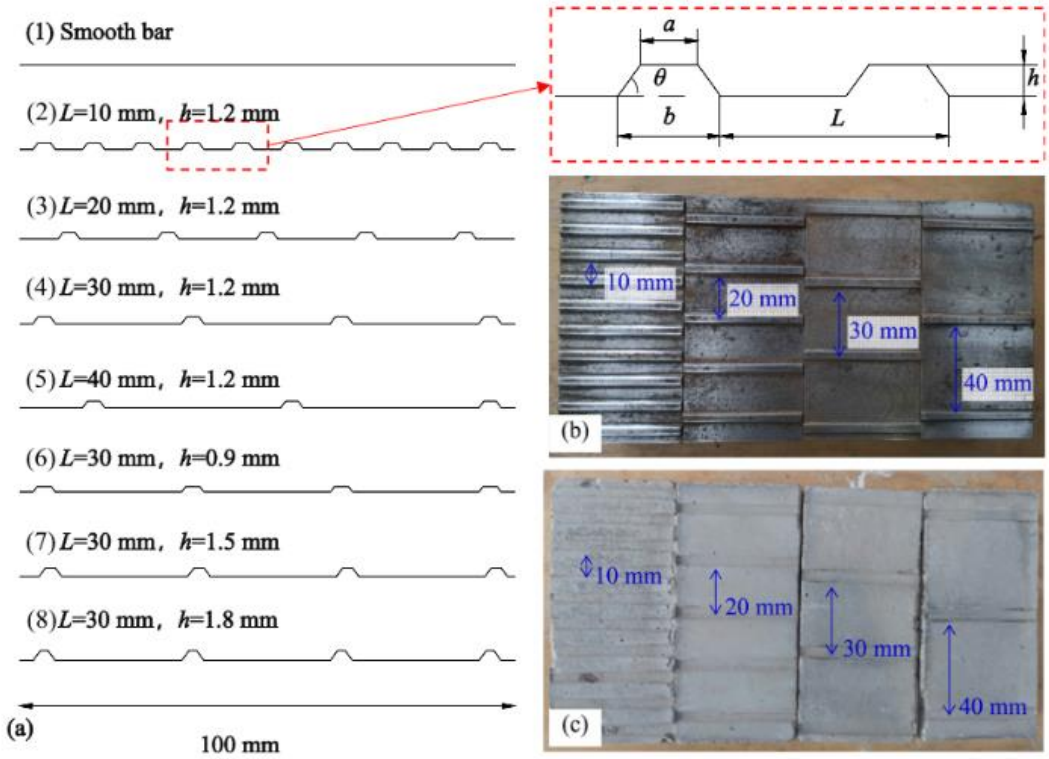

Figure 2.81. The prepared samples for tests: (a) steel plate specifications, (b) steel plates, and (c) grout specimens (Cui et al., 2020)

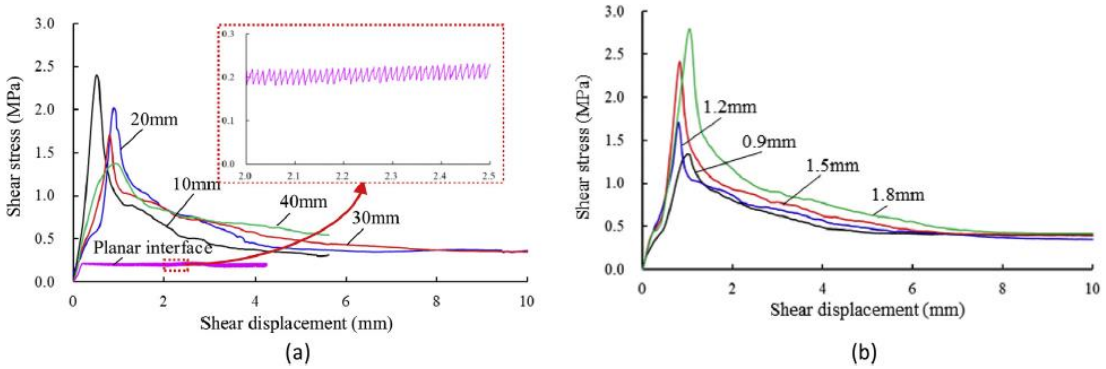

Figure 2.82. The hear bond and stress-displacement relationships of bolt-grout interface under CNL conditions: (a) effect of rib spacing, and (b) effect of rib height (Cui et al., 2020)

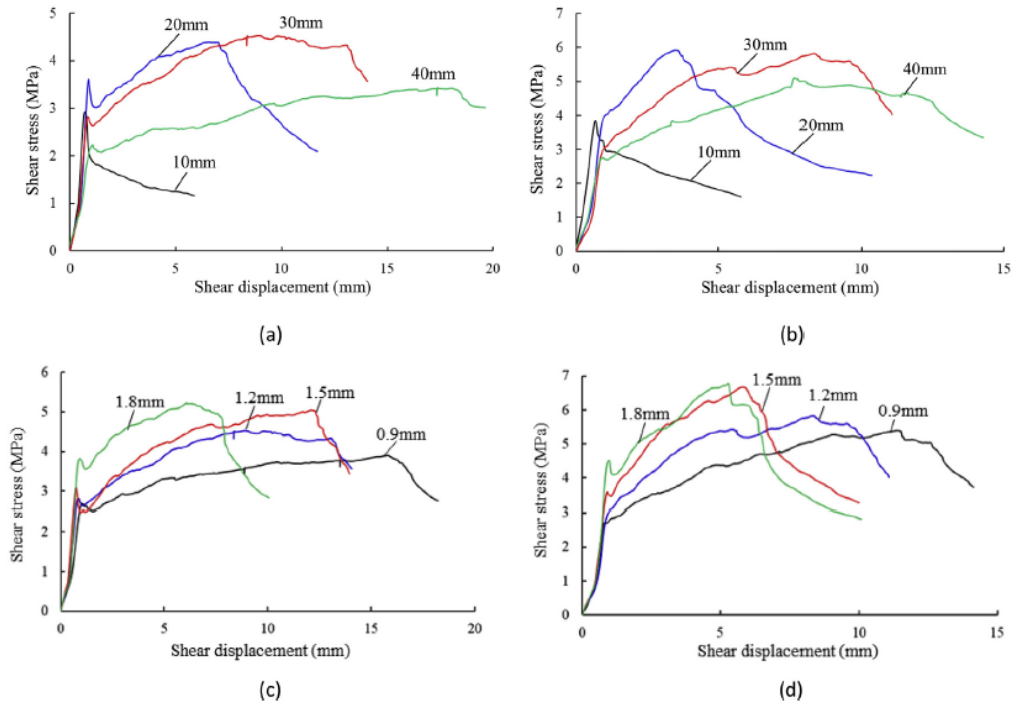

Figure 2.83. Shear stress-displacement relationships with different bolt surface profiles under CNS conditions with different normal stiffness (k_n): (a) effect of rib spacing k_n=10GPa/m, (b) effect of rib spacing k_n=100 GPa/m, (c) effect of rib height k_n=10 GPa/m, and (d) effect of rib height k_n=100 GPa (Cui et al., 2020)

2.18.4. Effects of encapsulation length on rock bolt performance

Embedment length is an important aspect of rock bolting, which significantly affects the load-displacement relationship. The embedment length can be designed to be within a range from short to long according to the purpose of the study.

Benmokrane et al., (1995) stated that the embedment length has to be short of less than four times of bolt diameter for a uniform shear stress along the bolt. In this study, the anchored lengths varied and were set at 4, 7, 11, and 14 times the anchor diameter for threaded bars and 4, 9, 14, and 20 times the anchor diameter for stranded

cables. The results of pullout tests on threaded bars and stranded cables are illustrated in Figure 2.84. As seen, the encapsulation length significantly influences the bearing capacity of the bolts.

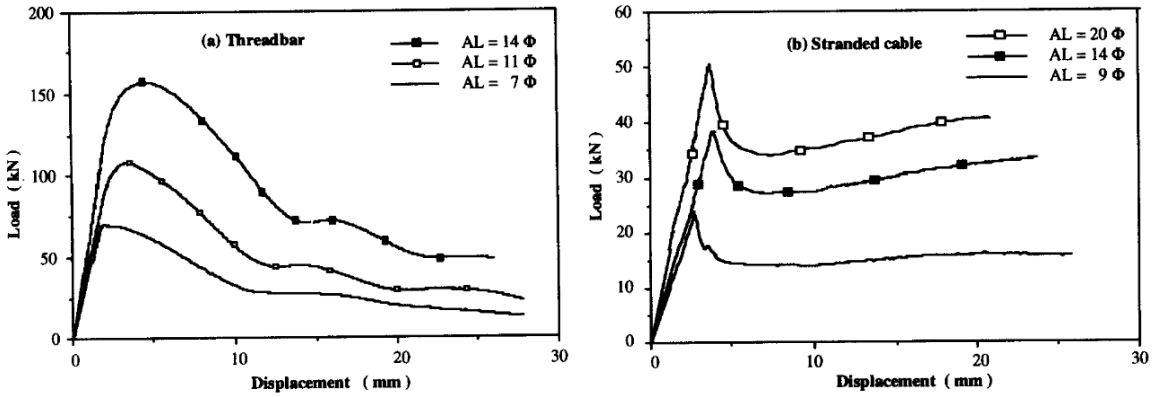

Figure 2.84. Effect of embedment length on the load-displacement behaviour (Benmokrane et al., 1995)

Kilic et al., (2003) examined the performance of rock bolts with different specifications and embedment lengths of 150, 247, 300 and 320 mm. The results are represented in Figure 2.85. The maximum pullout load increases almost linearly with the embedment length.

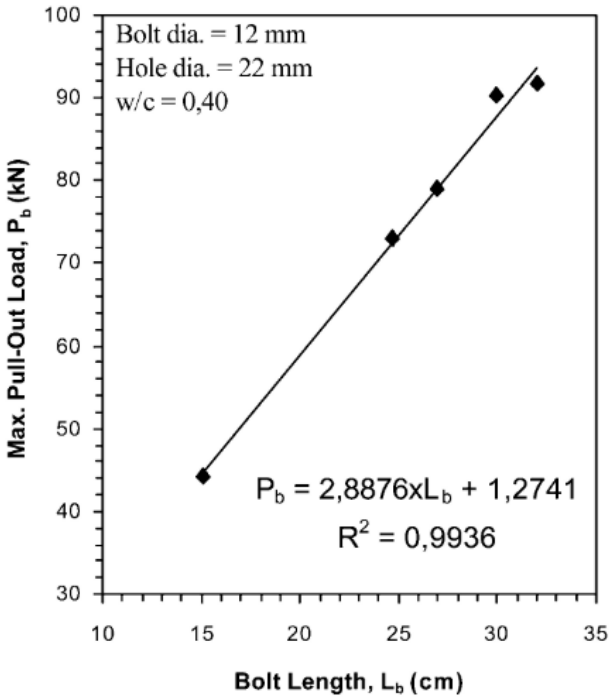

Figure 2.85. Relation between pullout capacity and embedment length for the bolt with 12 mm diameter (Kilic et al., 2003)

Blanco et al., (2013) developed an analytical tool to simulate the axial behaviour of anchored elements in different conditions. Utilising the newly developed tool to

predict the behaviour of encapsulated tendons demonstrates that the load-displacement correlation is dependent on embedment length. This relationship is illustrated in Figure 2.86, where the predicted load-displacement curves from six pull-out tests are presented. Despite using the same bolt and grouting materials, the curves differ due to the varying embedment lengths.

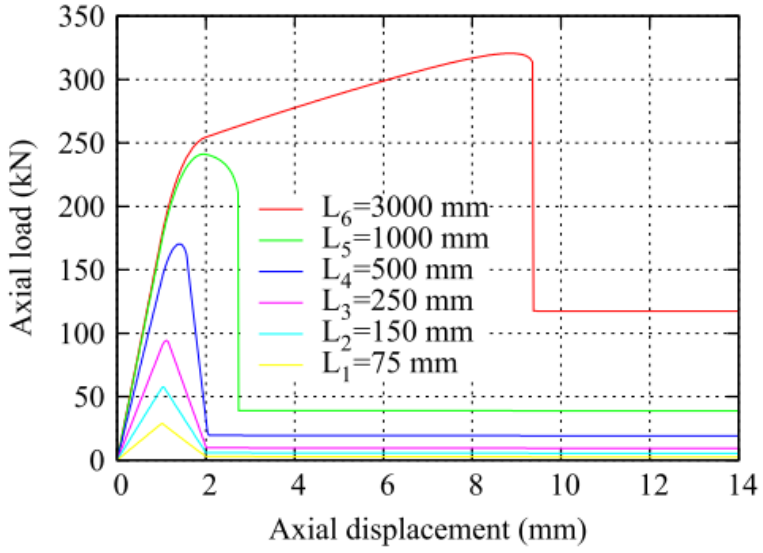

Figure 2.86. Simulated effect of embedment length on the pullout behaviour of rock bolts (Blanco et al., 2013)

Figure 2.87 presents the distribution of shear stress along the embedment length during the six tests depicted in Figure 2.86. In cases with shorter lengths, the shear stress is uniformly spread along L throughout the entire pulling process. However, with longer lengths, the shear stress distribution becomes non-uniform during the process, making the process of shear stress on the encapsulation length complex. As a result, analysing pull-out test outcomes is more straightforward for shorter lengths where a uniform distribution can be assumed.

Ma et al., (2013) evaluated the presented non-linear bond-slip model by conducting short-encapsulation pullout tests of 36 mm and 75 mm long bolts. To determine and investigate the full-range behaviour of fully grouted rock bolts, the embedment length is required to be long enough. However, short-length embedment can only present a partial behaviour of fully grouted rock bolts, which is valuable for evaluating analytical approaches for axial and shear behaviour. The consensus has been that the short encapsulation length should be in the range of 4 to 8 times the bolt diameter.

The encapsulation length basically determines whether the failure occurs in the

bolt or in another component. If the encapsulation length is sufficient to transfer all the load, then the bolt itself will fail once the applied load exceeds the ultimate capacity of the bolt. Alternatively, if the encapsulation length is insufficient, localised failure occurs where the induced stresses exceed the material strength (grout or rock). Figure 2.88 illustrates the possible load-slip relationships in the pull-out process of grouted rock bolts. At the critical encapsulation length, the anchorage strength of the unit exceeds the yield strength of the bolt. If the encapsulation length is much longer than the critical encapsulation length, the bolt failure occurs in the shank (Wee et al., 2016) (curve A). If the encapsulation length is slightly over the critical encapsulation length, bolt debonding occurs, however, the bolt undergoes plastic deformation (curves B and C). If the encapsulation is shorter than the critical encapsulation length, debonding of the bolt will occur before reaching the peak capacity (curve D). Ren et al., (2010) proposed a closed-form analytical solution for bolts with a critical encapsulation length showing snapback form (curve C). This model includes five stages: elastic stage (i), elastic-softening stage (ii), elastic-softening-debonding stage (iii), softening-debonding stage (iv), and debonding stage (v). The model exhibits a snapback form of the load-slip relation, although the authors could not capture the snapback phenomenon in the experimental tests. The absence of sufficient radial stiffness may lead to splitting failure (curve E).

Li et al., (2016) performed numerous pullout tests to ascertain the essential embedment length of a particular 20 mm rebar bolt frequently utilised for reinforcing rock in tunnels and underground caverns within Norway encapsulated with cementitious grout with w/c ratios of 0.4, 0.46 and 0.5. Figure 2.89 presents the load-displacement curves for rock bolts with a w/c 0.50. In Fig2.92a and b, the test results for bolts with an embedment length of 100 mm and 200 mm are displayed, respectively. Notably, all bolts in these groups slipped in the grout before reaching the yield load of the bolt shank. Figure 2.89c shows the test results for rock bolts with an embedment length of 300 mm. In this case, the shanks of all three bolts yielded initially, followed by slipping in the grout. As for the bolts with an embedment length of 400 mm (Figure 2.89d), there were no signs of slippage in the grout, leading to the termination of tests at 200 kN loads. Evidently, the critical embedment length for these bolts is less than 400 mm when considering this specific water-cement ratio.

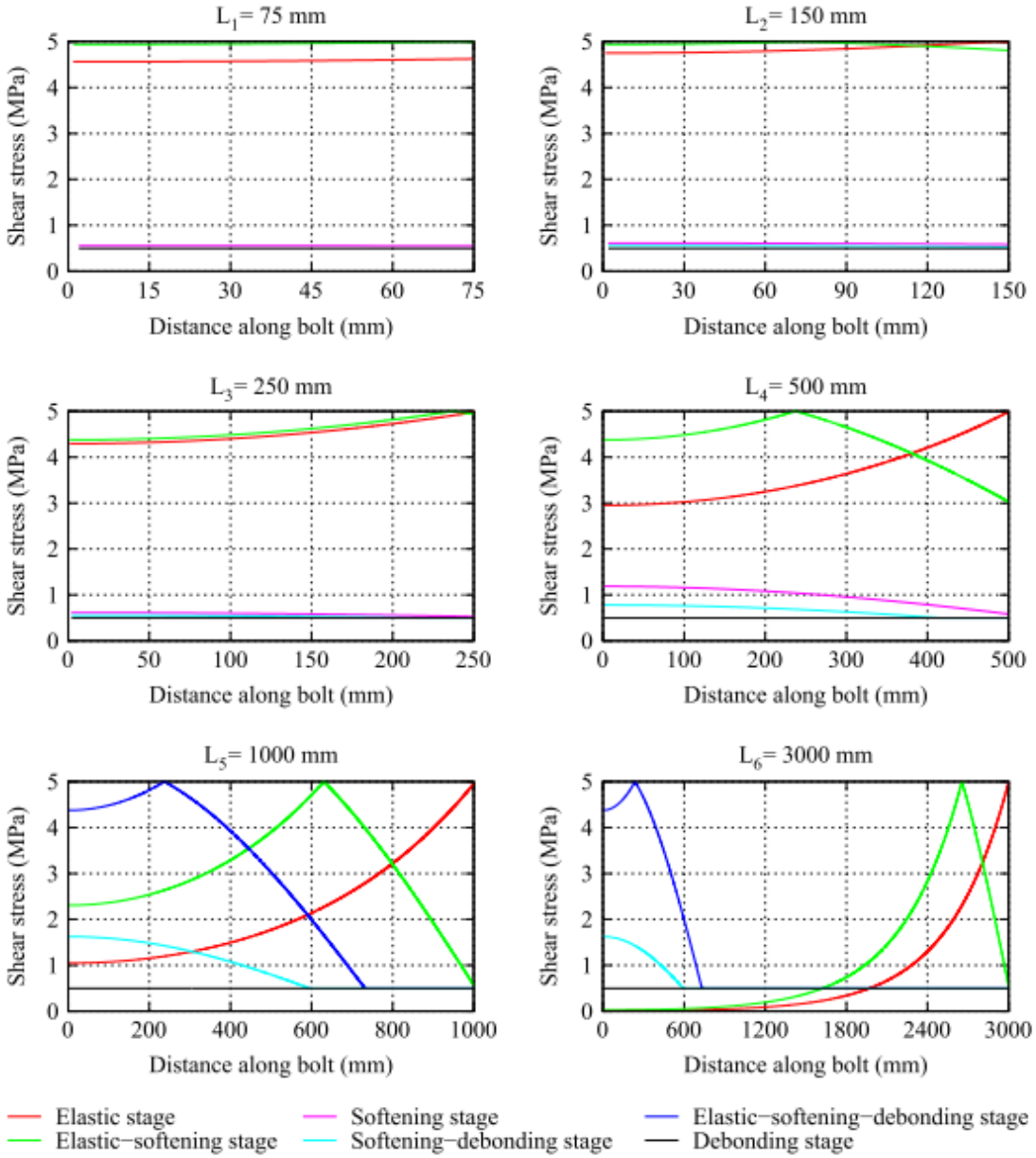

Figure 2.87. Shear distribution along the encapsulation length derived for the tests shown in Figure 2.86 (Blanco et al., 2013)

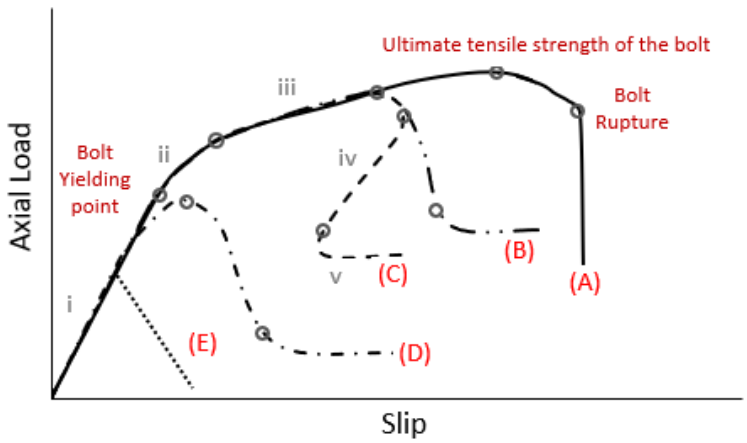

Figure 2.88. Load-displacement relation under different encapsulation lengths.

Figure 2.90 plots the ultimate pull loads of different rebar rock bolt specimens against their respective embedment lengths for three distinct water-cement ratios. The critical embedment length is determined by fitting a regression curve to the points representing slippage and finding the intersection with the strength line (at 200 kN) of the bolt shank. For the water-cement ratio of 0.40, the critical embedment length is approximately 250 mm, based on the test results of rock bolts excluding certain specimens. For the water-cement ratio of 0.46, the critical embedment length is approximately 320 mm, whereas the rock bolts with a 300 mm embedment length showed proximity to the ultimate load of the bolt shank. Similarly, for the water-cement ratio of 0.50, except for bolts with a 400 mm embedment length, the critical embedment length is approximately 360 mm.

2.19. Protective sheathed rock bolts

The long-term stability and safety of underground spaces rely heavily on the continuous monitoring of the long-term performance and integrity of reinforcing elements. The failure of these elements' integrity can lead to severe consequences. In urban tunnels, for instance, it can trigger collapses due to reinforcing corrosion, resulting in loss of life and significant economic costs. A major concern in underground structures is steel rebar corrosion, which can compromise the safety and integrity of retaining systems.

To protect rock bolts and cable bolts against corrosion, various methods like painting, galvanising, and coating are employed. Additionally, using a sheath around the tendon is an effective preventive measure against corrosion, abrasion, and impact damage. The sheathing technique involves surrounding the retaining element with an outer sheath made of plastic materials like High-Density Polyethylene (HDPE), PVC (polyvinyl chloride), or a combination of both. The main challenge in applying the sheathing technique is ensuring effective load transfer between the reinforcing element, the grout annuli, and the rock or soil. For example, corrugated plastic sheathing provides a better load mechanism between the inner and outer grout compared to smooth plastic sleeves. The effectiveness of the ground movement load mechanism on smooth plastic sleeves depends on the skin friction between the sleeve and grout. To overcome this issue, guidelines have been presented in the British standard code of practice for ground anchorages (BS 8081:1989) and the Roads and Maritime Services (RMS) quality assurance specification for soil nailing (R64). They recommend sinusoidal corrugations with a pitch between six and twelve times the

sleeve wall thickness and an amplitude not less than three times the wall thickness (Figure 2.91).

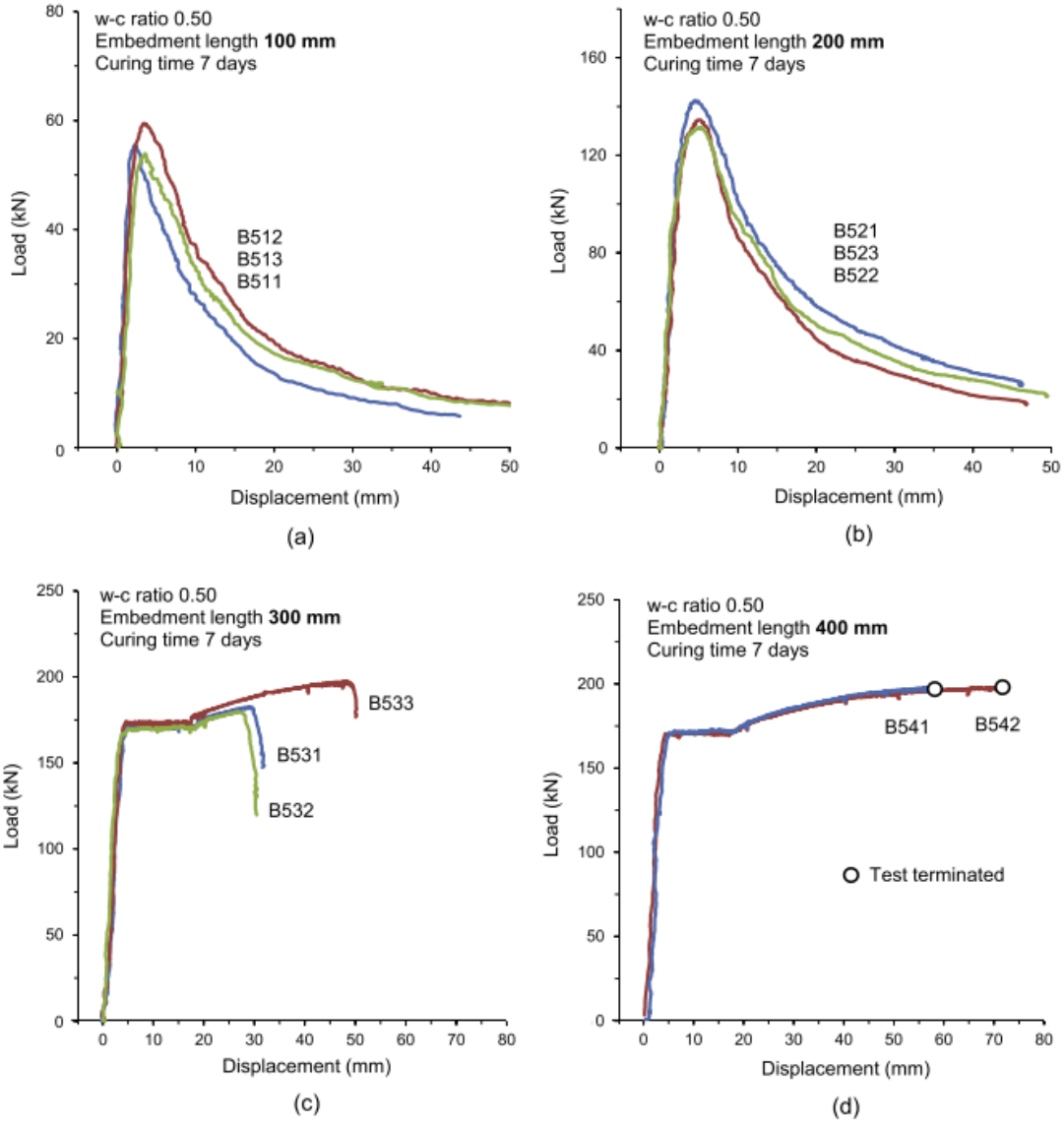

Figure 2.89. The results of pullout tests (encapsulation lengths range 100-400 mm) (Li et al., 2016)

There is limited research conducted on the impact of protective sheathing systems on the axial and shear behaviour of reinforcement systems. Aziz et al. (2017) conducted series of shear tests to investigate the impact of a corrugated plastic sheath on the shear behaviour of cable bolts and the integrity of the system. The tests involved using a steel cable with a 21.7 mm diameter and a 19-wire Superstrand cable bolt. For sheathing the cable bolt, an HDPE corrugated sleeve with a wall thickness of 2.0 mm, a pitch of 22 mm, and an amplitude of 6 mm was utilised (Figure 2.92).

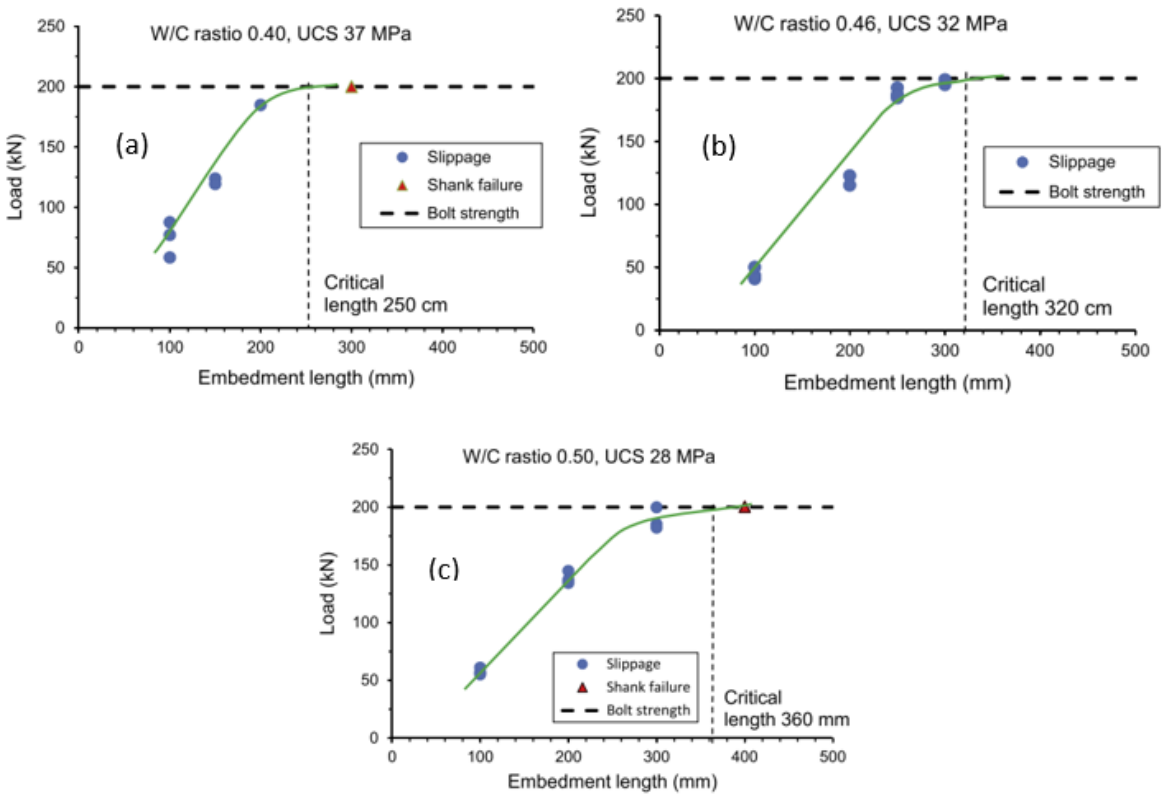

Figure 2.90. Potential relation between ultimate pullout load and embedment length for different grout mixtures (Li et al., 2016)

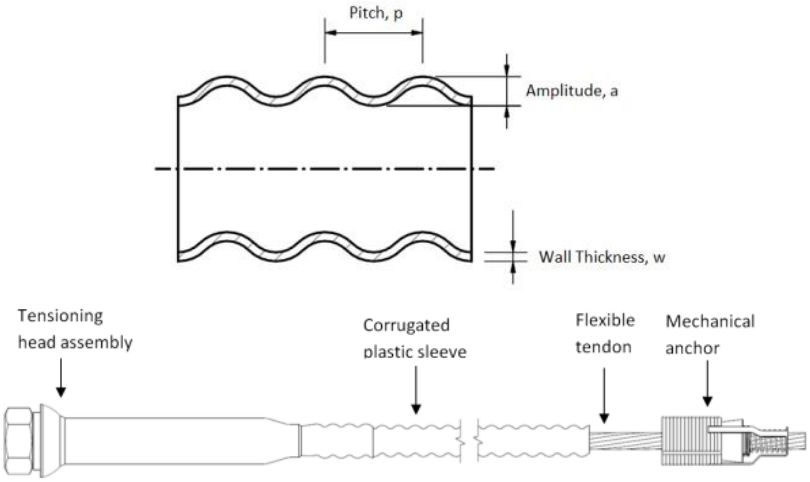

Figure 2.91. Protective sheathed tendon.

Figure 2.92. The cable and sheath used in the study (Aziz et al., 2017b)

During the guillotine shear tests, the sleeve was damaged when the displacements exceeded 24 mm (Figure 2.93).

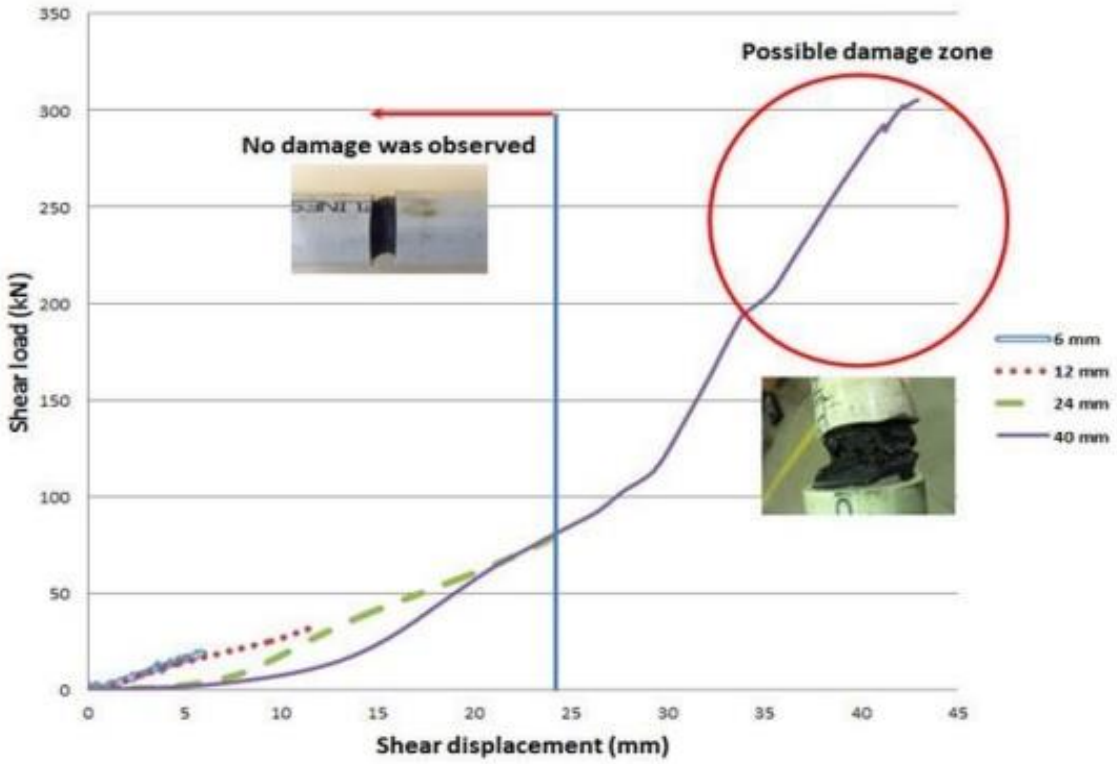

Figure 2.93. Results of guillotine shear tests conducted on the sheathed cable bolts (Aziz et al., 2017b)

Additionally, double-shearing tests were carried out to assess the potential impact caused to the protective coating of a cable bolt. The results indicated no damage to the sheath at vertical shear displacements of 15 mm and 20 mm (Figure 2.94).

Figure 2.94. The double shear specimen after the test (Aziz et al., 2017b)

2.20. The theoretical background of fully encapsulated rock bolts

There are two main methods to investigate the load transfer mechanism of rock

bolts including laboratory pull-out tests and field monitoring which can lead to mathematical solutions to predict the load transfer along rock bolts (Jin-feng and Peng-hao, 2019). Hawkes and Evans, (1951) carried out pull-out tests to prospect the distribution of shear stress along bolts. They concluded that the load distribution follows an exponential function, and the peak value takes place before any decoupling occurs (Figure 2.95). Farmer, (1975) developed theoretical and experimental research on the shear stress distribution along resin-encapsulated reinforcement elements and concluded that the mobilised shear resistance is comprised of anchoring resistance. Then an analytical model was developed to approximate the shear stress at the bolt-grout interface (Eq.4).

$$\frac{\tau_{(x)}}{\sigma_0} = 0.1\, e^{(-0.36\frac{x}{dt})} \tag{4}$$

where x is the distance between the measure and the free end, σ_0 is axial stress in the bolt, and dt is the bolt diameter.

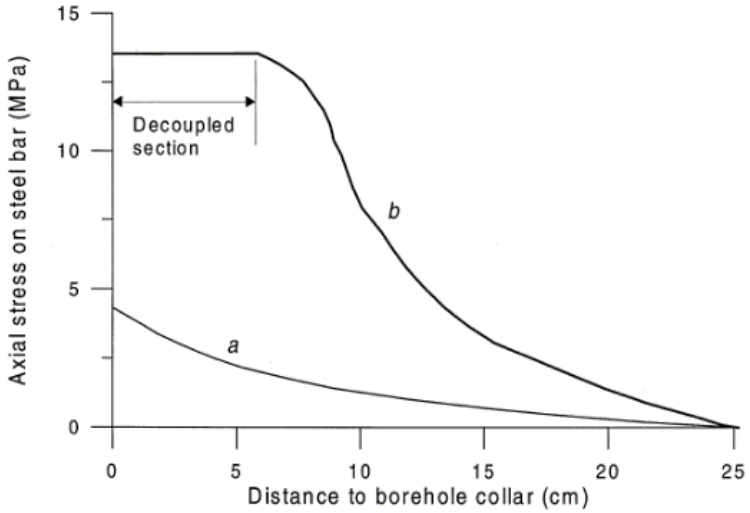

Figure 2.95. Axial load distribution along a fully grouted bolt (Li and Stillborg, 2000)

Signer, (1990) applied several bolts with strain gauges to study the axial load transfer mechanism. It was observed that axial load transfer follows an exponential distribution. Liu et al., (2014) conducted an anti-pull-out anchor experiment indicating that the anchorage load transfer properties vary along rock bolts at different depths. Li and Stillborg, (2000) developed an analytical model for fully encapsulated rock bolts by assuming the peak shear stress occurs a short distance from the loading point, diminishing exponentially to the free end (Figure 2.96).

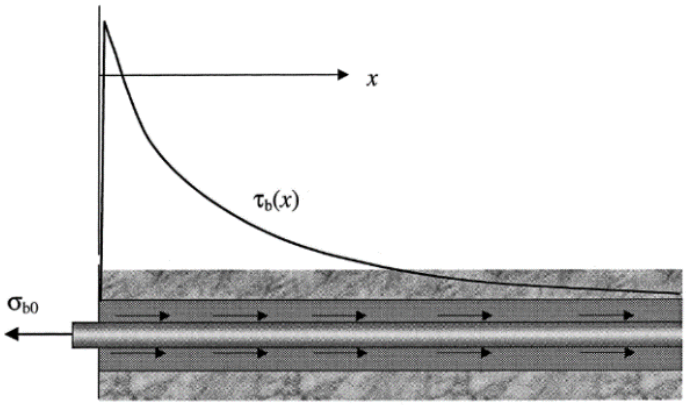

Figure 2.96. Shear stress along a full-encapsulated bolt subjected to a pull-out load before decoupling occurs (Li and Stillborg, 2000)

According to the piecewise function proposed by Li and Stillborg, (2000), the shear stress distribution is divided into four sections along fully grouted rock bolts. These sections include entirely decoupled (A), partially decoupled with a constant bond strength (B), partially decoupled with linearly increasing bond strength (C) and compatible deformation with no decoupling (D) (Figure 2.97).

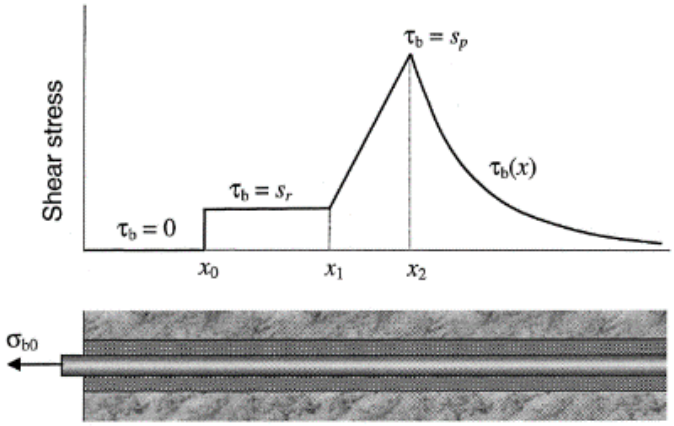

Figure 2.97. Distribution of shear stress along a full-encapsulated bolt subjected to a pull-out load after decoupling (Li and Stillborg, 2000)

The proposed model includes some assumptions which may limit the model's practicality. Before debonding, the following equations can obtain the shear stress distribution ($\tau_b(x)$) for a fully grouted bolt subjected to a pull-out load.

$$\tau_b(x) = \frac{\alpha}{2}\sigma_{b0} \cdot e^{\frac{-2\alpha x}{d_b}} \tag{5}$$

$$\alpha^2 = \frac{2G_r G_g}{E_b\left[G_r Ln\left(\frac{d_g}{d_b}\right) + G_g Ln\left(\frac{d_0}{d_g}\right)\right]} \tag{6}$$

$$G_g = \frac{E_g}{2(1+\gamma_g)} \tag{7}$$

$$G_r = \frac{E_r}{2(1+\gamma_r)} \tag{8}$$

where, σ_{b0} is the axial stress at the loading point, d_b is the bolt diameter, x is the distance from the loading end, α is the coefficient, E_b is Young's modulus of the bolt, E_r is Young's modulus of the grout, d_g is the diameter of the hole, γ_r is the Poisson's ratio of the surrounding rock mass, γ_g is the Poisson's ratio of the grout, d_0 is the distance of the centre of the hole from the point where the influence of the bolt disappears and G_g and G_r are the shear modulus of the grout and rock mass, respectively.

Thus the axial stress distribution along the bolt ($\sigma_b(x)$) can be calculated by:

$$\sigma_b(x) = \sigma_{b0} - \frac{\pi d_b}{A}\int_0^x \tau_b(x)dx = \sigma_{b0}\, e^{-2\alpha\frac{x}{d_b}} \tag{9}$$

$$\sigma_b(x) = \frac{2}{\alpha}\tau_b(x) \tag{10}$$

where A denotes the cross-sectional area of the bolt, and the remaining parameters have been defined above.

However, the axial and shear stress distribution along the bolt alters once debonding occurs. Developing a reliable mathematical model to simulate rock bolt bond-stress behaviour is a cumbersome task due to problem complexities. Various idealised linear and non-linear bond-slip models have been presented (Ko et al., 2014; Ma et al., 2013; Martín et al., 2011; Mousavi et al., 2017; Ren et al., 2010). Tri-linear bond-slip model is often used to mathematically represent the interfacial debonding behaviour of steel bolting systems. A usual tri-linear model consists of commonly there sections, as shown in Figure 2.98 including the hardening section (I) where the shear stress ascends linearly up to the pick point (S_1, τ_1), followed by softening section (II) where the shear stress along the interface decreases linearly down to (S_2, τ_2) and then the shear stress stays consonant at τ_2 representing residual frictional strength (III) after entire debonding (Benmokrane et al., 1995). The most cited model was developed by Ren et al., (2010). This approach represents the full range behaviour of fully grouted rock bolts to define the shear stress and bond-slip relation along the interface, axial load in the bolt and load-displacement relationship by adopting a tri-

linear bond-slip model (Figure 2.99).

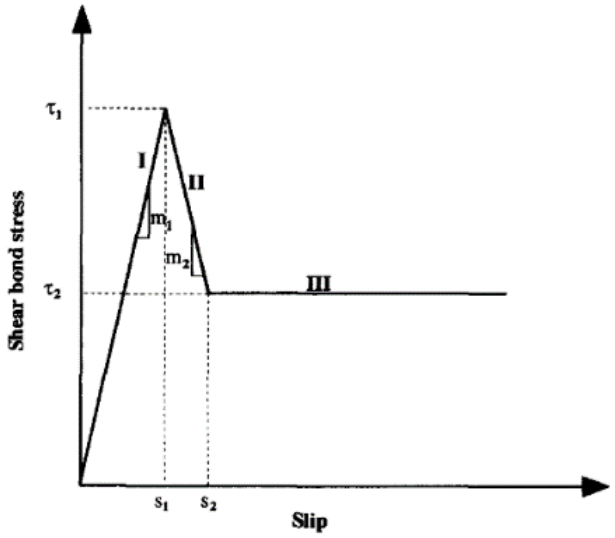

Figure 2.98. Idealised bond-slip relationship at the bolt-grout interface (Benmokrane et al., 1995)

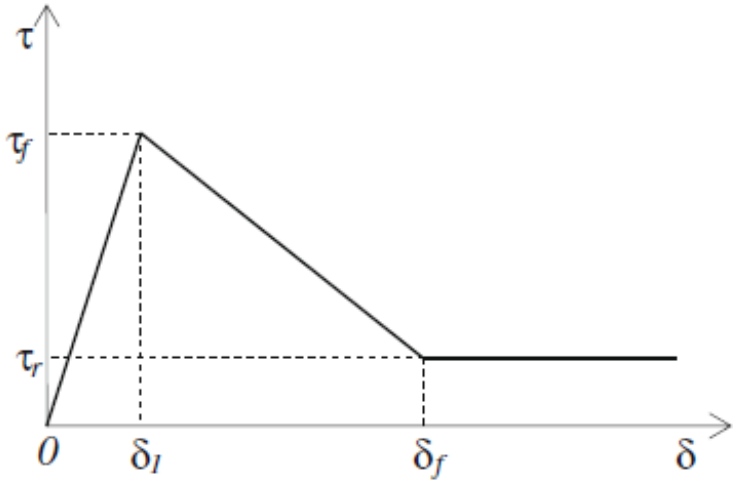

Figure 2.99. Trilinear bond-slip model (Ren et al., 2010)

The proposed full-range constitutive model consists of five distinguished stages, i.e., elastic, elastic-softening, elastic-softening-debonding, softening-debonding and debonding (Figure 2.100). Figure 2.101 represents the evolution of induced shear stress distribution along the bolt-grout interface in different stages.

It was noted in the proposed model that the encapsulation length must be significantly longer than the effective bond length to ensure that the ultimate load transfers effectively. In the process of developing governing equations, the deflection of the grout and surrounding rocks is assumed to be zero. As a result, the bolt was assumed to be under uniaxial tension and the bolt-grout interface under shear only, leading to an idealised interaction model as in Figure 2.102.

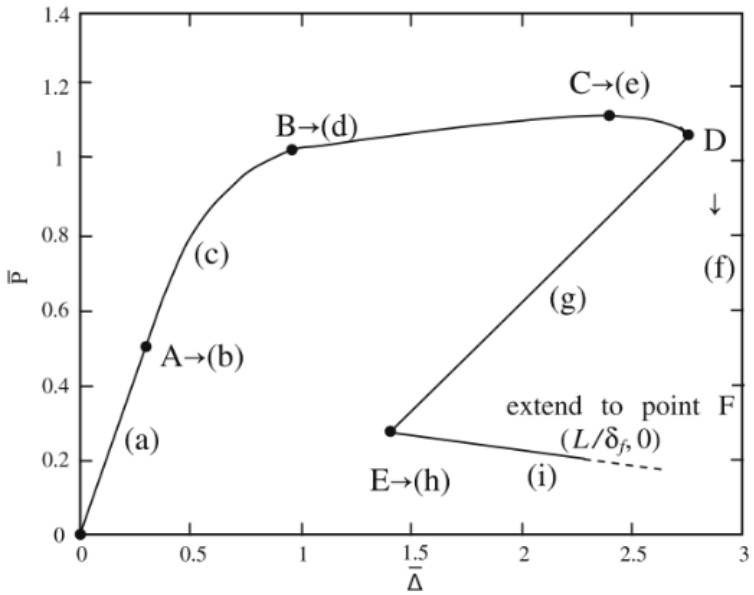

Figure 2.100. Full-range load-displacement behaviour when embedment length is long enough (Ren et al., 2010)

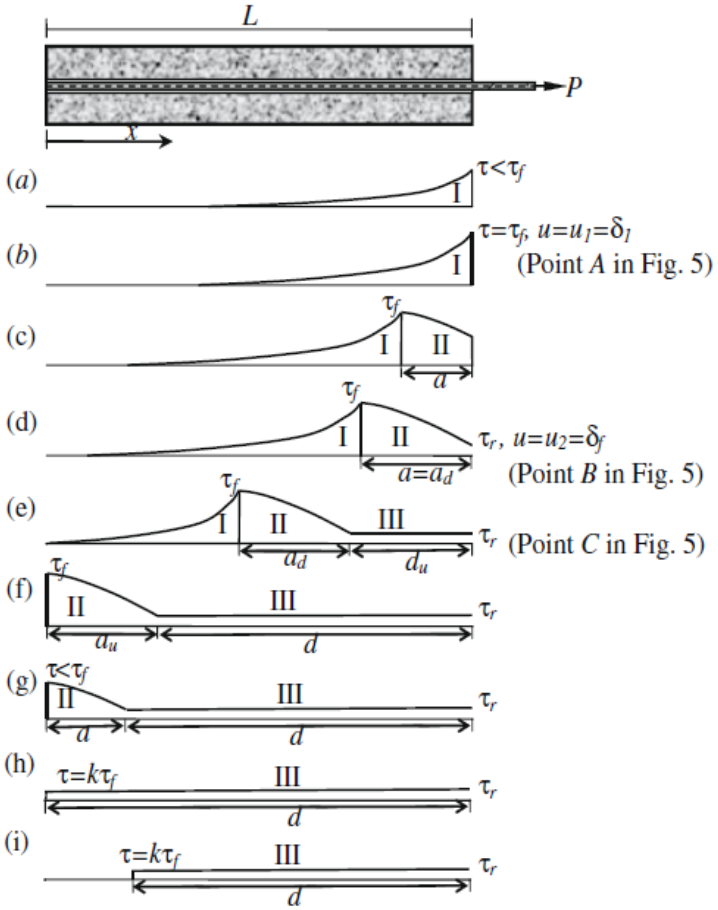

Figure 2.101. Evolution of shear stress along at bolt-grout interface: (a,b) Elastic stage, (c,d) elastic softening stage, (e,f) elastic-softening-debonding stage, (g) softening-debonding stage, (h,i) debonding stage. I, II, and III represent elastic, softening, and debonding (Ren et al., 2010)

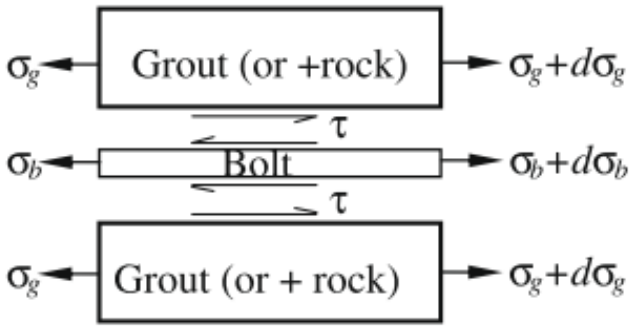

Figure 2.102. Stress equilibrium in bolt-grout interface (Ren et al., 2010)

The corresponding mathematical equations for the adopted tri-linear bon-slip model (Figure 2.99) are expressed as:

$$\tau(\delta) = \begin{cases} \dfrac{\tau_f}{\delta_1}\delta & \text{for } 0 \le \delta \le \delta_1 \\ \dfrac{k\tau_f(\delta - \delta_1) + \tau_f(\delta_f - \delta)}{\delta_f - \delta_1} & \text{for } \delta_1 \le \delta \le \delta_f \\ k\tau_f & \text{for } \delta_f \le \delta \end{cases} \tag{11}$$

where k is the ratio of the frictional residual strength τ_f to the peak shear stress τ_f.

According to the idealised model shown in Figure 2.99, the following fundamental equations for determining the behaviour of bolts in tension were established based on the force equilibrium consideration:

$$\frac{d\sigma_b}{dx} - \frac{2\tau}{r_b} = 0 \tag{12}$$

where σ_b is the axial stress along the bolt, τ is the induced interfacial shear stress, and r_b is the radius of the bolt.

The governing equations for axial stress in the bolt and shear stress in the bolt-grout interface for fully grouted rock bolts were expressed as:

$$\tau(\delta|x) = \frac{r_b E_b}{2} \cdot \frac{d^2\delta}{dx^2} \tag{13}$$

$$\sigma_b(\delta|x) = E_b \cdot \frac{d\delta}{dx} \tag{14}$$

Then, closed-form solutions were proposed to calculate the axial load distribution in the bolt, σ_b, interfacial shear stress distribution, τ, load-displacement relationship, P for each stage. For example, the final equations for the Elastic-Softening stage are as follows:

with $0 \le \delta \le \delta_1$ *or* $0 \le x \le L - a$

$$\tau = \frac{\tau_f \cosh(\lambda_1 x)}{\cosh(\lambda_1 (L-a))} \tag{15}$$

with $\delta_1 \le \delta \le \delta_f$ *or* $L - a \le \delta \le L$

$$\sigma_b = \frac{2\tau_f \sinh(\lambda_1 x)}{r_b \lambda_1 \cosh(\lambda_1 (L-a))} \tag{16}$$

$$\delta = (\delta_f - \delta_1)\left[\frac{\lambda_2 sin\left[\lambda_2 (x - L + a)\sqrt{1-k}\right] tanh[\lambda_1 (L-a)]}{\lambda_1 \sqrt{1-k}}\right] - \frac{cos\left[\lambda_2 (x - L + a)\sqrt{1-k}\right]}{1-k} + \frac{\delta_f - k\delta_1}{(1-k)(\delta_f - \delta_1)} \tag{17}$$

$$P = \frac{2\pi r_b \tau_f}{\lambda_2 \sqrt{1-k}}\left[\frac{\lambda_2 \sqrt{1-k}}{\lambda_1} \cos\left(a\lambda_2 \sqrt{1-k}\right) \tanh(\lambda_1 (L-a) + \sin(a\lambda_2 \sqrt{1-k})\right] \tag{18}$$

where τ_f, δ_1 and δ_f are defined in Figure 2.99, x is the distance from loading point, λ_1, λ_2 and k are coefficients.

The solution for the other stages can be found in the reference (Ren 2010). As can be seen, the presented model is not straightforward to apply in practice due to its complexity, and it needs a high volume of calibration.

Ma et al., (2013) developed a non-linear bond-slip model by applying the slip function presented by Zhou et al., (2010). The foundation of this model is based on the elasticity theory. Figure 2.103 schematically illustrates the axial and shear stress distribution at the column of the bolt and the bolt-grout interface, respectively.

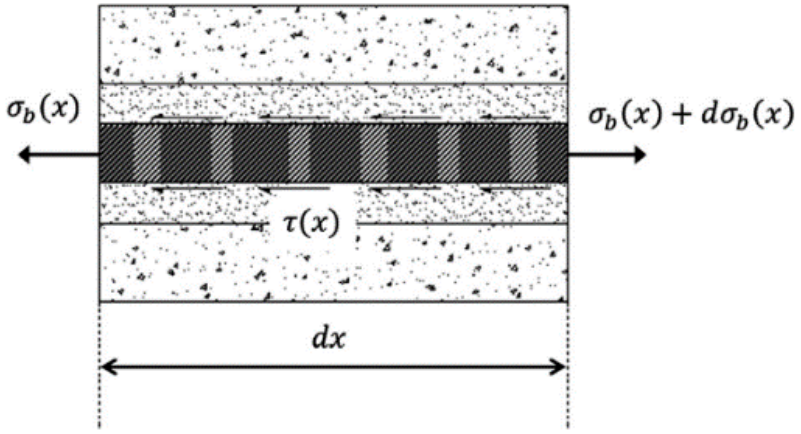

Figure 2.103. A schematic of axial and load stress distribution at bolt-grout interface (Ma et al., 2013)

According to this figure, the relationship between axial and shear stress was expressed as:

$$\tau(x) = \frac{d_b}{4} \cdot \frac{d\sigma_b}{dx} \tag{19}$$

where d_b is the bolt diameter, σ_b is the axial stress in the bolt, and τ is the interfacial shear stress.

Equation 19 indicates that shear stress at the interface can be obtained from the derivative of the axial stress function along the bolt (σ_b) over the length (dx); thus, shear stress distribution for the problem shown in Figure 2.103 can be illustrated similarly to the concept proposed by Li and Stillborg, (2000) (Figure 2.104), curve b in this figure shows a complete debonding for a length of bolt near loading end where the axial load is equal to the loading point. Then, there is a partially debonding section followed by the pick shear stress representative of a dramatic reduction in axial stress over the length of the bolt (dx). Beyond the pick value, the shear stress decreases exponentially but without any shear failure until the axial and shear stresses drop towards zero (at the far end of the rock bolt). Figure 2.104 shows schematically the shear stress distribution $\tau(x)$, strain $\varepsilon(x)$, and relative slip $s(x)$ along the bolt-grout interface of a fully grouted rock bolt. Bond-slip and load-slip relationships were presented as:

$$\tau(s) = \frac{E d_b}{4} \cdot \frac{a}{b^2} \cdot e^{-\frac{s}{a}} \cdot (1 - e^{-\frac{s}{a}}) \tag{20}$$

$$P(s) = \frac{E\pi d_b^2}{4} \cdot \frac{a}{b} \cdot (1 - e^{-\frac{s}{a}}) \tag{21}$$

where a and b are coefficients which are determined according to the system's conditions, s is the slip of the bolt at specific load and E is the elastic modulus of the bolt.

The following equations were proposed to calculate the axial stress and load at any specific point on the interface:

$$\sigma(x) = \frac{Ea}{b} \cdot \frac{1}{(1 + e^{-\frac{x - x_0}{b}})} \tag{22}$$

and

$$P(x) = \frac{E\pi d_b^2}{4} \cdot \frac{a}{b} \cdot \frac{1}{(1 + e^{-\frac{x - x_0}{b}})} \tag{23}$$

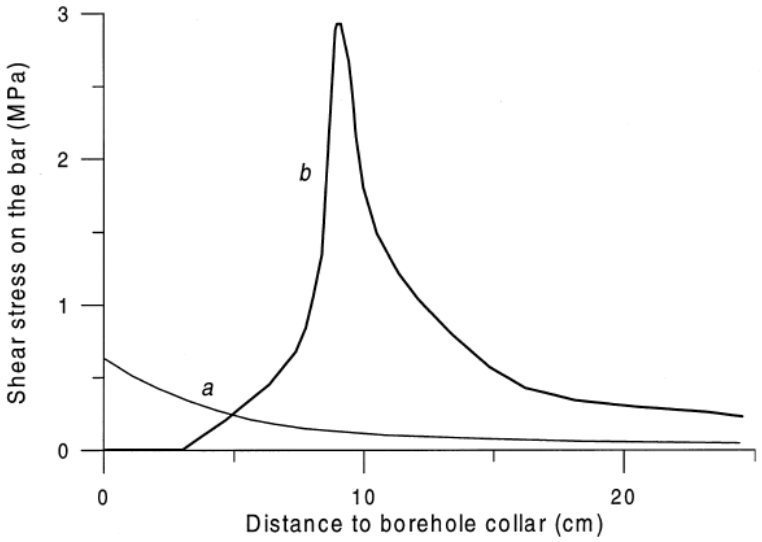

Figure 2.104. The shear stress along a fully grouted rock bolt (Li and Stillborg, 2000)

2.21. Summary and research gap

Rock bolts are widely used in mining and geotechnical engineering. They can effectively improve the stability of rock mass, and reduce the rock mass deformation, resulting in improved safety, cost and time. Regardless of the type, rock bolting systems generally develop forces in response to rock deformation and displacement. Fully grouted rock bolt installation is considered the most common rock bolt in mining and civil engineering. The failure of fully grouted rock bolts can occur in different modes, however, it has been acknowledged that failure at the bolt-grout interface is the ordinary mode. Investigating interfacial shear behaviour requires a deep understanding of axial load transfer mechanisms. To date, numerous laboratory tests have been conducted to characterise the behaviour of the bolt-grout interface. The results indicated that the system's interfacial and axial response depends on the rock bolt's mechanical and geometrical characteristics, mechanical characteristics of grout, geo-mechanical properties of the rock mass and boundary conditions.

Nevertheless, a lack of study is evident to systematically investigate the combined effects of the abovementioned factors on the rock bolting system axial behaviour. The combined effects refer to investigating the effects of host rock strength, confining pressure, grout strength, and the bolt type together on rock bolt behaviour. Specifically, the primary research gaps identified from the comprehensive literature review are as follows:

- The literature reports that the mechanical and thermal characteristics of UP, VE, and epoxy, with various formulations of matrix, filler, and other additives,

have been well-studied under different environmental and testing conditions. However, the literature lacks comprehensive studies that evaluate the axial performance of resin-embedded rock bolts at higher temperatures, which could simulate the underground conditions where the bolts are installed.

- The direct shear test provides useful data with the normal stress control system to investigate the effect of confining pressure on the performance of rock bolts, however, applying this test without considering the effect of circular confinement cannot represent real conditions. In real underground conditions, three main stresses are considered the confining stresses including σ_V, vertical stress, and σ_H and σ_h, horizontal stresses, which usually have different values. Several studies have been carried out to investigate the effect of these ground conditions via modified Hoek cell or passive confinement, however, there is no study in the literature to examine the real tri-axial confining stress conditions.
- The literature includes many experimental, numerical, and mathematical studies on the axial behaviour of rock bolts, however, there is a need to comprehensively analyse the performance of fully grouted rock bolts under different geotechnical conditions. Additionally, to the author's knowledge, there is no systematic research study to experimentally monitor the axial and shear behaviours along the rock bolt from the beginning of loading to the debonding as the applied strain gauges start to break as soon as displacement occurs. Recording the whole bolt deformation process will positively contribute to calibrating and evaluating the proposed mathematical and numerical models. Four fundamental questions regarding the axial load transfer mechanism of rock bolting should be discussed in different geotechnical conditions. They are (1) What is the effect of embedment length on the distribution of bond stress and failure of the system? (2) What is the effect of bonding material type on the bond stress distribution? (3) What is the relation between peak bond resistance and bonding material type? and (4) What is the effect of host rock properties on the bond stress distribution and failure mechanism of the bolts?
- As mentioned in the literature, various rock bolts are available in the market.

However, deformed rock bolts are typically studied under different conditions. Protective sheathed rock bolts are commonly used in areas with a risk of corrosion to steel rock bolts. While including a protective plastic sheath may impact the axial behaviour and performance of these bolts, there is a limited understanding of its effects on the axial behaviour of these types of rock bolts and, consequently, its influence on the bond stress distribution along the bolt.

The main motivations for this work are the research gaps mentioned above, which are addressed in Chapters 3 to 6.

CHAPTER 3: PAPER1- CHARACTERISATION OF MECHANICAL AND BONDING PROPERTIES OF ANCHORING RESINS UNDER ELEVATED TEMPERATURE

3.1. Introduction

The existing body of literature presented in Chapter 2 discusses extensively the mechanical and thermal properties of UP, VE, and epoxy resins; with consideration given to different matrix formulations, fillers, and additives in various environmental and testing settings. Nevertheless, there is a notable gap in the research concerning the axial performance of resin-embedded rock bolts installed in an underground opening at elevated temperatures. Such investigations are crucial as they aim to replicate the conditions found underground where these bolts are utilised.

Manuscript 1 presents the findings of a comprehensive experimental study that carefully addresses the aforementioned research gap. Firstly, an investigation was conducted on the mechanical properties, microstructures, thermal characteristics, and curing characteristics of four two-component anchoring resins. Subsequently, several pullout tests were performed on rock bolts that were encapsulated with resin to quantify the bonding characteristics of the resins under elevated temperatures. The temperature range for evaluating the pullout performance of the rock bolts was set at 20°C-250°C.

The viscoelasticity results revealed that 80% of the curing time of the used resins was achieved in 0.5-1 hour. Additionally, it was demonstrated by the Dynamic Mechanical Analysis tests that the mechanical characteristics of the resins were temperature-dependent. The mechanical and microscopic studies also indicated that the compressive strength of the resins depended on the mastic and the catalyst base, with water-based resins generally providing lower strength properties compared to the oil-based resins. Curing time was also found to be an important factor affecting the mechanical properties, even though the resins achieved 50% of the ultimate strength in only 1 hour.

A unique testing procedure was developed to simulate the underground conditions in relation to temperature transmission in rock bolting systems. Finally, it was observed that higher temperatures had a significant impact on the bond capacity of rock bolts.

International Journal of Rock Mechanics & Mining Sciences 170 (2023) 105506

Contents lists available at ScienceDirect

International Journal of Rock Mechanics and Mining Sciences

journal homepage: www.elsevier.com/locate/ijrmms

Characterization of mechanical and bonding properties of anchoring resins under elevated temperature

Hadi Nourizadeh [a,b,*], Ali Mirzaghorbanali [a,b], Kevin McDougall [c], L.H.J. Jeewantha [a], Peter Craig [d], Amin Motallebiyan [a], Behshad Jodeiri Shokri [a,b], Ashakan Rastegarmanesh [a], Naj Aziz [e]

[a] Centre for Future Materials (CFM), University of Southern Queensland, 4350, Australia
[b] School of Engineering, University of Southern Queensland, 4300, Australia
[c] School of Surveying and Built Environment, University of Southern Queensland, 4350, Australia
[d] Jennmar Australia Pty Ltd, Sydney, Australia
[e] School of Civil, Mining & Environmental Engineering, University of Wollongong, NSW, 2500, Australia

ARTICLE INFO

Keywords:
Rock bolts
Anchoring resin
Pullout tests
Bonding performance
Elevated temperature

ABSTRACT

Resin anchored rock bolts are widely used in the construction and mining industries to support and reinforce underground roadways and openings. However, increasing the depth of underground openings, particularly in coal mines, has presented a challenge for ground control designers due to the rise in geothermal heat and coal seam combustion. This study aims to comprehensively investigate the mechanical properties, microstructure, thermal and curing characteristics of the anchoring resins using Thermogravimetric Analysis, Dynamic Mechanical Analysis, and Differential Scanning Calorimetry tests. Pullout tests were conducted on resin encapsulated rock bolts to quantify their bonding performance at elevated temperatures ranging from 20 °C to 250 °C. The results showed that the mechanical properties of the resins are closely related to the type of curing agent, filler type and size, and curing time. The compressive strength and elastic modulus of the anchoring materials ranged from 51 to 103 MPa. DSC testing indicated that 65–83% of curing can be achieved in 30 min. At ambient conditions, good agreement was found between the compressive and shear properties of the anchoring resins and their corresponding bond resistance force. A heating and pull-out setup was fabricated to analyze the effects of temperature on the bonding performance of rock bolts chemically anchored in underground spaces. The results revealed a reduction in bonding capacity of the bolts by 6.6%–31.3% when the temperature of the environment reached 75 °C and 150 °C, respectively. The anchored bolts maintained up to 62.6% of their bonding resistance when the temperature increased to 250 °C. Temperature profiles measured by the thermocouples along the encapsulation length showed that the heat transition is independent of the resin type and more dependent on the rock bolt specification.

1. Introduction

Anchoring systems are commonly used for reinforcing and supporting ground and underground structures[1]. These systems can be classified into three main categories: stranded steel tendons (cable bolts), deformed or threaded steel bars (rock bolts), and glass fiber reinforced polymer bars (GFRP). Rock bolting can be anchored either mechanically using an expansion wedge or shell or chemically using bonding agents. Chemically anchored rock bolts are typically inserted into a pre-drilled hole in the host media and filled with a structural bonding agent. The function of the bonding agent is to transfer the anchoring load from the bolt to the surrounding rock mass and vice versa. There are two basic types of bonding materials: chemical and non-chemical. Cement-based materials, often called grout, are an example of non-chemical bonding agents and are not covered in this study. Unsaturated polyester resin (UPR), vinyl ester resin (VER), and epoxy resin are the most commonly used chemical bonding materials[2]. UPR-based bonding products are widely used in mine support and building strengthening projects due to their shorter cure time, good bonding strength, and low cost[3]. The thixotropic and viscosity nature of polyester-based resins enhances their

* Corresponding author. Centre for Future Materials (CFM), University of Southern Queensland, 4350, Australia.
E-mail address: hadi.nourizadeh@usq.edu.au (H. Nourizadeh).

https://doi.org/10.1016/j.ijrmms.2023.105506
Received 25 November 2022; Received in revised form 4 May 2023; Accepted 2 July 2023
1365-1609/© 2023 The Authors. Published by Elsevier Ltd. This is an open access article under the CC BY-NC-ND license (http://creativecommons.org/licenses/by-nc-nd/4.0/).

workability for various applications, although this group offers lower bonding capacity compared to vinyl ester and epoxy resins. The degradation process of UPR and VER under different conditions, such as exposure to chemicals, microwave radiation, and high temperature, has been studied, and it has been established that immersion in aggressive solvents and exposure to higher temperatures (e.g., 1000 °C) degrade and carbonize the matrix, while UV radiation causes additional cross-linking in the resins[4]. For anchor bonding applications, anchor resins can be distinguished by vial (two-component cartridge) and injection systems. The two-component cartridges typically consist of a tube of polyester film filled with polyester resins and a curing agent (catalyst), which is usually a peroxide like methyl ethyl ketone peroxide or benzoyl peroxide. A film barrier of polyester is used to prevent migration between the resin and the hardener. Inorganic fillers such as calcium carbonate ($CaCO_3$) and silica are usually added to the resin components to enhance the mechanical properties and minimize expenses. Several studies have been conducted to investigate the effect of filler content and particle sizes on the mechanical properties of polyester resins, and it has been reported that mechanical and bonding properties of resins can be enhanced by incorporating an optimum content of filler[5–8].

The behavior of resin-encapsulated anchors can be viewed from two perspectives: short-term properties, including gelling time, setting time (early curing time), and early bonding strength; and long-term properties, including bearing capacity against static and dynamic loads, and resistance to harsh and corrosive environments, temperature, and fire. The chemical formulation of resins is a critical characteristic, along with other parameters such as host rock mass condition, level of in-situ stress, and mechanical and geometric specifications of the anchoring element, which influence the performance of rock bolting systems. Curing of thermosetting resins is an exothermic and time-dependent chemical reaction that occurs once the components (resin and curing agent) are mixed. Gelation is an important factor achieved when the chemical reaction proceeds sufficiently such that the mixture achieves a flexible but non-flowing three-dimensional high molecular structure. The gel time, early and fully curing time, and viscosity of the product influence the suitability of chemically anchored rock bolts for particular applications[9].

There is a broad range of literature on the experimental and numerical investigation of the effects of different factors, such as mechanical properties of anchoring materials, confining stress, anchoring materials mixing and installation procedure, and rock bolt geometrical and mechanical properties, on the bond behavior of fully encapsulated rock bolts in ambient conditions[10–18]. Huang et al.[19] concluded that Basalt FRP bars anchored with resin with a higher elastic modulus have higher shear stiffness compared to the bars anchored with a lower elastic modulus. Pull-out tests conducted by Dudek and Kadela[20] on chemically bonded steel bars showed that the bearing capacity of the bars bonded by epoxy adhesive is slightly higher than those bonded using polyester resins. The results of various studies also show that mechanical characteristics of grout play a vital role in determining the bearing capacity of rock bolts and cable bolts[14,21–23].

Previous research studies have shown that the mechanical properties and load-bearing capacity of anchoring resins depend on temperature. Wang et al.[24] examined the effects of high temperature and low humidity on the mechanical properties of grouting materials in high-geothermal tunnels. They found that these factors have an adverse effect on cementitious grout. Jahani et al.[25] experimentally studied the influence of temperature on the mechanical properties of a structural adhesive and found that the mechanical properties decrease when the curing and post-curing temperature exceeds the glass transition temperature (T_g) of the adhesive. T_g is defined as the temperature range at which the state of a thermosetting resin changes from a glassy state to a rubbery state[26]. Previous research has shown that commonly used structural agents have T_g in the range of 40–70 °C, and their mechanical properties substantially change when the working temperature approaches the corresponding Tg[27,28]. It has been shown that for temperatures below 60 °C, the properties of chemical bonding agents are slightly affected. However, for temperatures above 60 °C, there is a significant reduction in bonding properties. Reis[29] measured the elastic modulus, flexural strength, and compressive strength of polymer mortars under different temperatures and concluded that the flexural and compressive strength decrease at elevated temperatures.

To characterize the bonding behavior of an encapsulated bolt in thermal environments, two sets of data are essential: the temperature distribution along the encapsulation length and the relationship between induced bond stress and temperature. The temperature profile along the bonded length is a time-dependent factor, but the testing configuration and method also affect the temperature distribution profile. There is limited literature regarding the investigation of the effects of elevated temperature on the bonding properties of chemically bonded anchors in concrete structures, particularly in underground applications. The experimental procedures and standards developed for investigating the performance of reinforcing materials in concrete structures under elevated temperature may not be suitable for underground applications because the conditions vary significantly. Temperature rises in underground spaces, such as tunnels and mines, can be due to fire, combustion, machine working, and geothermal heat. In concrete structures, the temperature elevation in the bond is closely dependent on the geometry of the concrete structure[30]. In underground structures, only the free end of the reinforcing element and the external fixtures are exposed to the ambient heat, regardless of the geometry of the opening (except in the presence of geothermal heat, which is transmitted from all directions). In determining the resistance to heat of rebars in concrete structures, the main thermal flux is usually subjected to the lateral sides of the concrete specimens[31,32]. The European Organization for Technical Assessment (EOTA) outlines that "The main thermal flux shall be oriented towards the lateral side of the concrete cylinder. The non-bonded part of the rebar shall not be directly exposed to the heat source"[33]. Al-Mansouri et al.[32] and Lakhani and Hofmann[34] observed a large difference in the temperature variation along the encapsulation depth for the specimens where the bolt itself was exposed to heat compared to the specimens where the bolt was insulated.

The literature reports that the mechanical and thermal characteristics of UP, VE, and epoxy, with various formulations of matrix, filler, and other additives, have been well-studied under different environmental and testing conditions[35–43]. However, the literature lacks comprehensive studies that evaluate the axial performance of resin-embedded rock bolts at higher temperatures, which could simulate the underground conditions where the bolts are installed. This paper presents a qualitative and quantitative discussion of the mechanical and thermal characteristics and behavior of commonly used anchoring UP resins. Additionally, the bearing performance of encapsulated rock bolts was investigated under elevated temperatures in simulated underground heating conditions. Furthermore, the interrelationship between the bearing capacity of rock bolts under ambient and elevated temperature conditions and the thermo-mechanical characteristics of the anchoring materials was examined, and the relevant failure patterns were analyzed. As previously stated, the conventional testing procedure developed for evaluating the effects of high temperatures on the performance of anchoring materials in concrete structures is not suitable for underground structures. To address this incompatibility, a new testing set-up was designed to mimic the conditions of these environments. The outcomes of this study may aid in developing standard testing methods for reinforcing materials used in underground applications. Moreover, the results of this study may inform the design and construction of more efficient and reliable rock support systems, leading to safer and more efficient underground excavations. Importantly, extending the depth of underground openings, particularly coal mines, increases the geothermal heat and combustion of coal seams, posing a challenge for ground control designers. Therefore, understanding the performance of anchoring materials at higher temperatures is crucial.

2. Experimental procedure

2.1. Materials

The study employed four types of two-component polyester resins (denoted as resins A, B, C and D), specifically synthesized for rock bolting, as the bonding agent. The polyester resin component of these resins contained styrene monomer and was filled with CaCO3 inert fillers of various particle sizes, ranging from 0.5 μm to 1300 μm. Two types of curing agents, a water-based and an oil-based catalyst, were utilized in the research. Both catalysts contained the same limestone filler but differed in the amount of benzoyl peroxide initiator. The specific mixing ratios of the resins and the catalysts are presented in Table 1. The resins were catalyzed using 20% w/w and 8% w/w of water-based and oil-based catalysts, respectively, as shown in the table. The components of the bonding resins used in this study are illustrated in Fig. 1.

2.2. Experimental program

The testing program was divided into three stages. In the first stage, the mechanical properties of the bonding agents, including their compressive, tensile, and shear characteristics, were determined. The compression test was conducted on specimens cured for 1 h, 1 day, 3 days, and 30 days to investigate the effect of curing time, while tensile and shear tests were only performed on specimens cured for 30 days. In the second stage, microstructural analysis of the failure surfaces obtained from the mechanical experiments was carried out, along with thermal analysis, including thermogravimetric analysis (TGA), differential scanning calorimetry (DSC), and dynamic mechanical analysis (DMA). This investigation was conducted to study the decomposition, storage modulus, curing rate, and T_g, which are important factors to consider when assessing the effect of temperature on the behavior of materials. The TGA and DMA tests were performed on specimens cured for 30 days, while the DSC test was carried out on uncured specimens and specimens cured for 0.5 h, 1 h, 24 h, 7 days, and 30 days. The DSC analysis was undertaken at different curing times to accurately quantify the curing percentage of the resins after mixing with the catalysts. The third stage of this experimental study investigated the bonding behavior and anchoring capacity of rock bolts under both room and elevated temperatures. As this study targeted the underground application of reinforcing materials, testing setups used in the literature were not considered suitable. Therefore, a unique heating and testing setup was developed to simulate the desired elevated temperature conditions. Pull-out tests were then conducted on the bonded rock bolts at room conditions and elevated temperatures of 75 °C, 150 °C, and 250 °C.

2.3. Mechanical tests

All the specimens for the mechanical, thermal, and pull-out analyses were prepared by mixing the main components of the resins using a laboratory mixer. The mixing process was carried out in a room with a temperature-controlled system set at 20 °C, and the mixing time and speed were set to 30 s and 500 rpm, respectively. Immediately after the mixing process was completed, the uncured resins were poured into the designated molds. The specimens were then demolded after 30 min and stored in a temperature-controlled environment at 20 °C to complete the curing process. The specimens were tested at the scheduled curing time frames. Table 2 summarizes the details of the mechanical tests performed on the specimens. The tests were executed following the ASTM standards listed in Table 2. To verify the accuracy and consistency of the results, the tests were repeated for each type of resin at the desired curing period (refer to Table 2). Conventional resistive strain gauges were used to instrument the specimens in compressive and tensile tests to measure the respective lateral and axial strains, and consequently calculate the compressive and tensile elastic modulus and Poisson's ratio. The tensile and V-notched shear (Iosipescu) tests were conducted using a 100 kN hydraulic servo-controlled MTS machine. A Wyoming shear testing fixture was used for the V-notched shear specimens. However, the compressive tests were performed using a 1000 kN hydraulic servo-controlled UTM machine due to the need for higher load before yielding. Fig. 2 illustrates the mechanical testing of the specimens.

Table 1
Resin components used in the study.

Items	Type A	Type B	Type C	Type D
Matrix resin	Polyester Resin	Polyester Resin	Polyester Resin	Polyester Resin
Filler	$CaCO_3$	$CaCO_3$	$CaCO_3$	$CaCO_3$
Filler particle size (μm)	10–425	0.5–425	10–1300	10–1300
Bulk density of resin mastic (kg/m^3)	1817	1746	1790	1795
Curing agent	Water-based	Oil-based	Water-based	Oil-based
Mixing mass ratio (resin: catalyst)	4:1	11.5:1	4:1	11.5:1

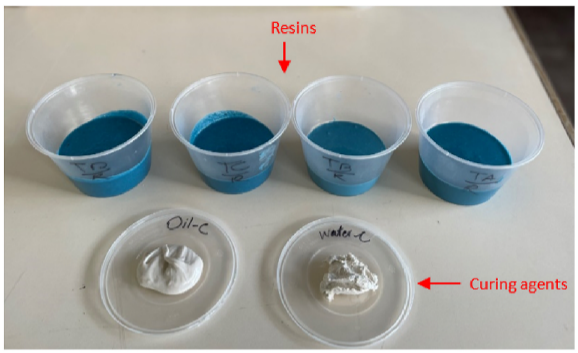

Fig. 1. Bonding resins components used in this study.

2.4. Microstructural and thermal analysis

The morphology of the specimens was observed using a Jeol Benchtop (JCM-6000) Scanning Electron Microscope (SEM). Non-isothermal analyses were also performed to determine the curing percentages, using a TA Instrument Discovery DSC-25. The uncured and cured samples (taken at 0.5 h, 1 h, 1 day, 7 days, and 30 days) were heated from 0 °C to 150 °C with a constant heating rate of 5 °C/min. For the DSC experiments, ~12 ± 0.1 mg of the sample was loaded into hermetically sealed aluminum pans using a manual crimper. Thermogravimetric analysis was carried out using a TA Instruments Discovery SDT 650. The temperature was raised from room temperature to 600 °C at a rate of 5 °C/min. Dynamic Mechanical Analysis (DMA) was conducted in accordance with ASTM D7028 standard, using a TA Instrument Hybrid Rheometer (Discovery HR-2). Rectangular specimens, with dimensions of 60 mm (L) × 12 mm (W) × 4 mm (T), were clamped in a dual cantilever fixture. Before beginning the test, the specimens were conditioned at 0 °C for 15 min, and then heated with a 5 °C/min rate until 120 °C under an oscillation mode at a frequency of 1 Hz. Fig. 3 illustrates the equipment and specimens used for the thermal analysis.

2.5. Pull-out tests under elevated temperatures

For the pull-out experiments, steel rock bolts with a nominal diameter of 22 mm (rib-to-rib), fully bonded in steel pipes with an outer

Table 2
Mechanical tests parameters.

Test	Curing age	Standard	Dimensions L × W × T (mm)	Geometry	N_R[c]	N_T[d]	Loading rate
Compressive	1h, 1day, 3days, 30days	ASTM:C579	50 × 50 × 50	Cubic	3	48	1.5 kN/s
Tensile	30days	ASTM:D638	120 × 10 × 10[a]	Dog bone	5	20	1 mm/min
Shear	30days	ASTM:D5379	76 × 20 × 10[b]	V-notched	5	20	1 mm/min

[a] Width at the middle of the specimens.
[b] The widths of the specimen at the notch is 11 mm.
[c] N_R: number of the tests at each testing group.
[d] N_T: total number of the tests.

Fig. 2. Mechanical testing, (a) compressive (b) tensile and (c) V-notched (Iosipescu).

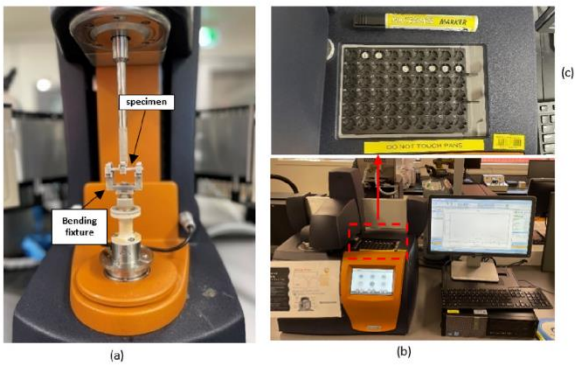

Fig. 3. Thermal analysis instruments, (a) Discovery HR-2, (b) DSC-25 and (c) DSC specimens in designated tray.

diameter of 43 mm, thickness of 5 mm, and length of 150 mm, were used. The rock bolts had a yield strength of 650 MPa, a tensile strength of 890 MPa, and an elastic modulus of 220 GPa. The pipes were rifled internally to mimic field conditions and ensure debonding occurred either in the bonding materials or at the bolt-resin interface. Freshly mixed resins were poured into the pipes, and the rock bolts were centrally installed using designated and fabricated centralizing tools. The specimens were stored at room temperature. The first set of experiments was conducted at room temperature, while the second group of tests was performed at elevated temperatures. To simulate rock bolt performance in underground applications, specialized heating and testing equipment was designed and fabricated. This consisted of an insulated heating chamber with a temperature range of 50 °C–400 °C. Thermocouples measured the system temperature and provided feedback to the control system. Once the chamber was installed under the middle crosshead of the 1000 kN UTM, the specimen was placed under the chamber by passing the bolt through the designated 40 mm hole in the center of the heating chamber. The free end of the rock bolts was clamped by the conical jaws located on the upper crosshead of the 1000 kN UTM. The middle crosshead was then adjusted so that the upper side of the steel pipe sat underneath the chamber. Three k-type thermocouples (named T1, T2, and T3) were positioned along and on the bolt at 30 mm, 80 mm, and 130 mm from the loading end. One thermocouple (T0) was attached to the bolt, 15 mm outside the encapsulation surface. The chamber was heated from room temperature to the set temperature at a rate of 10 °C/min. The specimen was kept at the set temperature for 30 min, and then the pull-out load was applied at a rate of 1 mm/min until debonding occurred. Table 3 and Fig. 4 illustrate the pull-out test experimental array and the pull-out experimental setup, respectively.

3. Results and discussion

3.1. Mechanical properties

In this section, the results obtained from the mechanical testing will be presented and discussed.

Table 3
Pull-out test experimentation.

Bonding type	Encapsulation length (mm)	Testing temperature (°C)	Number of tests	Exposure time to the desired temp (min)
Type A	150	24[a], 75, 150, 250	4	30
Type B	150	22[a]	1	n/a
Type C	150	22[a]	1	n/a
Type D	150	20[a], 75, 150, 250	4	30

[a] Room temperature.

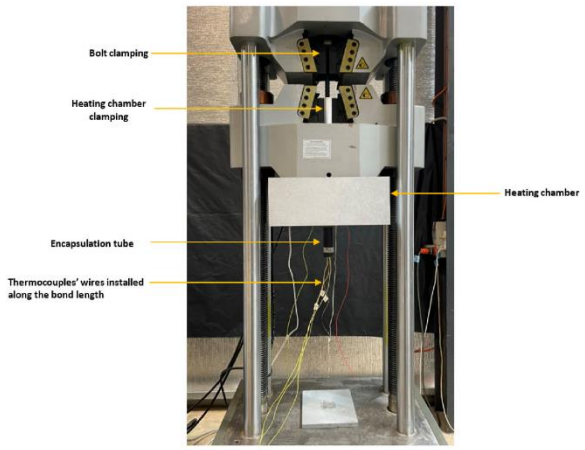

Fig. 4. Pull-out testing set-up.

3.1.1. Compressive properties

Table 4 presents a summary of the compressive test results after 30 days. Resins A and C showed the lowest compressive strength and elastic modulus. This is believed to be due to the challenge of effectively mixing water-based additives, which can create voids and defects in the cured specimens. The failure surface images of the specimens (Fig. 5) indicate that resins A and C have more porosity compared to resins B and D. Since the mechanical behavior of solids is often governed by flaws, it is reasonable to conclude that under compression, localized tensile stress is initiated at the defects, leading to crack propagation and eventual material failure. Microstructural effects, such as voids and second-phase particles (such as fillers and fibers), are the primary reasons for crack initiation and development in polymeric materials under compressive load[44].

Resin D exhibited an 86% higher compressive strength than resin C, despite using the same matrix resin and filler type and size, suggesting that the improvement is linked to the type of catalyst. Table 1 and Table 4 suggest that filler particle size also affects the mechanical properties of chemical bonding materials. Resin C demonstrated slightly higher compressive strength than resin A (~5.3%) despite using the same type and ratio of curing agent. The same trend was observed in resins B and D, where resin D exhibited higher compressive and elastic modulus than resin B (~9.9%), possibly due to a wider $CaCO_3$ particle size distribution in resin C. Bagherzadeh et al.7 noted that combining fillers with different particle sizes can enhance the compressive strength of anchoring bonds. When there is a sufficient amount of resin present, the voids are typically filled completely, resulting in maximum stress. Generally, finer particle sizes lead to higher strength properties of composite materials in particular tensile and flexural strengths[37]. The compressive tests conducted in the current study indicate that samples with a wider particle size distribution resulted in slightly stronger resin compared to those with a narrow particle size. This could be due to several factors, such as (1) a wider particle size distribution allows for more efficient packing of filler particles in the resin matrix, leading to a denser material with fewer voids and gaps, (2) the use of larger particles may result in a greater degree of interlocking between the particles in contact, and (3) a wider range of particle sizes may result in a more uniform distribution of filler particles within the resin matrix. Yeon et al.[45] reported an slight increase in the compressive strength of UPR polymer concrete with increase in the size of spherical filler particles. The compressive strength and elastic modulus of resin A were found to be the lowest among the tested resins, measuring 52 MPa and 4.71 GPa, respectively. On the other hand, resin D exhibited the highest compressive strength and stiffness. Its ultimate compressive strength and elastic modulus were measured to be 103 MPa and 8 GPa, respectively. This resin contained a wider range of filler particles and an oil-based curing agent, which resulted in higher strength and stiffness compared to the other resins. Fig. 6 depicts the compressive stress-strain curves of the specimens tested at room temperature. The compressive behavior of the specimens, as shown in Fig. 6, resembles the deformation process of quasi-brittle materials, which involves an elastic phase, strain hardening, peak stress, strain softening, and a sharp decline in stress[46]. All specimens exhibit linear stress-strain behavior in the elastic zone until approximately 85% of peak stress. At the end of this stage, peak stress is achieved, which is associated with specimen failure followed by a sudden decline in stress. At this stage, the absorbed energy is released suddenly in the form of crack propagation. This behavior is comparable to the post-peak behavior of brittle materials due to the sudden reduction in stress[47,48]. The maximum compressive stress was obtained at true strains of 1.1%, 1.2%, 1.49%, and 1.56% for resins A, B, C, and D, respectively. The Poisson ratio of the resins was also determined using the strain values obtained from strain gauges. It can be observed from Table 4 that the Poisson ratio ranges from 0.22 to 0.36.

Fig. 7 depicts the compressive stress-deformation curves for curing times of 1 h, 1 day, 3 days, and 30 days. It is evident that the compressive behavior of the tested anchoring resins is influenced by their curing time. Chen et al.[49] have identified five distinct stages of typical compressive stress-strain behavior for polymers: linear elastic stage, nonlinear elastic stage, yield-like (peak) stage, strain softening stage, and perfectly plastic behavior stage. Resins A and C cured for 1 h exhibited all five stages, while resins C and D cured for 1 h displayed only the first two stages followed by a strain hardening stage, with significant deformation occurring with slight increases in stress. As shown in Fig. 7, resins B and D exhibited ductile behavior for specimens tested at 1 h, whereas resin A displayed quasi-ductile behavior and resin C behaved like a typical polymer (elastic-yield (peak)-softening-plastic behavior). The stress of resins B and D slightly decreased after reaching 2.6% strain, while the limit was 1.7% for resins A and C tested at 1 h (Fig. 7). No distinct ductile-brittle transition point was observed in the post-peak region for specimens tested at 1 h.

A comparison of the stress-deformation curves presented in Fig. 7 indicates that the degree of ductility is a function of time and the catalyst type used. It can be concluded that the compressive stress-strain relationship of resins changes from ductile behavior at the early stages of curing (e.g., resin B and D at 1 h) to a quasi-brittle behavior when it hardens (e.g., resins A, B, C, and D at 30 days). Furthermore, it is clear that the resins with oil-based catalyst components (i.e., resins B and D) exhibit more ductility compared to the ones with water-based catalysts (i.e., resins A and C). This indicates that the curing process is faster in resins A and C in which the water-based catalyst was used. The curing degree of the specimens over time is described in detail later in Section 3.2. Resin B tested at 1 day and D tested at 1 day and 3 days still illustrate strain hardening behavior after the yielding point. Elastic-yield like (peak)-strain softening behavior presented in resins A and C at 1 day, 3 days, and 30 days, resin B at 3 and 30 days, and resin D at 30 days, is similar to the stress-strain behavior of polymer concrete with a high proportion of fly ash[50]. The basic response of the four specimens at the late stages of curing as shown in Fig. 7 is nearly identical. However, a

Table 4
Summary of the 30-day compressive tests.

Resin type	Resin A	Resin B	Resin C	Resin D
Ultimate Strength (MPa)	51.78 ± 0.51	93.78 ± 0.97	54.55 ± 1.65	103.05 ± 1.51
Young's Modulus (GPa)	4.71 ± 0.09	7.45 ± 0.06	4.78 ± 0.1	8.03 ± 0.07
Poisson ratio	0.22 ± 0.01	0.28 ± 0.02	0.23 ± 0.01	0.36 ± 0.04
Strain at ultimate strength (10^{-2})	1.112	1.274	1.491	1.561

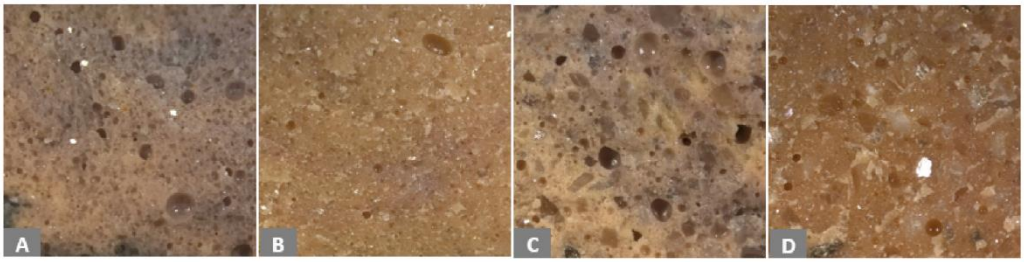

Fig. 5. Failure surface of the specimens from mechanical tests.

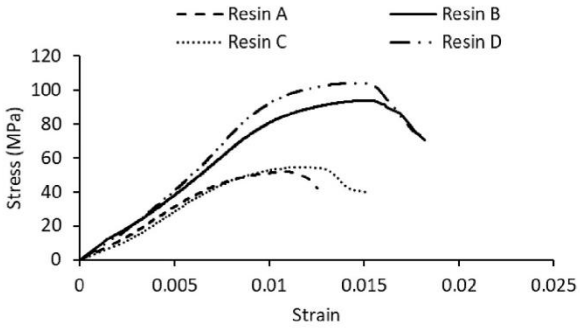

Fig. 6. Stress-strain behavior of different resin specimens tested at 30 days.

comparison of the stress-strain curves reveals that the descending rate of stress at the post-yield strain softening stage is greater at higher curing stages.

The results of the compressive tests conducted on different types of resins over time are summarized in Table 5 and Fig. 8. It is observed that the ultimate compressive strength and elastic modulus of the resins increase with curing time. For example, the compressive strength of resin A improved by 20%, 33%, and 57% after 1 day, 3 days, and 30 days of curing, respectively, compared to the 1-h specimen. Resin B exhibited an improvement of 43%, 56%, and 96%, while resin C and D showed an improvement of 35%, 53%, and 89%, and 40%, 66%, and 119%, respectively. This development in compressive strength is attributed to the curing of the resins, and the results indicate that the water-based catalyst promoted a faster hardening process at the very early stage of curing compared to the oil-based catalysts. In cases where strain hardening is not observed, the yield strength and peak strength become equivalent.

Fig. 9 depicts the macroscopic failure patterns of the specimens subjected to compression over different curing periods. In most cases, a cone-shaped rupture is clearly visible, but in a few cases (e.g., 1-h C, 1-Day B, and 1-Day D), debris covers the failure mode. The wedge in the compressive specimens forms an angle of approximately 45° with the vertical side of the specimen. In all specimens, failure began with a

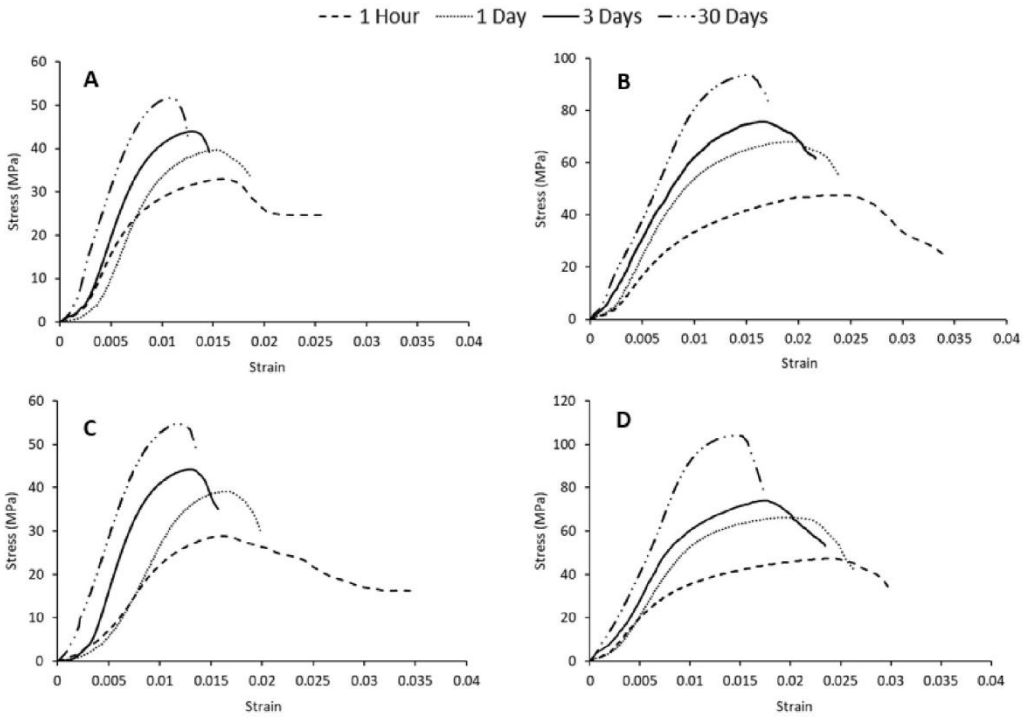

Fig. 7. Stress-deformation behavior of the resins at different curing ages.

Table 5
Compressive results over curing periods.

Resin Type	Parameters	1 Hour	1 Day	3 Days	30 Days
Resin A	Peak Strength (MPa)	32.9	39.6	43.9	51.7
	Yield Strength (MPa)	28.9	39.6	43.9	51.7
	Young's Modulus (GPa)	3.06	2.84	3.99	4.71
	Strain at yield (10^{-2})	1.02	1.52	1.33	1.12
	Strain at peak (10^{-2})	1.67	1.52	1.33	1.12
Resin B	Peak Strength (MPa)	47.6	68.1	74.6	93.7
	Yield Strength (MPa)	38.5	60.3	74.6	93.7
	Young's Modulus (GPa)	3.68	5.39	6.01	7.45
	Strain at yield (10^{-2})	1.28	1.22	1.61	1.5
	Strain at peak (10^{-2})	2.53	1.99	1.61	1.5
Resin C	Peak Strength (MPa)	28.8	39.1	44.3	54.6
	Yield Strength (MPa)	28.8	39.1	44.3	54.6
	Young's Modulus (GPa)	1.83	2.15	3.73	4.78
	Strain at yield (10^{-2})	1.63	1.67	1.33	1.18
	Strain at peak (10^{-2})	1.63	1.67	1.33	1.18
Resin D	Peak Strength (MPa)	47.3	66.3	78.6	103.9
	Yield Strength (MPa)	36.6	58.1	78.6	103.9
	Young's Modulus (GPa)	4.09	5.50	6.52	8.03
	Strain at yield (10^{-2})	1.06	1.18	1.68	1.48
	Strain at peak (10^{-2})	2.44	2.24	1.68	1.48

bulging deformation in the middle of the specimens, followed by the final cone-shaped failure. However, the degree of initial bulging varied based on the resin type and curing age. For example, among the specimens tested after 1 h, the resin D specimen exhibited the greatest degree of bulging, while the lowest degree was observed in resin A. The deformation measured in the middle of the specimens using mounted strain gauges indicated that the lateral deformation in specimen D before failure was greater than that of specimen C, which may result in a higher Poisson ratio for resin D tested at 1 h, as well as a higher degree of bulging compared to the other resins. Furthermore, the lateral strain values recorded during uniaxial loading exhibited a gradual reduction in the degree of bulging with increasing curing duration. After 1 day, the bulging was significantly reduced for resins A and C compared to resin B, and particularly for resin D. These failure patterns can be related to the post-yield stress-strain relationship presented in Fig. 7. Since the bulging deformation is greater in resins B and D than in resins A and C, it is assumed that post-yield hardening leads to greater bulging deformation. It should be emphasized that in all specimens, the bulging shape deformation was formed before the peak stress, after which cone-shaped failure occurred suddenly. Under compressive loading, the cross-sectional area of the specimen close to the loading platens tends to increase; however, frictional forces between the top and bottom surfaces of the specimens and the platens hinder the outward deformation, while the specimens at the middle expand outwardly when unconstrained. This deformation scheme leads to an initial bulging profile with the internal regions remaining unreformed, followed by a cone-shaped failure (Fig. 10).

3.1.2. Tensile properties

The results of the tensile tests are presented in Fig. 11. All types of resin exhibited a brittle behavior with nearly the same response. The stress-strain curves indicate that for resins A and C, stress increases linearly until reaching the ultimate tensile stress, whereas for resins B and D, the stress initially increases linearly and then is followed by a slight non-linear deformation. Table 6 summarizes the values of peak stress, corresponding strain, and elastic modulus. The results indicate that resin B exhibited the highest strength of 10.81 MPa, while resin D exhibited the highest elastic modulus (E = 20.76 GPa) in the tensile tests. The lowest values of tensile strength and modulus were recorded for resin C, which measured 7.29 MPa and 6.79 GPa, respectively. Comparing the results of the compressive tests (refer to Section 3.1.1) and the tensile tests shows that the strongest resin in compression does not necessarily offer the highest tensile strength. Similar to the compressive behavior, the tensile behavior of the resins is related to the particle size of the filler and the curing catalyst. The oil-based catalyst showed higher strength in tension due to the lower volume of imperfections, such as voids. In compression, particles ranging from micro to millimeter improved the strength; however, fine particles showed better tensile results. Similar effects of particle size on the tensile properties of thermosetting resins have been previously reported, where finer spherical filler particles of $CaCO_3$ presented higher strength due to a more efficient stress transfer mechanism. Mourad et al.[38] showed that a smaller particle size of filler contributes to the tensile strength, while the tensile modulus reduces. Interestingly, the compression and tensile moduli are nearly identical. Nonetheless, the tensile and elastic moduli of the specimens were of a similar magnitude to the compressive elastic modulus, meaning that resin D exhibited the highest elastic modulus valued at 20.76 GPa, and resin A had the lowest at 6.79 GPa.

3.1.3. Shear properties

The in-plane shear characteristics of the resin specimens were determined using a V-notched (Iosipesue) beam test. The testing principle can be idealized as a four-point flexural test with a rectangular specimen double-notched in the middle, as shown in Fig. 12a. Counteracting loads in the x and y directions (Fig. 12b) induce a bending moment, creating a high shear region in the middle of the specimen (Fig. 12c). The designed notches on the specimen affect the induced shear strain along the loading direction, generating uniform shear stress compared to conditions without the notches, which can lead to incline shear failure of the specimens (Fig. 12d)[51]. The shear stress can be determined by dividing the applied force by the cross-sectional area between the notches. The typical stress and corresponding crosshead displacement under shear loading are shown in Fig. 13. From the curves, it can be seen that the shear stiffness of the resins is almost equivalent in the initial stage, with resin B exhibiting the highest stiffness. Table 7 shows that, like the other mechanical tests, the inclusion of the oil-based catalyst provided better results in the shear testing. Among all resins, resin D recorded the highest shear strength, standing at 17.73 MPa,

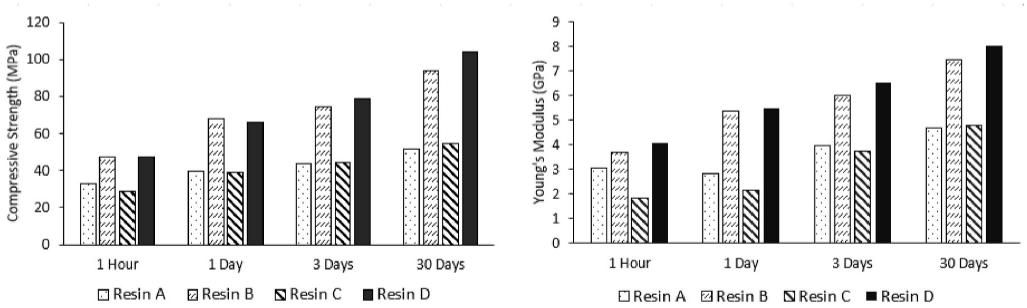

Fig. 8. Compressive strength and modulus of the resins over time.

Fig. 9. Failure patterns of the resins under compression over curing periods.

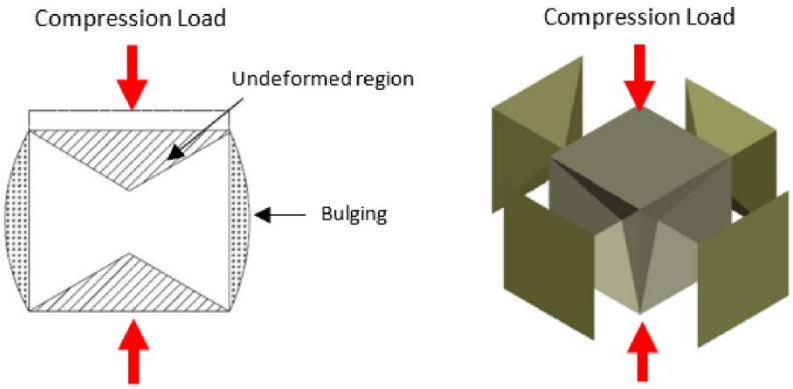

Fig. 10. Schematic of deformation and failure pattern under compression; adopted from Fiedler et al.[44]

followed by resin B with a shear strength of 14.92 MPa. The shear strength of resins A and C were 9.15 MPa and 10.22 MPa, respectively. The compressive and shear strengths of resin D were 9.8% and 18.8% higher than that of resin B, respectively, while the tensile strength of resin D was 11.6% lower than that of resin B. This indicates that shear strength is also influenced by the filler particle size, and resins with coarser fillers exhibit higher shear strength.

3.2. Microstructure and thermal properties

The morphology and viscoelastic properties of resins A, B, C, and D were systematically investigated. Morphological analysis is critical as it provides a wide range of useful information during research and development and particularly during failure analysis. Many analytical techniques are available to study material morphology, including microscopy, X-ray diffraction, thermal analysis, dynamic light scattering, porosimetry, and interferometry[52]. During morphological analysis, the size and shape of elements, voids, cracks, and the composition of morphological features are typically considered. The surface SEM images (× 24 mag) are shown in Fig. 14. The SEM micrographs reveal the appearance of surface voids with diameters ranging up to 551 μm. Furthermore, the SEM images illustrate that resins A and C were more porous than resins B and D. Additionally, resin D exhibited a more consistent surface with less void density than resin B. Specifically, the maximum void diameter for B was 310 μm, while the maximum void diameter for D was 215 μm.

The study also included an analysis of the thermo-mechanical properties of the different chemical configurations, with all samples mixed and cured under the same conditions. Additionally, DSC experiments were conducted to examine the specimens cured at 30 min, 60

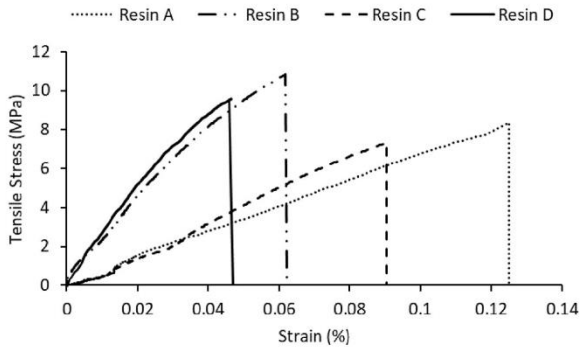

Fig. 11. Typical stress-strain behavior of the resins in tension.

Table 6
Summary of the tensile properties.

Parameters	Resin A	Resin B	Resin C	Resin D
Peak tensile stress (MPa)	8.35	10.81	7.29	9.55
Tensile modulus (GPa)	6.79	18.31	8.24	20.76
Strain at peak stress (%)	0.125	0.0618	0.0881	0.0466

min, 1 day, 7 days, and 30 days to determine the curing degrees. The typical results obtained from the DSC experiment for resin D are shown in Fig. 15. The figure indicates that the uncured resin D shows an exothermic peak after synthesis, while a quasi-linear response was observed after one day of synthesis. The reaction enthalpy can be calculated by integrating the area under the peak and the baseline[53]. The curing percentage of the resins can be quantified using the heat flow-temperature curves obtained from DSC experiments and Eq. (1).

$$\%\ Cure = \frac{[\Delta H_{uncured} - \Delta H_{cured}]}{\Delta H_{uncured}} \times 100\% \quad (1)$$

Where, $\Delta H_{uncured}$ is enthalpy under uncured resins and ΔH_{cured} is enthalpy under cured reins.

Table 7 presents the curing percentages of the resins at different time frames. The results show that after 30 min of synthesis, the maximum curing percentage was achieved for resin C at 91%, while resin B exhibited the slowest early curing process at 54%. Furthermore, resins A and D cured 83% and 70% after 30 min of synthesis, respectively. Therefore, a comparison of the results shows that the curing degree of resins C and A in the early stage of synthesis was much higher than that of resins B and D. The high curing rates may lead to the generation of a significant volume of air bubbles being trapped in the specimen. After one day, all the samples were cured by over 80%, which can be considered as the critical time to ensure that the anchoring resin is sufficiently hardened. After 30 days, the resins reached their maximum curing degrees, which were 92%, 97%, 98%, and 99% for resin A, B, C,

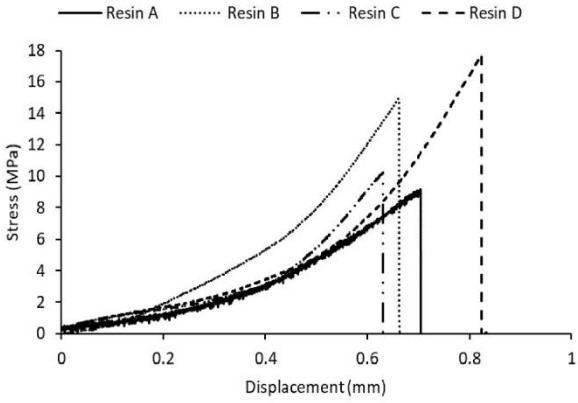

Fig. 13. Stress-displacement results of V-notched shear tests.

Table 7
Curing percentage of different resins over time.

Resins	Cured percentage†, %				
	30 Min.	1 Hour	1 Day	7 Day	30 Day
A	83	86	88	89	92
B	54	67	83	86	96
C	91	95	96	98	98
D	70	83	86	93	98

† Standard deviation < ±1.5%

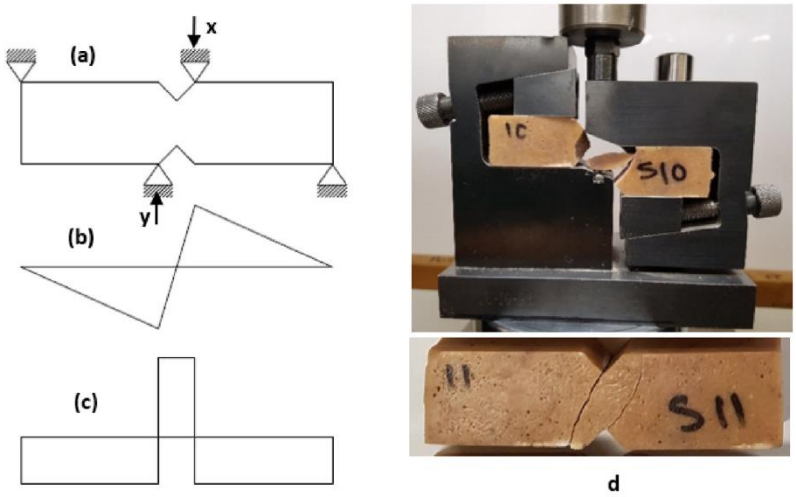

Fig. 12. (a) Schematic double notched specimen, (b) idealized bending moment diagram, (c) induced shear force and (d) typical failure after completion of the test; adopted from Merzkirch49.

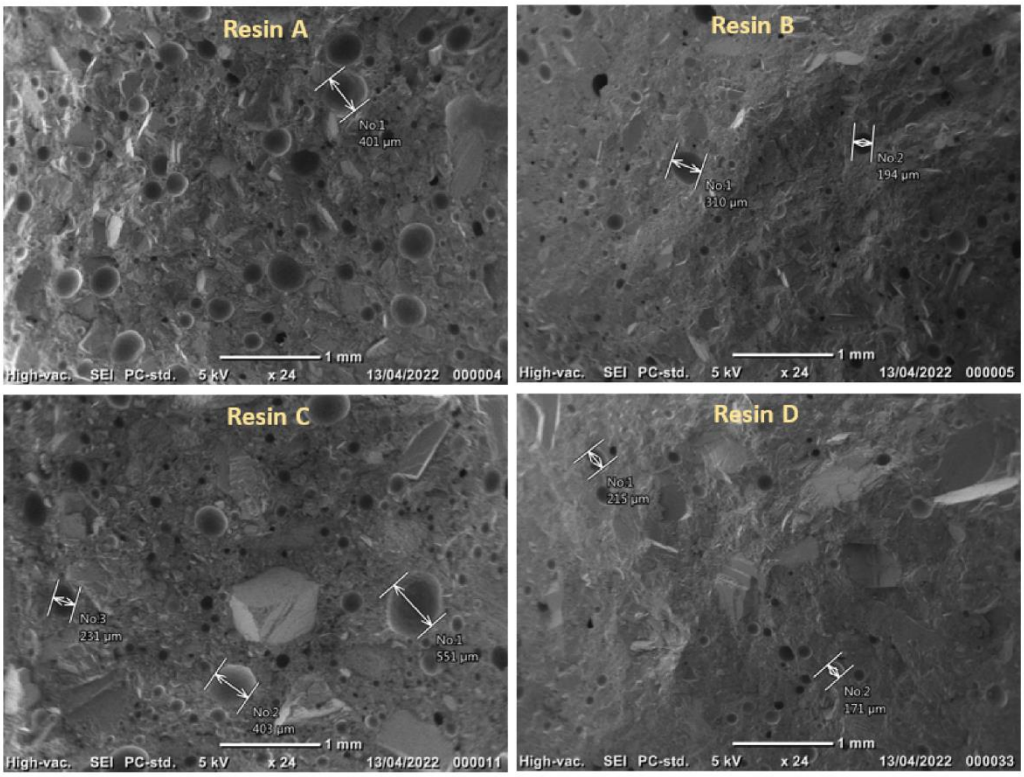

Fig. 14. SEM micrographs of resins A, B, C and D.

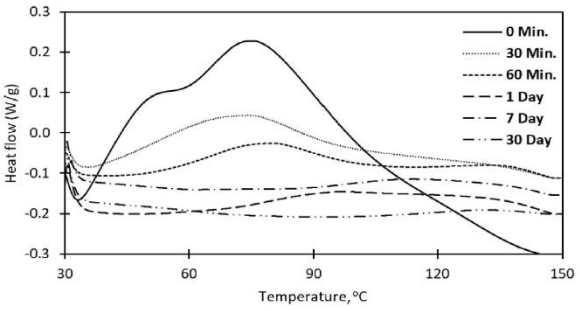

Fig. 15. DSC curing curves for resin D.

and D, respectively. There was no significant difference in the curing degrees of resins after 7 days, providing a solid platform for comparing the thermo-mechanical properties of the specimens.

Fig. 16 depicts the results obtained from the TGA experiments, and the respective decomposition temperatures are tabulated in Table 8. The experiments were carried out until 600 °C, and three main stages were identified. In stage (I), a significant mass loss was not observed at temperatures below 315 °C. In stage (II) (315 °C-420 °C), a rapid mass loss occurred due to the decomposition of the carbonate phase, which releases carbon dioxide[54]. The decomposition temperatures of all resins were found to be similar at approximately 340 ± 7 °C. Hence, it can be inferred that the resins will not decompose unless exposed to high temperatures (>340 °C). In stage (III) (above 420 °C), all specimens showed a mass drop of about 30%, resulting in the evaporation of resin, as observed from the residue. Numerous studies have been conducted on thermal gravimetric analysis (TGA) of unsaturated polyester resins all of which have yielded similar results where the rapid mass loss has been reported in range of 300–400 °C[39,42,43,55,56].

The storage modulus (E') obtained experimentally for resins A, B, C and D against temperature is shown in Fig. 17. According to the DMA tests summarized in Table 9, resin D exhibited the highest storage modulus of 7.64 ± 0.04 GPa, which is twice that of resin C at room temperature. Additionally, the storage moduli of resins A and B were 4.90 ± 0.01 and 6.22 ± 0.00 GPa, respectively at room temperature. From the storage modulus-temperature curves in Fig. 17, it is clear that the storage modulus of all the specimens decreases continuously with increasing temperature. The derivative of the storage modulus (E') with respect to temperature (T) provides valuable data. $\left(\frac{dE}{dT}\right) = \mathbf{0}$ represents the corresponding temperature at which the specimens lose their mechanical properties rapidly. Table 9 shows that the critical temperature for resins A, B, C and D is in the range of 55–63 °C. At 80 °C, all the specimens lost over 70% of their storage modulus at room temperature. According to Fig. 17, the maximum storage modulus at 80 °C was observed in resin D. Comparison shows that resin D properties are more consistent than those of resins A, B and C, since it recorded a higher storage modulus from 0 °C to 120 °C.

3.3. Temperature related pull-out behaviors

The investigation of the bond capacity of chemically encapsulated rebars under elevated temperature using pull-out tests can generally be divided into two methods: (a) heating the specimen until a desired temperature is reached, and then increasing the load until the specimen debonds, and (b) subjecting the specimen to a specific load while continuously heating it until failure occurs. For this study, the first

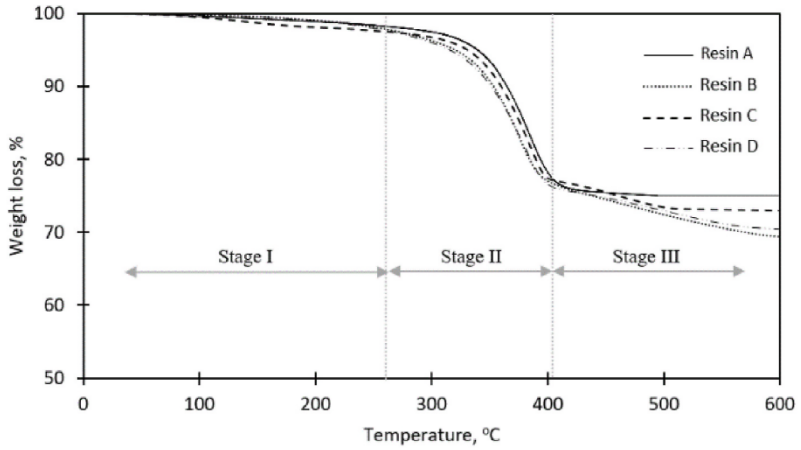

Fig. 16. TGA characterization curves of thermal decomposition for resins A, B, C and D.

Table 8
Thermal decomposition temperatures of all resins.

Resin type	Decomposition temperature (°C)
A	$347.25^{\pm 10.38}$
B	$336.81^{\pm 12.47}$
C	$344.89^{\pm 09.78}$
D	$331.44^{\pm 6.15}$

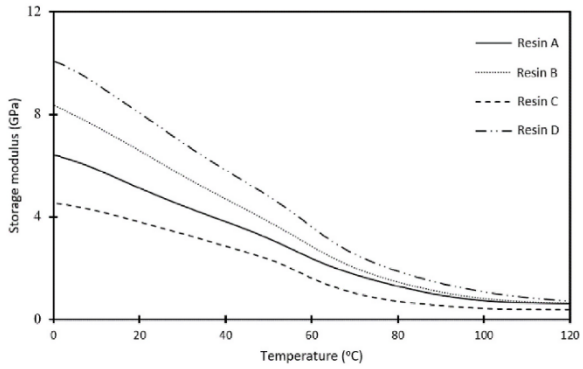

Fig. 17. DMA curves for the resins.

Table 9
Summary of the DMA test results.

Resin	Storage modulus at 23 °C (GPa)	Temperature (°C) at $\left(\frac{dE'}{dT}\right) = 0$
A	$4.90^{\pm 0.0154}$	$56.45^{\pm 0.19}$
B	$6.22^{\pm 0.00}$	$63.84^{\pm 0.01}$
C	$3.64^{\pm 0.02}$	$55.24^{\pm 0.34}$
D	$7.64^{\pm 0.04}$	$58.56^{\pm 0.87}$

technique was used. Fig. 18 displays the dimensions of the resin anchored-bolt specimens prepared for the pull-out tests, along with the positions of the thermocouples installed on the anchored bolts. Table 10 presents the temperature readings along the encapsulation length recorded during the heating and pull-out process. Temperature variation along the encapsulation depth for the specimen anchored using resin A is also illustrated in Fig. 19. A significant difference is observed between the temperatures recorded in the heating chamber and those measured along the encapsulation length. This temperature variation is a function of two parameters: the first is the encapsulation depth, and the second is the chamber's temperature. The recorded temperature decreases with increasing encapsulation length. Furthermore, at higher temperatures of the heating chamber, the temperature variation between the chamber and the thermocouples along the encapsulation length increases. For instance, the temperature variation between the chamber and T3 is 41.4 °C when the heater is set to 75 °C, while the variation increases to 170.3 °C when the chamber's temperature is increased to 250 °C. The difference between the room temperatures shown in Table 10 is related to temperature changes during a day. Fig. 20 shows the bond resistance force versus displacement obtained from the pull-out tests. As shown, the bond strength of the encapsulated bolts decreases slightly when the temperature increases from room temperature to 75 °C; however, at higher temperatures (150 °C and 250 °C), the reduction is significant. For the bolt encapsulated by resin A, the peak bond strength decreases from 99.3 kN tested at room temperature (24 °C) to 92.8 kN for the specimen tested at 75 °C, representing a reduction of 6.5%. Increasing the temperature to 150 °C and 250 °C resulted in a reduction of 21.1% and 37.4% in the peak bond strength, respectively.

The pull-out tests of the specimens encapsulated using resin D at elevated temperatures showed similar behavior, but with a slightly higher rate of reduction compared to resin A. When the testing chamber temperature was increased to 75 °C, the peak bond strength reduced by 7.6% from 139.2 kN to 128.5 kN. A reduction of 31.3% and 42.5% was observed in the peak bond resistance strength when the chamber temperature was increased to 150 °C and 250 °C, respectively. The slightly higher rate of reduction in the bond strength of encapsulated specimens of resin D compared to that of resin A is supported by the results of DMA tests. The DMA result represented in Fig. 17 shows that the storage modulus of the resin D specimen is the highest at all temperatures. However, the rate of reduction in the storage modulus (which is the slope of the curve) is higher for resin D compared to resin A. From the DMA curves, it is evident that the storage modulus decreases from 9.9 GPa to 2.6 GPa as the temperature increases from 0 °C to 70 °C, resulting in a 7.3 GPa reduction with a 70 °C increase in temperature. On the other hand, the storage modulus of resin A reduces by 3.5 GPa in the same temperature range. Furthermore, the DMA plots indicate that the storage modulus of resins becomes relatively close (0.5–1 GPa) as the testing temperature approaches 100 °C. This investigation suggests that at higher temperatures, the filler type and their particle size do not significantly influence the mechanical properties of the anchoring resins compared to their influence at lower temperatures. At higher

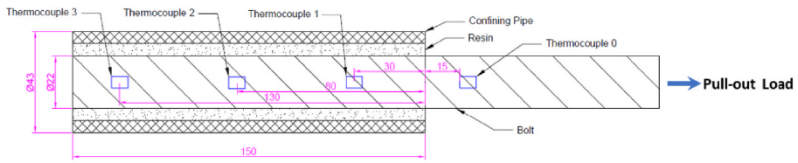

Fig. 18. Pull-out specimen with thermocouples.

Table 10
Temperature profiles along the encapsulation length.

Anchoring type	Recorded temperature by Thermocouples (°C)	Chamber Temperature			
		Room	75 °C	150 °C	250 °C
Resin A	T_0	24.2 ±	54.4	102.1	164.7
	T_1	0.6	39.1	69.6	110.2
	T_2		35.6	61.7	91.1
	T_3		33.6	56.2	79.7
Resin B	T_1	22.8 ±	N/A	N/A	N/A
	T_2	0.5			
	T_3				
Resin C	T_1	22.4 ±	N/A	N/A	N/A
	T_2	0.4			
	T_3				
Resin D	T_0	20.4 ±	49.8	98.3	176.4
	T_1	0.9	33.9	59.2	122.3
	T_2		32	47.4	102.4
	T_3		30.2	42.7	89.6

temperatures, the matrix of the bonding materials rapidly loses its mechanical properties. The DMA tests conducted in the range of 55–63 °C for the resins used in this study determined the critical temperature.

Fig. 21 displays the ultimate bond capacity of specimens encapsulated with resins A, B, C, and D. At room temperature, the highest bonding capacity of 139.2 kN was observed for the bolt embedded using resin D. Resin B also exhibited a high level of bonding strength of 124.3 kN. For specimens prepared with resins A and C, debonding occurred once the pull-out load exceeded 99.3 kN and 106.4 kN, respectively. The results of mechanical tests correlate well with the pull-out test results, indicating a good correlation between compressive and shear strength and bonding properties. However, a weak correlation was found between the tensile characteristics of the resins and bonding. Kilic et al.[12] suggested that bond strength logarithmically increases with an increase in the compressive strength of grouts. In another study, Teymen and Kılıç[14] concluded that grout mechanical characteristics affect shear and axial stress distributions along the embedment length. The bond strength of fully encapsulated rock bolts primarily depends on the shear characteristics of the bonding agent, including cohesion and internal friction angle, according to the failure modes of bolting systems. Fig. 22 illustrates the potential dependency of bond capacity and the mechanical properties of anchoring resins, which agrees with previous experimental and analytical research conducted to investigate rock bolting systems' failure modes. Shear-off/parallel shear failure is generally identified as the major mode of failure occurring at the bolt-grout

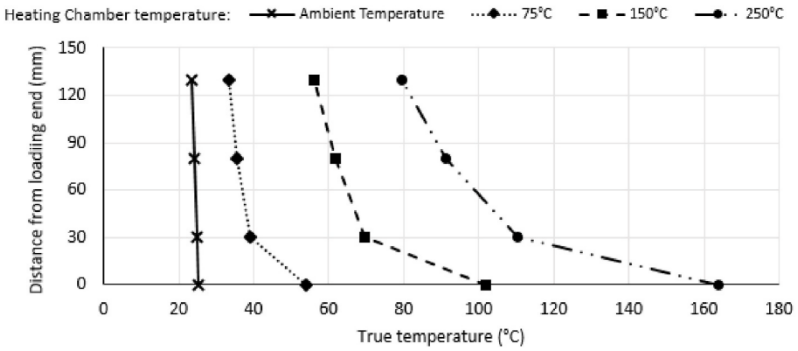

Fig. 19. Temperature variation along the encapsulation length for resin A.

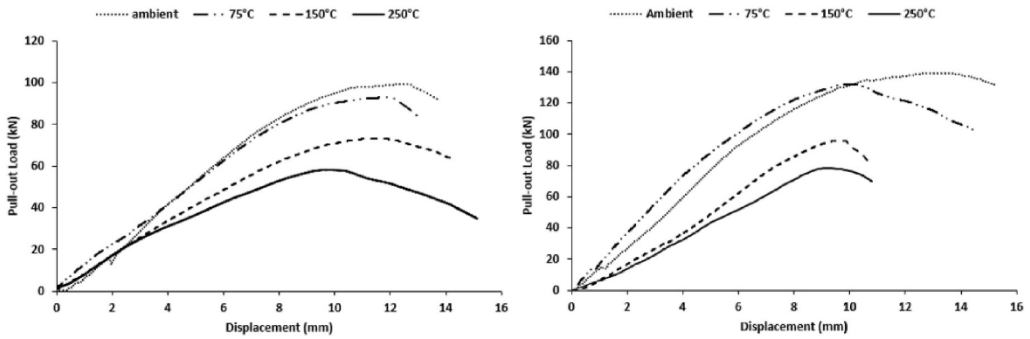

Fig. 20. Pull-out behavior of bolts encapsulated using resins A (left) and D (right) at elevated temperatures.

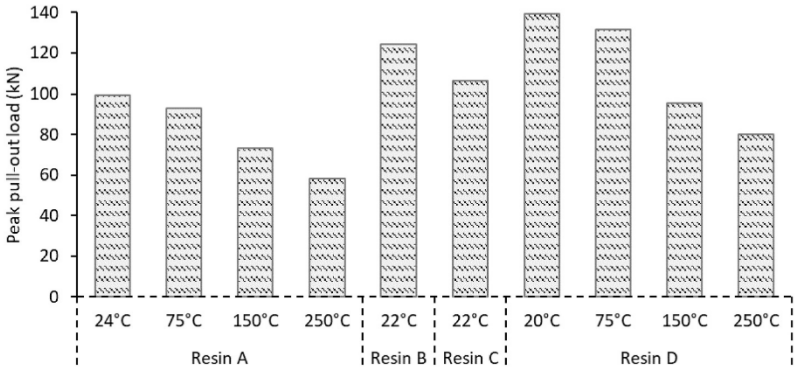

Fig. 21. Peak load measured for pull-out loads for bolts encapsulated resins A, B, C and D in different temperature conditions.

interface, given sufficient confinement pressure and surrounding media strength[57,58]. Fig. 23 shows that the main failure mode of bolts was bond failure (slippage of bolts) occurring at the bolt-resin interface. However, a small degree of cone-shape failure was also observed. No radial cracks, signs of splitting failure, or bolt rupture were observed during testing programs.

The shrinkage and expansion properties of bonding agents can affect the interfacial bond strength of anchors. Benmokrane[59] demonstrated that the introduction of an expansion agent decreases the compressive strength of the grout but improves the shear bond resistance. It was noted that when cast in the compression test mold, the bonding agent is free to expand in one direction, while grout injection in the borehole provides higher normal stress resulting in higher bond strength. Further investigations revealed that although the compressive and shear strengths of resin C are 47% and 42% less than those of resin D, respectively (resins C and D comprise the same fillers type and size, and only the catalysts are different), the bonding strength of resin C is 23% less than that of resin D. Similarly, with the same filler content in resins A and B, the compressive and shear strengths of resin A are 44% and 38% less than those of resin B, respectively; however, the bonding strength of resin A is only 20% less than that of resin B. To the best of the authors' knowledge, this can be attributed to the observed expansion properties in resins A and C. Additionally, Fig. 24 clearly shows that resins A and C expanded during the curing of the molded compressive specimens, imposing higher normal forces on the bolt surface during pull-out testing, while resins B and D remained in the mold's shape.

3.4. Limitation of the study

This study provides a detailed experimental explanation of the pull-out performance of encapsulated rock bolts using unsaturated polyester resins under elevated temperature. However, some limitations need to be noted and studied further. The analysis of the results revealed that the temperature profile along the encapsulation length is non-uniform, and therefore, the bearing capacity should be distributed according to the temperature distribution. Moreover, the thermosetting characteristics of the anchoring resins cause the bonding deterioration process due to heating to be path-dependent, which needs to be taken into account.

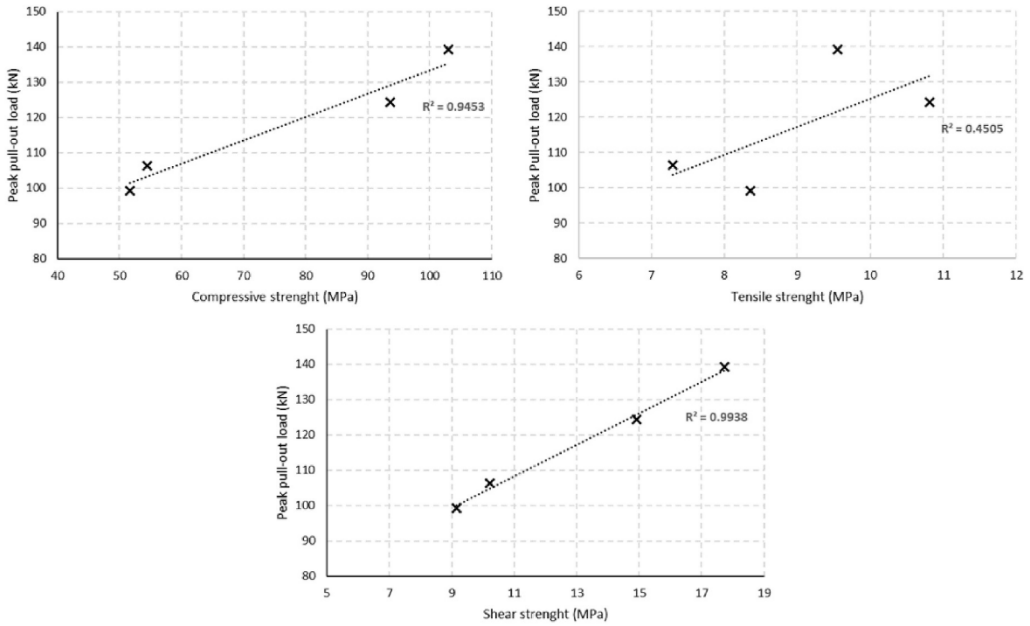

Fig. 22. Relationship between mechanical properties anchoring resins and the pull-out capacity of the encapsulated bolt.

Fig. 23. Failure of pull-out specimens embedded using resin A.

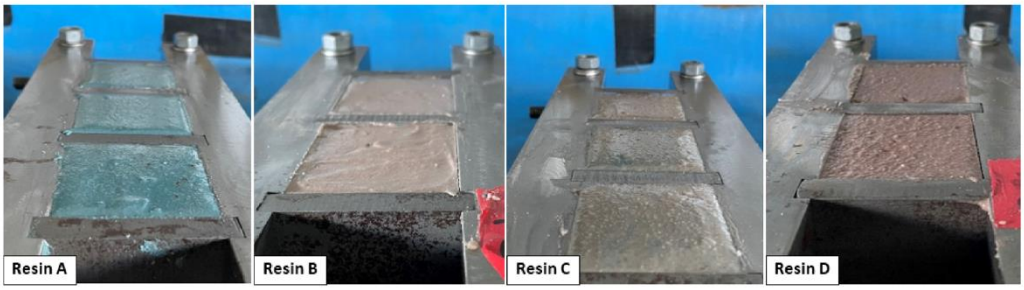

Fig. 24. Rising of the resins A and C before setting of the structure.

Further investigation is recommended to develop models and methods to address these limitations and improve the understanding of the performance of encapsulated rock bolts under elevated temperature conditions. In order to evaluate the long-term durability and reliability of the anchoring resins in actual working conditions, it is recommended to conduct further mechanical and pull-out tests specifically with higher encapsulation lengths installed in rock or concrete under elevated temperature and different heat exposure time. This will help gather data that can be used to improve the design and engineering of these materials.

4. Conclusions

Four two-component polyester-based anchoring resins were tested to characterize their mechanical, thermal, and bonding properties under various testing conditions. Two types of curing agents, including water-based and oil-based catalysts, were selected to mix with the resin matrices. The viscoelastic properties of the synthesized materials, as well as the compression, tensile, and shear properties, were comprehensively investigated. During the proof of concept, deformed rock bolts were encapsulated using the resins inside rifled steel pipes to determine the pull-out behavior of the bolting systems at room and elevated temperatures.

The TGA analysis revealed that the synthesized specimens decomposed at approximately 340 °C. DSC results showed that the curing degree of the specimens prepared by the water-based catalysts was slightly higher than that of oil-based specimens. Resins A and C reached 80% curing percentage in only 0.5 h, while resins B and D achieved this curing percentage in 1 h. According to the DMA results, the specimens' mechanical properties rapidly drop beyond 55–63 °C. Scanning electron microscopy micrographs illustrated that water-based catalyst used resins (A and C) are more porous compared to resins B and D. Thus, water-based agent was found to be the main reason causing the defects.

The compressive strength and elastic modulus of resins A, B, C, and D were found to be within the range of 51–103 MPa and 4.71–8.03 GPa, respectively. Extensive voids were found in the specimens prepared using the water-based catalysts (A and C) compared to oil-based catalyst included resins (B and D), representing lower strength and modulus. The hybridization of filler particle size from micro to millimeter can lead to higher compressive strength and modulus.

The tested resins were able to achieve almost 50% of their ultimate compressive strength (tested at 30 days) after only 1 h. The main failure mode observed in the specimens under compression was cone-shaped rupture. While the bulging profile was observed in the compressive tests, the degree of bulging was found to be a function of the catalyst type and curing time. The tensile peak strength and modulus ranged from 7.29 to 10.81 MPa and 6.79–18.31 GPa, respectively. Unlike compressive properties, smaller filler particle size improved the tensile strength. However, the relationship between the tensile modulus and filler particle size was found to be similar to the compressive modulus. The shear strength of the resins ranged from 9.15 to 17.73 MPa. At ambient conditions, the bond strength of the anchored bolts ranged from 99.3 to 139.2 kN, and a good agreement was found between the compressive and shear properties of the anchoring resins and their corresponding bond resistance force.

To simulate a pull-out test at elevated temperature, a unique experimental set-up was developed. The results showed that a reduction of 6.6%–31.3% in the bond capacity of the bolts was measured when the chamber temperature reached 75 °C and 150 °C, respectively. Interestingly, the bolts encapsulated in resins A and D were able to acquire 62.6% and 57.5% bond strength at 250 °C compared to the initial strength.

Overall, the study provides a comprehensive and novel experimental framework to understand the behavior of chemically anchored rock bolts in the tunneling and underground mining industries. The effect of external fixtures of rock bolting systems, such as surface plates and nuts, on the temperature profile along the encapsulation length may also be of interest to other researchers, but was not considered in this study.

Therefore, it is recommended to undertake further studies on the performance of chemically anchored rock bolts after elevated temperature exposure over a significant time period.

Declaration of competing interest

The authors declare the following financial interests/personal relationships which may be considered as potential competing interests: Hadi Nourizadeh reports a relationship with University of Southern Queensland that includes: employment.

Data availability

Data will be made available on request.

Acknowledgment

The in-kind support from Jennmar Australia and Minova Australia is greatly acknowledged.

References

1 Rastegarmanesh A, Mirzaghorbanali A, McDougall K, et al. Axial performance of cementitious grouted cable bolts under rotation constraint scenarios. *Rock Mech Rock Eng*. 2022. https://doi.org/10.1007/s00603-022-02950-4. Published online.
2 Contrafatto L, Cosenza R. Behaviour of post-installed adhesive anchors in natural stone. Construct Build Mater. 68:355-369. doi:10.1016/j.conbuildmat.2014.05.099.
3 Xue-gui S, Xian-jie D, Hong-hu Y, Ben-kui L. Research of the thermal stability of structure of resin anchoring material based on 3D CT. *Int J Adhesion Adhes*. 2016;68:161–168. https://doi.org/10.1016/j.ijadhadh.2016.03.005.
4 Pączkowski P, Puszka A, Gawdzik B. Investigation of degradation of composites based on unsaturated polyester resin and vinyl ester resin. *Materials*. 2022;15(4). https://doi.org/10.3390/ma15041286.
5 Witt R, Cizek E. Effect of filler particle size on resins. *Ind Eng Chem*. 1954;46(8):1635–1639.
6 Devi MS, Murugesan V, Rengaraj K, Anand P. Utilization of flyash as filler for unsaturated. *J Appl Polym Sci Polym Sci*. 1998;69(7):1385–1391. https://doi.org/10.1002/(SICI)1097-4628(19980815)69:7<1385::AID-APP13>3.0.CO;2-T.
7 Rahman GMS, Aftab H, Islam MS, Zobayer M, Mukhlish B, Ali F. Enhanced physico-mechanical properties of polyester resin film using CaCO3 filler. *Fibers Polym*. 2016;17(1):59–65. https://doi.org/10.1007/s12221-016-5612-y.
8 Bagherzadeh A, Jamshidi M, Monemian F. Investigating mechanical and bonding properties of micro/nano filler containing epoxy adhesives for anchoring steel bar in concrete. Construct Build Mater. 240. doi:10.1016/j.conbuildmat.2019.117979.
9 Fu M, Liu S, Jia H, He D. Experimental study of an orientation and resin-lifting device for improving the performance of resin-anchored roof bolts. *Rock Mech Rock Eng*. 2019;53(1):211–231. https://doi.org/10.1007/s00603-019-01906-5.
10 Rastegarmanesh A, Mirzaghorbanali A, McDougall K, et al. Axial response of resin encapsulated cable bolts in monotonic and cyclic loading. *Can Geotech J*. 2023. https://doi.org/10.1139/cgj-2022-0379. Published online.
11 Nourizadeh H, Williams S, Mirzaghorbanali A, McDougall K, Aziz N, Serati M. Axial behaviour of rock bolts-part (A) Experimental study. In: *Recource Operator.*. 2021.
12 Kılıc A, Yasar E, Celik AG. Effect of grout properties on the pull-out load capacity of fully grouted rock bolt. *Tunn Undergr Space Technol*. 2002;17:355–362.
13 Cao C, Nemcik J, Aziz N, Ren T. Analytical study of steel bolt profile and its influence on bolt load transfer. *Int J Rock Mech Min Sci*. 2013;60:188–195. https://doi.org/10.1016/j.ijrmms.2012.12.013.
14 Teymen A, Kılıç A. Effect of grout strength on the stress distribution (tensile) of fully-grouted rockbolts. *Tunn Undergr Space Technol*. 2018;77:280–287. https://doi.org/10.1016/j.tust.2018.04.022.
15 Ho D, Bost M, Rajot J. Numerical study of the bolt-grout interface for fully grouted rockbolt under different confining conditions. *Int J Rock Mech Min Sci*. 2019;119(September 2017):168–179. https://doi.org/10.1016/j.ijrmms.2019.04.017.
16 chun Ma H, hui Tan X, zhong Qian J, liang Hou X. Theoretical analysis of anchorage mechanism for rock bolt including local stripping bolt. *Int J Rock Mech Min Sci*. 2019;122(December 2018), 104080. https://doi.org/10.1016/j.ijrmms.2019.104080.
17 Liu S, He D, Fu M. Experimental investigation of surrounding-rock anchoring synergistic component for bolt support in tunnels. *Tunn Undergr Space Technol*. 2020;104. https://doi.org/10.1016/j.tust.2020.103531.
18 Wang W, Pan Y, Xiao Y. Synergistic resin anchoring technology of rebar bolts in coal mine roadways. *Int J Rock Mech Min Sci*. 2022;151. https://doi.org/10.1016/j.ijrmms.2022.105034.
19 Liu X, Yao Z, Xue W, Wang X, Huang X, Li Y. Experimental study of the failure mechanism of the anchorage interface under different surrounding rock strengths and ambient temperatures. *Adv Civ Eng*. 2021;2021:1–17. https://doi.org/10.1155/2021/6622418.
20 Dudek D, Kadela M. Pull-out strength of resin anchors in non-cracked and cracked concrete and masonry substrates. Procedia Eng. 161:864-867. doi:10.1016/j.proeng.2016.08.734.
21 Hyett AJ, Bawden WF, Reichert RD. The effect of rock mass confinement on the bond strength of fully grouted cable bolts. *Int Rock Mech Min Sci Geomech Abstr*. 1992;29(5):503–524.
22 Benmokrane B, Chennouf A, Mitri HS. Laboratory evaluation of cement-based grouts and grouted rock anchors. *Int J Rock Mech Min Sci Geomech Abstr*. 1995;32(7):633–642.
23 Yokota Y, Zhao Z, Nie W, Date K, Iwano K, Okada Y. Experimental and numerical study on the interface behaviour between the rock bolt and bond material. *Rock Mech Rock Eng*. 2019;52:869–879. https://doi.org/10.1007/s00603-018-1629-4.
24 Wang M, Hu Y, Jiang C, Wang Y, Liu D, Tong J. Mechanical characteristics of cement-based grouting material in high-geothermal tunnel. *Materials*. 2020;13(7). https://doi.org/10.3390/ma13071572.
25 Jahani Y, Baena M, Barris C, Perera R, Torres L. Influence of curing, post-curing and testing temperatures on mechanical properties of a structural adhesive. *Construct Build Mater*. 2022;324. https://doi.org/10.1016/j.conbuildmat.2022.126698.
26 Michel M, Ferrier E. Effect of curing temperature conditions on glass transition temperature values of epoxy polymer used for wet lay-up applications. Construct Build Mater. 231. doi:10.1016/j.conbuildmat.2019.117206.
27 Wang S, Stratford T, Reynolds TPS. Linear creep of bonded FRP-strengthened metallic structures at warm service temperatures. Construct Build Mater. 283. doi:10.1016/j.conbuildmat.2021.122699.
28 Yu C, Tian W, Zhang C, Chai S, Cheng X, Wang X. Temperature-dependent mechanical properties and crack propagation modes of 3D printed sandstones. Int J Rock Mech Min Sci. 146. doi:10.1016/j.ijrmms.2021.104868.
29 Laredo M, Theoretical R, Fluminense UF, Passo R. *Effect of Temperature on the Mechanical Properties of Polymer Mortars*. 2012;15(4):645–649. https://doi.org/10.1590/S1516-14392012005000091.
30 Pinoteau N, Heck J V, Rivillon P, et al. Prediction of failure of a cantilever–wall connection using post-installed rebars under thermal loading. Eng Struct. 56:1607-1619. doi:10.1016/j.engstruct.2013.07.028.
31 Amine M, françois Caron J, Pinoteau N, Forêt G. International Journal of Adhesion and Adhesives Mechanical behavior of adhesive anchors under high temperature exposure : experimental investigation. *Int J Adhesion Adhes*. 2017;78(July):200–211. https://doi.org/10.1016/j.ijadhadh.2017.07.004.
32 Al-Mansouri O, Mege R, Pinoteau N, Guillet T, Rémond S. Influence of testing conditions on thermal distribution and resulting load-bearing capacity of bonded anchors under fire. Eng Struct. 192:190-204. doi:10.1016/j.engstruct.2019.04.099.
33 European Assessment Document E. *Systems for Post-Installed Rebars Connections with Mortar*; 2020. http://www.eota.eu.
34 Lakhani H, Hofmann J. A numerical method to evaluate the pull-out strength of bonded anchors under fire. In: *3rd Int Symp Connect between Steel Concr*. 2017. Published online.
35 Yang H, Lee LJ. Comparison of unsaturated polyester and vinylester resins in low temperature polymerization. *J Appl Polym Sci*. 2001;79(7):1230–1242. https://doi.org/10.1002/1097-4628(20010214)79:7<1230::AID-APP100>3.0.CO;2-2.
36 McAlvin JE, Dowd ZS, Kinnin LF, et al. *Next Generation Novolac Epoxy Vinyl Ester Resins for Heat Resistant Composites. CAMX*. Compos Adv Mater Expo; 2016. Published online 2016.
37 yun Fu S, qiao Feng X, Lauke B, wing Mai Y. Effects of particle size , particle/matrix interface adhesion and particle loading on mechanical properties of particulate – polymer composites. *Compos Part B*. 2008;39:933–961. https://doi.org/10.1016/j.compositesb.2008.01.002.
38 Mourad AHI, Abu-Jdayil B, Hassan M. Mechanical behavior of Emirati red shale fillers/unsaturated polyester composite. *SN Appl Sci*. 2020;2(3):1–9. https://doi.org/10.1007/s42452-020-2284-4.
39 Lin Y, Jiang S, Gui Z, Li G, Shi X. Synthesis of a novel highly effective flame retardant containing multivalent phosphorus and its application in unsaturated polyester resins. *RSC Adv*. 2016;6:86632–86639. https://doi.org/10.1039/C6RA19798A.
40 Alif Z, Halim A, Azizi M, et al. Effect of silica aerogel – aluminium trihydroxide hybrid filler on the physio-mechanical and thermal decomposition behaviour of unsaturated polyester resin composite. *Polym Degrad Stabil*. 2020;182, 109377. https://doi.org/10.1016/j.polymdegradstab.2020.109377.
41 Preghenella M, Pegoretti A, Migliaresi C. Thermo-mechanical characterization of fumed silica-epoxy nanocomposites. Polymer (Guildf). 46(26):12065-12072. doi:10.1016/j.polymer.2005.10.098.
42 Tabatabai H, Janbaz M, Nabizadeh A. Mechanical and thermo-gravimetric properties of unsaturated polyester resin blended with FGD gypsum. *Construct Build Mater*. 2018;163:438–445. https://doi.org/10.1016/j.conbuildmat.2017.12.041.
43 Lavoratti A, Cristine L, José A. Dynamic-mechanical and thermomechanical properties of cellulose nanofiber/polyester resin composites. *Carbohydr Polym*. 2016;136:955–963. https://doi.org/10.1016/j.carbpol.2015.10.008.
44 Fiedlera B, Hojoa M, Ochiaia S, Schulteb K, Andoc M. Failure behavior of an epoxy matrix under different kinds of static loading. *Compos Sci Technol*. 2001;61.
45 Yeon JH, Lee HJ, Yeon J. Deformability in unsaturated polyester resin-based concrete: effects of the concentration of shrinkage-reducing agent and type of filler. *Materials*. 2020;13(3). https://doi.org/10.3390/ma13030727.
46 Gary G, Bailly P. Behaviour of quasi-brittle material at high strain rate. Experiment and modelling. *Eur J Mech Solid*. 1998;17(3).
47 Cai M, Hou PY, Zhang XW, Feng XT. International journal of rock mechanics and mining sciences post-peak stress. *Strain curves of brittle hard rocks under axial-strain-controlled loading*. 2021;147(September).
48 Gong F, Zhang P, Xu L. Damage constitutive model of brittle rock under uniaxial compression based on linear energy dissipation law. *Int J Rock Mech Min Sci*. 2022;160(September 2021), 105273. https://doi.org/10.1016/j.ijrmms.2022.105273.
49 Chen W, Lu F, Cheng M. Tension and compression tests of two polymers under quasi-static and dynamic loading. *Polym Test*. 2002;21.

50 Sampath C, Lokuge W, Islam M. Compressive strength characterization of polyester based fillers. *Adv Mater Res*. 2012;410:32–35. https://doi.org/10.4028/www.scientific.net/AMR.410.32.

51 Merzkirch M. *Mechanical Characterization Using Digital Image Correlation*. Cham: Springer; 2022. https://doi.org/10.1007/978-3-030-84040-2_3.

52 Popelka A, Zavahir S, Habib S. Morphology analysis. In: *Polymer Science and Innovative Applications: Materials, Techniques, and Future Developments*. 2020:21–68.

53 Flynn JH. Analysis of DSC results by integration. *Thermochim Acta*. 1993;217:129–149.

54 Cultrone G, Rodriguez-Navarro C, Sebastian E, Cazalla O, Dela Torre MJ. Carbonate and silicate phase reactions during ceramic firing. *Eur J Mineral*. 2001;13(3):621–634.

55 Lin Y, Yu B, Jin X, Hu Y. Study on thermal degradation and combustion behavior of fl ame retardant unsaturated polyester resin modi fi ed with a reactive phosphorus containing monomer. *RSC Adv*. 2016;6:49633–49642. https://doi.org/10.1039/C6RA06544A.

56 Lin Y, Jiang S, Hu Y, Chen G, Shi X, Peng X. Hybrids of aluminum hypophosphite and ammonium polyphosphate : highly effective flame retardant system for unsaturated polyester resin. *Polymer (Guildf)*. 2018;39(5):1763–1770. https://doi.org/10.1002/pc.24128.

57 Cao C, Ren T, Cook C, Cao Y. Analytical approach in optimising selection of rebar bolts in preventing rock bolting failure. *Int J Rock Mech Min Sci*. 2014;72:16–25. https://doi.org/10.1016/j.ijrmms.2014.04.026.

58 Cui G, Zhang C, Pan Y, Deng L, Zhou H. Laboratory investigation into effect of bolt profiles on shear behaviors of bolt-grout interface under constant normal stiffness (CNS) conditions. *J Rock Mech Geotech Eng*. 2020;12(6):1234–1248. https://doi.org/10.1016/j.jrmge.2020.03.010.

59 Benmokrane B, Zhang B, Chennouf A. Tensile properties and pullout behaviour of AFRP and CFRP rods for grouted anchor applications. *Construct Build Mater*. 2000;14:157–170.

3.2. Links and implications

The results from Chapter 3 have shed light on how the mechanical and thermal properties of encapsulation materials play a crucial role in influencing the bonding performance of fully encapsulated rock bolts. Specifically, a noteworthy correlation was observed between shear strength and the pullout performance of the rock bolts. Furthermore, our findings highlighted that elevated temperatures can lead to a significant reduction in the bonding performance of fully encapsulated rock bolts. The development of standardised testing methods for reinforcing materials employed in underground applications could potentially be facilitated by the outcomes of this study. Additionally, insights gained from this study could potentially inform the design and construction of rock support systems that are both more efficient and reliable, thereby contributing to the enhancement of safety and efficiency in underground excavations. Of particular significance is the fact that the extension of underground openings, particularly in coal mines, results in an elevation of geothermal heat levels and heightened combustion risks within coal seams, presenting a significant challenge for ground control designers. Consequently, it becomes imperative to place significant emphasis on comprehending the performance of anchoring materials under elevated temperature conditions. However, it is important to note that *in-situ* stresses also exert an influence on the axial performance of rock bolts. To gain a more comprehensive understanding of rock bolt behaviour, it is critically important to delve into, and thoroughly investigate, their performance under true triaxial confining conditions. This investigation into true confining conditions is the focal point of Chapter 4.

CHAPTER 4: PAPER 2- FAILURE CHARACTERISATION OF FULLY GROUTED ROCK BOLTS UNDER TRIAXIAL TESTING

4.1. Introduction

In Chapter 2, it was demonstrated that the axial performance of fully grouted rock bolts is significantly influenced by *in-situ* stress. However, the existing literature contains certain limitations in terms of comprehending precisely how fully grouted rock bolts behave under varying confining pressure conditions. In reality, underground openings are surrounded by a non-uniform stress state that can vary significantly within a rock mass. This non-uniformity can lead to variations in the mechanical response of rock bolts that cannot be accounted for by models developed previously.

Manuscript 2, presented in this chapter, qualitatively discusses an experimental study in which rock bolts embedded in cubic specimens of concrete were subjected to testing under triaxial stress conditions. In this study, a series of push tests were conducted under triaxial conditions, where non-uniform confining stresses ($\sigma_2 \neq \sigma_3$) were applied to cubic specimens to investigate the previously overlooked effect of intermediate principal stresses on rock bolt strength properties. The interaction between confining stresses and the principal stress ratio ($k=\sigma_2/\sigma_3$) and interfacial bond strength is examined in this study. The results reveal that as confining stresses increase from zero to higher levels, the pre-failure behaviour undergoes a transition from linear to non-linear forms, resulting in an increase in initial stiffness. Furthermore, the load-displacement curves demonstrate distinct behaviour in the post-failure phase at higher magnitudes of confining stresses, where higher stiffness is attained.

Journal of Rock Mechanics and Geotechnical Engineering xxx (xxxx) xxx

Contents lists available at ScienceDirect

Journal of Rock Mechanics and Geotechnical Engineering

journal homepage: www.jrmge.cn

Full Length Article

Failure characterization of fully grouted rock bolts under triaxial testing

Hadi Nourizadeh [a,*], Ali Mirzaghorbanali [b], Mehdi Serati [c], Elamin Mutaz [c], Kevin McDougall [d], Naj Aziz [e]

[a] Centre for Future Materials (CFM), School of Engineering, University of Southern Queensland, Toowoomba, QLD, 4350, Australia
[b] School of Engineering, University of Southern Queensland, Springfield Central, QLD, 4300, Australia
[c] School of Civil Engineering, University of Queensland, St Lucia, QLD, 4072, Australia
[d] School of Surveying and Build Environment, University of Southern Queensland, Toowoomba, QLD, 4350, Australia
[e] School of Civil, Mining & Environmental Engineering, University of Wollongong, Wollongong, NSW, 2500, Australia

ARTICLE INFO

Article history:
Received 12 January 2023
Received in revised form
31 May 2023
Accepted 14 August 2023
Available online xxx

Keywords:
Rock bolts
Bolt-grout interface
Bond strength
Push test
Triaxial tests

ABSTRACT

Confining stresses serve as a pivotal determinant in shaping the behavior of grouted rock bolts. Nonetheless, prior investigations have oversimplified the three-dimensional stress state, primarily assuming hydrostatic stress conditions. Under these conditions, it is assumed that the intermediate principal stress (σ_2) equals the minimum principal stress (σ_3). This assumption overlooks the potential variations in magnitudes of in situ stress conditions along all three directions near an underground opening where a rock bolt is installed. In this study, a series of push tests was meticulously conducted under triaxial conditions. These tests involved applying non-uniform confining stresses ($\sigma_2 \neq \sigma_3$) to cubic specimens, aiming to unveil the previously overlooked influence of intermediate principal stresses on the strength properties of rock bolts. The results show that as the confining stresses increase from zero to higher levels, the pre-failure behavior changes from linear to nonlinear forms, resulting in an increase in initial stiffness from 2.08 kN/mm to 32.51 kN/mm. The load-displacement curves further illuminate distinct post-failure behavior at elevated levels of confining stresses, characterized by enhanced stiffness. Notably, the peak load capacity ranged from 27.9 kN to 46.5 kN as confining stresses advanced from $\sigma_2 = \sigma_3 = 0$ to $\sigma_2 = 20$ MPa and $\sigma_3 = 10$ MPa. Additionally, the outcomes highlight an influence of confining stress on the lateral deformation of samples. Lower levels of confinement prompt overall dilation in lateral deformation, while higher confinements maintain a state of shrinkage. Furthermore, diverse failure modes have been identified, intricately tied to the arrangement of confining stresses. Lower confinements tend to induce a splitting mode of failure, whereas higher loads bring about a shift towards a pure interfacial shear-off and shear-crushed failure mechanism.

© 2023 Institute of Rock and Soil Mechanics, Chinese Academy of Sciences. Production and hosting by Elsevier B.V. This is an open access article under the CC BY-NC-ND license (http://creativecommons.org/licenses/by-nc-nd/4.0/).

1. Introduction

The stability of underground excavations is a primary concern for geotechnical and mining engineers seeking to improve workers safety, reduce environmental issues, and avoid financial loss. Rock bolts are generally considered the most adaptable and efficient reinforcement system in complex ground conditions (Li, 2017). The response of rock bolts to excitation or disturbance depends on the type of bolt, bolt arrangement in the field, and the mode of the subjected force, which can be predominantly shear, axial, or flexural (Chen, 2014; Li et al., 2014, 2019). However, the typical behavior is likely a combination of all the forces above (He et al., 2017).

The impact of surface geometry, identified by the bolt rib angle, height, spacing, width, and orientation, has been studied experimentally and numerically to optimize bolt performance (Aziz and Webb, 2003; Kılıc et al., 2003; Yokota et al., 2019; Cui et al., 2020). Grout acts as a medium for transmitting initiated stress from the bolt to the stable rock mass, and also to transfer the in situ stress from the surrounding rock to the bolt-grout interface. The interaction between the mechanical characteristics of the grout and rock bolt behavior has been well studied by many scholars who agree with the positive effects of stronger grouts on bolting performance (Kılıc et al., 2002; Li et al., 2016; Yu et al., 2019; Høien

* Corresponding author.
E-mail address: hadi.nourizadeh@unisq.edu.au (H. Nourizadeh).
Peer review under responsibility of Institute of Rock and Soil Mechanics, Chinese Academy of Sciences.

https://doi.org/10.1016/j.jrmge.2023.08.013
1674-7755 © 2023 Institute of Rock and Soil Mechanics, Chinese Academy of Sciences. Production and hosting by Elsevier B.V. This is an open access article under the CC BY-NC-ND license (http://creativecommons.org/licenses/by-nc-nd/4.0/).

Please cite this article as: Nourizadeh H et al., Failure characterization of fully grouted rock bolts under triaxial testing, Journal of Rock Mechanics and Geotechnical Engineering, https://doi.org/10.1016/j.jrmge.2023.08.013

et al., 2021; Nourizadeh et al., 2021). The bolt diameter and mechanical properties also affect the axial behavior of rock bolts (Chen et al., 2020). The process of bolt installation can also significantly impact the quality of encapsulation, consequently influencing the bond strength of the reinforcement system. Aziz et al. (2016) comprehensively studied the effects of grout thickness, borehole diameter, and resin mixing procedure via field and laboratory pull-push out tests. In the study by Ma et al. (2017), it was identified that improper mixing of resin components leading to the presence of gloving and air bubbles can markedly diminish the load-bearing capacity of sections spanning the encapsulation length. Furthermore, efforts have been undertaken to quantify the impact of bolt concentricity on anchoring capacity (Fu et al., 2019; Liu et al., 2020). These investigations were accompanied by innovative approaches leading to better resin mixing. Notably, achieving an optimal grout annulus thickness is a pivotal consideration, within practical constraints (Fabjanczyk and Tarrant, 1992; Fuller and O'Grady, 1994). The critical embedment length refers to the minimum grouted length of a specific rebar that has an anchorage strength greater than the yielding strength of the bolt. This length depends on the bond characteristics at the bolt-grout interface, uniaxial compression of grouts, and elastic-plastic behavior of the steel rod (Li et al., 2016; Høien et al., 2021).

Furthermore, the rock mass characteristics can heavily influence the critical failure mechanism, failure location, and bond stiffness in the design of rock bolt systems (Salcher and Bertuzzi, 2018; Hazrati et al., 2020). The axial slip of deformed reinforcing elements causes radial dilation, which is limited or inhibited by the rock mass's normal stiffness. A higher normal stiffness can lead to higher induced lateral confining stress and higher interfacial bond strength (Hyett et al., 1992; Yazici and Kaiser, 1992).

In situ stress has a crucial role in the failure mode of an excavation (Li, 2017). Conversely, external confining stress can enhance the performance of rock bolts (Blanco et al., 2013). Therefore, it is essential to carefully consider the effect of in situ stresses on the behavior of rock bolts for their design. Hyett et al. (1995) conducted a series of pull-out tests using modified Hoek cells under constant confining pressures. The experimental results indicated that the bond strength increases with confining pressure. In a study conducted by Thenevin et al. (2017), an array of pull-out tests was undertaken, with a distinct focus on the impact of confinement pressure. These tests were executed under two conditions: constant radial stiffness and constant radial load. This was accomplished using a triaxial cell with confining pressures extending up to 15 MPa. The outcomes of this investigation align with previous research, highlighting that elevated confining pressures yield a heightened peak bond strength. Kang et al. (2020) pointed out that, in practice, rock bolts are typically subjected to complex loading conditions rather than a simple pull-out load, significantly affecting their behavior. Apart from experimental studies, analytical and numerical models have also been developed to investigate the effect of confining stress on the axial behavior of rock bolts. Li et al. (2021) developed an analytical model based on the modified continuously yielding criterion to analyze the performance of rock bolts under constant confining pressure. However, this model is only suitable for uniform constant confining pressure and cannot be applied to other boundary conditions. Similarly, the failure models developed by Blanco et al. (2013), Ho et al. (2019) and Chen et al. (2020) also assume uniform confining stress conditions.

The studies mentioned above possess certain limitations when it comes to comprehending the behavior of fully grouted rock bolts under varying confining pressure conditions. The stress state surrounding underground openings is non-uniform and can differ significantly in different areas of a rock mass. This non-uniformity may result in variations in the mechanical response of rock bolts that cannot be captured by previously developed models. This paper qualitatively discusses an experimental study in which rock bolts embedded in cubic specimens of concrete were tested under triaxial stress conditions to address these limitations. Understanding the impact of confining stresses on rock bolt behavior by simulating actual in situ conditions can effectively inform the design and construction of more efficient and reliable rock support systems, leading to safer and more efficient underground excavations. The study investigates the interaction between confining stresses and the principal stress ratio ($k = \sigma_2/\sigma_3$) and interfacial bond strength. It should be noted that planes of zero shear stress were considered in the test design, where the normal stress components become principal ($\tau_{xy} = \tau_{yx} = 0, \sigma_x = \sigma_2, \sigma_y = \sigma_3$). Finally, the lateral displacement associated with the outer surfaces of the cubic specimen during push-out was analyzed. The results of this experimental study will contribute to a better understanding of the behavior of rock bolts under real ground conditions where varying levels of confining stresses are present. This advancement is expected to contribute to the development of designing, modeling, and application of strata control in underground openings.

2. Experimental program

The methodology utilized in this study involves the preparation of cubic concrete specimens as a simulated rock mass. Deformed rebars were subsequently installed and encapsulated in holes created in the center of the cubic specimens. Finally, push-out tests were conducted using a state-of-the-art true triaxial testing machine to investigate the behavior of rock bolts under varying triaxial conditions.

2.1. Specimen preparation

Short encapsulation (SE) was utilized to investigate debonding mechanisms of rock bolts. To prepare the surrounding material, concrete was mixed according to the design proposed by Serati et al. (2020), cast in a larger rectangular prismoidal mold, and kept in a moist room. After 70 d of curing, the concrete was cut into smaller specimens with dimensions of 60 mm × 60 mm × 37 mm ($L \times W \times H$). The specimens were trimmed, and a central hole with a diameter of ϕ35 mm was cored. M24 X Coal Bolt manufactured by Minova Australia was cut into equal-length pieces of 50 mm. The bolts were then centrally encapsulated in the hole using Stratabinder HS, a widely used cementitious grout in Australia produced by Minova Australia. Table 1 presents the mix design of the concrete and grout used in the sample preparation.

2.2. Experimental equipment

The primary method commonly used to investigate the behavior of rock bolts is to conduct pull or push tests, although both methods do not fully replicate field conditions (Cao et al., 2013). Recently, new deep learning methods have been developed to estimate the pull-out strength of anchors (Kovačević et al., 2021; Saleem, 2020). Previous research has indicated that, typically, the bearing capacity of bolts subjected to push tests tends to surpass that of bolts subjected to pull-out tests. However, these variations hinge on factors such as the materials employed and the specific testing methodologies adopted (Aziz et al., 2006). Nevertheless, the push-out approach can provide a good understanding of the behavior of reinforcing elements (Hyett et al., 1992). The current study employed push tests using a true triaxial testing facility at the Rock Mechanics laboratory of the Geotechnical Engineering Centre at the University of Queensland (UQ, Australia). The system can apply up to 850 kN of force on a wide range of cubic samples ranging from

Please cite this article as: Nourizadeh H et al., Failure characterization of fully grouted rock bolts under triaxial testing, Journal of Rock Mechanics and Geotechnical Engineering, https://doi.org/10.1016/j.jrmge.2023.08.013

Table 1
Concrete and grout mix design.

Artificial rock (concrete)								Grout	
Cement (General purpose) (kg/m^3)	Flyash (Grade 1) (kg/m^3)	Fine sand (0 −0.425 mm) (kg/m^3)	Medium sand (0 −4.75 mm) (kg/m^3)	Aggregate (1.18 −9.5 mm) (kg/m^3)	Superplasticizer (Alkali-free Tyro WR 174) (g/m^3)	Hydration control (Tyro HC 270) (g/m^3)	Water to binder (%)	Stratabinder HS (kg/m^3)	Water to binder (%)
345	115	153	1015	450	1	0.5	40	1510	35

50 mm to 200 mm in size. It can also simulate stress conditions at elevated temperatures of up to 100 °C for hydraulic fracturing and coupled thermo-hydro-mechanical testing on rock-like specimens (Fig. 1). To accurately measure the specimen volume change, each of the six actuators of the machine is equipped with three linear variable differential transformers (LVDTs). This LVDT system enables the measurement of deformation and displacement of tested rock bolt samples to calculate the average lateral dilation and bolt slippage (Purser et al., 2021). In this study, cubic specimens were placed on the pressure plates and confined from both the *X* and *Y* directions, as shown in Fig. 1.

For consistent and even loading, it is essential to accurately position the specimens by periodically verifying the testing setup. This involves ensuring that the pressure plates maintain contact with the specimen's surface. Any displacement of the specimen can lead to uneven loading, underscoring the importance of maintaining proper positioning. To create space for bolt slippage, a 12 mm thick steel spacer with a central hole of ϕ30 mm was positioned under the specimen on the *Z*1 side. The pressure plate on the *Z*2 side was then placed on the bolt and pushed at the desired rate. Fig. 1 also illustrates the dimensions of the specimens and the materials used in the experiments.

A series of triaxial push tests was undertaken on a total of 12 specimens. These tests were designed to analyze the response of grouted rock bolts under diverse confinement conditions. The mechanical attributes of both the concrete and the grout were determined through uniaxial compression tests (UCS), with the resultant values documented in Table 2 along with the specifications of the rock bolts. Non-destructive methods can also be applied to obtain the mechanical characteristics of materials (Azarafza et al., 2022).

To accurately analyze the influence of confining stress on the bolts subjected to a push-out force, four varying minor principal stresses (σ_3) with the values of 0, 2.5, 7, and 10 MPa were applied. The intermediate principal stresses (σ_2) were selected so that the ratio of intermediate principal stress to minor principal stress (k) was approximately 1, 1.5, and 2. To assess the validity of the measures, some of the tests were repeated. Table 3 specifies the confining stress program applied to the tests.

The cubic specimen was placed on the pressure plate on the *Z*1 side, and then the pistons were adjusted so that the pressure plates touched the surface of the specimen in the *X*1, *X*2, *Y*1, and *Y*2 directions. An initial load of 3 kN (referred to as seating load) was applied to the specimen in all directions. The loads in the *X* and *Y*

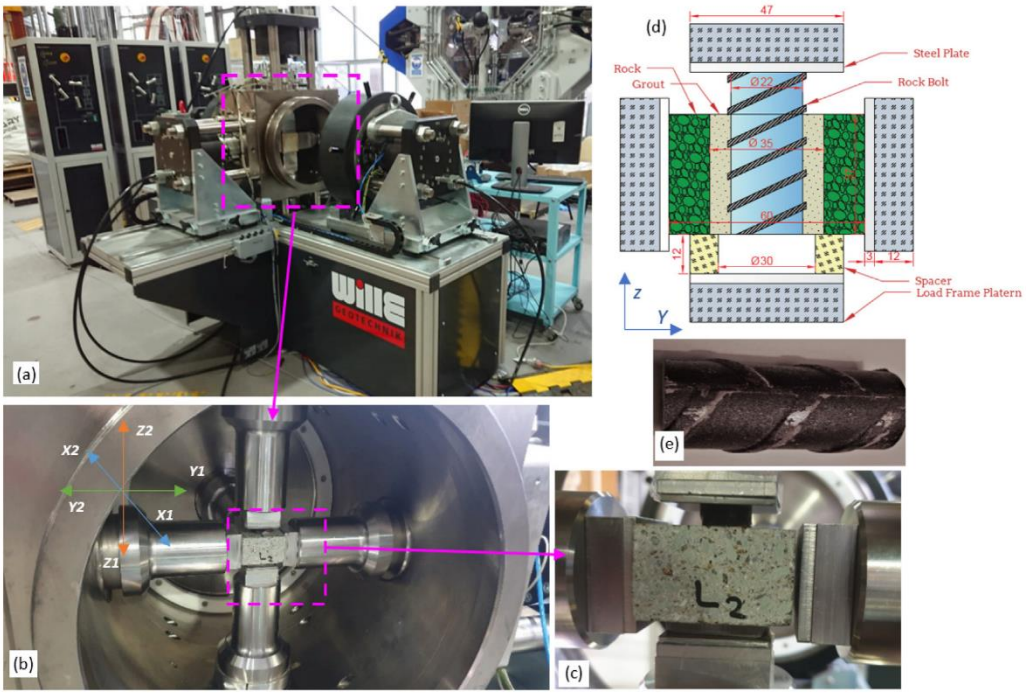

Fig. 1. The experimental setup used in this study, which includes (a) the true triaxial testing facility, (b, c) the arrangement of the chamber, pressure plates, pistons, and cubic specimens, (d) the dimensions of the specimens, and (e) the rock bolts used in the experiments.

Please cite this article as: Nourizadeh H et al., Failure characterization of fully grouted rock bolts under triaxial testing, Journal of Rock Mechanics and Geotechnical Engineering, https://doi.org/10.1016/j.jrmge.2023.08.013

Table 2
Mechanical properties of the materials.

Artificial rock		Bolt						Grout		
E (GPa)	UCS (MPa)	E (GPa)	Nominal diameter (mm)	Nominal area (mm^2)	Yield strength (MPa)	Tensile strength (MPa)	Anchorage length (mm)	E (GPa)	UCS (MPa)	γ
32	55	220	24	370	650	890	37	21.1	96	0.24

Note: E - Elastic modulus; UCS - Uniaxial compressive strength; γ - Poisson's ratio.

Table 3
Confining stress campaigns in the testing programs.

Principal stress	$k = 1$			$k = 1.5$			$k = 2$		
	Case A	Case B	Case C	Case D	Case E	Case F	Case G	Case H	Case I
σ_2 (MPa)	2.5	7	10	4	10	15	5	14	20
σ_3 (MPa)	25	7	10	2.5	7	10	2.5	7	10

directions (hereafter referred to as *X*-Load and *Y*-Load, respectively) were then increased hydrostatically at a rate of 3 kN/min until reaching 5 kN. After that, the loading rate was increased to 15 kN/min until the *X*-pressure reached the value of (σ_3). Subsequently, the load in the *X*-direction was maintained at a constant level, while the *Y*-load was increased until it reached the predetermined value of σ_2. When both the *X*- and *Y*-loads exceeded 5 kN, the pistons in the *Z2* direction began applying load at a rate of 5 kN/min until the bolt debonded. Fig. 2 shows a typical loading program for the testing.

The mechanical behavior of a grouted reinforcing element under axial loading is governed by the bond mechanism. Bond strength refers to the shearing resistance between the reinforcing element and grout. In rock bolting, bond strength can be described as the gripping effect of grout on the deformed bar's encapsulated length (Moosavi et al., 2005). The bond strength is generally considered a function of three components, namely adhesion between the grout and bolt, friction, and mechanical interlocking between bolt ribs. Before system failure (peak bond strength), mechanical interlocking plays a crucial role in the system bond capacity. Interlocking is dependent on the mechanical properties of grout materials, rock mass conditions, level of confining stress, and bolt surface configuration (Cao et al., 2013; Cui et al., 2020).

Fig. 3 illustrates the stress equilibrium for an encapsulated rock bolt at infinitesimal length de_l when subjected to a tensile stress of $\sigma_b + d\sigma_b$. It has been shown that bond strength is a function of confining stress, bolt surface configuration, grout and surrounding media quality. If slip failure at the bolt-grout interface is taken into consideration, the induced bond stress at the bolt-grout interface (f_{bu}) can be expressed as

$$f_{bu} = \frac{D_b}{4}\frac{d\sigma_b}{de_l} \quad (1)$$

where D_b is the effective diameter of the bolt, $d\sigma_b$ is the increment of tensile stress on the bolt, and de_l is the infinitesimal length of the bolt.

Studies have shown that the bond stress distribution along the embedment length of a long-anchored reinforcement is non-uniform and decreases towards the free end (Vlachopoulos et al., 2018). However, the average bonding stress can be effectively used for short embedment specimens. The normalized induced bond stress can be used as a strength criterion to analyze the axial behavior of bolts, especially in cases where different encapsulation lengths or bolt diameters are used. The average bonding stress ($\overline{f_{bu}}$) can be calculated by

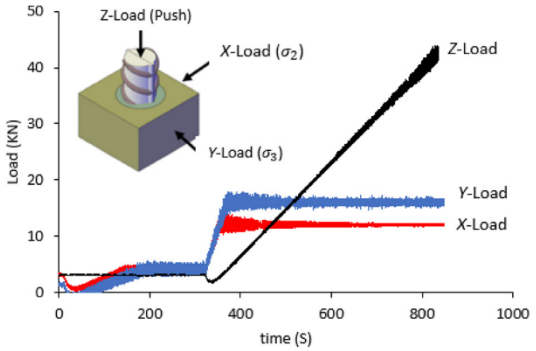

Fig. 2. A typical subjected load program on the specimens.

$$\overline{f_{bu}} = \frac{F_{bu}}{\pi D_b (e_l - s)} \quad (2)$$

where F_{bu} is the peak push load in the *Z2* direction, e_l is the encapsulation length (which is 37 mm in this study), and s is the bolt slip. However, since the bolt encapsulation length during testing is constant, s can be considered zero.

3. Experimental results and discussion

Confining stress stands as a pivotal factor influencing rock bolt behavior. Within underground openings, stresses might not uniformly manifest across all directions, underscoring the significance of scrutinizing rock bolting systems within authentic conditions. Despite this, the impact of deviatoric stress ($\sigma_2 \neq \sigma_3$) on the response of fully-grouted rock bolts has, to the authors' knowledge, largely been overlooked within the existing literature. The experiments reported in this paper were designed and conducted to investigate the behavior of fully-grouted rock bolts under biaxial confining conditions. The testing equipment used in this study the capability to record the necessary data for a comprehensive mechanical investigation, including load and displacement in three mutually perpendicular directions (*X*, *Y*, *Z*) with high accuracy. The outcomes derived from these experiments served as the foundation for the analysis of various aspects, encompassing axial behavior,

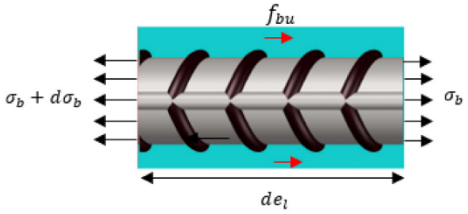

Fig. 3. Stress equilibrium of infinitesimal embedded rock bolt.

Please cite this article as: Nourizadeh H et al., Failure characterization of fully grouted rock bolts under triaxial testing, Journal of Rock Mechanics and Geotechnical Engineering, https://doi.org/10.1016/j.jrmge.2023.08.013

interfacial bond strength, deformation characteristics of the adjacent media, and the mechanism of system failure.

3.1. Push force and bolt slip relationship

The load-displacement relationship is a common approach for analyzing the behavior of fully grouted rock bolts. Various linear, nonlinear, and combined analyses have been presented for evaluating the performance of fully grouted rock bolts (Li and Stillborg, 2000; Ren et al., 2010; Martín et al., 2011; Ma et al., 2013; He et al., 2015; Bahrani and Hadjigeorgiou, 2016; Jahangir et al., 2021; Yue et al., 2022). A typical load-displacement model is shown in Fig. 4, which can be characterized by three distinct stages:

(1) A quasi-linear increase in the curve where the stiffness (the ratio of axial load to displacement) is constant, and the load-displacement response is in an elastic stage.
(2) An ascending curve where the axial load increases with slip until reaching the maximum load value, although the stiffness slightly decreases. It has been reported that debonding of rock bolts starts during the transition from stage 1 to stage 2 (Høien et al., 2021).
(3) A descending curve where the axial load decreases with bolt slip.

The load-slip curves of the tested specimens, which have the same embedment length and materials but different confining conditions, are presented in Fig. 5a-c, corresponding to the tests conducted with principal stress ratios of 1, 1.5, and 2, respectively. The results clearly indicate that the confining stresses have a significant strengthening effect on the samples. It can be observed that the axial load increases as slip increases from the beginning until reaching the peak load, after which it begins to decline. The curves generally consist of three stages, similar to Fig. 4: an initial linear growth, followed by a nonlinear ascending curve, and finally a strain softening stage. However, the increase in confinement stresses results in four primary changes in the resulting load-slip curves. Firstly, the transition from linear to nonlinear behavior occurs at lower slip magnitudes. Secondly, the stiffness in the linear elastic part increases significantly with higher confining stresses. Thirdly, the ultimate bearing capacity is influenced by the level of confinement. Finally, the peak load is attained at larger slip values. The load-slip curve can be classified into two main categories based on the pre-peak load-slip characteristics of the push-out tests, which are used to establish linear-nonlinear transformation models. In the cases where there are zero or low confining stresses (Fig. 5a), the failure mode resembles a brittle failure, exhibiting a distinct peak bond strength accompanied by strain-softening behavior. However, at higher confining stresses, failure exhibits a slight ductility, and the axial slip corresponding to the failure point tends to have higher magnitudes, followed by the occurrence of softening behavior. At $\sigma_2 = \sigma_3 = 0$, the load-slip curve initially shows linear growth until the load reaches 25.4 kN, which corresponds to 91% of the ultimate bearing capacity. This is followed by a nonlinear plastic phase until reaching the ultimate strength, and finally a sharp drop. In the case where $\sigma_2 = \sigma_3 = 2.5$ MPa, the linear elastic section transforms into a nonlinear curve when the load reaches 20.8 kN, equivalent to 72% of the ultimate strength, despite the peak load being only 3.5% higher compared to the case without confinement. As depicted in Fig. 5, the nonlinearity of the load-slip curves expands with an increase in confining stresses. In cases with a higher level of confining stresses (e.g. $\sigma_2 = 15$ MPa, $\sigma_3 = 10$ MPa and $\sigma_2 = 20$ MPa, $\sigma_3 = 10$ MPa), it becomes challenging to distinguish the linear portion. Consequently, the load-slip behavior can be characterized by a progressively nonlinear elastic-plastic response. Yeih et al. (1997) discussed the failure modes for rebars with and without confinement and concluded that confining force affects the peak load and the post-failure mechanism, while the pre-failure behavior is not affected. An experimental study conducted by Moosavi et al. (2005) reported the same statement and showed that the load-displacement curves overlap moderately before yielding points. Thenevin et al. (2017) demonstrated that elevating the confining stress leads to increased stiffness and peak load. However, it is important to note that the overall shape of the load-displacement curve remains unchanged despite these variations. Therefore, the results of the current study demonstrate that, in higher levels of confining stress, nonlinear bond models are more suitable; however, in the lower level of confinement, a combined linear and nonlinear model can be adopted. As opposed to the test without confining stress, the post-failure behavior of the tests with confining stress illustrates a smooth and progressive softening phase. Analyzing the bolt-slip curves also shows that the softening part of the curves becomes flatter in the cases with higher confining stresses (Fig. 5b and c). The main reason for this is the existence of the high level of confinement, and thus, the surrounding materials and grout can resist cracking and dilation. Also, the normal force at the bolt-grout interface causes a secondary interlocking after the main failure, thereby holding the bolt against the push load.

Expectedly, the bond capacity of specimens rises as the confining stresses increase. For instance, in the absence of confinement, the peak push load was measured 27.9 kN, whereas it increased to 28.9 kN, 36.3 kN, and 38.7 kN with uniform confining stresses ($\sigma_2 = \sigma_3$) of 2.5 MPa, 7 MPa, and 10 MPa, respectively. The same trend is observed for tests conducted with k values of 1.5 and 2, where the peak loads increase with the confining stress. However, some differences are visible in the pre- and post-failure phases, as discussed earlier. In the descending part of the load-slip curve, the rate of load decrease becomes slower with increasing confinement, thus the slope of the load-slip curve decreases. The linear approximation and averaging determines the slope of the curves in the post-failure stage to be 4.4, 3.7, 3.1, 2.9, 1.2 and 1.1 kN/mm for the tests conducted with $\sigma_2 = \sigma_3 = 0$ MPa, $\sigma_2 = \sigma_3 = 2.5$ MPa, $\sigma_2 = \sigma_3 = 7$ MPa, $\sigma_2 = 14$ MPa and $\sigma_3 = 7$ MPa, $\sigma_2 = 15$ MPa and $\sigma_3 = 10$ MPa, and $\sigma_2 = 20$ MPa and $\sigma_3 = 10$ MPa, respectively. Lower magnitudes of the slope indicate higher frictional resistance of the system against bolt slip. Thus, it can be concluded that the post-failure strength is improved with confinement. The slip corresponding to the maximum bond strength increases with higher levels of confinement. Conversely, the slope of the descending section of the curves immediately after the peak load decreases as the confinement increases. Therefore, it can be concluded that confining stresses significantly enhance the ductility of the samples. For the specimen without confinement, the

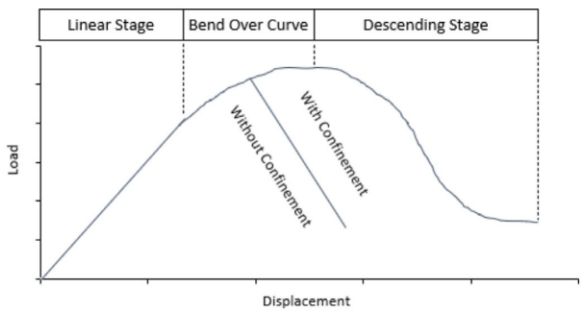

Fig. 4. A typical load-displacement curve for encapsulated rock bolt (with and without confining stress) (after Yeih et al., 1997).

Please cite this article as: Nourizadeh H et al., Failure characterization of fully grouted rock bolts under triaxial testing, Journal of Rock Mechanics and Geotechnical Engineering, https://doi.org/10.1016/j.jrmge.2023.08.013

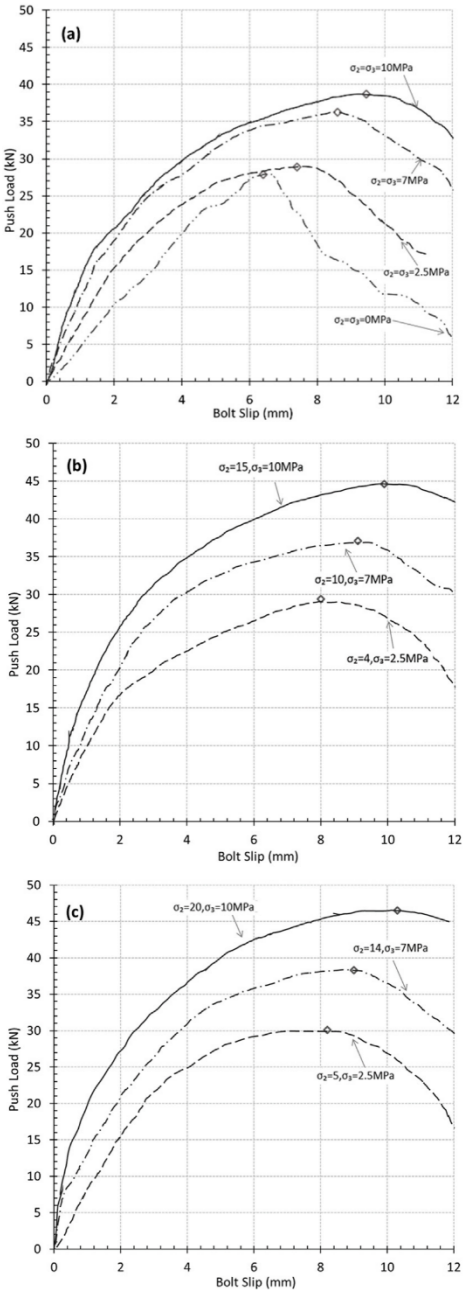

Fig. 5. Load-slip curves obtained from the tests conducted at three different principal stress ratios ($k = \sigma_2/\sigma_3$): (a) $k = 1$, (b) $k = 1.5$, and (c) $k = 2$.

displacement corresponding to the peak load was 6.3 mm, whereas the peak load displacement shifted to the right with an increase in confining stress, reaching 10.3 mm for the specimen subjected to the highest confining stresses ($\sigma_2 = 20$ MPa, $\sigma_3 = 10$ MPa). Table 4 presents the peak loads and corresponding slips for the tested specimens. The fluctuations observed in the ascending phase of the graphs can be attributed to lateral deformation and specimen dilation caused by bolt slip during the push-out process. These fluctuations are consistent with the variations observed in the force-time and displacement-time data recorded by the sensors in the X and Y directions (as shown in Fig. 2), indicating that the sensors on the lateral pistons require some time to adjust the confining stresses to the predefined values. Additionally, localized failure and damage occurring in the area near the loading point may also contribute to these fluctuations.

Stiffness is a crucial parameter for characterizing the load-slip performance of rock bolts subjected to a tensile load (Li et al., 2021). In rock bolting, stiffness is defined as the derivative of the load-slip curve with respect to the slip. Fig. 6 shows the stiffness-displacement curves for the case with $\sigma_2 = \sigma_3 = 0$ MPa and the cases where $k = 2$. The figure indicates that the stiffness (i.e. the slope of the load-displacement curve) for confined specimens decays exponentially before final failure occurs, while the stiffness for the specimen without confining stress increases until 0.5 mm of displacement followed by a gradual decrease until the system fails. Among all specimens, the specimen without confinement ($\sigma_2 = \sigma_3 = 0$) showed the minimum shear stiffness (2.08 kN/mm) at the beginning of the push-out tests. The initial shear stiffness was also calculated as 24.08 kN/mm, 28.07 kN/mm, and 32.51 kN/mm for the tests conducted with $\sigma_2 = 5$ MPa and $\sigma_3 = 2.5$ MPa, $\sigma_2 = 14$ MPa and $\sigma_3 = 7$ MPa, and $\sigma_2 = 20$ MPa and $\sigma_3 = 10$ MPa, respectively. Moreover, it is evident from the results that the stiffness of the confined specimens is significantly higher than that of the unconfined specimen during the initial stages of the testing. However, in certain degrees of displacement, the rigidity of the unconfined test slightly surpasses that of the confined tests. The abrupt decrease in stiffness for the unconfined specimen indicates a brittle ultimate failure, unlike the failure of specimens with confining stresses, which exhibits a semi-ductile behavior. Based on the presented results, it can be concluded that for confined specimens, the ultimate failure can be anticipated when the stiffness reaches approximately 1 kN/mm, regardless of the level of confinement.

3.2. Relationship between confining stress and interfacial peak bond strength

Fig. 7 shows the influence of the intermediate principal stress on the resultant interfacial bond stress of the system as a function of the principal stress ratio (k). As illustrated, the interfacial bond stress ($\overline{f_{bu}}$) calculated using Eq. (2) increases linearly with the intermediate principal stress (σ_2) at all k ratios. However, when σ_2 is kept constant, the bond stress is lower at higher k ratios. Interestingly, it was found that the bond stress in tests with $\sigma_2 = \sigma_3 = 7$ MPa is equal to that of the test with $\sigma_2 = 10$ MPa and $\sigma_3 = 7$ MPa, where ($\overline{f_{bu}}$) is 13.4 MPa. Fig. 7 also demonstrates that the impact of the principal stress ratio on ($\overline{f_{bu}}$) is more significant at higher values of σ_3. For instance, the difference between the bond strengths of points (a) and (b), where $\sigma_3 = 2.5$ MPa, is 0.21 MPa, while this difference increases to 0.65 MPa when σ_3 reaches 10 MPa (bond strength difference between points (c) and (d)). Additionally, it is observed that the trend lines (grey round-dot lines) increase slowly

Table 4
Peak load and corresponding slip for the tests.

Type	Value									
σ_3 (MPa)	0	2.5			7			10		
σ_2 (MPa)	0	2.5	4	5	7	10	14	10	15	20
Peak load (kN)	27.9	28.9	29.4	30.1	36	37.1	38.3	38.7	44.6	46.5
Slip at peak load (mm)	6.3	7.4	8	8.2	8.5	9	9	9.4	9.8	10.2

Please cite this article as: Nourizadeh H et al., Failure characterization of fully grouted rock bolts under triaxial testing, Journal of Rock Mechanics and Geotechnical Engineering, https://doi.org/10.1016/j.jrmge.2023.08.013

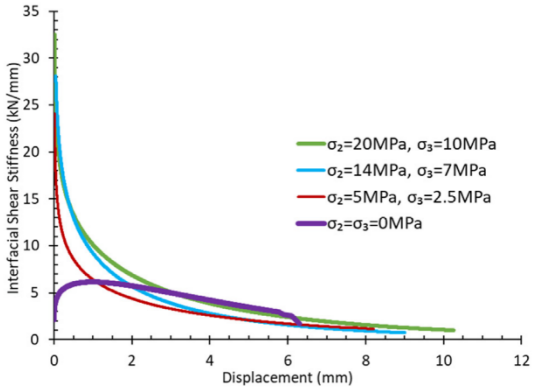

Fig. 6. Interfacial shear stiffness of the tests from beginning to the peak capacity for the test without confining stress and the tests with $k = 2$.

with an increase in σ_2, indicating a lower impact of k at higher levels of σ_2 compared to lower levels. It can be postulated that after a certain value of σ_2 and at the specified level of σ_3, interfacial bond strengths either remain constant or deteriorate. Further research with a higher level of confining stresses is required to effectively evaluate this hypothesis.

According to the test results, the bond strength at the bolt-grout interface increases linearly with σ_2 for a certain ratio of principal stresses (k) (Fig. 5). Similarly, higher values of σ_3 amplify the bearing capacity of the rock bolts. This statement is supported by continuously yielding criteria that have been employed in numerous analytical models. These models showcase that shear stiffness experiences enhancement as the normal force increases (Li et al., 2021). The results for k equal to 1 are consistent with previous studies. Thenevin et al. (2017) concluded that an increase in the confining pressure leads to a linear increase in peak pull-out force, and Moosavi et al. (2005) found an ascending linear relationship between bond capacity and confining pressure. Furthermore, at a specific level of σ_2, the specimen can withstand higher push loads in hydrostatic stress conditions compared to those with k values of 1.5 and 2. The adapted curves for any individual magnitude of σ_3 (grey dotted lines) show a logarithmic trend, as $\overline{f_{bu}}$ initially grows rapidly with σ_2 and then flattens. Based on the results and curves, it is anticipated that at a specific level of σ_2, $\overline{f_{bu}}$ may reach a maximum value followed by a marginal descending trend regardless of σ_3.

3.3. Response of the surrounding medium to bolt slip under biaxial confinement

The axial slip of deformed reinforcing elements generates radial dilation as a response to the induced radial stresses, which is inhibited or restricted by the normal stiffness of the rock mass and the state of confining stresses. The degree of radial displacement of the surrounding media is influenced by the surface geometry of the bolt. Splitting of grout is rare for round bars, highlighting the significance of bolt surface geometry. The dilation of the specimen in the X and Y directions was recorded with high accuracy using several displacement sensors. The results demonstrate a strong correlation between the state of confining stress and the level of dilatation. Deformations normalized to the specimen dimensions in both the X and Y directions can be employed to examine the influence of confining stresses on the lateral deformation of specimens during push-out tests, as described by Eqs. (3) and (4).

$$e_x = d_x/l_x, e_y = d_y/l_y \tag{3}$$

$$e_{xy} = e_x + e_y \tag{4}$$

where e_x and e_y are the principal relative deformations in the σ_2 and σ_3, respectively; d_x and d_y are the sums of deformations recorded by LVDTs in X_1, X_2 and Y_1, Y_2 directions, respectively; and l_x and l_y are the dimensions of the specimens in X and Y directions, respectively.

Fig. 8 shows the incremental relative deformation of the specimens in the X and Y directions (e_x, e_y, e_{xy}) with respect to the push load for the tests with $\sigma_2 = \sigma_3 = 0$ MPa, $\sigma_2 = \sigma_3 = 2.5$ MPa, $\sigma_2 = \sigma_3 = 10$ MPa, and $\sigma_2 = 20$, $\sigma_3 = 10$ MPa, respectively. A positive value indicates shrinkage of the specimen, while a negative value indicates dilation. In the case without confinement, e_x gradually decreases once the push load is applied, while e_y does not experience a visible change until the push load reaches 15 kN. Thereafter, expansion occurs in both directions with the load, and finally, e_x and e_y reach −11.98% and −3.8%, respectively, corresponding to 7.1 mm and 2.3 mm displacement. This magnitude of dilation is enough to disintegrate the specimen, as can be seen in Fig. 9. Failure due to dilation has been indicated numerically as the main failure mode in rock bolting (Shi et al., 2022). The lateral deformation response of the specimens is different when the confining stress is applied. As shown in Fig. 8, firstly, the specimens shrink to a certain level of push load (which increases with the increase of the confining stresses), followed by expansion, and then the lateral

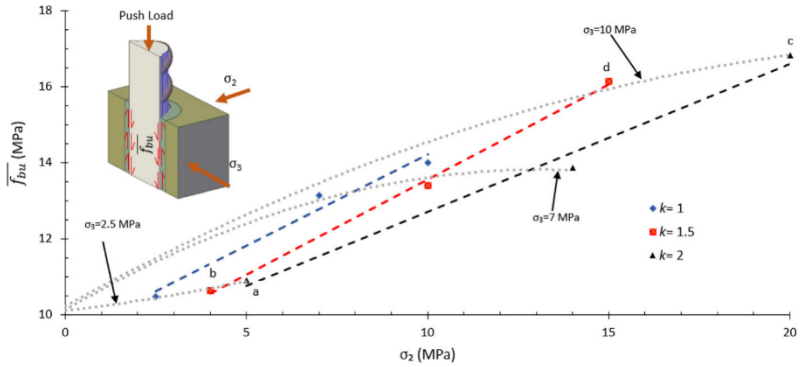

Fig. 7. The effects of confining stresses on the bond strength. Blue, red and black trend dashed lines indicate changes in the interfacial bond stress ($\overline{f_{bu}}$) with respect to σ_2 at the principal stress ratios ($k = \sigma_2/\sigma_3$) equal to 1, 1.5 and 2, respectively. Grey dashed curves represent the variation of $\overline{f_{bu}}$ with σ_2 at $\sigma_3 = 2.5$, 7 and 10 MPa (from bottom to top).

Please cite this article as: Nourizadeh H et al., Failure characterization of fully grouted rock bolts under triaxial testing, Journal of Rock Mechanics and Geotechnical Engineering, https://doi.org/10.1016/j.jrmge.2023.08.013

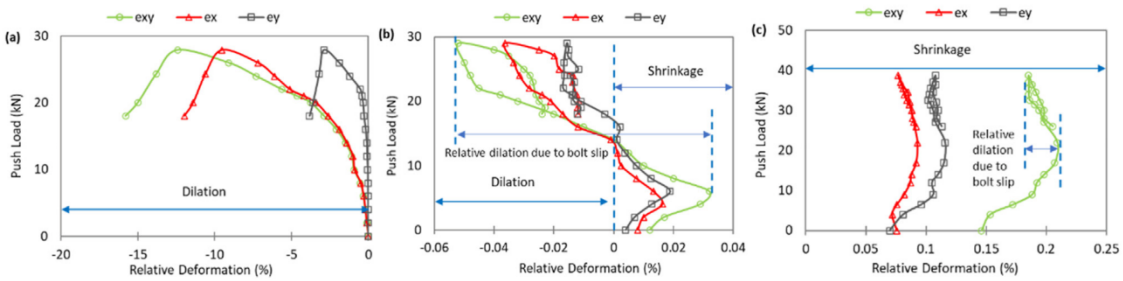

Fig. 8. Deformation of the lateral surfaces of the specimens when (a) $\sigma_2 = \sigma_3 = 0$ MPa, (b) $\sigma_2 = \sigma_3 = 2.5$ MPa, and (c) $\sigma_2 = \sigma_3 = 10$ MPa.

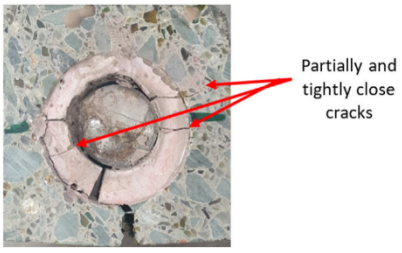

Fig. 9. Fractures in the specimen under no confinement condition.

deformation increases again somewhat. The initial shrinkage is associated with the continuous increase in σ_2 and σ_3, while the expansion of the specimens is due to the dilational force induced by the bolt slip at the bolt-grout interface. It should be noted that the initial relative deformation shown in the graphs is due to the primary confining stress applied before starting push loads. The results demonstrate that in lower levels of confinement, dilation is much higher. For instance, in the test with $\sigma_2 = \sigma_3 = 2.5$ MPa, the slip of the bolt causes a maximum of -0.052% dilation occurring at the peak load, while when the confining stresses increase to $\sigma_2 = \sigma_3 = 10$ MPa, the dilation phase was not detected, and the specimen was always in the shrinkage stage. Nevertheless, the slip of the bolt heals the shrinkage magnitude in both directions somewhat.

As shown in Fig. 8, in all cases, the degree of dilation in the *X* direction is higher than that in the *Y* direction. The reason is associated with the rib configuration along the bolt. As shown in Fig. 10, the bolt is manufactured with two types of ribs: the transversal ribs and the longitudinal ribs. The longitudinal ribs only extend in the *Y* direction and along the bolt with the width and height of 1.5 mm and 0.5 mm, respectively. However, the transversal ribs are designed and manufactured throughout the circumference of the bolt core so that the rib height decreases from 1.5 mm in the *X* direction to 0.5 mm in the *Y* direction (see the cross-section view in Fig. 10). Therefore, once the bolt slips, a higher level of bond stress and normal force is produced in the *X* direction compared to that in the *Y* direction.

The total measured deformation (e_{xy}) against bolt slip for all tests is presented in Fig. 11. Regardless of the level of confining stress, all graphs in Fig. 11 follow a similar pattern which can be divided into four distinct sections. Firstly, there is a sharp rise where there is no pushing load, but σ_2 and σ_3 increase simultaneously. Then, e_{xy} increases with bolt slip, but with less intensity compared to the previous section. This may be due to the fact that the induced dilation starts to confront the created compressive deformation by σ_2 and σ_3. Lateral deformation slightly inclines with bolt slip followed by a rise till testing finishes. In the lowest confining stress ($\sigma_2 = \sigma_3 = 2.5$ MPa), the relative lateral deformation (e_{xy}) initially undergoes a small level of shrinkage and then the specimen deforms outward due to the bolt slip once the bolt displacement reaches 0.55 mm. The lateral deformation of the artificial rock overtakes zero at around 4 mm of bolt displacement and reduces to around -0.05% at 7 mm of displacement, indicating that the unbound stress at the bolt-grout interface increases with bolt slip. The specimen then experienced a gradual shrinkage stage and finally e_{xy} settled at around -0.02% at 12 mm of bolt displacement. From the lateral deformation, it can be concluded that the bolt-grout interface is partially damaged, and consequently, the specimen showed contractional behavior. Similar behavior can be observed in all tests with different intensities of contraction and dilation. For instance, in the case with $\sigma_2 = 20$ MPa, $\sigma_3 = 10$ MPa, e_{xy} initially reached $+0.24\%$ at the desired confining stress, dropped to $+0.212\%$, and then increased to $+0.252\%$. As can be seen, unlike the previous case, the e_{xy} rate at the end of the test ($+0.252\%$) is higher than the one at the starting point ($+0.24\%$) due to the extensive damage at the bolt-grout interface in higher loads. In conclusion, following conclusions from these graphs are drawn:

(1) The results reveal that the degree of dilational deformation due to bolt displacement is significantly higher in lower confining stresses. In most cases, e_{xy} decreases with bolt slip and eventually reaches a point between the starting and minimum values. However, for specimens subjected to $\sigma_2 = 15$ MPa, $\sigma_3 = 10$ MPa and $\sigma_2 = 20$ MPa, $\sigma_3 = 10$ MPa, the contraction at the end of the tests is higher than the contraction degree at the beginning of the tests. This is believed to be due to the wider crush zone at the bolt-grout interface under higher confining stresses.

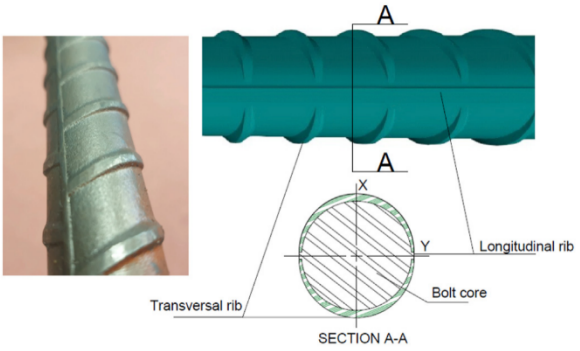

Fig. 10. Surface profile characterization of the rock bolt.

Please cite this article as: Nourizadeh H et al., Failure characterization of fully grouted rock bolts under triaxial testing, Journal of Rock Mechanics and Geotechnical Engineering, https://doi.org/10.1016/j.jrmge.2023.08.013

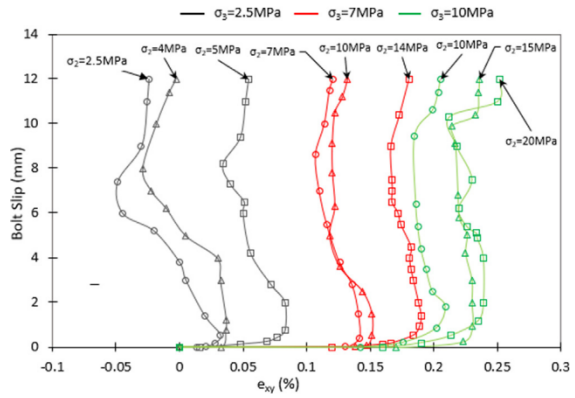

Fig. 11. Relationship between the total lateral deformation (e_{xy}) and bolt slip under varying confining conditions.

(2) In lower levels of confinement, the overall deformation of the specimen changes from contraction to dilatation, whereas in higher levels of confinement, the lateral deformation remains in a contraction state despite the occurrence of dilation to some extent in all cases.
(3) The maximum induced dilational deformation occurs when the bolt displacement reaches 7–10 mm, but this point tends to shift to the right with an increase in confining stresses.

3.4. Failure mechanism

The dominant failure mode in rock bolting systems is identified as the failure of the bolt-grout interface. This failure can occur in three main modes: dilational slip, grout sheared-off, grout shear-crushed, or a combination of these modes (Zhang et al., 2020). Previous studies have confirmed that the surface configuration of the bolt, mechanical properties of the grout, geo-mechanical properties of the surrounding rock mass, and level of confining stress define the failure mode at the bolt-grout interface (Cao et al., 2014; Cui et al., 2020; Zhang et al., 2020). According to the results of this research, the failure mode is intrinsically dependent on the confining stress conditions. Different failure patterns in the grout and surrounding artificial rock were recognized depending on the magnitudes of σ_2, σ_3, and the subjected push load. The confining stress applied to the outer surface of the cubic specimens resists dilation of the system, whereas the internal stress induced by bolt slip and distributed on the bolt-grout interface causes dilational deformation that may lead to radial fractures. The slip of the bolt may lever the fractures apart, causing the grout to react as a series of independent wedges (Hyett et al., 1995). The radial fractures occur where the tensile tangential stress exceeds the tensile strength of the grout and may expand to the surrounding rock. As shown in Fig. 9, where there is zero confinement stress, fractures in the grout and the bottom side of the specimen are fully developed and open, whereas partially and tightly closed fractures are visible on the other sides of the specimen. As the tensile tangential stress is attenuated by the distancing from the bolt-grout interface, it is highly unlikely that fractures occur in the surrounding rock but not in the grout annulus. In cases where the failure mechanism is pure dilational splitting, the surrounding medium is yielded by the slip of the bolt, and the induced inner stress can be exerted due to the expansion of the yielded medium. Fig. 7 illustrates that the shear stress generated along the encapsulation length results from the strain difference between two points on the bolt. In the absence of confining stress, the interlocking between the grout and bolt is the only factor that resists bolt slip, resulting in more uniform induced shear stress along the grouted length and minimum shear stress concentration, leading to dilation of the system instead of shearing the grout. However, as the confining stresses increase, more normal load acts on the bolt-grout interface, causing the induced shear stress near the loading point to become the highest, surpassing the shear strength of the grout. This leads to cutting of the grout asperities instead of creating dilational cracks in the grout and/or surrounding rock. Further loading extends the shear-off phenomenon to the free end section.

Photographs taken immediately after the experiments were carefully analyzed to investigate the potential relationship between testing parameters and failure patterns of the bolting systems. Fig. 12 presents images obtained from the crack detection analysis. During testing, the confining stresses σ_2 and σ_3 were applied on the X and Y directions, respectively. In Fig. 12a, where the external confining stresses in both directions are 2.5 MPa, radial fractures are visible in both the grout and rock, indicating that the system tends to fail under splitting. In the grout, fractures are distributed randomly, while in the rock, fractures propagate in the direction of principal stresses σ_2 and σ_3. When the level of confining stress increases to $\sigma_2 = \sigma_3 = 10$ MPa (Fig. 12d), fractures occur mostly in the grout but with lower density compared to Fig. 12a. In cases where the confining stress condition is not hydrostatic, the fracture mechanism is slightly different. The specimen shown in Fig. 12b had σ_2 and σ_3 set to 10 MPa and 7 MPa, respectively. Radial fractures grew in various directions of the grout, while in the rock, fractures were initiated only in the X direction. This may be due to the fact that 7 MPa stress subjected in the Y direction could not provide enough confinement to prevent dilation of the rock, allowing tensile tangential stress to overcome its mechanical strength. The failure mode of the specimen shown in Fig. 12e, where $\sigma_2 = 15$ MPa and $\sigma_3 = 10$ MPa, is very similar to that of the case shown in Fig. 12b, except that the fractures in the grout are largely in the X direction. This may be associated with an increase in the magnitude of σ_2 to 15 MPa, which limits the weak planes to the X direction. As the principal confining stresses reach 10 MPa and 20 MPa (Fig. 12f), cracks vanish in the surrounding materials. It was noticed that there is a single visible fracture in the artificial rock depicted in Fig. 12d and f, which was likely created by induced tangential stress at the grout-rock interface due to slight movement of the grout cylinder during testing. There might be micro-cracks in all cases; however, observation and image processing were not capable of detecting them. In high-stress confining conditions, Fig. 12f, only a few partial and tightly closed cracks developed in the grout, but this is unlikely to have contributed to the bolt failure. The edges of the specimen shown in Fig. 12e also got chipped, which could be due to higher stress concentration.

Direct observation of the bolt-grout interface after tests revealed that confinement conditions were a key factor dominating the interfacial failure modes. Fig. 13 illustrates the typical failure modes at the bolt-grout interface captured at the end of the push-out tests with different confining conditions. The results were analyzed by considering the type and severity of damage that occurred to the grout asperities. The failure mechanism of systems under push testing changes from pure splitting under zero confinement (Figs. 9 and 13a) to states where failure is a combination of splitting and shear-off, and the role of shear-off failure becomes more prominent when reaching higher levels of confinement. If the confining stress rises further, the failure mode of the system converts to shear-off and shear-crushed modes. From Fig. 13a, it can be observed that the interface damage in zero confining stress condition is minor, due to the fact that the failure mode of the bolt-grout interface was

Please cite this article as: Nourizadeh H et al., Failure characterization of fully grouted rock bolts under triaxial testing, Journal of Rock Mechanics and Geotechnical Engineering, https://doi.org/10.1016/j.jrmge.2023.08.013

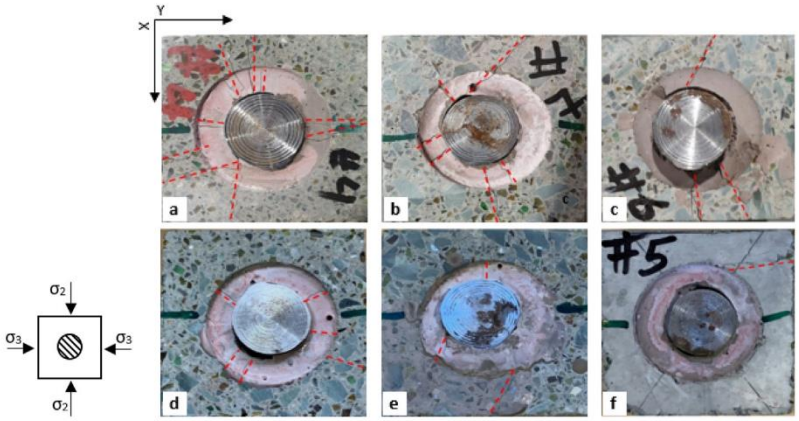

Fig. 12. Initiated and propagated fractures on specimens under various confinement conditions: (a) $\sigma_2 = \sigma_3 = 2.5$ MPa; (b) $\sigma_2 = 10$ MPa, $\sigma_3 = 7$ MPa; (c) $\sigma_2 = 14$ MPa, $\sigma_3 = 7$ MPa; (d) $\sigma_2 = \sigma_3 = 10$ MPa; (e) $\sigma_2 = 15$ MPa, $\sigma_3 = 10$ MPa; and (f) $\sigma_2 = 20$ MPa, $\sigma_3 = 10$ MPa.

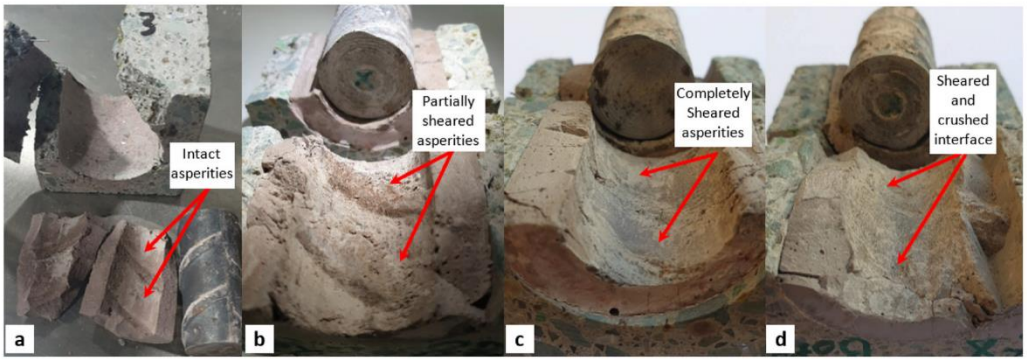

Fig. 13. Failure modes at the bolt-grout interface under different confining stresses: (a) Unconfined ($\sigma_2 = \sigma_3 = 0$ MPa); (b) $\sigma_2 = \sigma_3 = 2.5$ MPa; (c) $\sigma_2 = 10$ MPa, $\sigma_3 = 10$ MPa; and (d) $\sigma_2 = 20$ MPa, $\sigma_3 = 10$ MPa.

dilational slip failure and the specimen split radially. Thus, the grout asperities remained mostly intact and undamaged. Fig. 13b displays a combination of dilational failure and partially shear-off failure that occurred in the test where $\sigma_2 = \sigma_3 = 2.5$ MPa. In this case, the dilation of the specimen was not big enough to allow the ribs to completely slide over the grout asperities. Likewise, the confining force was also not large enough to make ribs completely cut off the grout asperities. Thus, grout asperities were compressed, flattened, and cut off concurrently to some extent. This interface failure mode was observed in cases A-D. When the confining stress increased to $\sigma_2 = 10$ MPa and $\sigma_3 = 10$ MPa, there was purportedly enough force to avoid ribs overriding. Thus, continuous push force led to a clean cut off the grout asperities (Fig. 13c). In this case, there are no signs of asperities left at the interface. With further increase in the confining stress to $\sigma_2 = 20$ MPa and $\sigma_3 = 10$ MPa, the damage became even deeper. In addition to the grout asperities, a layer of the grout was crushed, indicating a shear-crush failure mode (Fig. 13d). A noticeable degree of smashing was also observed in the vicinity of the rock bolt in cases D-F (refer to Table 3), similar to the statement shown in Fig. 13d, demonstrating a robust presence of shear-off and shear-crushed failure modes.

3.5. Limitation of this study

The result of this study indicates that the non-uniform confining stresses significantly affect the axial behavior of fully grouted rock bolts. However, some limitations in practice shall still be noted and studied further. Observations revealed that specimens were partially sensitive to confining load changes resulting in difficulties in analyzing the data. This could be because of the size of specimens which were small due to the limitation of the testing equipment. Nevertheless, the properties of the materials used in the study were representative of the common engineering materials. In addition, the effects of sample size, sample strength and encapsulation length on the rock and rock bolt behaviors have been reported in previous research studies. Accordingly, it is recommended to carry out further research utilizing different arrangements including encapsulation length, specimen size, surrounding media and grout strength and other confining stress regimes. Additionally, while the push-out test has been widely utilized as an effective method for examining the axial behavior of rock bolts, it is advisable to perform a pull-out test under triaxial conditions.

Please cite this article as: Nourizadeh H et al., Failure characterization of fully grouted rock bolts under triaxial testing, Journal of Rock Mechanics and Geotechnical Engineering, https://doi.org/10.1016/j.jrmge.2023.08.013

4. Conclusions

Rock bolts installed in underground excavations are typically exposed to complex confining loads in which the magnitudes of the principal stresses may vary. In this study, a true triaxial testing system was utilized to investigate the response of rock bolting systems to various biaxial confining conditions. The following conclusions are drawn from this investigation:

(1) The ultimate bearing capacity of grouted rock bolts depends on the confining stresses. Increasing the principal stresses to 2.5 MPa in both X and Y directions does not significantly enhance the bearing capacity. In this case, the increase in bearing capacity is only 3.5% compared to that with $\sigma_2 = \sigma_3 = 0$. However, when the principal stresses are raised to $\sigma_2 = \sigma_3 = 10$ MPa and $\sigma_2 = 20$ MPa and $\sigma_3 = 10$ MPa, a 38.7% and 66.6% increase in the peak load, respectively, is observed.

(2) The load-displacement curves indicate that the confinement condition has a significant effect on the behavior of system. A nearly linear relationship between load and displacement for the unconfined specimen was observed, while at lower levels of confinement, the load increased first linearly and then exponentially with displacement. In cases where the confining stresses increased to $\sigma_2 = 15$ MPa, $\sigma_3 = 10$ MPa and $\sigma_2 = 20$ MPa, $\sigma_3 = 10$ MPa, the load-slip curve became nonlinear from the start of the test. Considering the interfacial stiffness at the bolt-grout interface, stiffness decreased slightly until a displacement of 0.5 mm and then gradually decreased until failure occurred. In contrast, the initial stiffness of the confined specimens was dependent on the level of confining stress, but regardless of the confining level, it tended to decrease exponentially until failure occurred.

(3) A linear relationship can be observed between σ_2 and $\overline{f_{bu}}$ regardless of the rate of k. It was also noted that at a certain level of σ_3, the effect of σ_2 on τ_i gradually decreases. It is anticipated that at a particular level of σ_2, $\overline{f_{bu}}$ may not increase any further. It is also revealed that the effects of principal stress ratio on $\overline{f_{bu}}$ are more significant at higher values of σ_3.

(4) The relative lateral deformation curves of the specimens indicate that, for all cases, there are three discrete stages. The first stage involves shrinkage when confining stress is applied to the specimen, followed by a dilational stage when the bolt moves. The dilation rate decreases as the bolt slip reaches around 7 mm of displacement. After this point, the specimens tend to shrink again until the end of the test. The magnitude of confining stress dominates the shrinkage and dilational behavior.

(5) It was observed that at lower confinements, specimens tended to fail via splitting, while at higher loads, the failure mechanism changes to pure interfacial shear-off and shear-crushed. Radial fractures propagated in both the annulus area and artificial rock. However, in cases with medium levels of confinement, fractures only appeared in the grout zone. At higher levels of confining stress, no visible fracturing occurred.

Declaration of competing interest

The authors declare that they have no known competing financial interests or personal relationships that could have appeared to influence the work reported in this paper.

Acknowledgment

This work was financially supported by the School of Engineering, the University of Southern Queensland. The in-kind support from Minova Australia, in particular Mr. Robert Hawker, is greatly acknowledged.

References

Azarafza, M., Hajialilue Bonab, M., Derakhshani, R., 2022. A deep learning method for the prediction of the index mechanical properties and strength parameters of marlstone. Materials 15, 6899.
Aziz, N., Craig, P., Mirzaghorbanali, A., Nemcik, J., 2016. Factors influencing the quality of encapsulation in rock bolting. Rock Mech. Rock Eng. 49, 3189–3203.
Aziz, N., Jalalifar, H., Concalyes, J., 2006. Bolt surface configurations and load transfer mechanism. In: Aziz, Naj, Kininmonth, Bob (Eds.), Proceedings of the 2006 Coal Operators' Conference, Mining Engineering. University of Wollongong, Wollongong Australia, pp. 236–244.
Aziz, N., Webb, B., 2003. Study of load transfer capacity of bolts using short encapsulation push test. In: Aziz, Naj, Kininmonth, Bob (Eds.), Proceedings of the 2003 Coal Operators' Conference, Mining Engineering. University of Wollongong, Wollongong, Australia, pp. 72–80.
Bahrani, N., Hadjigeorgiou, J., 2016. Explicit reinforcement models for fully-grouted rebar rock bolts. J. Rock Mech. Geotech. Eng. 9, 267–280.
Blanco, L., Tijani, M., Hadj-hassen, F., Noiret, A., 2013. Assessment of the bolt-grout interface behaviour of fully grouted rockbolts from laboratory experiments under axial loads. Int. J. Rock Mech. Min. Sci. 63, 50–61.
Cao, C., Ren, T., Cook, C., 2013. Calculation of the effect of Poisson's ratio in laboratory push and pull testing of resin-encapsulated bolts. Int. J. Rock Mech. Min. Sci. 64, 175–180.
Cao, C., Ren, T., Cook, C., Cao, Y., 2014. Analytical approach in optimising selection of rebar bolts in preventing rock bolting failure. Int. J. Rock Mech. Min. Sci. 72, 16–25.
Chen, J., He, F., Zhang, S., 2020. A study of the load transfer behavior of fully grouted rock bolts with analytical modelling. Int. J. Min. Sci. Technol. 30, 105–109.
Chen, Y., 2014. Experimental study and stress analysis of rock bolt anchorage performance. J. Rock Mech. Geotech. Eng. 6, 428–437.
Cui, G., Zhang, C., Pan, Y., Deng, L., Zhou, H., 2020. Laboratory investigation into effect of bolt profiles on shear behaviors of bolt-grout interface under constant normal stiffness (CNS) conditions. J. Rock Mech. Geotech. Eng. 12, 1234–1248.
Fabjanczyk, M.W., Tarrant, G.C., 1992. Load transfer mechanisms in reinforcing tendons. In: Proceesding of the 11th International Conference on Ground Control in Mining. Wollongong, Australia, pp. 212–219.
Fu, M., Liu, S., Jia, H., He, D., 2019. Experimental study of an orientation and resin-lifting device for improving the performance of resin-anchored roof bolts. Rock Mech. Rock Eng. 53, 211–231.
Fuller, P., O'Grady, P., 1994. Flexible roof bolts: a new concept for strata control. In: Proceesding of the 11th International Conference on Ground Control in Mining. Wollongong, Australia, pp. 24–34.
Hazrati, M., Parviz, A., Hossein, M., Rad, S., 2020. In situ rock bolt pull tests performance in an underground powerhouse complex : a case study in Sri Lanka. Geotech. Geol. Eng. 38, 2227–2244.
He, L., An, X., Zhao, Z., 2015. Fully grouted rock bolts : an analytical investigation. Rock Mech. Rock Eng. 48, 1181–1196.
He, L., An, X.M., Zhao, X.B., Zhao, Z.Y., Zhao, J., 2017. Development of a unified rock bolt model in discontinuous deformation analysis. Rock Mech. Rock Eng. 51, 827–847.
Ho, D., Bost, M., Rajot, J., 2019. Numerical study of the bolt-grout interface for fully grouted rockbolt under different confining conditions. Int. J. Rock Mech. Min. Sci. 119, 168–179.
Høien, A.H., Li, C.C., Zhang, N., 2021. Pull-out and critical embedment length of grouted rebar rock bolts-mechanisms when approaching and reaching the ultimate load. Rock Mech. Rock Eng. 54, 1431–147.
Hyett, A.J., Bawden, W.F., Macsporran, G.R., Moosavi, M., 1995. A constitutive law for bond failure of fully-grouted cable bolts using a modified hoek cell. Int. J. Rock Mech. Min. Sci. Geomech. 32, 11–36.
Hyett, A.J., Bawden, W.F., Reichert, R.D., 1992. The effect of rock mass confinement on the bond strength of fully grouted cable bolts. Int. Rock Mech. Min. Sci. Geomech. Abstr. 29, 503–524.
Jahangir, E., Blanco-martín, L., Hadj-hassen, F., Tijani, M., 2021. Development and application of an interface constitutive model for fully grouted rock-bolts and cable-bolts. J. Rock Mech. Geotech. Eng. 13, 811–819.
Kang, H., Yang, J., Gao, F., Li, J., 2020. Experimental study on the mechanical behavior of rock bolts subjected to complex static and dynamic loads. Rock Mech. Rock Eng. 53, 4993–5004.
Kilic, A., Yasar, E., Atis, C.D., 2003. Effect of bar shape on the pull-out capacity of fully-grouted rockbolts. Tunn. Undergr. Space Technol. 18, 1–6.
Kılıc, A., Yasar, E., Celik, A.G., 2002. Effect of grout properties on the pull-out load capacity of fully grouted rock bolt. Tunn. Undergr. Space Technol. 17, 355–362.
Kovačević, M.S., Bačić, M., Gavin, K., 2021. Application of neural networks for the reliability design of a tunnel in karst rock mass. Can. Geotech. J. 58, 455–467.

Please cite this article as: Nourizadeh H et al., Failure characterization of fully grouted rock bolts under triaxial testing, Journal of Rock Mechanics and Geotechnical Engineering, https://doi.org/10.1016/j.jrmge.2023.08.013

Li, C.C., Stillborg, B., 2000. Analytical models for rock bolts. Int. J. Rock Mech. Min. Sci. 36, 1013–1029.
Li, C.C., 2017. Principles of rockbolting design. J. Rock Mech. Geotech. Eng. 9, 396–414.
Li, C.C., Kristjansson, G., Høien, A.H., 2016. Critical embedment length and bond strength of fully encapsulated rebar rockbolts. Tunn. Undergr. Space Technol. 59, 16–23.
Li, C.C., Stjern, G., Myrvang, A., 2014. A review on the performance of conventional and energy-absorbing rockbolts. J. Rock Mech. Geotech. Eng. 6, 315–327.
Li, D., Li, Y., Chen, J., Masoumi, H., 2021. An analytical model for axial performance of rock bolts under constant confining pressure based on continuously yielding criterion. Tunn. Undergr. Space Technol. 113, 103955.
Li, L., Hagan, P.C., Saydam, S., 2019. Hebblewhite, B., Zhang, C., A laboratory study of shear behaviour of rockbolts under dynamic loading based on the drop test using a double shear system. Rock Mech. Rock Eng. 52, 3413–3429.
Liu, S., He, D., Fu, M., 2020. Cfor bolt support in tunnels. Tunn. Undergr. Space Technol. 53, 4993–5004.
Ma, S., Aziz, N., Nemcik, J., Mirzaghorbanali, A., 2017. The effects of installation procedure on bond characteristics of fully grouted rock bolts. Geotech. Test J. 40.
Ma, S., Nemcik, J., Aziz, N., 2013. An analytical model of fully grouted rock bolts subjected to tensile load. Construct. Build. Mater. 49, 519–526.
Martín, L.B., Tijani, M., Hadj-hassen, F., 2011. A new analytical solution to the mechanical behaviour of fully grouted rockbolts subjected to pull-out tests. Construct. Build. Mater. 25, 749–755.
Moosavi, M., Jafari, A., Khosravi, A., 2005. Bond of cement grouted reinforcing bars under constant radial pressure. Cem. Concr. Compos. 27, 103–109.
Nourizadeh, H., Williams, S., Mirzaghorbanali, A., McDougall, K., Aziz, N., Serati, M., 2021. Axial behaviour of rock bolts-part (A) Experimental study. In: Aziz, Naj, Kininmonth, Bob (Eds.), Proceedings of the 2021 Coal Operators' Conference, Mining Engineering. University of Wollongong, Wollongong Australia, pp. 294–302.
Purser, R., El-Amin Mohmoud, M., Serati, M., Chen, Z., 2021. Determining rock elastic parameters using a new true-triaxial-based technique. In: Aziz, Naj, Kininmonth, Bob (Eds.), Proceedings of the 2021 Coal Operators' Conference, Mining Engineering. University of Wollongong, Wollongong Australia, pp. 285–293.
Ren, F.F., Yang, Z.J., Chen, J.F., Chen, W.W., 2010. An analytical analysis of the full-range behaviour of grouted rockbolts based on a tri-linear bond-slip model. Construct. Build. Mater. 24, 361–370.
Salcher, M., Bertuzzi, R., 2018. Results of pull tests of rock bolts and cable bolts in Sydney sandstone and shale. Tunn. Undergr. Space Technol. 74, 60–70.
Saleem, M., 2020. Assessing the load carrying capacity of concrete anchor bolts using non - destructive tests and artificial multilayer neural network. J. Build. Eng. 30, 101260.
Serati, M., Mutaz, E., Williams, D.J., Quintero Olaya, S., Karlovsek, J., Hanžic, L., 2020. Failure Mode of Concrete under Polyaxial Stresses. 54th U.S. Rock Mechs/Geomechanics Symposium, Golden, CO., The United States.
Shi, H., Song, L., Zhang, H., Chen, W., Lin, H., Li, D., 2022. Experimental and numerical studies on progressive debonding of grouted rock bolts. Int. J. Min. Sci. Technol. 32, 63–74.
Thenevin, I., Blanco-martín, L., Hadj-hassen, F., Schleifer, J., Lubosik, Z., Wrana, A., 2017. Laboratory pull-out tests on fully grouted rock bolts and cable bolts : results and lessons learned. J. Rock Mech. Geotech. Eng. 9, 843–855.
Vlachopoulos, N., Cruz, D., Forbes, B., 2018. Utilizing a novel fiber optic technology to capture the axial responses of fully grouted rock bolts. J. Rock Mech. Geotech. Eng. 10, 222–235.
Yazici, S., Kaiser, P.K., 1992. Bond strength of grouted cable bolts. Int. J. Rock Mech. Min. Sci. Geomech. Abstr. 29, 279–292.
Yeih, W., Huang, R., Chang, J.J., Yang, C.C., 1997. A pullout test for determining interface properties between rebar and concrete. Adv. Cement Base Mater. 5, 57–65.
Yokota, Y., Zhao, Z., Nie, W., Date, K., Iwano, K., Okada, Y., 2019. Experimental and numerical study on the interface behaviour between the rock bolt and bond. Material. Rock Mech. Rock Eng. 52, 869–879.
Yu, S., Zhu, W., Niu, L., Zhou, S., Kang, P., 2019. Experimental and numerical analysis of fully grouted long rockbolt load-transfer behavior. Tunn. Undergr. Space Technol. 85, 56–66.
Yue, Z., Li, A., Wang, P., Wang, P., 2022. An analytical analysis for the mechanical performance of fully-grouted rockbolts based on the exponential softening model. Int. J. Min. Sci. Technol. 32, 981–995.
Zhang, C., Cui, G., Chen, X., Zhou, H., Deng, L., 2020. Effects of bolt profile and grout mixture on shearing behaviors of bolt-grout interface. J. Rock Mech. Geotech. Eng. 12, 242–255.

Hadi Nourizadeh holds BEng, MEng, and PhD in Mining and Geotechnical Engineering. Following the completion of his doctoral studies, he embarked on a Postdoctoral Fellowship at the Centre for Future Materials (CFM), University of Southern Queensland. Within the realm of ground support engineering projects, his primary focus has honed in on ground control systems, specifically specializing in rock bolts and cable bolts. Dr. Nourizadeh's research revolves around a deep understanding of the axial and shear transfer mechanisms inherent in reinforcing elements, even under diverse geotechnical and thermal conditions. In addition to studying these transfer mechanisms, he actively explores and develops engineered bonding materials, such as cementitious grouts and polyester resins. The overarching objective is to optimize the performance of these bonding materials, ensuring their efficacy in real-world applications. Dr. Nourizadeh has published over 30 technical papers in leading and high-ranking journals, as well as international conferences. His expertise lies in the specialized fields of coal mining, resource mining, and geotechnical engineering. Prior to his current role, Dr. Nourizadeh served as a Lecturer at Sahand University of Technology from 2011 to 2018.

Please cite this article as: Nourizadeh H et al., Failure characterization of fully grouted rock bolts under triaxial testing, Journal of Rock Mechanics and Geotechnical Engineering, https://doi.org/10.1016/j.jrmge.2023.08.013

4.2. Links and implications

In this chapter, it was observed that the axial behaviour of rock bolts is influenced significantly by confining stresses. Furthermore, the outcomes demonstrated that the performance of rock bolts is influenced differently under triaxial confining stress conditions, which simulate field conditions, in contrast to studies conducted under simplified hydrostatic confining conditions. The implications of this study extend to the enhancement of design and construction practices for rock support systems, ultimately contributing to the achievement of safer and more efficient underground excavations. However, Chapter 4's experimental facilities and equipment have inherent limitations that restrict the investigation of other factors affecting rock bolt behaviour, such as embedment length, the conditions of the surrounding rock mass, and the mechanical properties of the encapsulation medium. These factors are addressed in Chapter 5.

CHAPTER 5: PAPER 3- UNVEILING AXIAL LOAD TRANSFER MECHANISM IN FULLY ENCAPSULATED ROCK BOLTS

5.1. Introduction

The literature reviewed in Chapter 2, as well as Chapters 3 and 4, highlight the impact of various factors on the axial behaviour of rock bolts, specifically addressing embedment length, encapsulation materials, and the characteristics of the surrounding rock mass. While the existing body of literature encompasses numerous experimental, numerical, and mathematical studies dedicated to the axial behaviour of rock bolts, a comprehensive analysis is warranted to fully grasp their performance under the combined influence of these factors across diverse geotechnical conditions. This study presents a comprehensive laboratory study on the pullout performance of fully grouted rock bolts and aims to address the fundamental questions regarding the axial load transfer mechanism of rock bolting. This information can also effectively contribute to assessing and improving the available analytical solutions for rock bolting design. Three types of chemical agents as well as three types of cementitious grouts with and without additives, were used to investigate their mechanical characteristics and influence on the axial behaviour of rock bolts. To determine the effect of surrounding rock mass, three different strengths of concrete ranging from 20-60 MPa were used. Pullout tests were performed on fully instrumented and encapsulated rock bolts installed in prepared concrete cylinders with varying encapsulation lengths. The purpose of the pullout experiments is to evaluate the combined effect of grout properties, surrounding rock quality, and embedment length on bond behaviour. Amongst the mechanical characteristics, the shear modulus of the bonding materials was found to be the most significant factor influencing axial load transfer and the bond stress distribution. The compressive strength of bonding materials, which is commonly used to assess performance, should not be the only factor considered, as shear properties were found more representative. The expansion characteristics of the bonding agents were also found to be effective in improving pullout performance. The study also provides a detailed explanation of how the mechanical properties of host rocks affect the pullout capacity of bolts. Specifically, it states that greater stiffness results in higher pullout strength.

Unveiling Axial Load Transfer Mechanism in Fully Encapsulated Rock Bolts

Hadi Nourizadeh[a,b], Ali Mirzaghorbanali[a,b], Kevin McDougall[c], Hani Mitri[d], Peter Craig[e], , Ashakan Rastegarmanesh[a], Naj Aziz[f]

[a] Centre for Future Materials (CFM), University of Southern Queensland, 4350, Australia
[b] School of Engineering, University of Southern Queensland, 4300, Australia
[c] School of Surveying and Built Environment, University of Southern Queensland, 4350, Australia
[d] Department of Mining and Materials Engineering, McGill University, Montreal, H3A 0E8, Canada
[e] Jennmar Australia Pty Ltd, Sydney, Australia
[f] School of Civil, Mining & Environmental Engineering, University of Wollongong, NSW, 2500, Australia

Abstract

Determining the axial load transfer mechanism of rock bolts under various conditions is paramount for ensuring efficient reinforcement in rock structures, advancing our understanding of rock support and ability to design robust engineering solutions. This paper presents the results of an experimental study aimed at investigating the factors affecting axial load transfer mechanisms in fully encapsulated rock bolts including embedment length, mechanical characteristics of bonding materials, and host rock conditions. The results show that increasing the embedment length improves the pullout capacity, but only up to a critical length, beyond which the ultimate strength and bond stress distribution remain constant. Amongst the mechanical characteristics, shear modulus of the bonding materials was found the most significant factor influencing axial load transfer and the bond stress distribution. Compressive strength of bonding materials, which is commonly used to assess performance, should not be the only factor considered, as shear properties were found more representative. The expansion characteristics of the bonding agents were also found to be effective in improving pullout performance. The study also provides a detailed explanation of how the mechanical properties of host rocks affect the pullout capacity of bolts. Specifically, it states that greater stiffness result in higher pullout strength.

Key words: Rock bolts, bonding materials, pullout tests, bond stress distribution, anchoring grouts and resins.

1. Introduction:

Rock reinforcement is a common approach used in tunnels, underground structures, underground excavations to stabilise and enhance the capacity of the rock mass (Rastegarmanesh et al., 2023, 2022). This method comprises a wide range of materials and techniques, among which rock bolting is one of the most effective and economical (Grasselli, 2005). Rock bolts vary in terms of design and material, but the fully grouted rock bolt is the most widely used in practice (Høien et al., 2021; Nourizadeh et al., 2021). Once a rock bolt is installed in a borehole and grouted, it interacts with the grouting materials and the surrounding rock mass as soon as deformations occur in the rock mass. Due to displacements in the rock mass, the load is transferred from the unstable rock to the grouting materials and then to the bolt and subsequently to the intact rocks. This complex interaction restrains rock movement along a discontinuity and controls rock deformation along the grouted length. When a grouted bolt is subjected to a tensile force, the induced axial stress in the rod is distributed across the bolt-grout interface, the grout, the grout-rock interface, and the rock. The load is transferred and redistributed between the bolt and the host rock by bond (shear) resistance in the grout resulting from adhesion and mechanical interlocking between the bolt-grout and the grout-rock (Signer, 1990). The uneven surfaces of the bolt and drill hole provide irregular contacts at the bolt-grout and grout-rock interfaces. When the bolt is subjected to a load, stress concentration occurs at these asperities and irregularities, and the bond strength comes into play in the form of interlocking. Various types of failure can occur in response to axial bolt loads, and the type, magnitude, and direction of the distributed stress, along with the material properties of the components, dictate the main failure mode of the system. The encapsulation length basically determines whether failure occurs in the bolt or in another component. If the encapsulation length is sufficient to transfer all the load, then the bolt itself will fail once the applied load exceeds the ultimate capacity of the bolt. Alternatively, if the encapsulation length is insufficient, then localised failure takes place where the induced stresses exceed the material strength (either grout or rock). In the cross-sectional view, analytical solutions indicate that the induced bond stress is maximum at the bolt-grout interface and decreases exponentially with distance from the interface (Tepfers, 1979). Therefore, it is reasonable to assume that if the surrounding rock is relatively strong and bonding at the grout-rock interface is sufficient to withstand localised stresses, then failure occurs at the bolt-grout interface. This

failure mode has been often reported as the main failure in the literature, although fractures, partial failure, and deformation in other parts have been observed to occur simultaneously. When debonding at the bolt-grout interface occurs, the deformation of the other parts can usually be neglected (Antino et al., 2016). In this case, the axial behaviour of the rock bolt can be effectively studied by examining the stress distribution along the bolt-grout interface. Pullout tests are frequently employed to assess the axial behaviour and anchorage capacity of grouted rock bolts. However, non-destructive testing techniques are also utilised for the same purpose (Wu et al., 2019). Studies have shown that the evolution of stresses along the encapsulation length is non-uniform, and that the stresses decrease with distance from the loading point. Initially, the peak bond stress is captured near the loading end, but it decreases once debonding occurs and shifts incrementally towards the free end Farmer, (1975) investigated the axial behaviour of fully grouted rock bolts and developed a theoretical model showing that the bond stress attenuates exponentially from the loading point to the far end of the bolt. The proposed theory was comparable to experimental results at lower anchor loads. Li and Stillborg, (2000) introduced a bond model for fully grouted rock bolts that illustrates how the bond stress develops from the loading end to the free end. The proposed model consists of four main parts, including a fully decoupled part where the bond stress is zero, a partially decoupled part with constant residual bond strength, a linear softening part which reaches the peak strength, and finally a compatible deformation part where the bond stress decreases exponentially towards the free end of the bolt. The latter stage can be matched with the elastic stage introduced in other models. Benmokrane et al., (1995) assumed an average distribution of bond stress along the anchored length and expressed a trilinear debonding model between the induced bond stress and global slip based on experimental investigations. Afterwards, numerous trilinear bond-slip models were proposed, including those by. Li et al., (2021), Martín et al., (2011), Cai et al., (2004), Ren et al., (2010), Chen et al., (2020), Ma et al. (Ma et al., 2013), Chen and Li, (2022) and Zhou et al., (2010). Instrumented rock bolts using electric sensors, such as resistive strain gauges and fiber optics, have also been effectively used to measure axial strain along the anchored length to estimate the load. This information can be used to quantify the induced bond stress along the encapsulation length (Chen et al., 2020; Farmer, 1975; Freeman, 1978; Huang et al., 2013; Singer et al., 1997; Teymen and Kılıç, 2018; Vlachopoulos et al., 2018; Zhang et al., 2006). Several factors,

including rock bolt geometry, bolt surface configuration, mechanical characteristics of the bolt, grout, and host rock, boundary conditions, anchorage length, drilling quality and drillhole diameter, annulus thickness, and installation and grouting quality affect the axial behaviour and bearing capacity of grouted bolts. Some of these factors can be engineered to improve the system performance. Thus, a proper understanding of the combined effects of these factors is essential for practical rock bolting design.

Figure 1 illustrates the possible load-slip relationships in the pull-out process of grouted rock bolts. At the critical encapsulation length, the anchorage strength of the unit exceeds the yield strength of the bolt. If the encapsulation length is much longer than the critical encapsulation length, the bolt failure occurs in the shank (Wee et al., 2016) (curve A in Figure 1). If the encapsulation length is slightly over critical encapsulation length bolt debonding occurs, however, bolt undergoes a plastic deformation (curves B and C in Figure1). If the encapsulation is shorter than the critical encapsulation length, debonding of the bolt will occur before reaching the peak capacity (curve D in Figure 1). Ren et al., (2010) proposed a closed-form analytical solution for bolts with a critical encapsulation length showing snapback form (curve C in Figure 1). This model includes five stages: elastic stage (i), elastic-softening stage (ii), elastic-softening-debonding stage (iii), softening-debonding stage (iv), and debonding stage (v). The model exhibits a snapback form of the load-slip relation, although the authors could not capture the snapback phenomenon in the experimental tests. The absence of sufficient radial stiffness may lead to splitting failure (curve E in Figure 1).

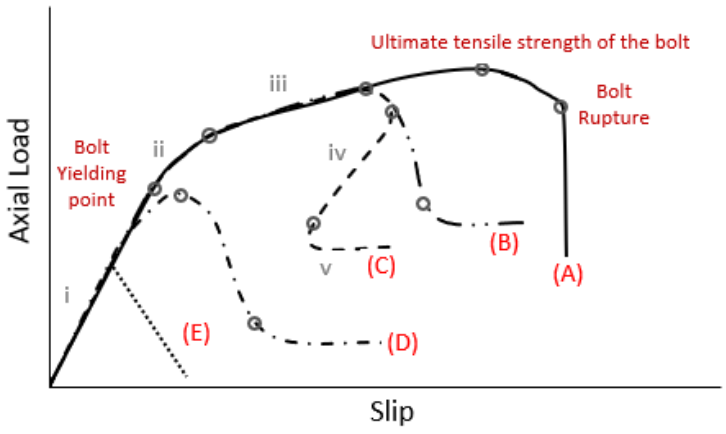

Figure 1. Potential load-slip relations for fully grouted rock bolts (adopted from (Li et al., 2016; Ren et al., 2010; Zou et al., 2020)).

Rock mass conditions play a vital role in the failure mode of rock bolting systems. The high quality of the host rock not only assures that the failure will not occur in the rock, but it may also enhance the performance of the system (Moosavi et al., 2005). The axial slip of deformed bars generates radial dilation, which is inhibited or restricted by the normal stiffness of the rock mass. Hyett et al., (1992) indicates that in higher radial stiffness, dilation is suppressed, and shear-off failure occurs at the bolt-grout contact, leading to greater load-bearing capacity, whereas in lower radial stiffness, the propagation of radial cracks through the grout annulus is predictable, resulting in a decrease in radial stress at the bolt-grout interface and thus an instantaneous reduction in the bond resistance to pull-out. Yilmaz et al., (2013) conducted pullout tests on chemical anchors embedded in weak concrete, indicating the positive contribution of the concrete strength to the bond strength. On the contrary, Cao et al., (2014) reported the insignificance of the host rock uniaxial compressive strength (UCS) ranging from 30-136 MPa on the pullout capacity of rock bolts.

It has been shown that the mechanical properties of the bonding agent have a significant impact on the response of rock bolts. For example, Yokota et al., (2019) found that the interfacial shear stiffness is slightly lower for specimens prepared with low-strength mortar. Teymen and Kılıç, (2018) concluded that the bond strength of fully grouted rock bolts increases logarithmically with an increase in the shear strength of the grout. However, in the experimental studies conducted by Benmokrane et al., (2000) and McKay and McKay and Erki, (1993), a clear relation between grout strength and anchor performance was not observed. Benmokrane et al., (1995) indicated that an increase in the modulus of elasticity of grouts can result in higher radial stiffness at the bolt-grout interface and, therefore, improve bond strength. Nourizadeh et al., (2023) found that the shear properties of the bonding agent are the primary factor that significantly impacts the performance of fully encapsulated rock bolts.

The literature includes many experimental, numerical, and mathematical studies on the axial behaviour of rock bolts, however, there is a need to comprehensively analyse the performance of fully grouted rock bolts under different geotechnical conditions. This study presents a comprehensive laboratory study on the pullout performance of fully grouted rock bolts and aims to address the four fundamental questions regarding the axial load transfer mechanism of rock bolting. They are (1) What is the effect of embedment length on the distribution of bond stress and failure of the system? (2) What is the effect of bonding material type on the bond

stress distribution? (3) What is the relation between peak bond resistance and bonding material type? and (4) What is the effect of host rock properties on the bond stress distribution and failure mechanism of the bolts? The results should provide useful insights for the design and selection of rock bolts for various engineering applications. This information can also effectively contribute to assessing and improving the available analytical solutions for rock bolting design. Three types of chemical agents as well as three types of cementitious grouts with and without additives were used to investigate their mechanical characteristics and influence on the axial behaviour of rock bolts. To determine the effect of surrounding rock mass, three different strengths of concrete ranging from 20-60 MPa were used. Pullout tests were performed on fully instrumented and encapsulated rock bolts installed in prepared concrete cylinders with varying encapsulation lengths. The purpose of the pullout experiments is to evaluate the combined effect of grout properties, surrounding rock quality, and embedment length on bond behaviour. The evolution of the interfacial bond stress along the encapsulation length was also determined by measuring and recording strain values on the mounted strain gauges. Section 2 presents an overview of the materials employed, including their mechanical characteristics. Section 3 delves into the detailed results and analysis of the pullout tests. Lastly, Section 4 succinctly outlines the main findings, providing a concise summary.

2. Experimental Campaign

To perform a thorough evaluation of the axial behaviour of rock bolts across various geotechnical conditions and applications, a selection of materials was made. These materials encompassed concrete as the surrounding medium, along with encapsulation agents exhibiting diverse applications and mechanical characteristics. This approach ensured a comprehensive understanding of the performance and efficacy of rock bolts in different scenarios. The chosen materials were carefully considered to ensure accurate and reliable assessments.

2.1. Materials

Firstly, steel rock bolts were equipped with resistive strain gauges along the bolt. The rock bolt is first inserted in a hole that is created in the centre of the concrete cylinder. The hole is then filled with one of five different types of bonding agents according to the experimental plan. Concrete batches were prepared with three different mix designs to achieve the desired properties.

2.1.1. Surrounding media

Three different mixtures of concrete were formulated and designed to achieve M20, M40, and M60 concrete properties based on AS-1379. The prepared concrete batches were cast in steel pipes AS/AZS 1163 with an outer diameter of Ø165.1 mm and a wall thickness of 5.4 mm to mimic the rock mass formation with relatively soft to hard strengths. The radial stiffness of the pipe used in this study is sufficient to simulate the infinity and stiffness of the desired surrounding rocks (Cao et al., 2016). It is recommended to use thicker walls as the strength of the concrete increases, however, in this study, we aimed to purely evaluate the effect of concrete strength itself, so using steel tubes with different geometry was deemed unnecessary. Table 1 presents the composition of the concrete mix designs used.

Table 1 . Summary of concrete mixtures used in the experimental program[a].

Batch	Portland Cement[b] (Kg)	Aggregate[c] (Kg)	Sand (Kg)	Flyash (Kg)	GGBS[d] (Kg)	Silica Fumes (Kg)	Superplastisizer[e] (ml)	Shrinkage Reducing agent[f] (ml)	Water (lit)	W/binder (%)
M20	261	1081	809	0	65	0	0	1000	168	51.4
M40	323	1183	597	138	0	0	4584	4250	168	36.4
M60	472	987	654	87.3	0	24.3	11647	10500	168	28.7

[a]Numbers are for 1 m^3 of wet concrete
[b]General Purpose Portland cement
[c]Nominal maximum size of the aggregate is 10 mm
[d]Grand Granulate Blast-Furnace Slag
[e]Sika® ViscoCrete 10
[f]Sika® Control Plus

Cylindrical samples were prepared to determine the mechanical properties of the concrete. The specimens were prepared and cured according to ASTM C192 , ASTM C39, and ASTM C469 standards. Two sets of perpendicular 30 mm resistive strain gauges were mounted on two diametrically opposite sides and in the middle of the cylindrical sample with (200 mm (H)×100 mm (D)) to determine the modulus of elasticity and Poisson's ratio. Figures 2 and 3 illustrate the mechanical characteristics of the concrete grades used. The average compressive strength of the concrete was determined to be 22.8, 42.5, and 63.3 MPa, representing weak, medium, and hard rocks, respectively. The elastic modulus of the specimens was measured to be between 31.2-41.7 GPa, which is proportional with the compressive strength. However, no clear relation was found between Poisson's ratio and other properties. Concrete cylinders were cast in five different lengths namely 100, 150, 200, 300, and 400 mm, which correspond to the encapsulation length of the bolts. Prior to casting the concrete, a 28 mm PVC tube was centrally placed in the mould using 3D printed special caps to create the hole. A flexible polyvinyl tube with a 4 mm diameter was

wound around the central PVC tube to create a rifled borehole and to mimic the field drilling condition (Figure 4). To ensure a uniform interfacial shear stress throughout the encapsulation length, the rifling was designed with a pitch of zero.

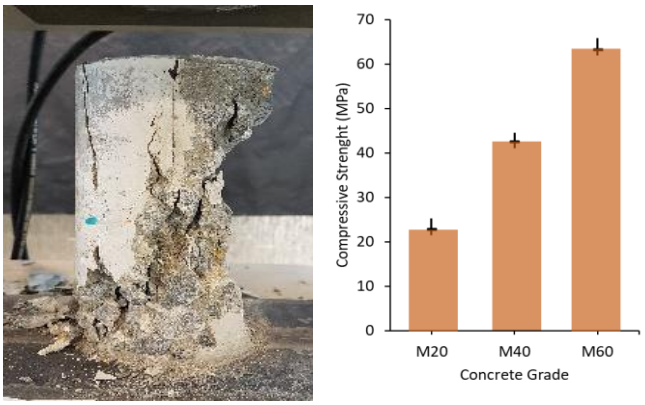

Figure 2. Strength characteristics of concrete grades used as host medium.

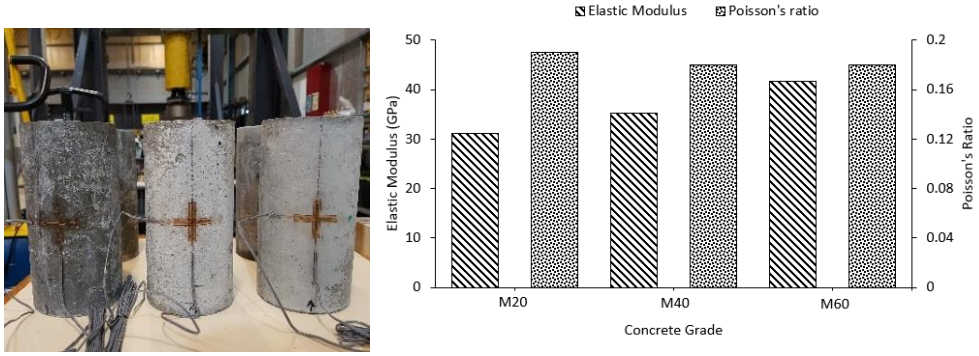

Figure 3. Elastic modulus and Poisson's ratio of concrete grades used as host medium.

Figure 4. Concrete casting and rifling the holes; (a) revolving flexible tube around the central PVC pipe for rifling purposes, (b) 3D printed cap for centralising the central pipe, (c) concrete casting in the steel pipes with the central hole, and (d) rifled holes obtained after concrete curing.

2.1.2. Bonding materials

Five types of bonding agents were used in this study to encapsulate the rock bolts, consisting of two cement-based grouts, hereafter referred to as G1 and G2, and three types of two-component polyester resins, hereafter referred to as R1, R2, and R3. The aim was to comprehensively reveal the effectiveness of bonding materials with a wide range of properties. G1 is a plain grout with a water-grout (w/g) ratio of 0.25, while G2 is an expansive grout made by adding 1% of an expanding agent, Sika® Quellmittel 1, to G1 grout in the laboratory with a w/g ratio of 0.25. R1, R2, and R3 are specifically synthesised for rock bolting and are based on polyester-based resins diluted with styrene monomer and filled with $CaCO_3$ as the insert fillers. Resins R1 and R2 were catalysed using an oil-based catalyst (C1) at a concentration of 8% weight per weight of the total product (%w/w). On the other hand, R3 was activated using a water-based catalyst (C2) at a ratio of 20% w/w. Both catalysts contain the same $CaCO_3$ fillers, but the proportion of benzoyl peroxide is different.

Mixing of the grouts and resins was performed using a laboratory scale mixer according to the recommended mixing time and mixing speed by the supplier in a temperature-controlled system set to 20°C. Immediately after mixing, the bonding material was pumped into the concrete holes for encapsulation. It was also used to make moulds for the determination of the mechanical characteristics. Compressive strength tests were instrumented using resistive strain gauges to measure the lateral and axial strains and consequently calculate the elastic modulus and Poisson's ratio. Table 2 presents a summary of the mechanical tests conducted on the bonding materials used. Figures 5-7 depict the results of mechanical tests of the bonding materials applied in this study. The results indicate that the highest magnitudes of compressive strength were recorded by R1 and R2 at 102.5 and 96.4 MPa, respectively. Among the cementitious grouts, G1 is the strongest in compression, standing at 86.6 MPa. The lowest compressive strength was found to be 50.6 and 46.9 MPa for R3 and G2, respectively. Although the resins exhibited better compressive strength, cementitious grouts G1 and G2 showed stiffer behaviour in compression, resulting in a higher elastic modulus, which was measured at 27.2 and 20.1 GPa, respectively. The elastic modulus of the resins, R1, R2, and R3, was found to be much less compared to the cementitious grouts at 8.03, 7.45, and 4.71 GPa, respectively. Similarly, the resins represented higher relative deformation in the direction perpendicular to loading, leading to higher Poisson’s ratios than grout. The Poisson’s

ratio was found to be 0.16, 0.18, 0.48, 0.47, and 0.43 for G1, G2, R1, R2, and R3, respectively.

Table 2. Summary of the mechanical tests performed on the bonding materials.

Test	Standard	Specimen Geometry
Compressive	ASTM C579 & ASTM C109	Cubic
Tensile	ASTM D638 & ASTM C307	Dog-Bone
Shear	ASTM D5379	V-notched[1] and Cylindrical[2]

[1] Resin specimens, [2]Grout specimens

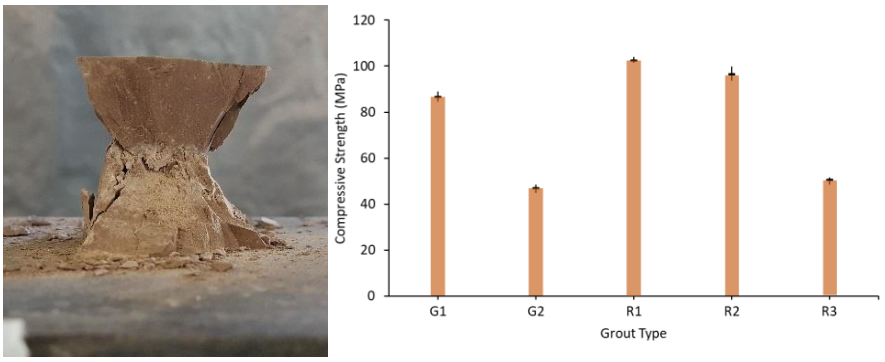

Figure 5. Compressive strength of the bonding materials.

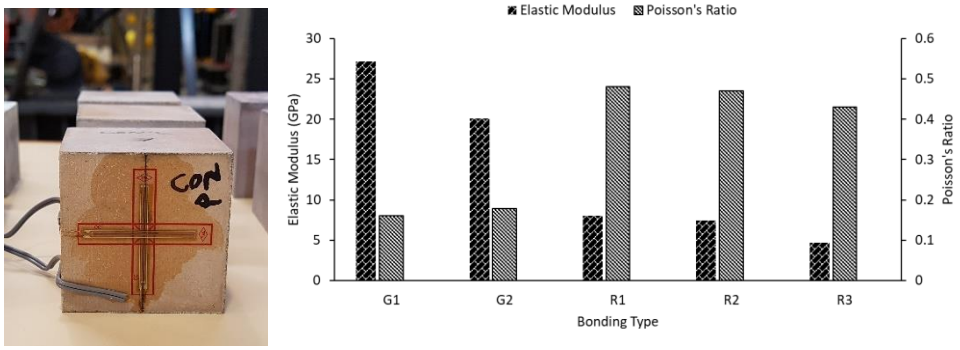

Figure 6. Elastic modulus and Poisson's ratio of the bonding materials.

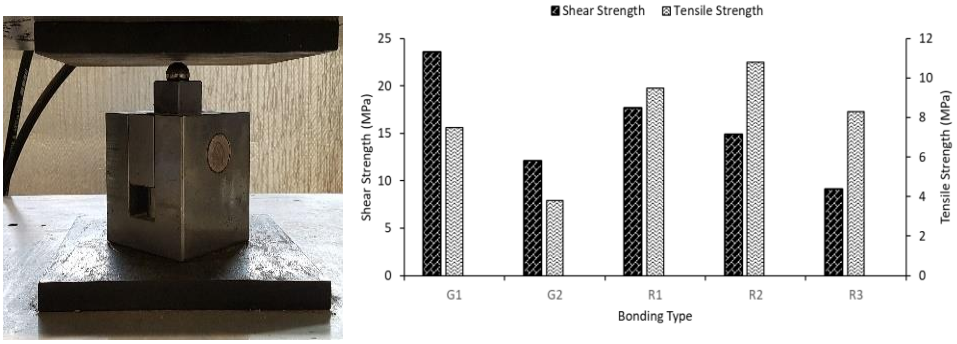

Figure 7. Tensile and shear strengths of the bonding materials.

2.1.3. Rock bolt and instrumentation

Deformed steel M24 X Coal Bolts, manufactured by Minova Australia, were

used as rock bolts in the tests, with varying lengths. Coal Bolts are often used in Australia for rock support and have a core diameter of 22 mm and a nominal total (rib to rib) diameter of 24 mm. Table 3 lists the geometrical and mechanical characteristics of the Coal Bolts. The rock bolts were modified with a pair of opposed, right-angle U-shaped grooves (4 × 4 mm) for instrumentation purposes. These grooves were machined diametrically along the longitudinal ribs of the rock bolts. Axial deformation was monitored by mounting resistive strain gauges along the embedment length. This method has been successful in monitoring the axial deformation of rock bolts in previous technical developments (Signer, 1990). The resistive strain gauges were 3 mm in length with a nominal gauge resistance of 120 Ω and were bonded directly inside the grooves using Cyanoacrylate adhesive. This allowed the induced strain in the rock bolts to be directly transferred to the coupled strain gauges, and the resulting electrical signals were received in the data acquisition system. Strain gauges were mounted at 50 mm intervals along the bolt. Due to space constraints in passing the lead wires, the strain gauges were bonded one between the opposed grooves. In order to protect the strain gauges and lead wires, an organic and non-acidic sealant was applied to fully cover the instruments and the grooves. Figure 8 schematically illustrates the position of the strain gauges and the instrumentation arrangement used for the preparation of the pullout specimen with a 400 mm encapsulation length. This arrangement was followed for the preparation of all pullout specimens with varying encapsulation lengths, although the number of mounted strain gauges varied. Three, four, five, seven, and nine strain gauges were applied to bolts with 100, 150, 200, 300, and 400 mm encapsulation lengths, respectively. A tensile strength test was also conducted to determine the tensile properties of the bolt with opposite grooves (Figure 9). The yield and ultimate tensile strength of the bolt decreased to 595 MPa and 829 MPa, respectively, after making the grooves.

Table 3. Physical and mechanical properties of the rebar bolt.

E (GPA)	Nominal cross section area (mm^2)	Core Diameter (mm)	Nominal Bolt Diameter (mm)	Yield Strength (MPa)	Ultimate tensile strength (MPa)	A_{gt} (%)
210	370	22	24	650	890	8

2.2. Pullout tests

For the pullout tests, an instrumented Coal Bolt was fully bonded inside the holes that were created in the concrete cylinders using G1, G2, R1, R2, and R3. The

arrangement of the pullout tests is presented in Table 4. As shown, the testing campaign includes 17 pullout tests that were conducted on specimens with three types of concrete, five types of bonding agents, and five different encapsulation lengths. A specific jig was designed for performing the pullout tests (Figure 10a). Initially, the jig was clamped onto the lower crosshead of a 1000 kN universal tensile machine, and then the specimens were placed inside the jig. The loading end of the bolt was passed through a 150 mm hole in the upper plate of the jig and then gripped by the machine's jaws. Figures 10b and 10c display top and bottom views of the pullout specimens. Two displacement sensors, LVDTs, were employed to monitor and measure the displacement of the bolt. One was located on the tensile machine's upper crosshead, while the other one was located underneath the specimen (Figure 10d). The upper LVDT was used to measure the displacement of the bolt from the loading end, while the lower one was used for measuring the slip of the free end of the bolt. This arrangement was designed to monitor the differences between displacements and deformations that developed at the loading and free ends. Once the specimen was set up, the strain lead wires of the strain gauges were connected to the data acquisition system, and the bolt was pulled out by a loading rate of 1 mm/sec.

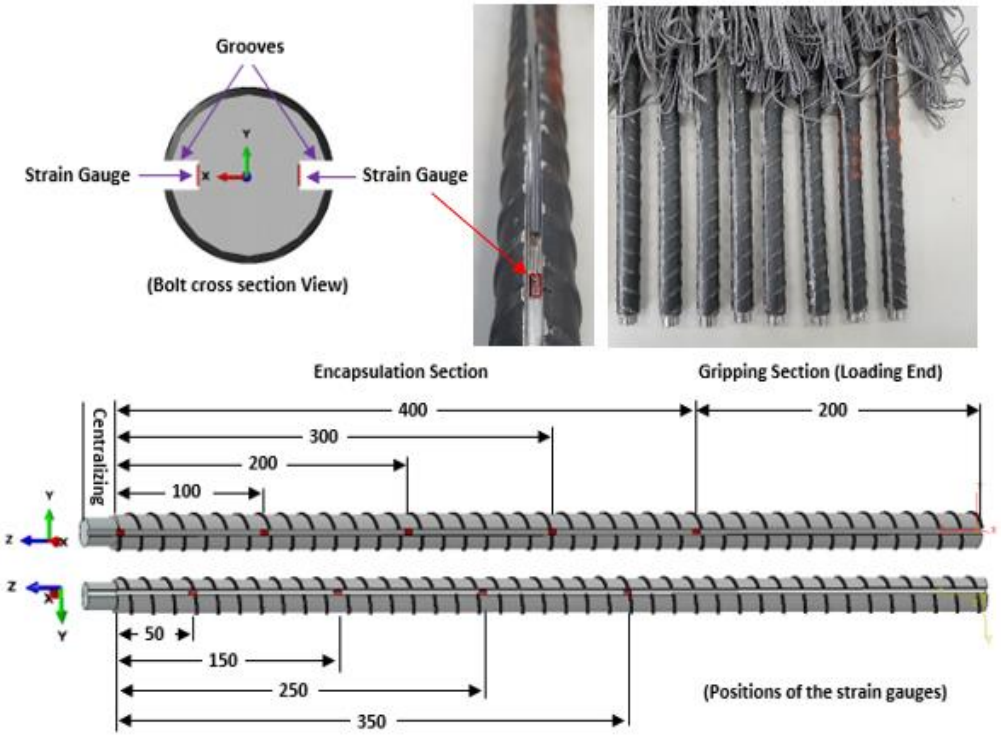

Figure 8. Bolt instrumentation with 400 mm encapsulation. Red coloured squares are strain gauges.

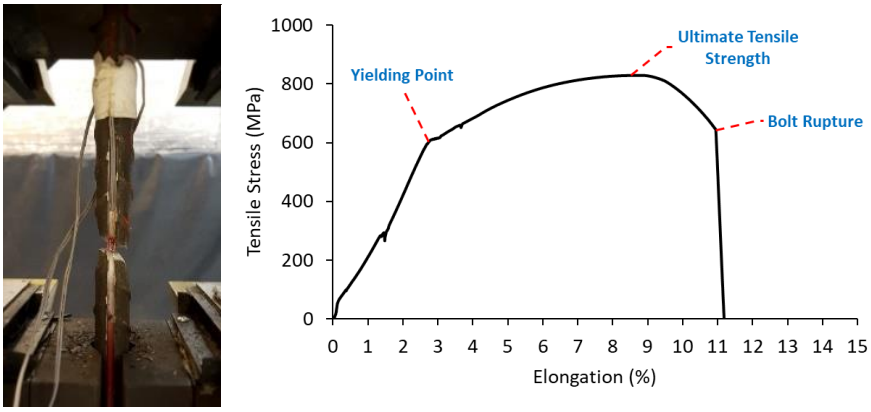

Figure 9. Tensile behaviour of the grooved bolts.

3. Pullout test results and discussion

Table 4 provides an overview of the pullout testing program, including the encapsulation length, grout type, concrete grade, and overall failure mode. To simplify the analysis of the test results, the specimens were grouped into series labelled A, B, C, D, and E. The pullout test results will be discussed in Section 3.1, which focuses on the effects of the encapsulation length on the pullout results, and Section 3.2, which presents the results of pullout tests related to the grout types and the influence of the host medium on the performance of fully embedded rock bolts.

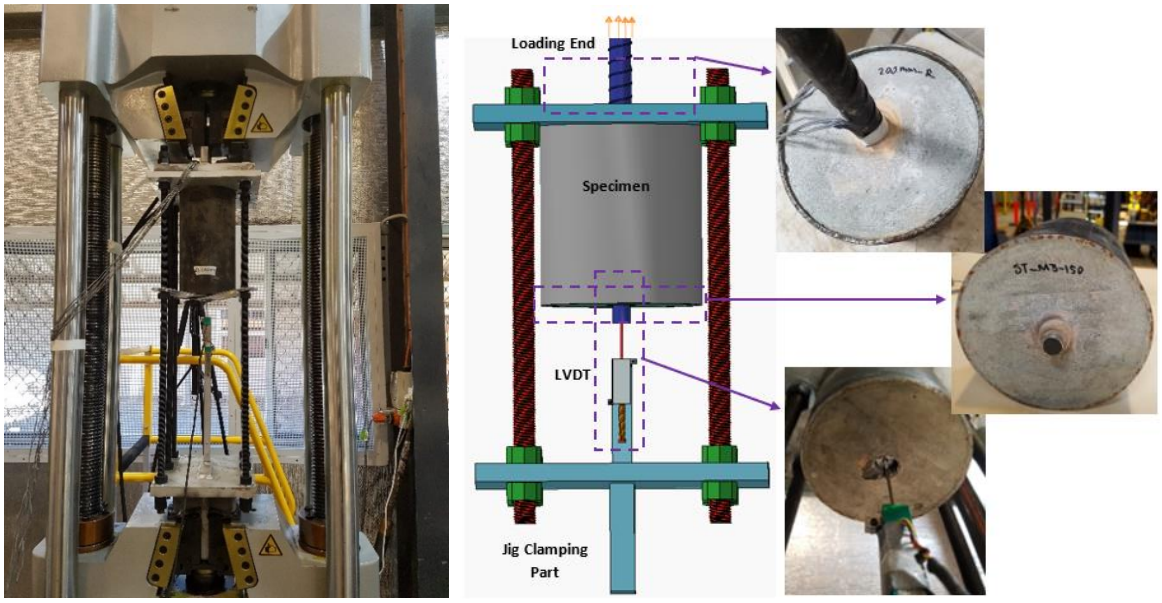

Figure 10. Pullout test arrangement including the jig and specimen and the adjusted LVDT adjusted on the end of the bolt.

3.1. Effect of embedment length

Eight pullout tests were conducted on specimens with varying embedment lengths, ranging from 100 mm to 400 mm, and were encapsulated using two different bonding agents, namely G1 and R2. However, all tests used concrete grade M40 for

the host medium. The results are presented below.

Table 4. Overview of the pullout test program.

Series	Specimen	Encapsulation Length (mm)	Grout Type	Main Failure	Concrete Grade
A	A1	100	G1	Slip	M40
	A2	200	G1	Slip	M40
	A3	300	G1	Bolt rupture	M40
	A4	400	G1	Bolt rupture	M40
B	B1	100	R2	Slip	M40
	B2	200	R2	Slip	M40
	B3	300	R2	Slip	M40
	B4	400	R2	Bolt rupture	M40
C	C1	150	G2	Slip	M20
	C2	150	G2	Slip	M40
	C3	150	G2	Slip	M60
D	D1	150	R1	Slip	M20
	D2	150	R1	Slip	M40
	D3	150	R1	Slip	M60
E	E1	150	R3	Slip	M20
	E2	150	R3	Slip	M40
	E3	150	R3	Slip	M60

3.1.1. Load-displacement relation

Figure 11 shows the load-displacement curves for series A and B specimens. Bolt rupture occurred in specimens A3, A4, and B4, while the other specimens showed full slip debonding failure. Bolt B3 was pulled out with a force close to the ultimate tensile strength of the bolt just before necking phenomenon occurred in the bolt. Furthermore, bolt B3 was pulled out with a force above its yielding capacity. According to the results, the load-displacement relation can be divided into three general categories regardless of the type of bonding agent (Høien et al., 2021). These are: bolt slip occurs when the pullout load level is less than the yielding capacity of the bolt, bolt slip occurs when the pullout load is between the yielding capacity and ultimate tensile capacity of the bolt, and lastly, the system fails due to bolt rupture.

The first type of failure is observed in A1, A2, B1, and B2, in which bolt slip takes place before the pullout load reaches the yield load of the bolt. This type of failure is associated only with the elastic deformation of the bolt bar, and thus plastic deformation shall not be observed. As shown in Figure 11, the displacement increases with load linearly until reaching a specific point after which the load-displacement relationship is not linear, and the slope of the curve decreases continuously till reaching the peak load.

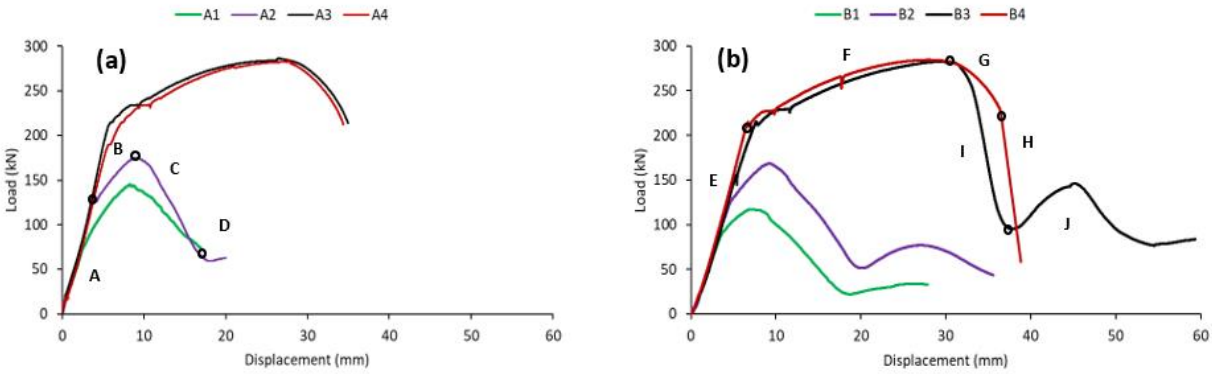

Figure 11. Load-displacement curves of pullout tests for the specimens having anchorage length 100-400 mm; a) encapsulated with cementitious grout G1, and b) encapsulated specimens with resin R2.

It was interestingly found that the axial pullout stiffness (ratio of load over displacement) of the curves in the initial linear stage for all A1-A4 and B1-B4 specimens is equivalent and equal to 35 kN/mm regardless of the type of bonding agent and encapsulation length. Further analysis of the results indicates that the initial linear growth of the load-displacement (e.g., section A in Figure 11a) is associated with the elastic deformation of the whole system. However, critical plastic deformation due to debonding or failure at bonding or surrounding material initiates once the change in the slope of the curve appears (e.g., section B). To support this assumption, loading of the test A4 was paused once the load reached 150 kN, and the specimen was examined in detail. No slip failure was observed in the specimen. Nevertheless, a cone-shaped failure was obvious in the concrete which can be neglected. Therefore, it is concluded that the initial linear growth (section A) in load-displacement can be considered as non-slip elastic deformation, while the section between the end of the linear section and the peak point (section B) is comprised of both elastic deformation and slip failure which is termed slip-elastic deformation. Slip-elastic deformation ends up with peak load followed by continuous reduction in the load vs. displacement (section C). At this stage, bonding material is sheared off continuously till there is no obstacle against slip of the bolt. When irregularities at the bolt-grout interface are all smoothed, only friction remains between the contacts as the effective resistance, and if the encapsulation length remains constant, the frictional residual strength will keep steady (section D). As shown in Figure 11, higher encapsulation length provides higher residual strength. On the contrary, the load-displacement curves of A3, A4, and B4 resemble the curve of a bolt tensile test, including elastic, strain hardening, necking,

and final rupture of the bolt (sections E, F, G, and H in Figure 11b). However, a portion of the total force was utilised for localised debonding at the collar's vicinity, in addition to creating cone failure in the concrete. This behaviour indicates that increasing the anchorage length beyond a certain point does not enhance the bolt's performance. The B3 bolt, with 300 mm of anchorage, was pulled out when the load approached the ultimate tensile capacity of the bar. The load-displacement curve is similar to the B4 curve in the elastic and strain hardening parts (sections E and F). However, just before necking, the system begins to debond along the encapsulation length, leading to continuous reduction of the load-displacement (section I) until reaching the frictional residual strength (section J).

3.1.2. Embedment length vs. pullout characteristics relationship

Figure 12 shows the relation between the embedment length and peak pullout load obtained from the test series A and series B. The data points are the values obtained from the pullout tests, but the trend lines have been enveloped to delineate the approximate patterns and predict values beyond the immediate data set. The peak pullout load vs embedment length curve can be divided into three main linear parts. Stage (i) represents the embedment length less than the length corresponding to the bolt yield capacity (<268 mm in series B), stage (ii) represents the embedment length that corresponds to the pullout capacity in the range of the yield strength and ultimate tensile strength of the bolt (268-300 mm in series B), and stage (iii) represents the embedment length equal to or greater than the critical embedment length, where the pullout capacity is equal to the ultimate tensile strength of the bolt (>300 mm in series B). The findings cover a wide range of performances of rock bolts associated with the embedment length and emphasise the significance of stage (ii), where a small increase in the embedment length (≈32 mm in series B) causes a significant improvement in the performance of the bolt (80 kN in series B). It is evident that the contribution of the embedment length to the pullout capacity in stage (ii) is related to the ratio of yield strength over tensile strength of steel bars, which is typically in the range of 0.7-0.85. However, more emphasis is placed on the gradient in stage (ii), which is significantly higher than that of stage (i). The critical embedment length for series A (point X) has been approximately determined by a trend enveloped similar to the trend of series B. The range of the embedment length for stages (i), (ii), and (iii) of

series A was found approximately to be <247 mm, 247-282 mm, and >282 mm, respectively.

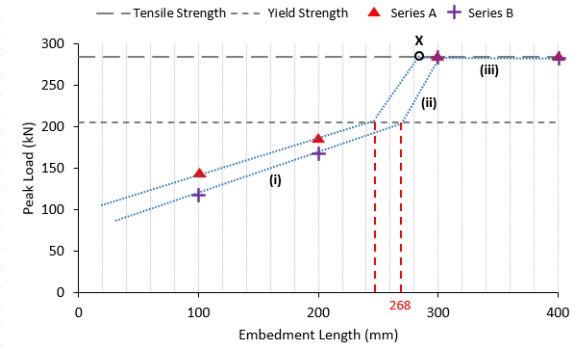

Figure 12. Relationship between embedment length and peak pullout strength.

Comparison of the results also indicates that, for the same embedment length, the bearing capacity of grouted rock bolts using G1 is 10-20% higher than that of bolts encapsulated using R1 bonding agent, even though the compressive strength of G1 is 15% less than that of R1. This signifies that the compressive strength of the bonding agent should not be considered as the sole parameter influencing the bearing capacity of the system. The effect of mechanical characteristics of the bonding materials on the behaviour of rock bolts will be discussed in detail in section 3.1.3. Table 5 summarises the pullout characteristics of the series A and B tests. In general, the higher the embedment length, the higher the ultimate capacity, stiffness, and frictional residual strength. For instance, in series A, an increase in the embedment length from 100 mm to 200 mm and from 200 mm to 300 mm increases the ultimate bearing capacity by 29% and 62%, respectively. This improvement for series B was measured at 43% and 69%. It can also be seen that an increase in the embedment length shifts the corresponding displacements at the peak loads to the right.

Table 5. Summary of the pullout tests results for series A and B.

Specimen	Embedment Length (mm)	Peak Load (kN)	Displacement at peak (mm)	Residual strength (kN)	Rate of ascending in section 1 (kN/mm)	Rate of ascending in section 2 (kN/mm)	Descending rate (kN/mm)
A1	100	143	8.4	50.3	34.5	12.21	9.9
A2	200	176	8.9	64.5	34.5	12.18	15.56
A3	300	285	27.7	0	34.5	N/A	N/A
A4	400	285	27.6	0	34.5	N/A	N/A
B1	100	117	6.8	33.6	33.3	7.23	10.09
B2	200	168	9.4	49.2	33.3	10.5	11.97
B3	300	284	28	81	33.3	N/A	N/A
B4	400	284	28	0	33.3	N/A	N/A

3.1.3.Bond stress distribution along the embedment length for series A and B

Bond refers to the shear resistance induced between the bolt bar and bonding materials in response to the pullout load. It has been shown that the bond stress generated at the bolt-grout interface and along the embedment length of a fully grouted rock bolt is non-uniform, although it is common to assume a uniform bond stress distribution for short embedment specimens. Bond stress distribution can be technically quantified by measuring the longitudinal elongation degrees of the bolt along the embedment length using sensors such as strain gauges. Figure 13 schematically shows the stress equilibrium at a section of a grouted bolt with a length of Δx. Assuming three main conditions, i.e., (1) a uniform bond stress distribution along Δx,(2) no energy loss in other forms such as creating fractures, cracks, and damages, and (3) no deformation in the host rock, we can write the following force equilibrium for Figure 13:

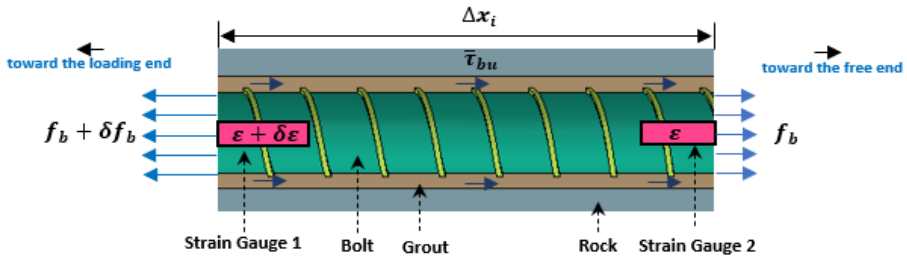

Figure 13. Stress equilibrium in a length of embedded rock bolt.

$$f_b + \delta f_b = f_b + \bar{\tau}_{bu}(\pi d_b \Delta x) \quad (1)$$

where $f_b + \delta f_b$ is the force subjected at strain gauge 1, f_b is the bolt force acting at strain gauge 2, $\bar{\tau}_{bu}$ is the induced interfacial shear stress at the bolt-grout interface, d_b is the nominal diameter of the bolt, and Δx is the distance between the strain gauges. Applying constitutive equation ($\sigma = \varepsilon . E$) in Eq.1 the following equation is achieved:

$$(\varepsilon + \delta\varepsilon) E a_b = \varepsilon E a_b + \bar{\tau}_{bu}(\pi d_b \Delta x) \quad (2)$$

where $\varepsilon + \Delta\varepsilon$ is the strain value measured by strain gauge 1, E is the elastic modulus of the bolt, a_b is the cross area of the bolt and ε is the strain value measured by strain gauge 2. By simplifying Eq.2, interfacial bond stress along Δx can be calculated as follows:

$$\bar{\tau}_{bu} = \frac{\delta\varepsilon E d_b}{4\Delta x} \quad (3)$$

Therefore, monitoring the elongation of bolts along the embedment length due to the pullout load is an effective way to determine the interfacial bond stress

distribution. This information is essential for developing efficient constitutive models for the axial performance of anchored bolts. It should be noted that the equations presented for a full-scale anchored bolt are only applicable if the free end of the bolt is assumed to be fixed in the loading direction and restrained from any displacement. The consistency of the data presented in this section, as compared to similar studies in the literature, lies in three factors: Firstly, the presented data covers the whole pullout process, rather than just partial data. Secondly, most of the possible failure types in rock bolting are individually investigated. Finally, the combined effect of other parameters such as grout and host rock quality was also investigated.

Figures 14 and 15 illustrate that the distribution of bond stress relies on the failure mode of the system, such as shank rupture and failure at the bolt-grout interface. However, a close relation between the interfacial bond stress and the pullout load applied is evident. This suggests that the induced bond stress increases with the increase in the pullout load, irrespective of the embedment length and distance. Furthermore, the results indicate that the maximum bond stress along the embedment length may not be attained at the maximum pullout load, and it can occur before or after these points.

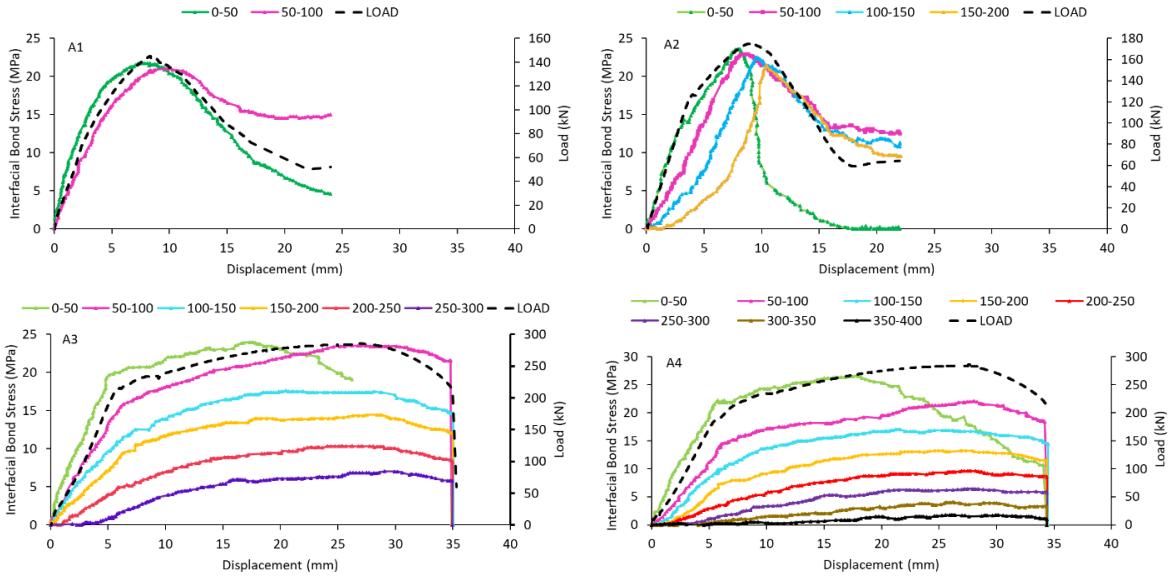

Figure 14. Bond stress distributions for the series A tests (legends refer to the distances on the encapsulation length in mm).

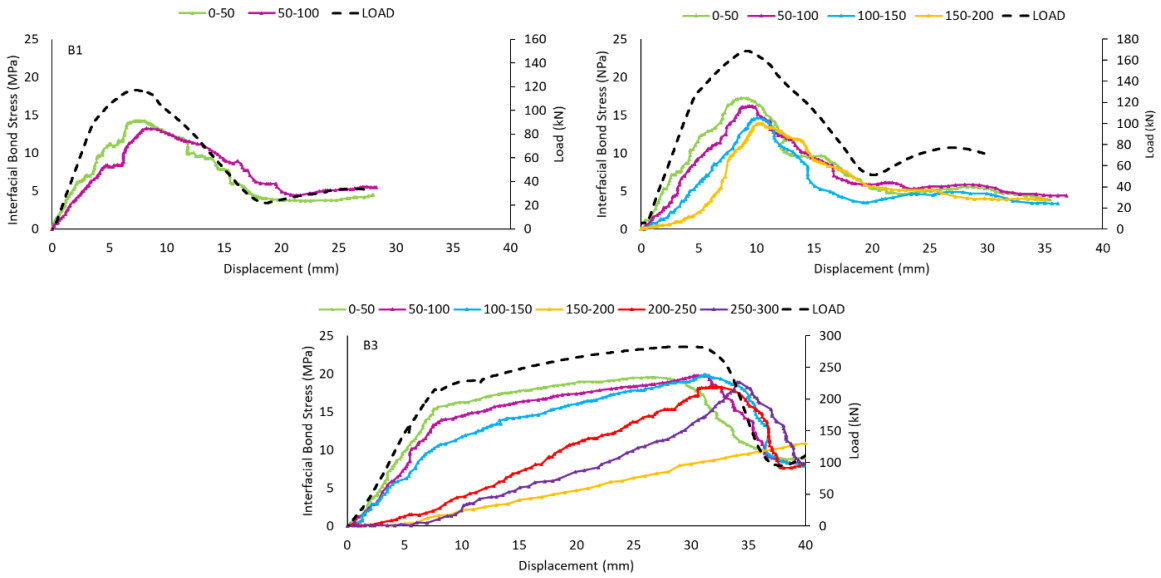

Figure 15. Bond stress distribution for the series B tests (legends refer to the distances on the encapsulation length in mm).

During tests A1 and A2, where fully debonding of the bolt was achieved, the peak bond stress for the instrumented sections ranged between 21-23.5 MPa. The analysis of the results showed that debonding of the bolts initially started from the loading end and then extended towards the free end of the bolt, accompanied by a slight displacement of the bolts. In test A1, the highest magnitude of bond stress at the 0-50 mm section occurred when the pullout load reached 139 kN, which is 97.2% of the peak load. Similarly, in the 50-100 mm section of test A1, the maximum bonding stress of 21.09 MPa was achieved when the pullout load reduced to 136 kN (95.1% of the peak load). In test A2, the peak bond stress for the 0-50, 50-100, 100-150, and 150-200-mm sections was measured as 23.58, 22.9, 22.5, and 21.46 MPa, respectively, at pullout loads of 170, 175, 162, and 156 kN. These results demonstrate that debonding in the vicinity of the loading end begins before the pullout load reaches its peak value. However, debonding of the deeper sections occurs at the peak load or in the post-peak part of the loading. The bond stress curve for the 0-50 mm section of test A2 displays an unusual behaviour where the bond stress settles at zero level at the displacement of 17.5 mm. Examination of the specimen after the completion of the test revealed that a cone-shaped damage at the grout and concrete caused 29 mm of the bolt to become unembedded, and then further slip of the bolt continuously contributed to the extension of the unembedded section until 17.5 mm of slip, after which the strain values became identical along the 0-50 mm section, resulting in zero

bond resistance. A similar behaviour was observed in test B2. However, the bond stress curve reached a zero value at higher displacement, which was due to the depth of the cone damage being 13 mm. In both A3 and A4 tests, the bond stress curve for the 0-50 mm section (the green line) switched to a descending trend at the displacement of 15-20 mm, which can be attributed to the initiation and propagation of circumferential cracks created at the grout.

Table 6 presents the magnitudes of interfacial bond stress induced at 50, 100, 150, and 200 kN pullout loads for tests A1-A4 and B1-B3. The results show that as the embedment length increases, the subjected pullout load diffuses over a longer length. Due to the longer bonded length, stress concentration is minimised. This means that at a specific level of pullout load, the induced interfacial bond stress at a particular section is lower in a longer embedment length. For example, at 50 kN of pullout load, the bond stress at the first section (0-50 mm) for A1, A2, A3, and A4 was measured at 10.41, 6.86, 5.47, and 4.65 MPa, respectively. Similar conditions can be noted at higher load levels and at other sections as well. This becomes more critical when comparing the distribution of bond stress of specimens with different bonding agents (e.g., A1 and B1, A2 and B2, and A3 and B3). The results indicate that at a particular level of pullout load, series B tests generally exhibited lower bond stresses compared to series A. For instance, at 100 kN, the bond stress was recorded at 14.06 and 8.15 MPa for A1 and B1 at the 50-100 mm section, respectively. Similarly, at 150 kN and 100-150 mm section, bond stress was measured at 8.16 and 6.64 MPa for A3 and B3, respectively. The reason can be attributed to the mechanical properties of the bonding agent, in particular, the modulus of elasticity.

3.1.4. Bond stress distribution Vs mechanical properties of encapsulation materials

Figure 16 illustrates the potential response of rock bolting systems embedded in bonding materials with different mechanical characteristics when subjected to pullout forces. In any type of bonding material encapsulating rock bolts are loaded axially in pull or push out, as shown in Figure 16a, the bonding agent serves to transfer axial load from the bolt to the host rock through bond stresses distributed along the encapsulation length. Figure 16b shows the equilibrium balance of the differential element in the embedded region. The following basic equilibrium equations can be presented based on this statistically indeterminate problem:

$$\frac{dp(x)}{dx} = \pi d_b \tau_b(x) \tag{4a}$$

$$\frac{\partial \sigma_g(x,y)}{\partial x} + \frac{\partial \tau_g(x,y)}{\partial y} = 0 \tag{4b}$$

$$\frac{\partial \sigma_r(x,y)}{\partial x} + \frac{\partial \tau_r(x,y)}{\partial y} + X_r = 0 \tag{4c}$$

where $p(x)$ is the axial force subject to the bolt at the position of x, $\tau_b(x)$ is the resultant bond stress on the bolt, $\sigma_g(x,y)$ is the axial stress in the bonding agent parallel to the rock bolt at (x,y), $\tau_g(x,y)$ is the induced shear stress in the bonding agent and at the position of (x,y), $\sigma_r(x,y)$ is the axial stress in the host rock parallel to the rock bolt at (x,y), $\tau_r(x,y)$ is the shear stress in the host rock and X_r is the body force of the host rock acting at x direction. In the above differential equations, the body force of the bolt and the bonding agent are ignored as they are relatively small compared to the host rock. Since it is difficult to solve the problem only by the existing equilibrium equations and boundary conditions, the basic shear-lag model as the most fundamental concepts in the load transfer mechanism between bonded members is adopted. The bonding agent is relatively thin compared to the bolt and the host rock thus it can be assumed that the bonding agent does not carry significant axial forces, therefore $\frac{\partial \sigma_g(x,y)}{\partial x} = 0$ and $\tau_g\left(x, y \left|{}^{r_b+\eta}_{r_b}\right.\right) = \tau_b(x)$. The constitutive laws and shear-lag model for fully encapsulated rock bolts can be expressed as follows:

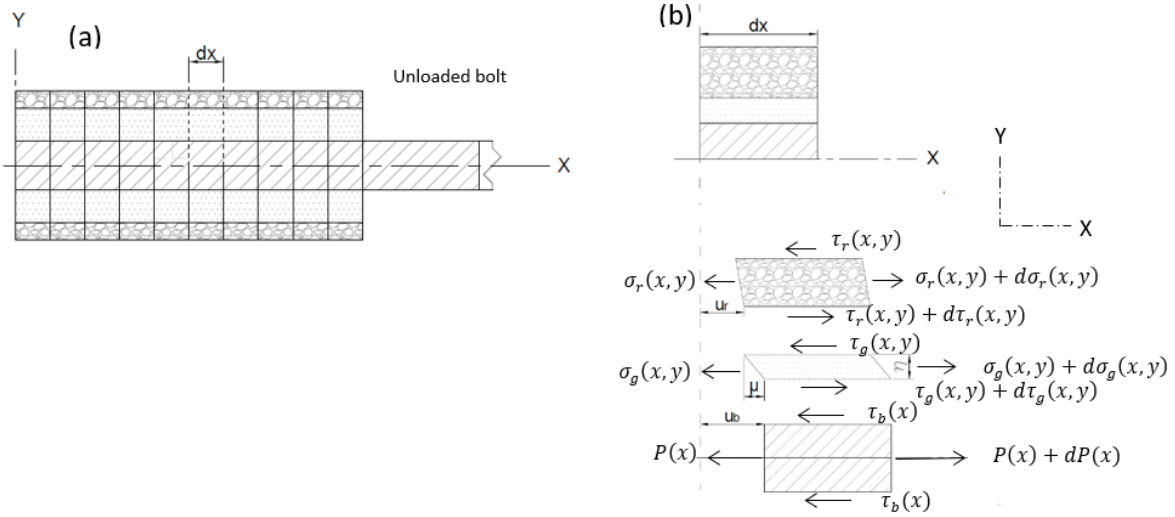

Figure 16. (a) Encapsulated bolt subjected to a tensile load, and (b) Deformation and stress distribution in an infinitesimal length.

$$\tau_b(x) = G_g \gamma_{xy} = G_g \left(\frac{\partial (u_g)_x}{\partial y} + \frac{\partial (u_g)_y}{\partial x}\right) \tag{5}$$

where G_g and γ_{xy} are the shear modulus of the bonding agent and the shear strain of the bonding agent in the xy plane, respectively. $(u_g)_x$ and $(u_g)_y$ are the displacement of the bonding element at the x and y directions, respectively. u_y is relatively much smaller than u_x due to the lower magnitude of resultant stress parallel to the y axis, thus it can be neglected for simplifications.

$$\tau_b(x) = G_g\left(\frac{u_b(x,0)-u_r(x,r_b+\eta)}{\eta}\right) \quad (6)$$

where G_g is the shear modulus of the bonding agent and γ and η are the shear strain and thickness of the bonding agent. u_b and u_r are displacement of the bolt and host rock in the direction of loading, respectively as shown in Figure16b. Taking derivative from the Eqs. 4a and 6 with respect to x, respectively, yields:

$$\frac{d^2P(x)}{dx^2} = 2\pi r_b \frac{d\tau_b(x)}{dx} \quad (7)$$

$$\frac{d\tau_b(x)}{dx} = \frac{G_g}{\eta}\left(\frac{du_b(x,0)}{dx} - \frac{du_r(x,r_b+\eta)}{dx}\right) = \frac{G_g}{\eta}\left(\varepsilon_b(x,0) - \varepsilon_r(x,r_b+\eta)\right) \quad (8)$$

where $\varepsilon_b(x,0)$ is the bolt strain and $\varepsilon_r(x,r_b+\eta)$ is the host rock strain at the edge of $r_b+\eta$ induced by applying axial load of $P(x)$ at the position of x.

$$\varepsilon_b(x,0) = \frac{P(x)}{\pi r_b^2 E_b} \quad (9)$$

Where E_b is the elastic modulus of the bolt. Considering the shear modulus of host rock as G_r, the distributed shear stress and axial strain in the host rock can be expressed as

$$\tau_{rx}(x,y) = G_r\gamma_{xy} = G_r\left(\frac{\partial(u_r)_x}{\partial y} + \frac{\partial(u_r)_y}{\partial x}\right) \quad (10)$$

By neglecting the shear deformation in y direction, ε_r is expressed as

$$\varepsilon_{rx}(x,r_b+\eta) = \frac{\sigma_{rx}(x,r_b+\eta)}{E_r} + \frac{R\tau_{rx}(x,r_b+\eta)}{G_r} \quad (11)$$

where $\varepsilon_r(x,r_b+\eta)$ is the strain of the host rock at the grout-rock interface, σ_{rx} is the stress parallel to loading direction, and E_r and R are the elastic modulus and thickness of the host rock, respectively. Substituting Eqs. 9, 10 and 11 into Eq. 7 yields

$$\frac{d^2P(x)}{dx^2} = \frac{2\pi r_b G_g}{\eta}\left(\frac{P(x)}{\pi r_b^2 E_b} - \left(\frac{\sigma_{rx}(x,r_b+\eta)}{E_r} + \frac{R\tau_{rx}(x,r_b+\eta)}{G_r}\right)\right) \quad (12)$$

$$\frac{d^2P(x)}{dx^2} - \phi^2 P(x) = f(\sigma_{rx},\tau_{rx}) \quad (13)$$

where $\phi = \sqrt{\frac{2G_g}{\eta r_b E_b}}$, and the general solution to the homogeneous equation

(i.e., $f(\sigma_{rx}, \tau_{rx}) = 0$) is:

$$P(x) = C_1 e^{\phi x} + C_2 e^{-\phi x} \quad (14)$$

where C_1 and C_2 are constants determined by initial and boundary conditions. The expression of $\tau_b(x)$ is as follows:

$$\tau_b(x) = \phi(C_1 e^{\phi x} - C_2 e^{-\phi x}) \quad (15)$$

The distribution of bond stress τ_b is schematically illustrated in Figure 17 based on Eq. 15. This equation indicates that when investigating the effect of encapsulation materials on the performance of fully embedded rock bolts while keeping other factors identical, the shear modulus of the encapsulation material has the most significant impact on the axial load transfer along the encapsulation length and, consequently, the distribution of induced bond stress at the bolt grout interface. As seen, an increase in the shear modulus of the bonding material results in an increase in the magnitude of bond stress along the embedment length. This is consistent with the experimental results presented in Figures 14-15 and Table 6, as discussed above, since the shear modulus of the bonding agents used in A and B series of tests is 11.7 and 2.9 GPa, respectively.

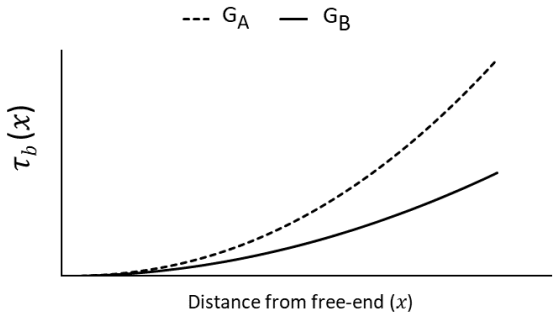

Figure 17. Schematic of the effect of shear modulus of the bonding materials (G) on the bond stress distribution based on Eq.15 for two different types of bonding materials including A and B where $G_A > G_B$.

Figure 18 depicts the bond stress profile along the embedment length at load levels of 50%, 75%, and 100% of the peak load, as well as at the post-peak residual strength for the tests that were fully debonded (i.e., A1, A2, B1, B2, and B3). The results indicate that, generally, the bond stress at a specific pullout load level decreases from the loading end to the free end, although there are exceptions, particularly in the post-peak residual bond strength of A2, B2, and B3. In A2, the 150-200 mm section does not present bond resistance due to the cone-shaped damage

created at the collar's vicinity after the peak load was achieved. The depth of the cone damage for A2 was measured at 43 mm from the specimen surface, fully covering the 150-200 mm section and 13 mm of the 100-150 mm section. Similar cone-shaped damage was observed in A3, A4, B2, B3, and B4, but with different depths, which will be discussed in detail in Section 3.1.4. Additionally, it is evident that the initial residual bond strength in the sections towards the free end is higher. This may be due to the fact that the debonding damage to the encapsulation and/or radial dilation, as a consequence of bolt elongation/slip, is less at the vicinity of the free end, while the sections closer to the loading end are completely damaged at that specific elongation.

Moreover, it is interesting to note that the initial residual bond stress is higher than the bond stress induced by 75% of the peak load at the 0-50 mm section for the specimens shown in Figure 18. The results show that the minimum bond stress is achieved at the vicinity of the free end when the pullout load is equal to or less than the peak load. In A1, B1, and B2, the maximum bond stress corresponding to the peak load was found at the section close to the loading end, while in A2 and B3, it was measured at the 100-150 mm and 200-250 mm sections, respectively. This indicates that in the latter specimens, debonding of the embedded section at the collar occurred before the pullout load reached the peak load.

3.1.5. Failure pattern of the specimens with different embedment lengths

The failure modes of specimens tested under pullout conditions can be investigated from two perspectives: the first is the cone-shaped damage that occurs at the host rock and encapsulation media near the loading end, and the second is failures that occur at the bolt-bonding material interface. The cone-shaped damage is visible in all specimens except A1, but the depth and area of the damage differ, as shown in Figure 19. From observations and further investigations, it can be concluded that the intensity of the cone-shaped damage may be associated with two main factors: 1) the maximum pullout load applied, and 2) the failure mode. Among all specimens, B3 and A2, which satisfied both conditions, exhibited the greatest degree of damage with cone heights of 35 and 26 mm, respectively. The specimens that failed due to bolt rupture (i.e., A3, A4, and B4) and specimen B1 showed shallow damage, while there was no obvious cone-shaped damage in A1.

In terms of failure at the bolt-bonding material interface, three basic modes of failure were observed: 1) shear-off failure, 2) a combination of hackle cracks and

shear-off, and 3) hackle cracks.

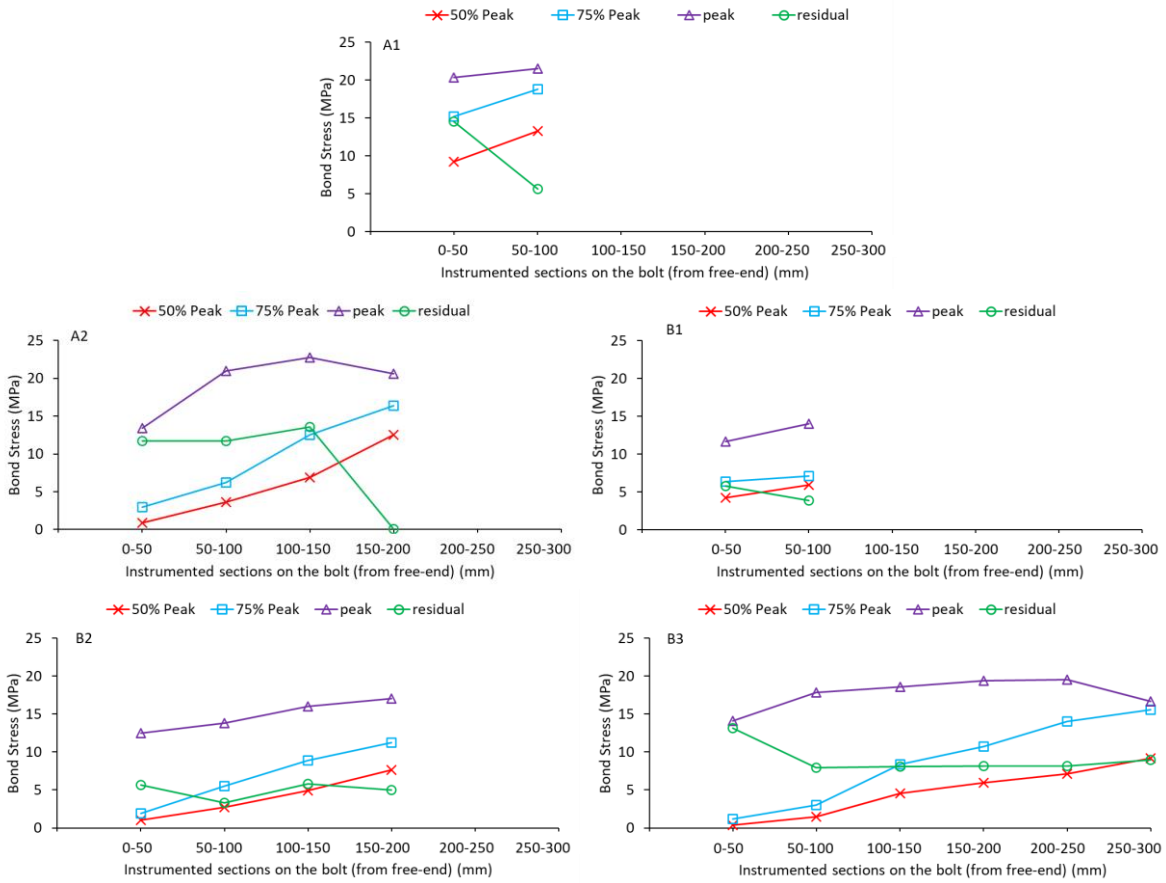

Figure 18. Bond stress profile along the embedment length corresponding to the loads of 50% of peak load, 75% of peak load, peak load, and residual capacity.

Shear-off failure was observed in A1, A2, B1, and B2 and occurs due to bolt slip, where irregularities in the bonding materials created by the surface profile of the rock bolt are sheared off and the interface becomes smooth (Figure 20a&b). This type of failure was the dominant failure mode in cases where the peak pullout load was below the yielding capacity of the bolt. For a direct observation of the state of the specimens after testing, they were longitudinally sliced, and the observation revealed that the bolt-grout surface roughness is distinct depending on the type of encapsulation material. In specimens encapsulated by G1, the grout irregularities are crushed and partially sheared (Figure20b, while the bolt-resin surface of specimens encapsulated using resin e.g., R2, were completely sheared and crashed off (Figure 20a) This may be associated with the mechanical properties of the bonding materials, in particular, the shear strength and the radial stiffness. The radial stiffness provides resistance against the radial deformation induced by the radial component (f_r) of the

force acting on the bolt surface, as shown in Figure 21a. The radial stiffness of the G1 grout obtained from Eq.17 is over three times that of R2 (Zhao et al., 2021).

$$k_s = E_g(r_2^2 - r_1^2)/[(r_2^2 + r_1^2) + (r_2^2 - r_1^2)\nu_g - 2r_2^2\Phi] \quad (17)$$

where k_s is the radial stiffness, E_g and ν_g are the elastic modulus and Poisson's ratio of the grout, respectively, r_1 and r_2 are shown in Figure 21b which are the diameter of the bolt and the hole, respectively, and the factor Φ is expressed as:

$$\Phi = \frac{2r_1^2}{E_g(r_2^2 - r_1^2)} \Big/ \left[\frac{1+\nu_r}{E_r} + \frac{(1-\nu_g)r_2^2 + (1+\nu_g)r_1^2}{E_g(r_2^2 - r_1^2)}\right] \quad (18)$$

where E_r and ν_r are the elastic modulus and Poisson's ratio of the host rock, respectively.

The second type of failure at the bolt-grout interface, which is a combination of circumferential cracks and shear-off failure, was only observed in the B3 specimen, as shown in Figure 20c. However, circumferential cracks themselves are also visible in the A3, A4, and B4 specimens, as illustrated in Figure 20d. These cracks are a series of cracks inclined at roughly 45° to the host rock, but they are effectively arrested as they approach the host rock. The circumferential cracks, which are only seen at a distance of 44-65 mm from the surface, can be associated with the level of pullout load and thus the degree of elongation. Once the resultant strain exceeds the elastic capability of the encapsulation media, the cracks begin to form. Apparently, the density of the cracks increases as they approach the loading end, where the strain on the bolt is maximum, leading to extensive damage and thus causing a crush-off zone (Figure 20d). Therefore, it can be concluded that the inclined cracks in the encapsulating media can only occur in cases where there is considerable elongation in the bolt (e.g., beyond the yield strength of the bolt) before debonding of the system occurs.

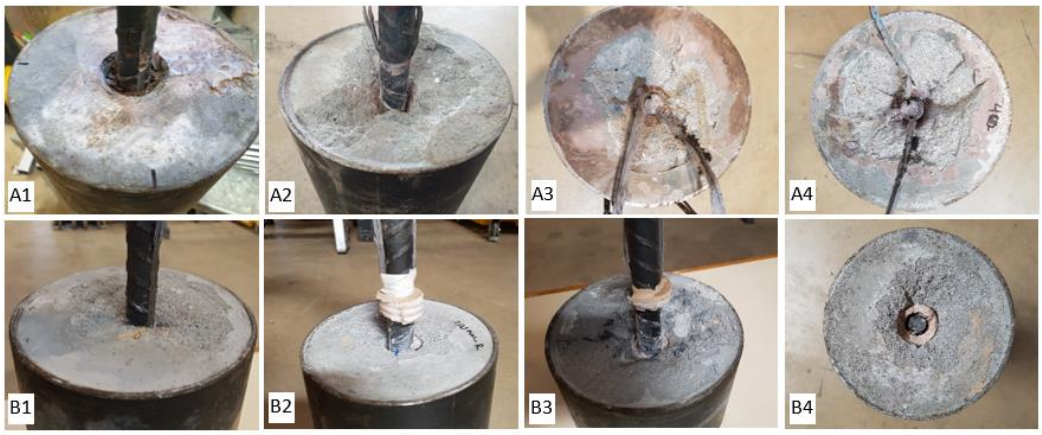

Figure 19. Cone-shape damage at the loading end of the specimens with different embedment lengths.

Table 6. Bond stress magnitudes at different pullout loads and sections along the embedment length for tests A1-A4 and B1-B3.

					50 kN					
	Sections	0-50	50-100	100-150	150-200	200-250	250-300	300-350	350-400	Average
Series A	A1	10.41	6.51							8.46
	A2	6.86	3.36	1.29	0					2.87
	A3	6.47	3.88	3.23	2.46	0.77	0.1			2.81
	A4	8.56	3.15	1.41	0.54	0.36	0.36	0.019	0.016	1.8
Series B	B1	5.65	3.68							4.66
	B2	5.15	2.7	1.52	0.23					2.4
	B3	3.86	3.09	2.7	1.54	0.64	0.1			1.98
					100 kN					
	Sections	0-50	50-100	100-150	150-200	200-250	250-300	300-350	350-400	Average
Series A	A1	14.06							16.14	18.22
	A2	6.99	4.40	1.16					6.34	12.82
	A3	8.29	6.47	4.66	2.07	0.25			5.58	11.78
	A4	6.31	4.57	2.12	1.43	0.38	0.25	0.12	3.47	12.59
Series B	B1	8.15							9.33	10.52
	B2	6.93	3.83	1.11					4.99	8.12
	B3	5.79	5.02	3.73	0.9	0.38			3.86	7.34
					150 kN					
	Sections	0-50	50-100	100-150	150-200	200-250	250-300	300-350	350-400	Average
Series A	A2	19.43	17.22	11.01	4.66					13.08
	A3	15.93	10.36	8.16	6.08	2.97	0.38			7.31
	A4	17.14	9.47	7.37	4.41	2.14	0.92	0.39	0.28	5.26
Series B	B2	13.37	11.03	8.57	4.82					9.44
	B3	10.3	7.98	6.44	5.28	1.41	0.51			5.32
					200 kN					
	Sections	0-50	50-100	100-150	150-200	200-250	250-300	300-350	350-400	Average
Series A	A2	13.08								
	A3	7.31	19.68	13.47	9.97	7.38	4.27	1.03		
	A4	5.26	22.22	14.55	10.53	7.57	3.56	1.99	0.94	0.29
Series B	B2	9.44								
	B3	5.32	13.91	11.98	9.79	6.82	1.93	0.64		

3.1.6. Relation between the mechanical properties of the encapsulation media and pullout performance of the system

Comparing the bond stress curves shows that bolt debonding occurs only when the interfacial bond stress induced along the embedment length reaches a specific level. For series A, where cementitious grout G1 is used, the bond stress is constrained to 21.7-23.6 MPa, while for series B, specimens were debonded when the bond stress is in the range of 14.3-19.9 MPa. Further investigation on the potential correlation between debonding behaviour and the mechanical properties of the encapsulation media indicates that shear properties are the dominant characteristics among other properties, such as compressive and tensile strengths, which dictate the ultimate bearing capacity of rock bolting systems. As shown in Figures 5 and 6, although R2 has higher compressive and tensile strengths at 102.5 and 10.8 MPa,

respectively, compared to G1's strengths at 86.6 and 7.5 MPa, the debonding capacity of specimens encapsulated using G1 is higher, as outlined above. On the other hand, the shear strength of G1 and R2 is 23.6 and 14.9 MPa, respectively, demonstrating that the shear strength of the bonding agent has a greater influence on performance. In terms of bond stress distribution, the shear modulus of the bonding agent dominantly defines the bond stress distribution, along with other mechanical characteristics.

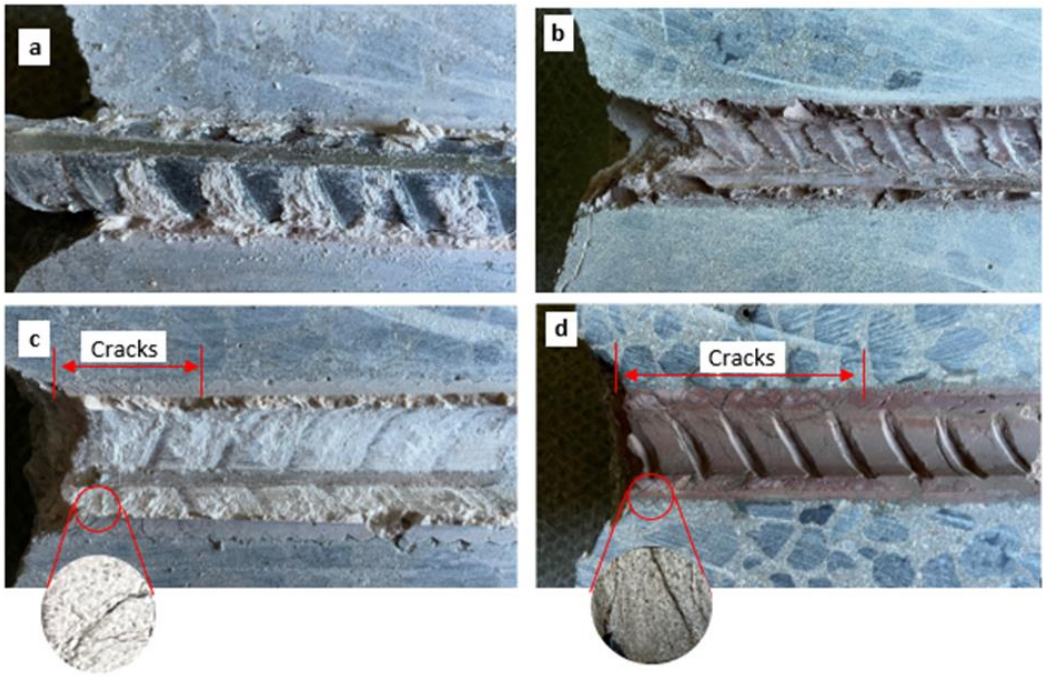

Figure 20. Failure at the bolt-encapsulation material interface.

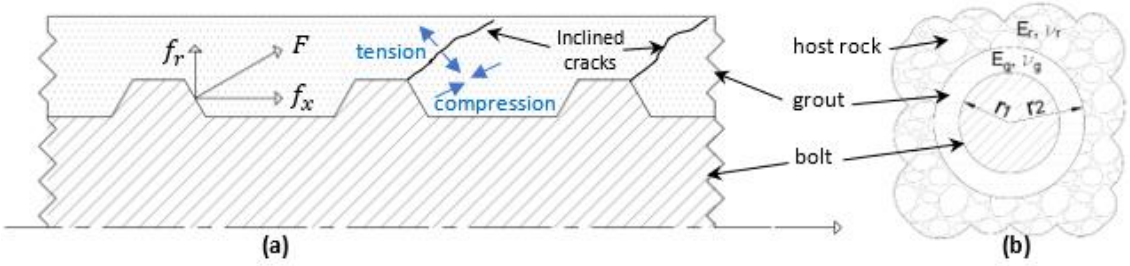

Figure 21. (a) Exaggerated illustration of the forces subjected at the ribs and the formation inclined cracks, (b) sketch illustrating the parameters used in Eqs. 17-18, (adopted from (Zhao et al., 2021)).

3.2. Effects of the grout and host rock properties on the debonding behaviour

For further analysis of the effects of bonding material type, as well as the effects of host rock conditions on the axial performance of rock bolts, nine additional pullout tests were conducted on 150 mm bolts encapsulated in three grades of concrete

cylinder, including M20, M40, and M60, using three different encapsulation media, including G2, R1, and R3. Figures 22a-22c represent the load-displacement curves obtained from the pullout tests, and Figure 22d shows the relation between the peak pullout load and the concrete grades for different bonding materials.

In terms of the effect of the type of bonding material, it was found that at an identical concrete grade (e.g., M20), the highest bearing capacity was represented by the bolt encapsulated using G2 grouting materials, followed by R1, and lastly, R3. The shear and compressive strengths of the bonding agent used in the C series (G1) are lower than that of the D series (54% and 31%); nonetheless, the peak pullout capacity of C1, C2, and C3 is 80%, 60%, and 50% higher than that of D1, D2, and D3, respectively. The reason is rooted in the expansion characteristics of the G2 grout which provided an additional normal force contributing to the shear pullout performance of the rock bolt. For expandable bonding materials, it is commented that when cast in moulds for mechanical testing, the bonding agent is free to expand in one direction, while grout injection in the borehole provides higher normal stress resulting in higher bond strength (Benmokrane et al., 2000). Thus, mechanical testing of the expandable materials cast and prepared in conventional moulds may result in imprecise results. Amongst all the bonding materials used in this study, specimens bonded using R3, i.e., E1, E2, and E3, exhibited the lowest pullout capacity, as seen in Figure 22c. This was predicted as R3 also showed lower strength properties compared to the bonding agents.

The results presented in Figure 22 demonstrate that the strength of the host rock significantly contributes to the pullout capacity of rock bolts. Axial slip of deformed reinforcing elements generates radial dilation, which is inhibited or restricted by the normal stiffness of the rock mass. A higher radial stiffness may lead to a higher induced lateral confining stress and higher interfacial bond strength (Hyett et al., 1992; Yazici and Kaiser, 1992). The peak pullout load of specimens bonded using G2 grout improved from 210.1 kN to 223.6 kN and then to 231.9 kN as the host rock compressive strength increased from 20 MPa to 40 MPa and then 60 MPa. This indicates an improvement of 6.3% and 3.7%, respectively. Similar improvement in the pullout capacity with an increase in the host rock strength was observed in the other series. In the D series tests, an increase in the host rock compressive strength from 20 MPa to 40 MPa and then 60 MPa caused an improvement in the peak pullout load from 116.1 kN to 139.2 kN and then to 154.6 kN, respectively. This indicates respective

improvements of 19.8% and 11%. Considerable progress can also be observed in the pullout performance of series E with an increase in the concrete compressive strength. In E1, where the bolt was installed in a concrete cylinder with 20 MPa compressive strength, the peak pullout load measured 76.9 kN. This value increased to 93.3 kN and 109.3 kN when the concrete strength increased to 40 MPa and 60 MPa, respectively. This represents an increase of 21.3% and 17.2%, respectively. Figure 23 illustrates the effects of the concrete strength and grout on the peak bearing capacity of the bolt.

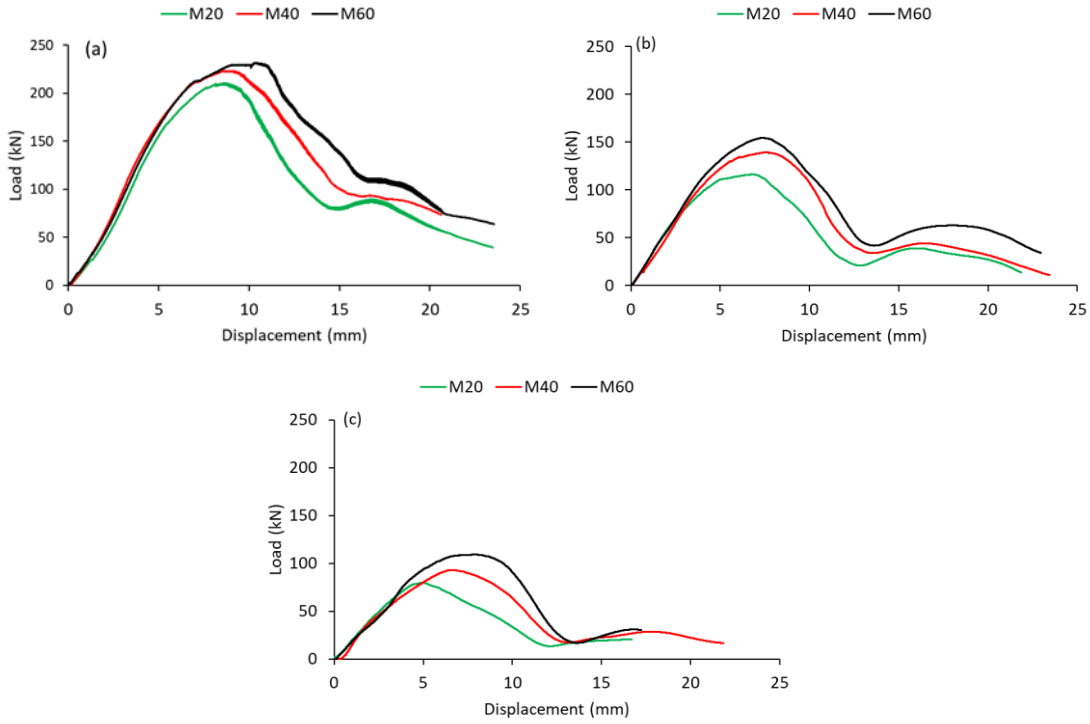

Figure 22. The effects of the host rock strength and the encapsulation media type on the pullout performance of rock bolts; (a) series C tests, (b) series D tests, and (c) series E tests.

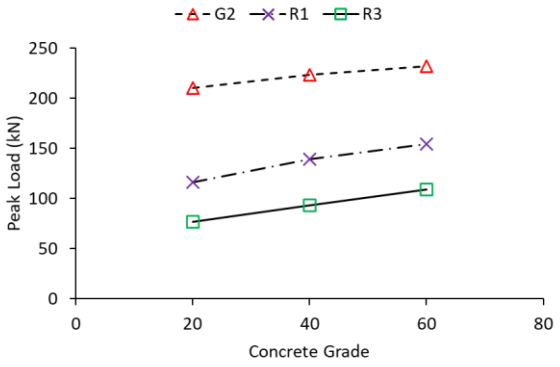

Figure 23. peak pullout load vs. host rock strength and the bonding type.

4. Conclusion

This study has investigated the mechanical properties of bonding materials and the axial behaviour of fully encapsulated rock bolts. The study aimed to understand the effects of embedment length, bonding materials, and host rock conditions on the performance of rock bolts. Mechanical testing was conducted to comprehensively investigate the compressive, tensile, and shear strengths of the bonding materials. Elastic modulus, Poisson's ratio, and shear modulus of the bonding materials were also quantified to analyse the factors affecting the bond stress distribution along the embedment length.

Pullout tests were conducted using deformed steel M24 X Coal Bolts embedded in concrete with three different strength grades. Five types of bonding materials, including two types of cementitious grouts (G1 and G2) and three types of polyester resins (R1, R2, and R3), were used to evaluate the effects of bonding materials on the axial load transfer mechanism of rock bolts. Strain gauges were used to measure the effects of embedment length on the axial performance of rock bolts.

The load-displacement curves for the fully debonded specimens (A1, A2, B1, and B2) exhibited two main trends: an initial linear segment followed by a non-linear one. The linear segment correlated well with the elastic behaviour of the steel bolt, indicating that plastic deformation of the bonding system i.e., debonding of the bolt, began when the non-linear behaviour commenced. Increasing the embedment length from 100 mm to 200 mm improved the peak pullout strength by 29-43%. This improvement increased to 62-69% when the embedment length was further increased to 300 mm. However, once the embedment length exceeded the critical length, the peak pullout load became constant and equal to the tensile strength of the bolt bar. Increasing the embedment length beyond the critical embedment length did not improve the bolting system's performance, as demonstrated by A3 and A4, with 300 mm and 400 mm embedment lengths respectively, which showed a peak pullout capacity of 285 kN. Comparing the results led to the conclusion that the compressive strength of the bonding agent alone cannot predict the pullout performance. For example, the pullout strength of grouted rock bolts using G1 was found to be 10-20% higher than that of bolts encapsulated using R1 bonding agent, even though G1's compressive strength was 15% less than R1's.

The results obtained from strain gauges showed that the distribution of bond stress depends on the failure mode of the system (i.e., shank rupture and failure at the

bolt-grout interface). However, it was found that the level of induced bond stress increases with the increase in pullout load, regardless of the embedment length and distance. The results also revealed that as the embedment length increases, the subjected pullout load diffuses over a longer length, reducing stress concentration. Concerning the mechanical characteristics of the bonding materials, the shear modulus has the most significant impact on the axial load transfer along the encapsulation length and, consequently, on the distribution of induced bond stress at the bolt-grout interface. From the experimental results and the developed mathematical models, it was concluded that at a specific level of load, a higher shear modulus leads to higher bond stress at a desired distance.

In terms of the failure pattern at the bolt-grout interface, three main forms of damage were identified, including shear-off, a combination of shear-off and inclined cracks near the collar, and only inclined cracks without effective debonding. The damage pattern primarily depends on the failure mode of the system and the level of the peak pullout load. Further investigation revealed that the expansion characteristics of the bonding agent are an effective factor in significantly improving the pullout capacity of fully grouted rock bolts. Among all the specimens, series D exhibited the highest bearing capacity values where an expandable grout, G2, was used. The results presented in Figure 21 show that the strength of the host rock significantly contributes to the pullout capacity of the bolts. It was found that an increase in the compressive strength of the concrete from 20 MPa to 60 MPa resulted in an increase of approximately 3-20% in the pullout strength of the bolt.

References

Antino, T.D., Sneed, L.H., Carloni, C., Pellegrino, C., 2016. Effect of the inherent eccentricity in single-lap direct-shear tests of PBO FRCM-concrete joints. Compos. Struct. 142, 117–129. https://doi.org/10.1016/j.compstruct.2016.01.076

AS 1379, 1997. Specification and supply of concrete. Aust. Stand.

ASTM C109, 2020. Standard Test Method for Compressive Strength of Hydraulic Cement Mortars (Using 2-in. or [50 mm] Cube Specimens). ASTM Int. https://doi.org/10.1520/C0109_C0109M-20

ASTM C192, 2015. Standard Practice for Making and Curing Concrete Test Specimens in the Laboratory. ASTM Int. https://doi.org/10.1520/C0192_C0192M

ASTM C307, 2023. Standard Test Method for Tensile Strength of Chemical-Resistant Mortar, Grouts, and Monolithic Surfacings. ASTM Int. https://doi.org/10.1520/C0307-18

ASTM C39, 2021. Standard Test Method for Compressive Strength of Cylindrical Concrete Specimens. ASTM Int. https://doi.org/10.1520/C0039_C0039M-21

ASTM C469, 2021. Standard Test Method for Static Modulus of Elasticity and Poisson's Ratio of Concrete in Compression. ASTM Int. https://doi.org/10.1520/C0469_C0469M-14

ASTM C579, 2023. Standard Test Methods for Compressive Strength of Chemical-Resistant Mortars, Grouts, Monolithic Surfacings, and Polymer Concretes. ASTM Int. https://doi.org/10.1520/C0579-18

ASTM D5379, 2021. Standard Test Method for Shear Properties of Composite Materials by the V-Notched Beam Method. ASTM Int. https://doi.org/10.1520/D5379_D5379M-19E01

ASTM D638, 2022. Standard Test Method for Tensile Properties of Plastics. ASTM Int. https://doi.org/10.1520/D0638-14

Benmokrane, B., Chennouf, A., Mitri, H.S., 1995. Laboratory evaluation of cement-based grouts and grouted rock anchors. Int. J. Rock Mech. Min. Sci. Geomech. Abstr 32, 633–642.

Benmokrane, B., Zhang, B., Chennouf, A., 2000. Tensile properties and pullout behaviour of AFRP and CFRP rods for grouted anchor applications. Constr. Build. Mater. 14, 157–170.

Cai, Y., Esaki, T., Jiang, Y., 2004. An analytical model to predict axial load in grouted rock bolt for soft rock tunnelling. Tunn. Undergr. Sp. Technol. 19, 607–618. https://doi.org/10.1016/j.tust.2004.02.129

Cao, C., Ren, T., Cook, C., Cao, Y., 2014. Analytical approach in optimising selection of rebar bolts in preventing rock bolting failure. Int. J. Rock Mech. Min. Sci. 72, 16–25. https://doi.org/10.1016/j.ijrmms.2014.04.026

Cao, C., Ren, T., Zhang, Y., Zhang, L., Wang, F., 2016. Experimental investigation of the effect of grout with additive in improving ground support. Int. J. Rock Mech. Min. Sci. 85, 52–59. https://doi.org/10.1016/j.ijrmms.2015.12.010

Chen, J., He, F., Zhang, S., 2020. A study of the load transfer behaviour of fully grouted rock bolts with analytical modelling. Int. J. Min. Sci. Technol. 30, 105–109. https://doi.org/10.1016/j.ijmst.2019.12.010

Chen, J., Li, D., 2022. Numerical simulation of fully encapsulated rock bolts with a tri-linear constitutive relation. Tunn. Undergr. Sp. Technol. 120, 104265. https://doi.org/10.1016/j.tust.2021.104265

Farmer, I.W., 1975. Stress distribution along a resin grouted rock anchor. Int. J. Rock Mech. Min. Sci. Geomech. Abstr. 12, 347–351.

Freeman, T.J., 1978. Behaviour of fully bonded rock bolts in the kielder experimental tunnel. Int. J. Rock Mech. Min. Sci. Geomech. Abstr. 15, 37–40. https://doi.org/doi:10.1016/0148-9062(78)91073-2

Grasselli, G., 2005. 3D Behaviour of bolted rock joints: experimental and numerical study. Int. J. Rock Mech. Min. Sci. 42, 13–24. https://doi.org/10.1016/j.ijrmms.2004.06.003

Høien, A.H., Li, C.C., Zhang, N., 2021. Pull-out and Critical Embedment Length of Grouted Rebar Rock Bolts-Mechanisms When Approaching and Reaching the Ultimate Load. Rock Mech. Rock Eng. 54, 1431–1447. https://doi.org/10.1007/s00603-020-02318-6

Huang, M., Zhou, Z., Huang, Y., Ou, J., 2013. A distributed self-sensing FRP anchor rod with built-in optical fiber sensor. Measurement 46, 1363–1370. https://doi.org/10.1016/j.measurement.2012.12.012

Hyett, A.J., Bawden, W.F., Reichert, R.D., 1992. The effect of rock mass confinement on the bond strength of fully grouted cable bolts. Int. Rock Mech. Min. Sci. Geomech. Abstr 29, 503–524.

Li, C., Stillborg, B., 2000. Analytical models for rock bolts. Int. J. Rock Mech. Min. Sci. 36, 1013–1029.

Li, C.C., Kristjansson, G., Høien, A.H., 2016. Critical embedment length and bond strength of fully encapsulated rebar rockbolts. Tunn. Undergr. Sp. Technol. 59, 16–23. https://doi.org/10.1016/j.tust.2016.06.007

Li, D., Li, Y., Chen, J., Masoumi, H., 2021. An analytical model for axial performance of rock bolts under constant confining pressure based on continuously yielding criterion. Tunn. Undergr. Sp. Technol. Inc. Trenchless Technol. Res. 113, 103955. https://doi.org/10.1016/j.tust.2021.103955

Ma, S., Nemcik, J., Aziz, N., 2013. An analytical model of fully grouted rock bolts subjected to tensile load. Constr. Build. Mater. 49, 519–526. https://doi.org/10.1016/j.conbuildmat.2013.08.084

Martín, L.B., Tijani, M., Hadj-hassen, F., 2011. A new analytical solution to the mechanical behaviour of fully grouted rockbolts subjected to pull-out tests. Constr. Build. Mater. 25, 749–755. https://doi.org/10.1016/j.conbuildmat.2010.07.011

McKay, K.S., Erki, M.A., 1993. Grouted anchorages for aramid fibre reinforced plastic prestressing tendons. Can. J. Civ. Eng. 20, 1065–1069. https://doi.org/doi:10.1139/l93-137

Moosavi, M., Jafari, A., Khosravi, A., 2005. Bond of cement grouted reinforcing bars under constant radial pressure. Cem. Concr. Compos. 27, 103–109. https://doi.org/10.1016/j.cemconcomp.2003.12.002

Nourizadeh, H., Mirzaghorbanali, A., Mcdougall, K., Jeewantha, L.H.J., Craig, P., Motallebiyan, A., Jodeiri, B., Rastegarmanesh, A., 2023. Characterisation of mechanical and bonding properties of anchoring resins under elevated temperature. Int. J. Rock Mech. Min. Sci. 170, 105506. https://doi.org/10.1016/j.ijrmms.2023.105506

Nourizadeh, H., Williams, S., Mirzaghorbanali, A., McDougall, K., Aziz, N., Serati, M.,

2021. Axial behaviour of rock bolts-part (A) Experimental study, in: Resource Operator Conference. Springfield, Queensland, Australia, pp. 294–302.

Rastegarmanesh, A., Mirzaghorbanali, A., McDougall, K., Aziz, N., Anzanpour, S., Nourizadeh, H., Moosavi, M., 2023. Axial Response of Resin Encapsulated Cable Bolts in Monotonic and Cyclic Loading. Can. Geotech. J. https://doi.org/https://doi.org/10.1139/cgj-2022-0379

Rastegarmanesh, A., Mirzaghorbanali, A., McDougall, K., Aziz, N., Anzanpour, S., Nourizadeh, H., Moosavi, M., 2022. Axial Performance of Cementitious Grouted Cable Bolts Under Rotation Constraint Scenarios. Rock Mech. Rock Eng. https://doi.org/10.1007/s00603-022-02950-4

Ren, F.F., Yang, Z.J., Chen, J.F., Chen, W.W., 2010. An analytical analysis of the full-range behaviour of grouted rockbolts based on a tri-linear bond-slip model. Constr. Build. Mater. 24, 361–370. https://doi.org/10.1016/j.conbuildmat.2009.08.021

Signer, S.P., 1990. Field verification of load transfer mechanics of fully grouted roof bolts, 9301. United States. Bureau of Mines.

Singer, S.P., Cox, D., Johnston, J., 1997. A method for the selection of rock support based on bolt loading measurements, Spokane Research Centre, NIOSH.

Tepfers, R., 1979. Cracking of concrete cover along anchored deformed reinforcing bars. Mag. Concr. Res. 31.

Teymen, A., Kılıç, A., 2018. Effect of grout strength on the stress distribution (tensile) of fully-grouted rockbolts. Tunn. Undergr. Sp. Technol. 77, 280–287. https://doi.org/10.1016/j.tust.2018.04.022

Vlachopoulos, N., Cruz, D., Forbes, B., 2018. Utilising a novel fiber optic technology to capture the axial responses of fully grouted rock bolts. J. Rock Mech. Geotech. Eng. 10, 222–235. https://doi.org/10.1016/j.jrmge.2017.11.007

Wee, S., Kang, S., Hai, K., Yang, E., 2016. Experimental and analytical investigation on bond-slip behaviour of deformed bars embedded in engineered cementitious composites. Constr. Build. Mater. 127, 494–503. https://doi.org/10.1016/j.conbuildmat.2016.10.036

Wu, Y., Hao, Y., Tao, J., Teng, Y., Dong, X., 2019. Non-destructive testing on anchorage quality of hollow grouted rock bolt for application in tunneling , lessons learned from their uses in coal mines. Tunn. Undergr. Sp. Technol. 93. https://doi.org/10.1016/j.tust.2019.103094

Yazici, S., Kaiser, P.K., 1992. Bond strength of grouted cable bolts. Int. J. Rock Mech. Min. Sci. Geomech. Abstr. 29, 279–292.

Yilmaz, S., Özen, M.A., Yardim, Y., 2013. Tensile behaviour of post-installed chemical anchors embedded to low strength concrete. Constr. Build. Mater. 47, 861–866. https://doi.org/10.1016/j.conbuildmat.2013.05.032

Yokota, Y., Zhao, Z., Nie, W., Date, K., Iwano, K., Okada, Y., 2019. Experimental and

Numerical Study on the Interface Behaviour Between the Rock Bolt and Bond Material. Rock Mech. Rock Eng. 52, 869–879. https://doi.org/10.1007/s00603-018-1629-4

Zhang, B., Benmorkane, B., Ebead, U.A.A., 2006. Design and Evaluation of Fiber-Reinforced Polymer Bond-Type Anchorages and Ground Anchors. Int. J. Geomech. 166.

Zhao, T., Zhang, Y., Li, C.C., 2021. Radial stiffness of rock bolt samples and required thickness of the steel tube in impact tests. Int. J. Rock Mech. Min. Sci. 146, 104886. https://doi.org/10.1016/j.ijrmms.2021.104886

Zhou, Y.-W., Wu, Y.-F., Yun, Y., 2010. Analytical modeling of the bond–slip relationship at FRP-concrete interfaces for adhesively-bonded joints. Compos. Part B Eng. 41, 423–433. https://doi.org/10.1016/j.compositesb.2010.06.004

Zou, X., Sneed, L.H., D'Antino, T., 2020. Full-range behaviour of fiber reinforced cementitious matrix (FRCM)-concrete joints using a trilinear bond-slip relationship. Compos. Struct. 239. https://doi.org/10.1016/j.compstruct.2020.112024

5.2. Links and implications

In this chapter, a comprehensive investigation was conducted into the axial behaviour of steel rock bolts under various geotechnical conditions. Valuable insights were gleaned from the results, and these offer significant contributions to the design and selection of rock bolts for a wide range of engineering applications. This information can also serve as an effective means of assessing and enhancing the available analytical solutions for rock bolting design. In Australia, the prevalent practice following rock excavation involves the installation of a rock bolt system to provide primary support, necessitating a design lifespan of 50 to 100 years. The conventional rock bolts are typically crafted from carbon steel, rendering them susceptible to corrosion in their operational environments, often due to exposure to groundwater. By contrast, protective sheathed rock bolts are engineered to utilise in corrosive environments where the risk of degradation is notably high. Curiously, the literature has largely overlooked the investigation of the axial behaviour of these protective sheathed rock bolts. Hence, there exists a pressing need to examine comprehensively the axial performance of these specialised rock bolts and draw comparisons with the conventional rock bolt behaviour elucidated in Chapter 5. This investigation serves as the main topic of Chapter 6.

CHAPTER 6: PAPER 4- EXPLORING THE AXIAL PERFORMANCE OF PROTECTIVE SHEATHED ROCK BOLTS THROUGH LARGE-SCALE TESTING

6.1. Introduction

In chapters 3-5, the performance of steel rock bolts was examined under diverse conditions. It was demonstrated that comprehending the axial load transfer mechanism of rock bolts under various conditions is vital for optimising reinforcement in rock structures, advancing our understanding of rock support, and enabling the design of robust engineering solutions. Typically manufactured from carbon steel, rock bolts are susceptible to corrosion when exposed to groundwater in their operational environments. To address the durability of rock bolts, it is crucial to develop and implement corrosion protection measures that ensure a high level of safety. Commonly, corrosion protection for rock bolts relies on the coating of the steel bars. However, in corrosive environments, plastic protective sheathed rock bolts are frequently employed.

This study presents an extensive experimental investigation on a large scale, with the primary objective of exploring the axial load transfer mechanism of protective sheathed rock bolts across various scenarios. Additionally, the examination delved into the failure mode of these systems, with the aim of identifying the weakest component when subjected to pullout loading under different conditions. The findings of this study yield valuable insights into the behaviour and performance of sheathed rock bolt systems under varying conditions, thereby enhancing our understanding of their mechanical responses and potential vulnerabilities.

Exploring the Axial Performance of Protective Sheathed Rock Bolts through Large-Scale Testing

Hadi Nourizadeh[a,b], Ali Mirzaghorbanali[a,b], Kevin McDougall[c], Naj Aziz[d]

[a] Centre for Future Materials (CFM), University of Southern Queensland, 4350, Australia
[b] School of Engineering, University of Southern Queensland, 4300, Australia
[c] School of Surveying and Built Environment, University of Southern Queensland, 4350, Australia
[d] School of Civil, Mining & Environmental Engineering, University of Wollongong, NSW, 2500, Australia

Abstract

Understanding the axial load transfer mechanism of rock bolts under diverse conditions is essential for optimising reinforcement in rock structures, advancing our comprehension of rock support, and facilitating the design of robust engineering solutions. This paper reports the outcomes of an extensive experimental investigation, focusing on the axial behaviour of protective sheathed rock bolts employed in corrosive environments, assessed through pull tests. Three distinct testing setups were designed to evaluate comprehensively the performance of these rock bolts in various scenarios. The results indicated that the failure characteristics and axial behaviours of sheathed rock bolts differ significantly from conventional counterparts. The findings revealed two primary failure modes in sheathed rock bolts: bolt rupture and slip at the grout-sheath interface, based on the testing arrangement and encapsulation length. The lack of adhesion and interlocking at the grout-sheath interface prevents shear stress at the bolt-grout interface from reaching its maximum potential strength, resulting in grout damage manifesting as circumferential cracks. This, in turn, initiates crack formation, reducing the system's bond strength. Additionally, it causes slip at the grout-sheath interface to occur at lower pull loads. It can be inferred that the inner surface of the plastic sheath lacks the necessary structural integrity to withstand high loads, significantly impacting bond stress distribution and failure modes. The results demonstrate that the protective sheath remains intact up to an axial displacement of 28 mm, irrespective of the testing configuration. Additionally, it was observed that the maximum bond stress at the bolt-grout interface falls within the range of 6-8.7 MPa, which is below the shear strength of the grout. Consequently, achieving failure at the bolt-grout interface is not feasible.

Key words: Rock bolts, Sheath, Corrosive environment, Axial performance

1. Introduction

Rock reinforcement is a widely utilised technique within the mining and construction industries, particularly in tunnels and underground excavations (Li, 2017; Singh et al., 2020). The primary goal of this method is to enhance the stability and bolster the load-bearing capacity of the rock mass (Martín et al., 2011; Rastegarmanesh et al., 2022). Ensuring the integrity of the reinforcement is a key priority within these industries, as the failure of these materials can lead to substantial financial implications and pose a risk to human safety. In Australia, the predominant practice following rock excavation is to install a rock bolt system to provide primary support (Chen et al., 2022). This method comprises a wide range of materials and techniques, including rock bolting, which is one of the most effective and economical techniques (Grasselli, 2005; Singh et al., 2022). Rock bolts exhibit diversity in design and material, and they can be classified according to various criteria, including their anchoring mechanism, materials, application, installation, and the mode of reinforcement system (Li et al., 2014; Thompson et al., 2012; Windsor, 1997). Regarding the mode of reinforcement system, rock bolts can be categorised as being either active or passive reinforcements (Fahimifar and Ranjbarnia, 2009; He et al., 2015; Li, 2017; Thompson et al., 2012). The core disparity between these methodologies resides in the fact that active rock bolts exert a force onto the rock immediately upon installation, while passive rock bolts hinge on the rock's internal movement to trigger the reinforcement procedure (Peter et al., 2022).

Active rock bolts typically comprise plain steel rods equipped with a mechanical anchor (expansion shell) at one end, and a plate and nut on the other (Thompson et al., 2012; Windsor, 1997). These bolts are consistently tensioned post-installation. In situations requiring short-term use, the bolts are typically retained without grouting (Kilic et al., 2003). However, in cases necessitating long-life application, the resin or cementitious grout fills the space between the bolt and rock (Windsor, 1997). By contrast, for passive rock bolts, comprising fully grouted rock bolts and consistently frictional rock bolts like Swellex and Split Set, pre-tensioning is not feasible. Instead, the reinforcement element comes into play when the rock mass commences movement (Li et al., 2014).

Irrespective of the reasons for using rock bolts, they are usually manufactured from carbon steel, making them susceptible to corrosion due to the potential exposure to groundwater in their operational environments (Cao et al., 2013; Ma et al., 2013).

Various forms of corrosion occur in rock bolts, including crevice, pitting, stress corrosion cracking (SCC), and organic corrosion (Chen et al., 2021, 2018; Wu et al., 2019). Among these, pitting stands out as the most challenging, as it reduces the cross-sectional area of the bar. Aziz et al., (2014) conducted a study on the long-term exposure of full-size bolts to a corrosive environment. The results show a reduction of up to 12.80% in the cross-sectional area of the bolts observed during the investigation.

Despite the distinctions in the corrosion types, they all share a common feature which is their exposure to corrosive environments. Corrosion can potentially undermine the load-bearing capacity of rock bolts through various mechanisms (Craig et al., 2021). These mechanisms include diminishing the strength characteristics of the bar due to cross-sectional area reduction, creating cracks on the rebar, and progressively weakening the adhesive bond with the surrounding material over time. A contemporary approach in tunnel design involves the utilisation of rock bolts for enduring reinforcement. In the Australian context, it has become common to designate a design lifespan of 50 to 100 years for these foundational support components. The life expectancy of rock bolts can be addressed by developing and applying corrosion protection measures that provide a substantial level of safety. Corrosion protection of rock bolts commonly relies on the coating of the steel bar including cathodic sacrificial coating (zinc, zinc chrome, zinc epoxy, etc.) and barrier-type coating (epoxy, polyurethane, plastic, etc.) (Ma et al., 2018). An additional solution to address the corrosion issue is using rock bolts with protective sheathing. These specialised bolts are carefully designed to utilise in corrosive environments where the risk of degradation is notably high. The protective sheathed bolts introduce an innovative solution to rectify the shortcomings inherent in conventional reinforcement systems, particularly those stemming from corrosion vulnerabilities. Comprising a steel bar integrated with point anchor expansion shells and accompanying face plates, the protective sheathed bolts employ a hemispherical dome and a nut to establish tension against the rock at the exposed end of the bolt. Furthermore, the incorporation of grouting subsequent to the initial bolt installation contributes to the long-term reinforcement of the structure. This bolt is placed within a corrugated high-density polyethylene (HDPE) sheath, designed to facilitate the grouting process once the bolt is in position. The hollow hemispherical dome component serves as the entry point for grout injection, through a designated hole within the dome.

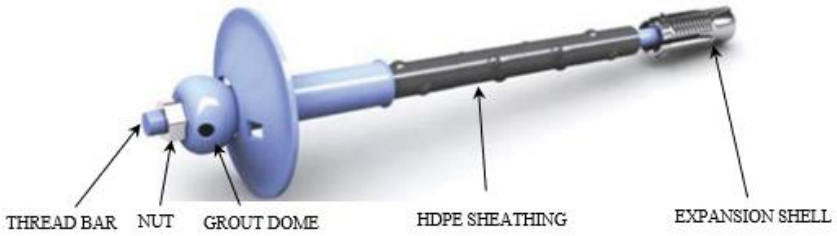

Figure 1. HDPE protective sheathed bolt (Türkmen, 2009).

Generally, the failure patterns of a bolting system define the ultimate load capacity of a rock bolt. Therefore, understanding the nature of any failure occurring in any reinforcement system is essential. Investigating failure behaviour requires a deep understanding of load transfer mechanisms. Rock bolts can experience diverse loading scenarios, ranging from pure shear to tensile loading, often combined with, or compounded by, rotational forces. Nonetheless, when it comes to rock bolts embedded in tunnel rooves, their common failure mode tends to be caused by tension.

The existing literature highlights the extensive number of laboratory tests undertaken to study the behaviour of various rock bolt types, spanning both mechanically-anchored and frictionally-anchored variations. Nevertheless, despite these endeavours, a gap in research persists, particularly in the comprehensive examination of plastic sheathed rock bolts behaviour where a combination of anchoring techniques is complemented by the inclusion of a protective sheath. One of the challenges linked to the inclusion of a protective plastic sleeve around the reinforcing tendon lies in guaranteeing the efficient transfer of loads among the tendon, the grout annuli, and the surrounding ground.

Aziz et al., (2017) conducted a laboratory investigation to assess the integrity of plastic-sheathed cable bolts. The outcomes of both single and double shear tests revealed that the corrugated plastic sheath exhibited noteworthy resistance against shear loads, enduring without substantial damage up to a maximum displacement of 33 mm. Bertuzzi, (2004) conducted an assessment of corrosion-protective anchors situated within tunnels in Sydney, Australia. Additionally, shear tests were carried out on these samples. The study's outcome highlighted that the protective plastic sheaths sustained damage at an approximate shear movement of 15 mm. Villaescusa and Wright, (1999) conducted a series of laboratory and field experiments aimed at establishing the pullout strength of the components of sheathed bolts, with a minimum threshold of 15 kN. The findings demonstrated a substantial enhancement in pullout

capacity through the grouting of sheathed bolts, yielding an impressive increase to over 150 kN per meter of encapsulation length.

This study introduces an extensive experimental investigation on a large scale, with the primary objective of exploring the axial load transfer mechanism of the plastic sheathed rock bolts across various scenarios. Additionally, the examination delved into the failure mode of the systems, seeking to identify the weakest component in the context of pullout loading at different conditions. The outcomes of this study provide valuable insights into the behaviour and performance of the protective sheathed bolting systems under varying conditions, contributing to a deeper understanding of its mechanical response and potential vulnerabilities.

2. Experimental program

2.1. Experimental design

To comprehensively assess the axial behaviour of corrosion protective sheathed bolts, three distinct experimental campaigns were implemented within the pullout testing program, as schematically depicted in Figure 2. These campaigns encompassed the following scenarios: (1) a conventional pullout test featuring an encapsulation length of 1000 mm and a free end, with the load applied directly on the bolt; (2) a double embedment pullout test employing an encapsulation length of 900 mm, still with a free end, but the load being applied on the steel pipes and the other end is fixed; and (3) a double embedment pullout test featuring an effective encapsulation length of 500 mm, without any free end, and with the load applied to the steel pipe. The intent behind the first testing configuration was to replicate *in situ* pullout testing conditions, where the load acts directly on the bolt. In the second testing configuration, the purpose was to simulate practical field conditions where the potential failure of one component (either the external fixtures like the nut/dome or the expansion shell) could lead to bolt slip. However, it is important to note that the other side was securely welded, thereby preventing any slip. The third test was designed to simulate a scenario in the field where both the external fixtures and the expansion shells retain their structural integrity until the steel bar's ultimate capacity is reached. Hence, the primary objective was to assess the system's integrity, particularly focusing on the condition of the protective sheath as the load approached the tensile strength of the bars. For the latter two designs, a joint was incorporated to replicate the presence of a rock mass discontinuity, representing the point where the slip of rock

blocks is initiated, thereby activating the bolts. Throughout the tests, the opening of the joint was tracked using a Linear Variable Differential Transformer (LVDT) to assess the condition of the plastic sheath against displacements. This monitoring assumes significance for designers and engineers, as the plastic sheath must remain intact and undamaged to provide enduring protection against corrosion for the system's entire lifespan. The experimental design encompassed two types of bolts, namely Type-1 and Type-2. The geometric and mechanical attributes of these bolts are tabulated in Table 1. Notably, the bars differ in their geometry and strength properties, as shown in Figure 3. For instance, the Type-1 bolt has a diameter of 24 mm, with yielding and ultimate strengths of 220 kN and 330 kN, respectively.

In contrast, the Type-2 bolt features a nominal diameter of 26 mm, with yielding and ultimate strengths of 533 kN and 620 kN, respectively. In total, six distinct testing scenarios were executed, and certain scenarios were repeated to ensure the precision of the test results. Table 2 provides a concise summary of the conducted tests.

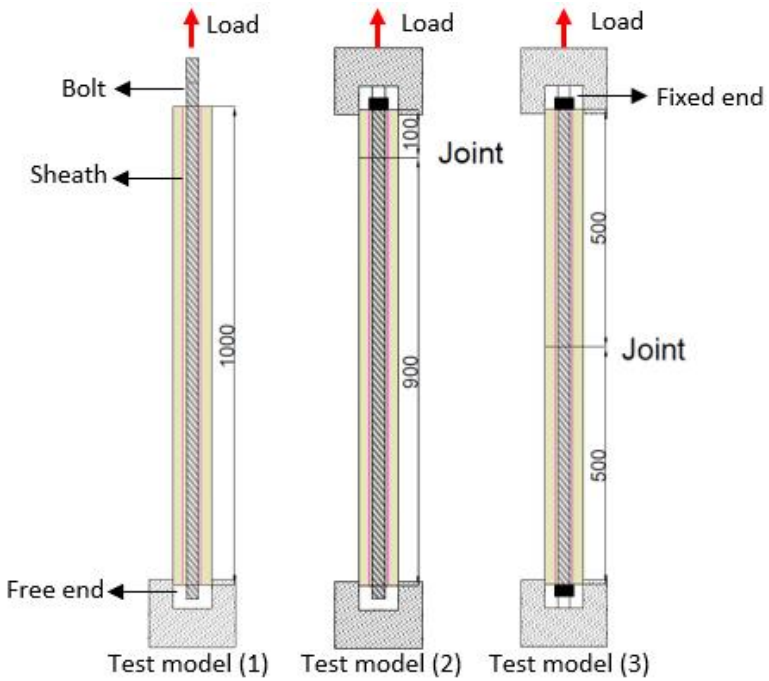

Figure 2. Schematic view of the testing design.

Table 1. Geometric and mechanical characteristics of the protective sheathed bolts used in the tests.

Bolt type	Nominal Diameter	Sheath outside diameter	Sheath thickness	Elastic modulus	Yield strength	Tensile strength	Agt
	(mm)	(mm)	(mm)	(GPa)	(kN)	(kN)	(%)
Type-1	26	43.6	3	200	530	620	8
Type-2	21	35.2	3	200	220	360	8

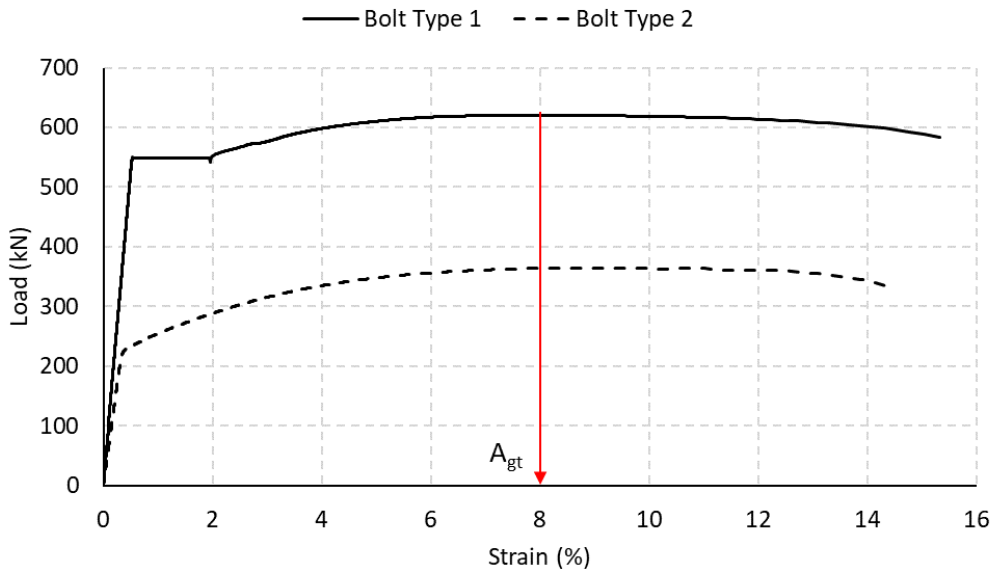

Figure 3. Elongation behaviour of the Type-1 and Type-2 used in the study.

Table 2. Summary of the testing campaign.

Test ID	Testing model*	Bolt type	Effective encapsulation length (mm)*	Bolt slip
A	(1)	Type-2	1000	Free end and loading end
B	(2)	Type-2	900	Only free end
C	(3)	Type-2	500	Slip not allowed
D	(3)	Type-2	500	Slip not allowed
E	(2)	Type-1	900	Only free end
F	(3)	Type-1	500	Slip not allowed

* Refer to Figure 2.

2.2. Specimens design and preparation

A selection of materials was made to thoroughly evaluate the axial behaviour of the protective sheathed bolts across various designs. These materials included a steel hollow bar as the surrounding materials, cementitious grout as the bonding agent and the bolts with the plastic protective sheaths as illustrated in Figure 4a. As shown, the protective plastic sheaths exhibit two types of irregularities on their external surface: circumferential threads and embossed ridges. Additionally, the internal surface features dents. The steel hollow bars (Figure 4b), having an 80 mm outer diameter and a 12 mm thickness, were internally rifled (Figure 4c). This internal rifling served two purposes: simulating field conditions and preventing failures at the junction of the hollow bar and the grout. Additional accessories were designed and manufactured to facilitate the centralisation of the bolts and to enhance the grouting process.

Figure 4. The materials used for specimen preparation including a) Type-1 and Type-2 bolts with the plastic sheaths, b) the manufactured hollow bars, and c) the internal rifling of the pipes.

A specialised approach was implemented to assess bolt deformation along the encapsulation length and to derive the axial load distribution and bond stress across this length. Specifically, the steel bars underwent design modifications for tests (2) and (3). These modifications involved incorporating double-sided triangular grooves, each covering an area of approximately 20 mm². The purpose of these grooves was to provide a suitable surface for mounting resistive strain gauges.

Figures 4 and 5 illustrate both the arrangement of the grooves and the placement of the resistive strain gauges on the bolt.

Figure 5. Grooves, instrumentation, and mounting strain gauges on the steel bars.

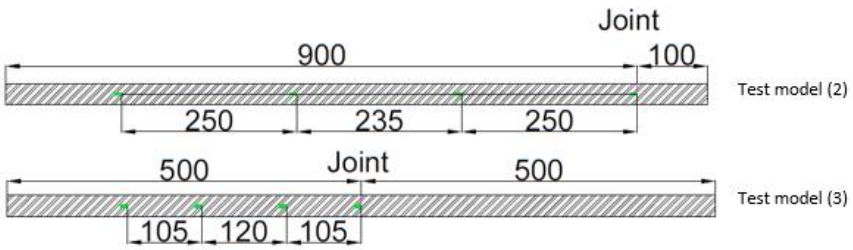

Figure 6. Positions of the strain gauges installed on the bars.

In the process of encapsulating the bolts within the hollow bars, a cementitious grout was employed. This grout was prepared by mixing it with water at a grout ratio of 22%, and it was subsequently introduced into the samples via pumping. The objective was to ensure the complete filling of the gaps between the bar and the plastic sheath, and also between the plastic sheath and the hollow bar. The compressive strength of the grout was determined to be approximately 53±1.2 MPa. Figure 7 shows the prepared specimen for testing model (3). As previously noted, the specimen arrangement in the testing model (1) was devised to allow movement of the bar at both ends. However, in the case of the testing model (2), one end of the bolt was permitted to move freely, whilst the opposite end was welded in order to restrain its movement. Conversely, testing model (3) involved welding the bolts at both ends, immobilising any potential movement along the bolt's length. Figure 7 illustrates the ends of the specimens according to test objectives.

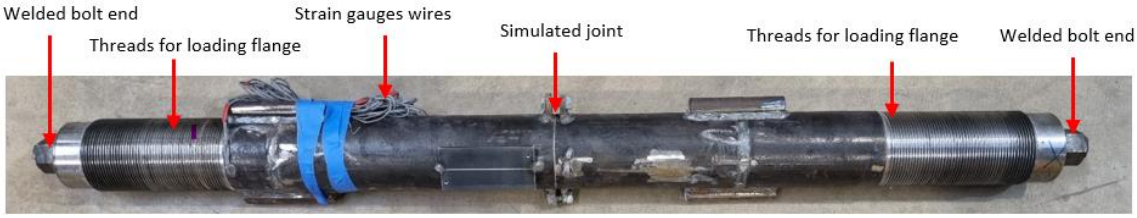

Figure 7. Completed specimen for test model (3).

Figure 8. Conditions of the bolt ends to fulfil the test objectives.

The samples were tested using a large-scale 1000 kN universal testing machine. The application of load was achieved through a hydraulic system, with calibrated load cells and LVDTs employed for measuring both the load and displacement. Upon placing the specimen in the testing machine, the clamps located on the upper crosshead and middle crosshead were tightened to secure the specimens using flanges that were screwed onto the specimens (Figure 8).

Additionally, apart from the load sensors incorporated within the 1000 kN machine, one LVDT was installed on the simulated joint to measure the displacement of the joint, as depicted in Figure 9.

3. Test results and discussion

The findings from the pull tests were analysed and discussed from three distinct perspectives:

1) Load-Displacement relationship: this section explores the connection between applied load and displacement obtained from the pull tests.

2) Bond stress distribution along the encapsulation length: the distribution of the bond stress along the length of the encapsulation is examined in this section.

3) Failure mechanism investigation: the failure mechanism is studied through the longitudinal slicing of the specimens and detailed observational analysis.

3.1. Load-displacement relation

Figure 10 illustrates the load-displacement curves derived from pull tests conducted on the Type-1 bolts using different testing models. Among the specimens, Tests A and B exhibited failures due to debonding at the grout-sheath interface, while specimen D experienced failure due to bar rupture. In specimen C, the test was halted at 2.5% elongation to investigate the protective sheath conditions at this specific elongation.

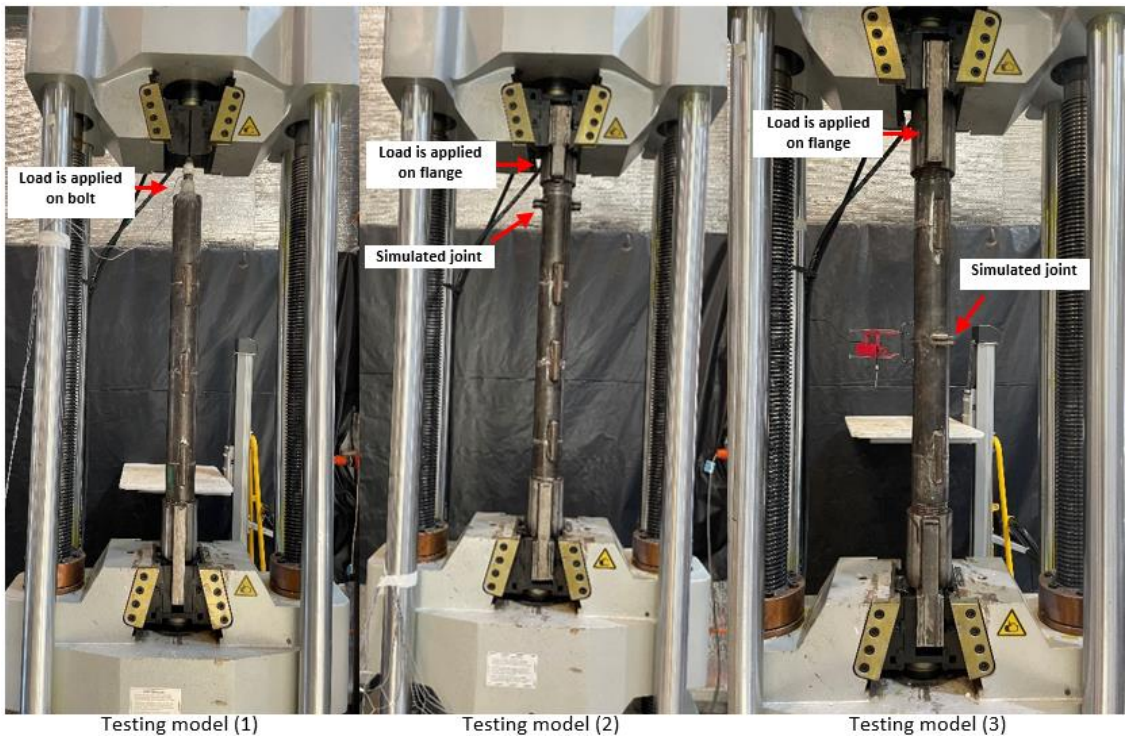

Figure 9. Testing setup for different experimental programs.

In both series A and B, regardless of the loading arrangement, similar load-displacement behaviour was observed. As depicted in Figure 11, in Series A, the load increased linearly with displacement up to 498 kN at 16.2 mm displacement. Beyond this point, the load remained nearly constant with further displacement. This point (498 kN, 16.2 mm) marked the onset of global debonding within the system. The initial linear growth indicated elongation of the steel bar, potentially causing damage to the grouting materials near the loading point. The relevant literature suggests that conventional fully grouted rock bolts exhibit shear-off damage at the bolt-grout interface in such cases (Cui et al., 2020; Hyett et al., 1992). However, these tests yielded circumferential cracks within the grout-filled space between the bolt and the sheath, deviating from shear-off damage. These circumferential cracks most likely stemmed from induced tensile stress within the grout due to the elongation of the bolt. Cracks were initiated once this tensile stress approached the grout's tensile strength. The bolt and grout column were extracted from the system during specimen A's debonding process, as depicted in Figure 12. For an in-depth analysis of the post-test failure patterns, refer to Section 4.3.

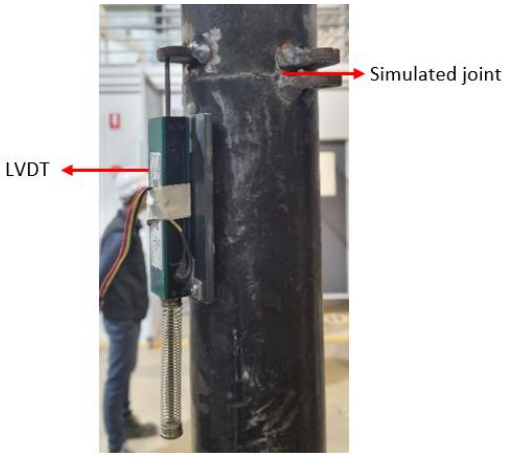

Figure 10. LVDT installed on the joint to measure the corresponding displacements.

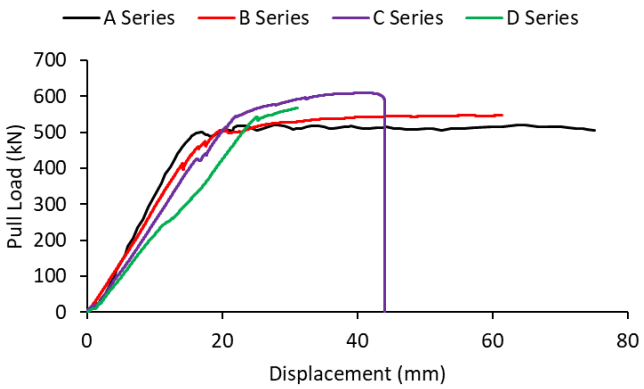

Figure 11. Load-displacement relation for the tests conducted on the Type-2 bolts.

The load-displacement relationship in the series B test mirrors that of series A. Once the load reaches 502 kN at 19.9 mm displacement, the load increase relative to displacement drops notably, and further load increments occur only minimally. The variation in load and displacement values at which debonding of the systems initiates in series A and B can be ascribed to the plastic sheath's efficacy in series B, slightly shifting the corresponding point to the right. Figure 13 shows specimen B following the test. As depicted, the protective plastic sheath underwent rupture caused by considerable stretching. Nevertheless, monitoring the specimen's conditions during the test revealed the plastic sheath remained intact until reaching a displacement of 27 mm. Additionally, there was an observable 47 mm slip at the free end, as illustrated in Figure 13.

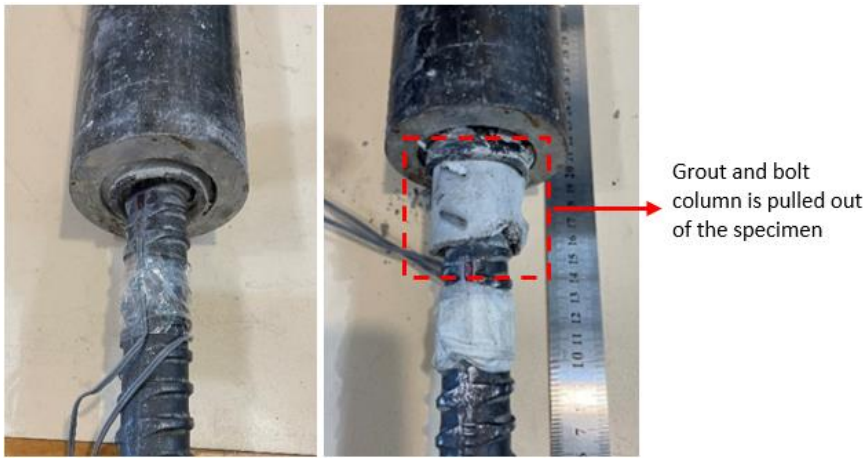

Figure 12. Conditions of the specimen in the series A test: before test (left) and after test (right).

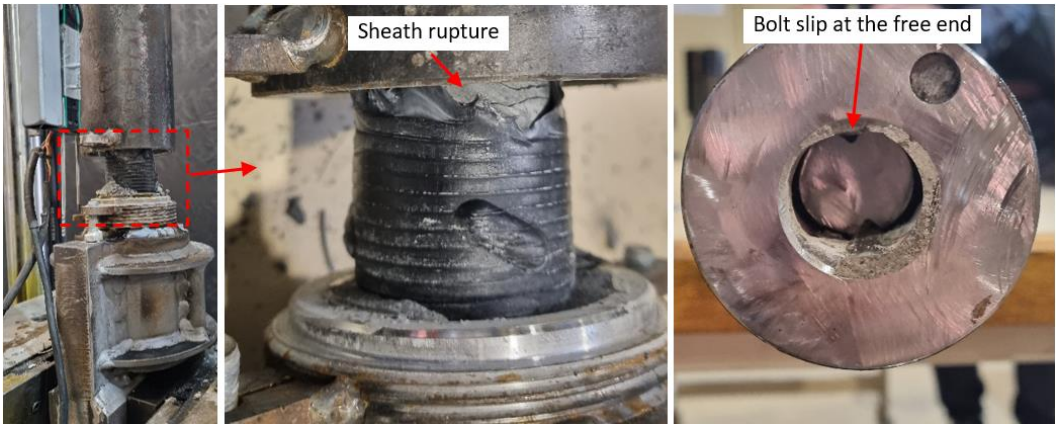

Figure 13. Conditions of specimen B after testing.

The results obtained from the testing of series A and B demonstrate that when the bolt is permitted to slip, the grout-sheath interface emerges as the most vulnerable element within the system (the encapsulation length is under 1000 mm), where debonding failure occurs. This failure at this interface can be attributed to inadequate

friction between the grout and the inner surface of the sheath. This friction deficiency might be attributed to the specific configuration of the plastic sheath's inner surface.

In contrast, the load applied to specimen C surpassed the yield strength of the bar, which is approximately 535 kN. This caused the bolt to deform plastically and reach the ultimate tensile strength, measured at 610 kN. This was followed by necking and eventually, the bolt ruptured at a displacement of 44 mm. During testing, it was observed that the sheath stretched alongside the bolt's deformation. Notably, the sheath remained intact until the bolt ruptured, at which point the sheath was torn completely. For a visual of specimen C after testing, see Figure 14. The results of test C highlight that the load levels in tests A and B remained below the bar's yield strength. This indicates that the critical embedment length in this specific bolting system exceeds 1000 mm.

Test D followed the same approach as test C, yielding comparable results. However, the test was concluded at around 31 mm displacement, equivalent to a load of 568 kN. This was done to specifically monitor the condition of the specimen, particularly the state of the protective sheath, at this specific displacement. Figure 15 illustrates that the sheath remained undamaged and intact, indicating that the corrosion protection measure effectively functions at this level of load and displacement.

Figure 14. The conditions of specimen C after testing.

Figure 15. The conditions of specimen D after testing.

Figure 16 displays the load-displacement curves from tests E and F. Despite differing specimen arrangements, the curves exhibit a high degree of alignment. In test E, where the bar slip from the free end was allowed, the bolt's encapsulation length was adequate to surpass its yield strength (230 kN at 10 mm displacement). Progressing further, the system reached its ultimate tensile strength (320 kN at 45 mm displacement), ultimately rupturing at 285 kN and a displacement of 50 mm. The conditions of the specimen post-test are depicted in Figure 16a. Monitoring during testing revealed that the plastic sheath's strength properties closely resembled those of the sheath utilised in Type-2 bolts. This similarity was evident as both sheaths sustained damage at a displacement of 28 mm.

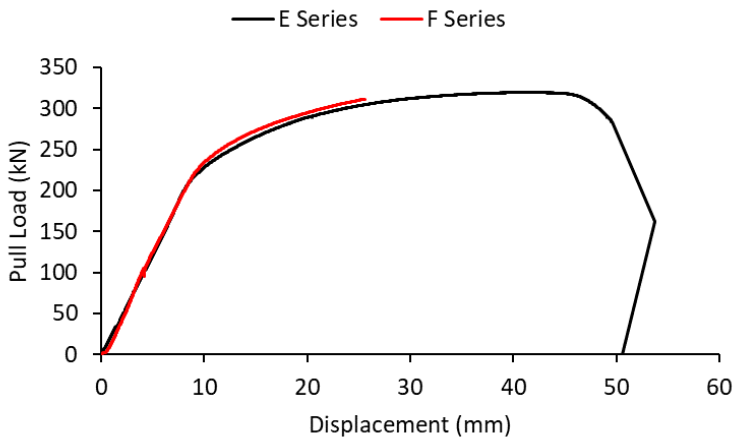

Figure 16. Load-displacement relation for the tests conducted on the Type-1 bolts.

Figure 17. Conditions of the Type-1 specimens after testing: a) test E and b) test F.

3.2. Bond stress distribution along the encapsulation length

Bond pertains to the resistance to shear forces that develops between the bolt and the materials it is bonded to when subjected to a pullout load. Research has revealed that the stress distribution resulting from this bonding at the interface of the bolt and grout and along the length where the rock bolt is fully embedded is not consistent. Despite this, it is often assumed that bond stress distribution is uniform in cases involving short embedded specimens. The measurement of the extent of longitudinal elongation of the bolt along its embedded length through devices like strain gauges allows for the technical quantification of this bond stress distribution. In Figure 18, a schematic is given of the stress equilibrium within a section of a grouted bolt with a specific length (Δx). Under the assumptions of four key conditions, namely 1) the problem is in the elastic stage, 2) a uniform distribution of bond stress across Δx; 3) the absence of energy dissipation in other forms like the creation of fractures, cracks, or damage; and 4) the absence of deformation in the surrounding rock; the force equilibrium equation for Figure 18 can be formulated as follows:

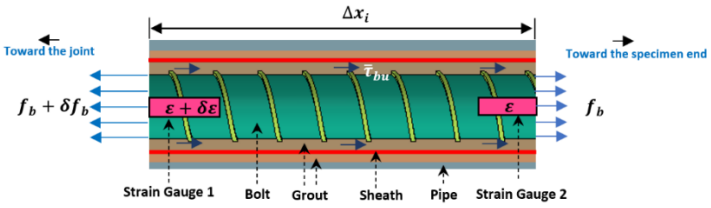

Figure 18. Stress equilibrium in a length of embedded rock bolt.

$$f_b + \delta f_b = f_b + \bar{\tau}_{bu}(\pi d_b \Delta x) \quad (1)$$

where $f_b + \delta f_b$ is the force applied at strain gauge 1, while f_b signifies the force within the bolt at strain gauge 2. The interfacial shear stress at the bolt and grout interface is denoted as $\bar{\tau}_{bu}$, and d_b stands for the bolt's nominal diameter. The separation between the strain gauges is represented by Δx.

Applying constitutive equation ($\sigma = \varepsilon . E$) in Eq.1 the following equation is achieved:

$$(\varepsilon + \delta\varepsilon)Ea_b = \varepsilon Ea_b + \bar{\tau}_{bu}(\pi d_b \Delta x) \quad (2)$$

where $\varepsilon + \Delta\varepsilon$ is the strain measured by strain gauge 1, E is the elastic modulus of the bolt, a_b is the cross area of the bolt and ε is the strain measured by strain gauge 2.

By simplifying Eq.2, interfacial bond stress along Δx can be achieved as follows:

$$\bar{\tau}_{bu} = \frac{\delta\varepsilon E d_b}{4\Delta x} \quad (3)$$

Hence, monitoring the elongation of bolts throughout the embedded length due to the pullout force offers an efficient approach to ascertain the distribution of bond stress at the interface. This knowledge is crucial for the development of accurate models governing the axial behaviour of rock bolts. Although several research efforts have explored the interfacial bond stress in conventional rock bolts, the influence of a protective sheath on axial stress distribution remains unaddressed in existing literature. Investigating this aspect can enhance our comprehension of how axial loads are transferred in such rock bolts, which can ultimately lead to more practical bond-slip models necessary for effective ground control design.

Figure 18 shows that the distribution of bond stress generated along the grout interface in Tests B, C, E, and F. The measurements are taken at various distances from the loading point, with 50 kN load increment intervals. As shown, the pattern of bond stress distribution is influenced by both the specific test type and the system failure mode.

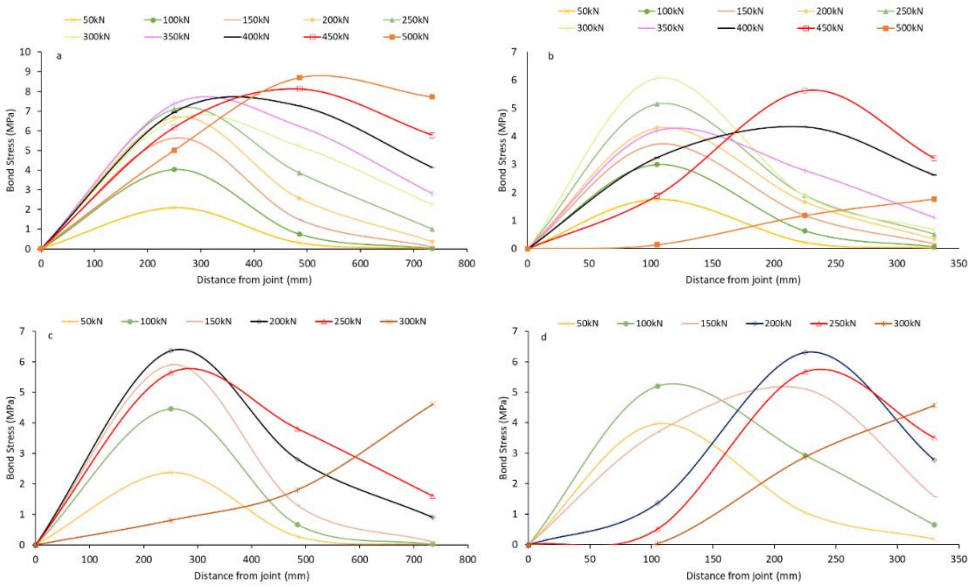

Figure 19. Bond stress distribution along the encapsulation length for a) Test B, b) Test C, c) Test E and d) Test F.

In the graphs depicted in Figure 19, a consistent pattern emerges: at lower levels of axial loading, the interfacial bond stress is most pronounced in the immediate vicinity of the load application point and progressively diminishes with increasing distance from it. Consider Test B as an illustrative case, as presented in Figure 19a. The interfacial bond stress between the first and second strain gauges, spanning a distance of 0-225 mm, achieves its maximum value of 7.5 MPa under a 350 kN axial load. However, the bond stress decreases the further one moves away from the load point. Furthermore, Figure 19a reveals a noteworthy phenomenon.

When the applied axial load is less than 150 kN, the interfacial bond stress at a distance of 735 mm drops to zero. Conversely, when the load surpasses 150 kN, the bond stress remerges and gradually escalates with the increasing load. The reduction in bond stress beyond the 150 kN threshold at the 225 mm point can be attributed to the system's debonding, specifically in that region. By contrast with other cases, Figure 19a demonstrates that once the applied load reaches 500 kN, the induced bond stress attains its peak, ranging between 7.7-8.7 MPa, within the distance interval of 485-735 mm. This particular behaviour can be correlated with the observed failure mode in the specimen, characterised by debonding occurring at the grout-sheath interface, and a relatively constant load is sustained until the conclusion of the test. Notably, in instances where debonding transpires within a specimen section, such as the 0-225 mm range in Test B, the bond stress tends to shift deeper into the specimen and persists until complete debonding of the system is attained. Such behaviour is conventionally observed in the context of fully grouted rock bolts (refer to relevant literature). However, in the case of protective sheathed rock bolts, this behaviour deviates, as failure predominantly manifests in two distinct modes: a rupture in the bolt shank and failure at the grout-sheath interface.

In Test C, as illustrated in Figure 19b, a similar trend emerges, with bond stress initially peaking in the proximity of the loading point and gradually diminishing with increasing distance. Notably, this test records instances where bond stress registers at zero at a distance of 330 mm when subjected to a load of 150 kN or less. Analysing the graph reveals that debonding within the 0-105 mm section transpires as soon as the applied load reaches 300 kN. Subsequently, the bond stress decreases within this section, while concurrently, bond stress increases in the deeper section, specifically the range of 105-225 mm. When the load reaches 500 kN, the bond stress significantly diminishes, nearly reaching zero at the 0-105 mm, 1.8 MPa at 105-225 mm and

1.7 MPa at 225-330 mm. This suggests that complete debonding occurred in the 0-225 mm section, and partial debonding at 225-330 mm. Consequently, once debonding transpires in a specific section, the bond stress redistributes to the adjacent section deeper within the encapsulation length.

In Test E, depicted in Figure 19c, the highest recorded bond stress reached 6.4 MPa within the 0-225 mm range, corresponding to a 200 kN load. Notably, partial debonding emerges in this section once the applied load exceeds 200 kN. Following a pattern observed in previous tests, debonding at 0-250 mm leads to a redistribution of bond stress to the 250-485 mm section, where the bond stress increases to 3.8 MPa at a 250 kN load. Reduction in the bond stress at the 250-485mm section once the axial load increases to 300 kN can be associated with the debonding of the system at this section. The results indicate that full debonding is evident in the 0-250 mm segment, while in the 250-485 mm section, partial debonding resulted in a notable reduction in bond stress.

In Test F, as illustrated in Figure 19d, the bond stress initially increases with the applied load within the 0-105 mm range, reaching 5.2 MPa at 100 kN. Subsequently, a decrease in bond stress is observed due to partial debonding, ultimately leading to complete debonding within this section and the bond stress dropping to zero. Notably, as soon as debonding occurs at 0-105 mm, there is a substantial increase in bond stress observed in the 105-225 mm section. Remarkably, the bond stress within the 105-225 mm section reaches 6.3 MPa, corresponding to a 200 kN load. However, the bond stress in this section decreases afterwards, indicating significant debonding in this region, with the bond stress transferring to the 225-330 mm section. The highest recorded bond stress within the 225-330 mm section reached 4.6 MPa, corresponding to a 300 kN pull load.

3.3. Failure mechanism of the specimens

In the existing literature, investigations into the failure modes of specimens subjected to pullout conditions typically considered two key aspects: firstly, the cone-shaped damage that occurs near the loading end within the host rock and encapsulation material, and secondly, failures that happened at the interface between the bolt and the bonding material. These latter failures often manifested as either bolt ruptures or failures at the bolt-grout interface. In this study, using a waterjet system to slice the specimens has shed light on the prevalent failure modes in sheath-protected

bolts compared to conventional rock bolting systems. It was observed that, unlike conventional systems, sheath-protected bolts primarily exhibited bolt rupture as their mode of failure. However, this holds true only when the encapsulation length is sufficiently long or when the anchoring and external fixtures are robust enough to withstand the applied load without failing.

Tests A and B share almost identical failure characteristics. In both cases, circumferential cracks, oriented at approximately 90 degrees, are visible within the grout situated between the bolt and the protective sheath, spanning a length of about 130 mm. Beyond this point, no cracks were visible. Further investigations suggested that the absence of shear-off failure at the bolt-grout interface indicated that these circumferential cracks likely resulted from tensile stress induced by the bolt's elongation, exceeding the tensile strength of the grout. Further examination revealed an apparent shear failure at the grout-sheath interface. Consequently, the primary failure mode in Tests A and B can be attributed to slipping at the grout-sheath interface.

In Test C, extensive cracking was evident over a distance of 210 mm from the joint, followed by inclined cracks with lower density extending another 290 mm. However, beyond this length, the grout appeared to be intact. This failure pattern closely aligned with the bond stress distribution presented in Figure 19b. For instance, the reduction in bond stress at the 500 kN load within the 0-225 mm range indicated extensive debonding and failure in this segment. Consequently, the axial load was transferred toward the end of the specimen, and resulted in reduced bond stress. It's also worth noting that the protective sheath experienced extensive stretching at the joint, leading to sheath rupture.

In Test E, grout damage was observed at the bolt-grout interface along the entire encapsulation length. Due to slippage occurring at this interface, the irregularities on the sheath's surface, known as dents, were sheared off. Three types of cracks were identified along the encapsulation length: densely distributed cracks perpendicular to the bolt axis within the region located 200 mm from the joint, less densely distributed cracks perpendicular to the bolt axis from 200 mm to 400 mm, and a region from 400 mm to 900 mm where the grout appeared to be crushed. In the first two regions, debonding was evident at the bolt-grout and grout-sheath interfaces. By contrast, in the third region, the grout at the bolt-grout interface seemed to remain intact without visible damage. The bond stress distribution presented in Figure 19c

supported this failure mode, with the low bond stress in the 0-485 mm section at an axial load of 300 kN correlated with the described level of debonding. It can be concluded that while the grout was fully damaged at the grout-sheath interface (0-900 mm) and partially damaged at the bolt-grout interface (approximately 0-400 mm), the bolt failure occurred at the shank near the joint when the load reached 320 kN.

In Tests F, grout damage was observed at the bolt-grout interface on both sides of the joint (500-500 mm). The extent of grout damage, in terms of cracks between the bolt and sheath, extended to approximately 320 mm from the joint on both sides. Notably, significant cracks were evident in the vicinity of the joint (within 120 mm). Importantly, there was no bolt slippage, as indicated by the intact irregularities on the grout surface created by the bolt ribs. This suggests that the grout's failure type was not shear-off but rather resulted from the induced elongation of the bolt. The circumferential cracks observed were a consequence of tensile stress rather than shear stress distribution at the bolt-grout interface.

4. Conclusion

In this study, the behaviour of plastic-sheathed rock bolts under various testing conditions was investigated. The primary objective was to gain insights into how the inclusion of protective sheaths affects the transfer of axial loads in these bolts. Two types of protective sheathed bolts, Type-1 and Type-2, were examined, and three different test setups were designed to explore the dynamics of rock bolting in a comprehensive way. To analyse bond stress distribution along the sheath, strain gauges were installed on the bolts, and six pull tests were conducted.

Overall, two distinct trends in the load-displacement curves were observed, regardless of the bolt type, depending on the test setup. When the expansion shell and external fixtures could sustain the tensile capacity of the bolt or when the encapsulation length exceeded a critical threshold (900 mm for Type-1 and over 1000 mm for Type-2), the system failed due to bolt rupture. In such cases, the load-displacement curves followed the tensile behaviour of the bolts. If these conditions were not met, the system failed through debonding at the grout-sheath interface, known as slip failure.

Type-1 and Type-2 bolts experienced the first type of failure at peak loads of 320 kN and 610 kN, respectively. The second type of failure, characterised by grout-sheath interface debonding, was only observed in Type-2 bolts, commencing at a load

of 500 kN, ultimately resulting in the extraction of the grout and bolt column from the specimen.

The analysis of strain gauge data revealed that bond stress distribution is dependent upon the specimen's failure mode. The peak bond stress measured within all specimens fell in the range of 6-8.7 MPa. It was observed that when debonding occurred in one section of the specimen, the bond stress in that section decreased and shifted to other sections. In slip failure cases, the bond stress remained relatively constant along the intact encapsulation length (7.7-8.7 MPa in Test B). However, in Test C, extensive debonding at a 500 kN load significantly reduced bond stress in those sections.

Interestingly, shear-off failures at the bolt-grout interface were not detected, which is a phenomenon that is commonly observed in conventional rock bolting systems. Instead, grout shear failures at the grout-sheath interface were observed, which are a characteristic of slip failure. Generally, circumferential cracks oriented approximately 90° to the bolt's direction were observed regarding damage and cracks. These cracks resulted from the extensive elongation of the bolt, and the low adhesive and interlock strength between the grout and sheath allowed the induced tensile stress to surpass the grout's tensile strength, initiating crack formation. These failure patterns were effectively related to the distribution of bond stress.

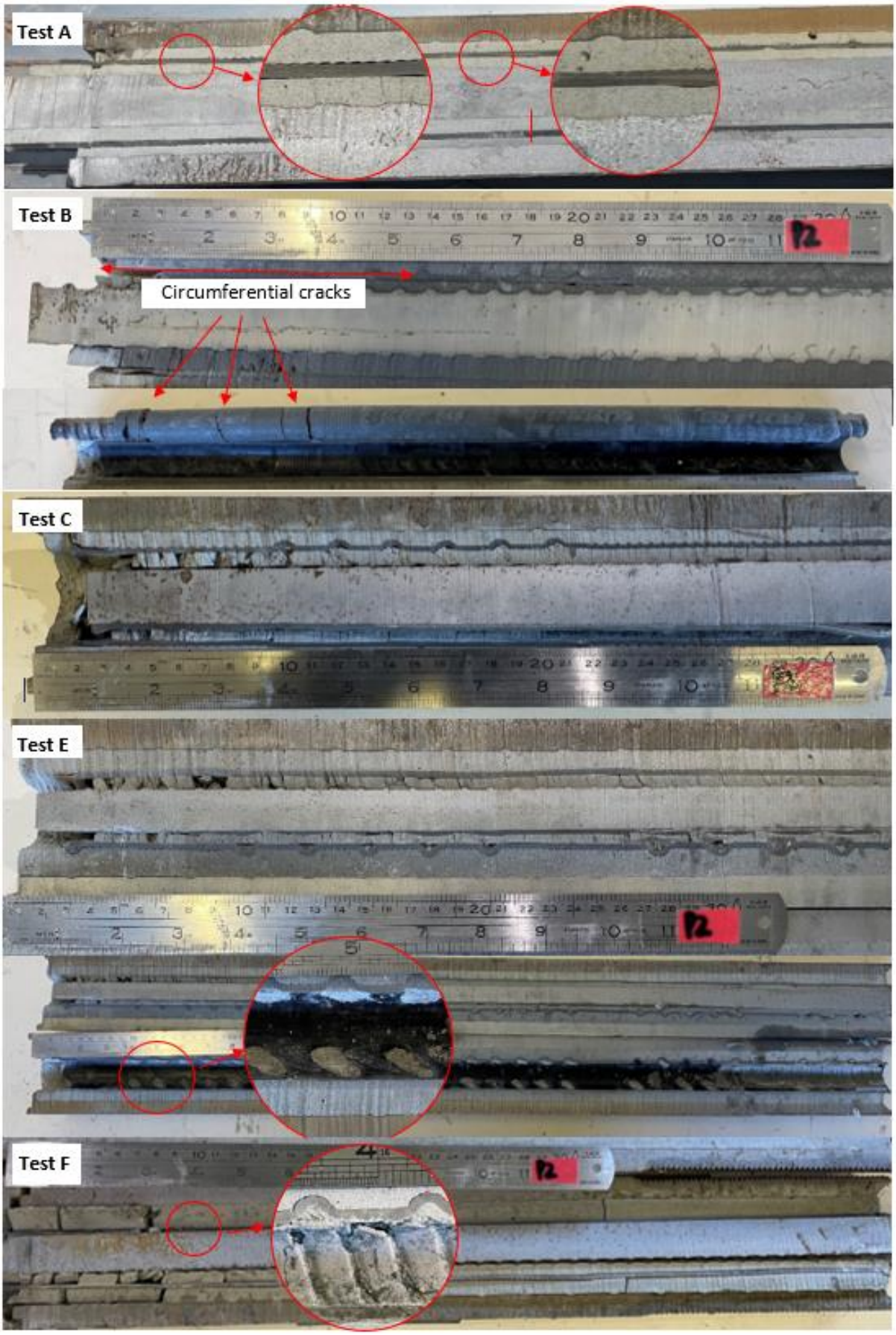

Figure 20. Conditions of the specimens after testing.

References

Aziz N, Craig P, Nemcik J, Hai F, Craig P, Nemcik J, et al. Rock bolt corrosion – an experimental study. Min Technol 2014;9009. https://doi.org/10.1179/1743286314Y.0000000060.

Aziz N, Mirzaghorbanali A, Holden M. The extent of shearing and the integrity of protective sleeve coating of cable bolts of protective sleeve coating of cable bolts. Coal Oper. Conf., Wollongong, Australia: 2017, p. 240–6.

Bertuzzi R. 100-year design life of rock bolts and shotcrete. Gr. Support Min. Undergr. Constr., London: Taylor & Francis Group; 2004.

Cao C, Jan N, Ren T, Naj A. A study of rock bolting failure modes. Int J Min Sci Technol 2013;23:79–88. https://doi.org/10.1016/j.ijmst.2013.01.012.

Chen H, Kimyon O, Ramandi HL, Manefield M, Kaksonen AH, Morris C, et al. Microbiologically influenced corrosion of cable bolts in underground coal mines : The effect of Acidithiobacillus ferrooxidans. Int J Min Sci Technol 2021;31:357–63. https://doi.org/10.1016/j.ijmst.2021.01.006.

Chen H, Lamei H, Craig P, Crosky A, Saydam S. Tunnelling and Underground Space Technology incorporating Trenchless Technology Research Stress corrosion cracking of cable bolts in tunnels : An in-situ testing approach. Tunn Undergr Sp Technol Inc Trenchless Technol Res 2022;123:104421. https://doi.org/10.1016/j.tust.2022.104421.

Chen H, Lamei Ramandi H, Walker J, Crosky A, Saydam S. Failure of the threaded region of rockbolts in underground coal mines. Min Technol 2018;127:146–54. https://doi.org/10.1080/14749009.2018.1428060.

Craig P, Lamei H, Chen H, Vandermaat D, Crosky A, Hagan P, et al. Stress corrosion cracking of rockbolts : An in-situ testing approach. Constr Build Mater 2021;269:121275. https://doi.org/10.1016/j.conbuildmat.2020.121275.

Cui G, Zhang C, Pan Y, Deng L, Zhou H. Laboratory investigation into effect of bolt profiles on shear behaviors of bolt-grout interface under constant normal stiffness (CNS) conditions. J Rock Mech Geotech Eng 2020;12:1234–48. https://doi.org/10.1016/j.jrmge.2020.03.010.

Fahimifar A, Ranjbarnia M. Analytical approach for the design of active grouted rockbolts in tunnel stability based on convergence-confinement method. Tunn Undergr Sp Technol 2009;24:363–75. https://doi.org/10.1016/j.tust.2008.10.005.

Grasselli G. 3D Behaviour of bolted rock joints: experimental and numerical study. Int J Rock Mech Min Sci 2005;42:13–24. https://doi.org/10.1016/j.ijrmms.2004.06.003.

He L, An X., Zhao Z. Fully Grouted Rock Bolts : An Analytical Investigation. Rock Mech Rock Eng 2015:1181–96. https://doi.org/10.1007/s00603-014-0610-0.

Hyett AJ, Bawden WF, Richert D. The Effect of Rock Mass Confinement on the Bond Strength of Fully Grouted Cable Bolts. Int J Rock Mech Min Sci Geomech Abstr

1992;29:503–24.

Kilic A, Yasar E, Atis CD. Effect of bar shape on the pull-out capacity of fully-grouted rockbolts. Tunn Undergr Sp Technol 2003;18:1–6. https://doi.org/https://doi.org/10.1016/S0886-7798(02)00077-9.

Li CC. Principles of rockbolting design. J Rock Mech Geotech Eng 2017;9:396–414. https://doi.org/10.1016/j.jrmge.2017.04.002.

Li CC, Stjern G, Myrvang A. A review on the performance of conventional and energy-absorbing rockbolts. J Rock Mech Geotech Eng 2014;6:315–27. https://doi.org/10.1016/j.jrmge.2013.12.008.

Ma KJ, Stankus J, Faulkner D. Development and evaluation of corrosion resistant coating for expandable rock bolt against highly corrosive ground conditions. Int J Min Sci Technol 2018;28:145–51. https://doi.org/10.1016/j.ijmst.2017.12.023.

Ma S, Nemcik J, Aziz N. An analytical model of fully grouted rock bolts subjected to tensile load. Constr Build Mater 2013;49:519–26. https://doi.org/10.1016/j.conbuildmat.2013.08.084.

Martín LB, Tijani M, Hadj-hassen F. A new analytical solution to the mechanical behaviour of fully grouted rockbolts subjected to pull-out tests. Constr Build Mater 2011;25:749–55. https://doi.org/10.1016/j.conbuildmat.2010.07.011.

Peter K, Moshood O, Oluwatomisin P. An Overview of the Use of Rockbolts as Support Tools in Mining Operations. Geotech Geol Eng 2022;40:1637–61. https://doi.org/10.1007/s10706-021-02005-5.

Rastegarmanesh A, Mirzaghorbanali A, McDougall K, Aziz N, Anzanpour S, Nourizadeh H, et al. Axial Performance of Cementitious Grouted Cable Bolts Under Rotation Constraint Scenarios. Rock Mech Rock Eng 2022. https://doi.org/10.1007/s00603-022-02950-4.

Singh P, Jang H, Spearing AJS. Improving the Numerical Modelling of In-Situ Rock Bolts Using Axial and Bending Strain Data from Instrumented Bolts. Geotech Geol Eng 2022;40:2631–55. https://doi.org/10.1007/s10706-022-02051-7.

Singh P, Spearing AJS, Jessu K. Analysis of the Combined Load Behaviour of Rock Bolt Installed Across Discontinuity and Its Modelling Using. Geotech Geol Eng 2020;38:5867–83. https://doi.org/10.1007/s10706-020-01398-z.

Thompson AG, Villaescusa E, Windsor CR. Ground Support Terminology and Classification: An Update. Geotech Geol Eng 2012;30:553–80. https://doi.org/10.1007/s10706-012-9495-4.

Villaescusa E, Wright J. Reinforcement of underground excavations using the CT Bolt. Rock Support Reinf. Pract. Min., London: Routledge; 1999. https://doi.org/https://doi.org/10.1201/9780203740460.

Windsor CR. Rock reinforcement systems. Int J Rock Mech Min Sci 1997;34:919–51.

Wu S, Lamei H, Chen H, Crosky A, Hagan P, Saydam S. Mineralogically influenced stress corrosion cracking of rockbolts and cable bolts in underground mines. Int J Rock Mech Min Sci 2019;119:109–16. https://doi.org/10.1016/j.ijrmms.2019.04.011.

6.2. Links and implications

This Chapter introduces an extensive experimental investigation focusing on large scale testing, aiming to understand the axial load transfer mechanism of the plastic sheathed rock bolts. Furthermore, the analysis explored the primary failure mode of these rock bolts. Three distinct testing setups were designed to evaluate comprehensively the performance of protective sheathed rock bolts in various conditions. The results indicated that the failure characteristics and axial behaviours of these rock bolts vary from the conventional rock bolts. The investigation carried out in this chapter fulfils the gap highlighted in the literature review. The findings provide valuable insights into the behaviour and performance of the protective sheathed bolting systems under varying conditions, contributing to a deeper understanding of their mechanical response and potential vulnerabilities.

CHAPTER 7: DISCUSSION AND CONCLUSION

Rock bolts have widespread applications in mining and geotechnical engineering, effectively enhancing rock mass stability while reducing deformations. This results in improved safety, cost efficiency, and time management. Nevertheless, there is a crucial need for in-depth investigations into the axial behaviour of rock bolts under various geotechnical conditions. Specifically, our understanding is lacking when it comes to how rock bolt systems respond to elevated temperatures, triaxial pressure, and variations in parameters like encapsulation length, grout properties, and rock characteristics. Additionally, with the increasing use of sheathed rock bolts in corrosive environments, there is a demand for a closer examination of their performance under axial loads. These critical aspects of research have been somewhat neglected, limiting their practical applicability. To address these knowledge gaps, this thesis conducted comprehensive experimental and analytical studies, delving into the axial load transfer mechanisms of various types of rock bolts under a range of conditions. The outcomes of this research significantly enhance our comprehension of how rock bolts handle axial loads, providing valuable insights for the selection and design of rock bolts for diverse engineering applications. Furthermore, this knowledge has the potential to greatly enhance and assess current solutions for rock bolt design. The major findings from this work are presented in the succeeding sections.

7.1. State-of-the-art review of axial behaviour of rock bolting systems

The stability of underground excavations is a primary concern for geotechnical and mining engineers seeking to improve workers' safety, reduce environmental issues, and avoid financial loss. Rock bolts are generally considered the most adaptable and efficient reinforcement system in complex ground conditions. Amongst the different types of rock bolts, fully grouted rock bolt installation is considered the most common type of rock bolt in mining and civil engineering. The failure of fully grouted rock bolts can occur in different modes, however, it has been acknowledged that failure at the bolt-grout interface is the ordinary mode. The investigation of interfacial shear behaviour requires a deep understanding of axial load transfer mechanisms. To date, numerous laboratory tests have been conducted to characterise the behaviour of the bolt-grout interface. The results indicated that the system's interfacial and axial response depends on the rock bolts mechanical and geometrical characteristics, mechanical characteristics of grout, geo-mechanical

properties of the rock mass, boundary conditions and environmental conditions such as groundwater and temperature. Amongst these factors, bolt geometry, bolt mechanical characteristics and grout composition and mixture can be engineered and optimised for the preferable performance. However, other factors such as confining stresses, rock mass quality and environmental conditions are intrinsic characteristics and cannot be modified. Nevertheless, a lack of study is evident to systematically investigate the combined effects of the factors mentioned above on the axial behaviour of rock bolting systems. The combined effects refer to the investigation of the effects of host rock strength, confining pressure, elevated temperature, and grout strength characteristics together on rock bolt behaviour. From this extensive review, the following findings were drawn:

- Grout acts as a medium to transfer initiated stress from the bolt to the stable rock mass and also to transfer the *in-situ* stress from the surrounding rock to the bolt-grout interface. The interaction between the mechanical characteristics of the grout and rock bolt behaviour has been well studied, however, the effects of combined thermo-mechanical properties of encapsulation materials, in particular resins, have not been well studied in underground applications.

- *In-situ* stress has a crucial role in the failure mode of an excavation. Conversely, external confining stress can enhance the performance of rock bolts. Therefore, it is essential to carefully consider the effect of *in-situ* stresses on the behaviour of rock bolts for their design. The existing studies in the literature have certain limitations in understanding the behaviour of fully grouted rock bolts under varying confining pressure conditions. In reality, the stress state surrounding underground openings is non-uniform and can differ significantly in different areas of a rock mass. This non-uniformity may result in variations in the mechanical response of rock bolts that cannot be captured by previously developed models.

- Rock mass characteristics can heavily influence the critical failure mechanism, failure location, and bond stiffness in the design of rock bolt systems. The axial slip of deformed reinforcing elements causes radial dilation, which is limited or inhibited by the rock mass's normal stiffness. A higher normal stiffness can lead to higher induced lateral confining stress and higher interfacial bond strength. However, the effect of encapsulation length and the encapsulation materials' strength properties, combined with the surrounding rock mass' properties, has been neglected.

- An extensive number of laboratory tests were undertaken to study the behaviour of various rock bolt types, spanning both mechanically and frictionally anchored variations. Nevertheless, despite these endeavours, a gap in research persists, particularly in the comprehensive examination of the axial performance of the plastic protective sheathed rock bolts, where a combination of anchoring techniques is complemented by the inclusion of a protective sheath.

7.2. Characterisation of mechanical and bonding properties of anchoring resins under elevated temperature

Mechanical and thermal characteristics and behaviour of commonly used anchoring Unsaturated Polyester Resins (UPR) were studied. Additionally, the bearing performance of encapsulated rock bolts was investigated under elevated temperatures in simulated underground heating conditions. Furthermore, the interrelationship between the bearing capacity of rock bolts under ambient and elevated temperature conditions and the thermo-mechanical characteristics of the anchoring materials was examined, and the relevant failure patterns were analysed. From the findings of this investigation, the following conclusions were drawn:

- **Thermal characteristics:** The TGA analysis revealed that the synthesised specimens decomposed at around 340°C. Using water-based catalysts led to slightly higher curing degrees compared to oil-based ones, with Resins A and C achieving 80% curing in 0.5 hr, while Resins B and D needed 1 hr. The mechanical properties of the specimens significantly decreased beyond 55-63°C. Scanning electron microscopy showed that water-based catalysts resulted in more porous resins compared to oil-based ones, causing defects.

- **Mechanical properties:** Compressive strength and elastic modulus of the resins ranged from 51-103 MPa and 4.71-8.03 GPa, respectively. Water-based catalyst resins had more voids, leading to lower strength and modulus than oil-based catalyst resins. Varying filler particle sizes, ranging from micro to millimetre, showed potential for improving compressive strength and elastic modulus.

- **Curing characteristics**: The tested resins achieved nearly 50% of their ultimate compressive strength after just 1 hour. Specimens under compression displayed cone-shaped rupture and varying degrees of bulging, influenced by catalyst type and curing time. Tensile strength ranged from 7.29 to 10.81 MPa, with smaller filler particle sizes improving it. Shear strength ranged from 9.15 to 17.73 MPa. The

bond strength of anchored bolts at ambient conditions ranged from 99.3-139.2 kN, correlating well with compressive and shear properties.

- **Bonding characteristics in elevated temperatures:** In a unique setup simulating elevated temperatures, the bond capacity of bolts decreased by 6.6% to 31.3% at 75°C and 150°C, respectively. However, Resins A and D managed to retain 62.6% and 57.5% of their bond strength at 250°C compared to the initial strength.

7.3. Failure characterisation of fully grouted rock bolts under triaxial testing

This study qualitatively discusses an experimental study in which rock bolts embedded in cubic specimens of concrete were tested under triaxial stress conditions. In this study, a series of push tests were conducted under triaxial conditions, where non-uniform confining stresses ($\sigma_2 \neq \sigma_3$) were applied to cubic specimens to investigate the previously neglected effect of intermediate principal stresses on rock bolt strength properties. This non-uniformity may result in variations in the mechanical response of rock bolts that cannot be captured by previously developed models. The study investigated the interaction between confining stresses and the principal stress ratio ($k=\sigma_2/\sigma_3$) and interfacial bond strength. It should be noted that planes of zero shear stress were considered in the test design, where the normal stress components become principal ($\tau_{xy}=\tau_{yx}=0$, $\sigma_x=\sigma_2$, $\sigma_y=\sigma_3$). Finally, the lateral displacement associated with the outer surfaces of the cubic specimen during push-out was analysed. Here are the key findings:

- **Ultimate bearing capacity:** The ultimate bearing capacity of grouted rock bolts depends on the confining stresses. Increasing principal stresses to 2.5 MPa in both directions does not significantly enhance the bearing capacity; it only increases by 3.5% compared to no confining stress. However, when principal stresses are raised to $\sigma_2=\sigma_3=10$ MPa and $\sigma_2=20$ and $\sigma_3=10$ MPa, a substantial 38.7% and 66.6% increase in peak load, respectively, is observed.

- **Load-displacement behaviour:** Confinement conditions strongly affect the behaviour of the system. Unconfined specimens exhibit a nearly linear relationship between load and displacement, whereas, at lower levels of confinement, the load increases linearly and then exponentially with displacement. When confining stresses reach $\sigma_2=15$ MPa, $\sigma_3=10$ MPa, and $\sigma_2=20$ MPa, $\sigma_3=10$ MPa, the load-slip curve becomes non-linear from the beginning. The interfacial stiffness at the bolt-grout

interface slightly decreases until a 0.5 mm displacement, then gradually decreases until failure. For confined specimens, initial stiffness depends on the level of confining stress, but it tends to decrease exponentially until failure.

- **Interfacial shear stress:** There's a linear relationship between σ_2 and interfacial shear stress, regardless of the magnitude of principal stress ratios. The effect of σ_2 on interfacial shear stress gradually decreases at a certain level of σ_3. Principal stress ratios have a more significant impact on interfacial shear stress at higher σ_3 values.
- **Lateral deformation:** Relative lateral deformation curves show three distinct stages for all cases. Initially, there's shrinkage when confining stress is applied, followed by dilation as the bolt moves. The dilation rate decreases as bolt slip reaches around 7 mm, and then specimens tend to shrink again until the test's end. The magnitude of confining stress primarily influences shrinkage and dilational behaviour.
- **Failure mechanisms:** Failure mechanisms vary with the level of confinement. At lower confinements, specimens tend to fail via splitting, while at higher loads, the failure mechanism shifts to pure interfacial shear-off and shear-crushed modes. Radial fractures appear in both the annulus area and artificial rock. However, at medium levels of confinement, fractures only appear in the grout zone. At higher levels of confining stress, no visible fracturing occurs.

7.4. Unveiling axial load transfer mechanism in fully encapsulated rock bolts

This study presents a comprehensive laboratory study on the pullout performance of fully grouted rock bolts and aims to address the four fundamental questions regarding the axial load transfer mechanism of rock bolting. They are: (1) What is the effect of embedment length on the distribution of bond stress and failure of the system? (2) What is the effect of bonding material type on the bond stress distribution? (3) What is the relation between peak bond resistance and bonding material type? and (4) What is the effect of host rock properties on the bond stress distribution and failure mechanism of the bolts? The results should provide useful insights for the design and selection of rock bolts for various engineering applications. This information can also effectively contribute to assessing and improving the available analytical solutions for rock bolting design.

Three types of chemical agents as well as three types of cementitious grouts

with and without additives, were used to investigate their mechanical characteristics and influence on the axial behaviour of rock bolts. To determine the effect of surrounding rock mass, three different strengths of concrete ranging from 20-60 MPa were used. Pullout tests were performed on fully instrumented and encapsulated rock bolts installed in prepared concrete cylinders with varying encapsulation lengths. The purpose of the pullout experiments is to evaluate the combined effect of grout properties, surrounding rock quality, and embedment length on bond behaviour. The evolution of the interfacial bond stress along the encapsulation length was also determined by measuring and recording strain values on the mounted strain gauges. The key findings of this study are presented as detailed below.

- **Load-displacement behaviour:** Fully debonded specimens displayed two main trends in load-displacement curves: an initial linear segment representing the elastic behaviour of the steel bolt, followed by a non-linear phase indicating plastic deformation in the bonding system (debonding of the bolt). Increasing embedment length from 100 mm to 200 mm improved peak pullout strength by 29-43%, further increasing to 62-69% at 300 mm. Beyond a critical length, the peak pullout load remained constant, equal to the bolt bar's tensile strength.

- **Effect of bonding agent:** The compressive strength of the bonding agent alone couldn't predict pullout performance. For instance, grouted rock bolts with G1 had 10-20% higher pullout strength than those with R1 bonding agents, even though G1's compressive strength was 15% lower than R1's.

- **Distribution of bond stress:** Bond stress distribution depends on the system's failure mode (shank rupture or bolt-grout interface failure). Bond stress increased with a higher pullout load, regardless of embedment length. Longer embedment length diffused pullout load over a larger area, reducing stress concentration. The shear modulus of bonding materials had a significant impact on axial load transfer and bond stress distribution at the bolt-grout interface.

- **Failure patterns:** Three main damage patterns were identified at the bolt-grout interface: shear-off, a combination of shear-off and inclined cracks near the collar, and inclined cracks without effective debonding. These patterns depended on the system's failure mode and peak pullout load.

- **Effect of expansion in bonding agents:** The expansion characteristics of the bonding agent played a crucial role in improving pullout capacity. Series D, using

an expandable grout (G2), exhibited the highest bearing capacity.

- **Surrounding rock strength:** The concrete's compressive strength significantly influenced bolt pullout capacity. Increasing concrete strength from 20 MPa to 60 MPa resulted in a 3-20% increase in pullout strength.

7.5. Exploring the axial performance of protective sheathed rock bolts through large-scale testing

This study aimed to investigate the behaviour of plastic-sheathed rock bolts under various testing conditions, particularly focusing on how protective sheaths influence axial load transfer. Two types of protective sheathed rock bolts, Type-1 and Type-2, were studied across three different test setups to comprehensively understand the behaviour of these types of rock bolting systems. To analyse bond stress distribution along the sheath, strain gauges were applied to the bolts, and six pull tests were conducted. The following conclusions were drawn from the main findings of this study:

- **Load-displacement curves:** Two distinct trends emerged in the load-displacement curves, independent of bolt type, based on the test setup. When the expansion shell and external fixtures could handle the bolt's tensile capacity or when the encapsulation length exceeded a critical threshold (900 mm for Type-1, over 1000 mm for Type-2), the system failed due to bolt rupture. In these cases, the load-displacement curves followed the tensile behaviour of the bolts. If these conditions weren't met, the system failed through debonding at the grout-sheath interface, known as slip failure.

- **Failure modes:** Type-1 and Type-2 bolts experienced the first type of failure at peak loads of 320 kN and 610 kN, respectively. The second type of failure, involving grout-sheath interface debonding, occurred exclusively in Type-2 bolts, commencing at a 500 kN load, eventually leading to the extraction of grout and the bolt column.

- **Bond stress distribution:** Analysis of strain gauge data revealed that bond stress distribution depended on the specimen's failure mode. Peak bond stress within all specimens ranged from 6 to 8.7 MPa. In cases of debonding in one section, bond stress decreased and shifted to other sections. In slip failure instances, bond stress remained relatively constant along the intact encapsulation length (7.7-8.7 MPa in Test B). However, in Test C, extensive debonding at a 500 kN load substantially reduced bond stress in those sections.

- **Failure patterns:** Notably, shear-off failures at the bolt-grout interface, common in conventional rock bolting systems, were absent. Instead, grout shear failures at the grout-sheath interface were observed, characteristic of slip failure. Typically, circumferential cracks, approximately 90° to the bolt's direction, indicated damage. These cracks resulted from extensive bolt elongation and the lower adhesive and interlock strength between the grout and sheath, allowing tensile stress to exceed the grout's tensile strength, and initiating crack formation. These failure patterns were closely related to bond stress distribution.

7.6. New opportunities and future research

The exploration of rock bolt axial behaviour across various conditions in this thesis has yielded fresh insights into the performance of rock bolting systems. Building upon the findings from Chapters 3 to 6, several avenues for further research and opportunities to enhance our understanding of rock bolt behaviour emerge, including:

- This study has revealed that the temperature profile along the encapsulation length is non-uniform. Consequently, the bearing capacity can be influenced by this temperature distribution. Delving deeper into the effect of temperature profile non-uniformity may yield valuable insights into the bonding characteristics of resin-encapsulated rock bolts.

- The thermosetting nature of anchoring resins introduces a path-dependent bonding deterioration process when subjected to heating. Exploring this phenomenon in conjunction with the thermal properties of encapsulation materials can provide a deeper understanding of the process.

- Pullout test results underscore the importance of embedment length in rock bolt performance. Investigating longer encapsulation lengths in rock or concrete under elevated temperatures and varying heat exposure durations can generate data essential for enhancing material design and engineering.

- This study considered resins with filler sizes ranging from micrometres to millimetres. Exploring the influence of nano-fillers on the temperature-related behaviour of resin-encapsulated rock bolts holds potential for improved material design and engineering.

- Observations have indicated that specimens exhibit partial sensitivity to changes in confining loads, posing challenges in data analysis. Further research into the impact of specimen size on rock bolt behaviour under confining conditions,

especially in situ, may provide deeper insights.

- The effects of sample size, sample strength, encapsulation length, and surrounding media on rock and rock bolt behaviours have been explored. It is recommended to conduct additional research using various combinations of these parameters, including different encapsulation lengths, specimen sizes, surrounding media, grout strengths, and diverse confining stress conditions.
- While push-out testing has been a valuable method for assessing axial rock bolt behaviour, performing pull-out tests under triaxial conditions is advisable to gain a more comprehensive understanding of the subject.

REFERENCES

Al-mansouri O, Mege R, Pinoteau N, Guillet T, Rémond S. Influence of testing conditions on thermal distribution and resulting load- bearing capacity of bonded anchors under fire. Eng Struct 2019;192:190–204. https://doi.org/10.1016/j.engstruct.2019.04.099.

Amine M, Caron J, Pinoteau N, Forêt G. International Journal of Adhesion and Adhesives Mechanical behavior of adhesive anchors under high temperature exposure : Experimental investigation. Int J Adhes Adhes 2017;78:200–11. https://doi.org/10.1016/j.ijadhadh.2017.07.004.

Antino TD, Sneed LH, Carloni C, Pellegrino C. Effect of the inherent eccentricity in single-lap direct-shear tests of PBO FRCM-concrete joints. Compos Struct 2016;142:117–29. https://doi.org/10.1016/j.compstruct.2016.01.076.

Atlas Copco. Rock Reinforcement Product catalogue 2008.

Aziz N, Craig P, Nemcik J, Hai F, Craig P, Nemcik J, et al. Rock bolt corrosion – an experimental study. Min Technol 2014;9009. https://doi.org/10.1179/1743286314Y.0000000060.

Aziz N, Jalalifar H, Concalyes J. Bolt surface configurations and load transfer mechanism. Proc. Coal Oper. Conf., Wollongong, NSW, Australia: University of Wollongong; 2006, p. 236–44.

Aziz N, Jalalifar H, Remennikov A. Optimisation of the bolt profile configuration for load transfer enhancement. Proc. Coal Oper. Conf., Wollongong, NSW, Australia: University of Wollongong; 2008, p. 125–31.

Aziz N, Majoor D, Mirzaghorbanali A. Strength Properties of Grout for Strata Reinforcement. Procedia Eng 2017a;191:1178–84. https://doi.org/10.1016/j.proeng.2017.05.293.

Aziz N, Mirzaghorbanali A, Holden M. The extent of shearing and the integrity of protective sleeve coating of cable bolts of protective sleeve coating of cable bolts. Coal Oper. Conf., Wollongong, Australia: 2017b, p. 240–6.

Aziz N, Webb B. Study of load transfer capacity of bolts using short encapsulation push test. Coal Oper. Conf., Wollongon, Australia: 2003, p. 72–80.

Bagherzadeh A, Jamshidi M, Monemian F. Investigating mechanical and bonding properties of micro/nano filler containing epoxy adhesives for anchoring steel bar in concrete. Constr Build Mater 2020;240. https://doi.org/10.1016/j.conbuildmat.2019.117979.

Benmokrane B, Chennouf A, Mitri HS. Laboratory evaluation of cement-based grouts and grouted rock anchors. Int J Rock Mech Min Sci Geomech Abstr 1995;32:633–42.

Benmokrane B, Zhang B, Chennouf A. Tensile properties and pullout behaviour of AFRP and CFRP rods for grouted anchor applications. Constr Build Mater

2000;14:157–70.

Beyl ZS. Rock Pressure and Roof Support (Parts I– VI). Colliery Eng 1945.

Bieniawski ZT. Rock mechanics design in mining and tunnelling. Balkema Publishers; 1984.

Blanco L, Tijani M, Hadj-hassen F, Noiret A. Assessment of the bolt-grout interface behaviour of fully grouted rockbolts from laboratory experiments under axial loads. Int J Rock Mech Min Sci 2013;63:50–61. https://doi.org/10.1016/j.ijrmms.2013.06.007.

Brown ET. Rock mechanics in Australia. Nternational J Rock Mech Min Sci 2002;39:529–38.

Cai Y, Esaki T, Jiang Y. An analytical model to predict axial load in grouted rock bolt for soft rock tunnelling. Tunn Undergr Sp Technol 2004;19:607–18. https://doi.org/10.1016/j.tust.2004.02.129.

Cao C, Jan N, Ren T, Naj A. A study of rock bolting failure modes. Int J Min Sci Technol 2013a;23:79–88. https://doi.org/10.1016/j.ijmst.2013.01.012.

Cao C, Nemcik J. Failure modes of rockbolting 2012:137–53.

Cao C, Nemcik J, Aziz N, Ren T. Analytical study of steel bolt profile and its influence on bolt load transfer. Int J Rock Mech Min Sci 2013b;60:188–95. https://doi.org/10.1016/j.ijrmms.2012.12.013.

Cao C, Ren T, Cook C. Calculation of the effect of Poisson's ratio in laboratory push and pull testing of resin-encapsulated bolts. Int J Rock Mech Min Sci 2013c;64:175–80. https://doi.org/10.1016/j.ijrmms.2013.08.034.

Cao C, Ren T, Cook C, Cao Y. Analytical approach in optimising selection of rebar bolts in preventing rock bolting failure. Int J Rock Mech Min Sci 2014;72:16–25. https://doi.org/10.1016/j.ijrmms.2014.04.026.

Chang X, Wang G, Liang Z, Yang J, Tang C. Study on grout cracking and interface debonding of rockbolt grouted system. Constr Build Mater 2017;135:665–73. https://doi.org/10.1016/j.conbuildmat.2017.01.031.

Che N, Wang H, Jiang M. DEM investigation of rock/bolt mechanical behaviour in pull-out tests. Particuology 2020. https://doi.org/10.1016/j.partic.2019.12.006.

Chen H, Kimyon O, Ramandi HL, Manefield M, Kaksonen AH, Morris C, et al. Microbiologically influenced corrosion of cable bolts in underground coal mines : The effect of Acidithiobacillus ferrooxidans. Int J Min Sci Technol 2021;31:357–63. https://doi.org/10.1016/j.ijmst.2021.01.006.

Chen J, He F, Zhang S. A study of the load transfer behavior of fully grouted rock bolts with analytical modelling. Int J Min Sci Technol 2020a;30:105–9. https://doi.org/10.1016/j.ijmst.2019.12.010.

Chen J, He F, Zhang S. A study of the load transfer behavior of fully grouted rock bolts with analytical modelling. Int J Min Sci Technol 2020b;30:105–9. https://doi.org/10.1016/j.ijmst.2019.12.010.

Chen Y. Experimental study and stress analysis of rock bolt anchorage performance. J Rock Mech Geotech Eng 2014;6:428–37. https://doi.org/10.1016/j.jrmge.2014.06.002.

Chong Z, Yue T, Yao Q, Li X. Experimental and numerical investigation of crack propagation in bolting systems strengthened with resin-encapsulated rock bolts. Eng Fail Anal 2021;122:105259. https://doi.org/10.1016/j.engfailanal.2021.105259.

Contrafatto L, Cosenza R. Behaviour of post-installed adhesive anchors in natural stone. Constr Build Mater 2014;68:355–69. https://doi.org/10.1016/j.conbuildmat.2014.05.099.

Conway CC. Roof supportwit h suspension rods. Min Congr J 1948;34:32–7.

Cui G, Zhang C, Pan Y, Deng L, Zhou H. Laboratory investigation into effect of bolt profiles on shear behaviors of bolt-grout interface under constant normal stiffness (CNS) conditions. J Rock Mech Geotech Eng 2020;12:1234–48. https://doi.org/10.1016/j.jrmge.2020.03.010.

Devi MS, Murugesan V, Rengaraj K, Anand P. Utilization of Flyash as Filler for Unsaturated. J Appl Polym Sci Polym Sci 1998;69:1385–91. https://doi.org/https://doi.org/10.1002/(SICI)1097-4628(19980815)69:7<1385::AID-APP13>3.0.CO;2-T.

DSI Australia. DSI Product Catalogue 2018.

Dudek D, Kadela M. Pull-Out Strength of Resin Anchors in Non-cracked and Cracked Concrete and Masonry Substrates. Procedia Eng 2016;161:864–7. https://doi.org/10.1016/j.proeng.2016.08.734.

European Assessment Document E. Systems for post-installed rebars connections with mortar. 2020.

Fabjanczyk MW, Tarrant GC. Load transfer mechanisms in reinforcing tendons. 11th Int. Conf. Gr. Control Min., Wollongong, Australia: 1992, p. 212–9.

Farmer IW. Stress distribution along a resin grouted rock anchor. Int J Rock Mech Min Sci Geomech Abstr 1975;12:347–51.

Feng X, Xue F, Carvelli V, Zhao T, He F, Wang D. A novel rock bolting system exploiting steel particles. Int J Min Sci Technol 2022;32:1045–58. https://doi.org/10.1016/j.ijmst.2022.08.003.

Forbes J. Progress in roof bolting. Proc. Illinois Min. Inst., 1950, p. 21–7.

Freeman TJ. Behaviour of fully bonded rock bolts in the kielder experimental tunnel. Int J Rock Mech Min Sci Geomech Abstr 1978;15:37–40. https://doi.org/doi:10.1016/0148-9062(78)91073-2.

Fu M, Liu S, Jia H, He D. Experimental Study of an Orientation and Resin-Lifting Device for Improving the Performance of Resin-Anchored Roof Bolts. Rock Mech Rock Eng 2019;53:211–31. https://doi.org/10.1007/s00603-019-01906-5.

Galvin JM. Ground engineering - principles and practices for underground coal mining. Gr Eng - Princ Pract Undergr Coal Min 2016:1–684. https://doi.org/10.1007/978-3-319-25005-2.

Gardener F. History of Rock Bolting. Rock Bolting, Wollongong, Australia: 1971.

Grundy CF. Notable water tunnel. Water Power 1951.

Hagan P, Chen J. The load transfer mechanism of fully grouted cable bolts under laboratory tests 2014:137–46.

Hawkes JM, Evans RH. Bond stresses in reinforced concrete columns and beams. J Inst Struct Eng 1951;29.

Hazrati M, Parviz A, Hossein M, Rad S. In Situ Rock Bolt Pull Tests Performance in an Underground Powerhouse Complex : A Case Study in Sri Lanka. Geotech Geol Eng 2020;38:2227–44. https://doi.org/10.1007/s10706-019-01159-7.

He L, An XM, Zhao XB, Zhao ZY, Zhao J. Development of a Unified Rock Bolt Model in Discontinuous Deformation Analysis. Rock Mech Rock Eng 2017;51:827–47. https://doi.org/10.1007/s00603-017-1341-9.

Ho D, Bost M, Rajot J. Numerical study of the bolt-grout interface for fully grouted rockbolt under different confining conditions 2019;119:168–79. https://doi.org/10.1016/j.ijrmms.2019.04.017.

Hong S, Park S-K. Uniaxial bond stress-slip relationship of reinforcing bars in concrete. Adv Mater Sci Eng 2012;2012:1–12. https://doi.org/10.1155/2012/328570.

Huang M, Zhou Z, Huang Y, Ou J. A distributed self-sensing FRP anchor rod with built-in optical fiber sensor. Measurement 2013;46:1363–70. https://doi.org/10.1016/j.measurement.2012.12.012.

Hutchinson J, Diederichs MS. Cablebolting in underground mines. BiTech Publishers Ltd; 1996.

Hyett AJ, Bawden WF, Macsporran GR, Moosavi M. A constitutive law for bond failure of fully-grouted cable bolts using a modified hoek cell. Int J Rock Mech Min Sci Geomech 1995;32:11–36.

Hyett AJ, Bawden WF, Reichert RD. The effect of rock mass confinement on the bond strength of fully grouted cable bolts. Int Rock Mech Min Sci Geomech Abstr 1992;29:503–24.

Ito F, Nakahara F, Kawano R, Kang S., Obarae Y. Visualization of failure in a pull-out test of cable bolts using. Constr Build Mater 2001:263–70.

Jahani Y, Baena M, Barris C, Perera R, Torres L. Influence of curing, post-

curing and testing temperatures on mechanical properties of a structural adhesive. Constr Build Mater 2022;324. https://doi.org/10.1016/j.conbuildmat.2022.126698.

Jennmar Australia. HARD ROCK CATALOGUE 2017.

Jin-feng Z, Peng-hao Z. Analytical model of fully grouted bolts in pull-out tests and in situ rock masses. Int J Rock Mech Min Sci 2019;113:278–94. https://doi.org/10.1016/j.ijrmms.2018.11.015.

Kang H, Yang J, Gao F, Li J. Experimental Study on the Mechanical Behavior of Rock Bolts Subjected to Complex Static and Dynamic Loads. Rock Mech Rock Eng 2020;53:4993–5004. https://doi.org/10.1007/s00603-020-02205-0.

Karabin GJJ, Debevec WJ. Comparative evaluation of conventional and resin bolting systems. 1977.

Keeley DE. Guniting at the McIntyre Mine. 1934.

Kilic A, Yasar E, Atis CD. Effect of bar shape on the pull-out capacity of fully-grouted rockbolts. Tunn Undergr Sp Technol 2003;18:1–6. https://doi.org/https://doi.org/10.1016/S0886-7798(02)00077-9.

Kim H, Rehman H, Ali W, Naji AM, Kim Jung-joo, Kim Jonguk, et al. Classification of Factors A ff ecting the Performance of Fully Grouted Rock Bolts with Empirical Classification Systems. Appl Sci 2019;9. https://doi.org/doi:10.3390/app9224781.

Kılıc A, Yasar E, Celik AG. Effect of grout properties on the pull-out load capacity of fully grouted rock bolt. Tunn Undergr Sp Technol 2002;17:355–62. https://doi.org/https://doi.org/10.1016/S0886-7798(02)00038-X.

Ko H, Matthys S, Palmieri A, Sato Y. Development of a simplified bond stress–slip model for bonded FRP–concrete interfaces. Constr Build Mater 2014;68:142–57. https://doi.org/10.1016/j.conbuildmat.2014.06.037.

Kömürlü E, Kesimal A. Rck Bolting from Past to Present in 20 Inventions. J Undergr Resour 2016:69–85.

Kovari K. History of the sprayed concrete lining method-part I: milestones up to the 1960s. Tunn Undergr Sp Technol 2003;18:57–69.

Lakhani H, Hofmann J. A numerical method to evaluate the pull-out strength of bonded anchors under fire. 3rd Int Symp Connect between Steel Concr 2017.

Laredo M, Theoretical R, Fluminense UF, Passo R. Effect of Temperature on the Mechanical Properties of Polymer Mortars 2012;15:645–9. https://doi.org/10.1590/S1516-14392012005000091.

Li B, Qi T, Zhengzheng W, Yang L. Back analysis of grouted rock bolt pullout strength parameters from field tests. Tunn Undergr Sp Technol Inc Trenchless Technol Res 2012;28:345–9. https://doi.org/10.1016/j.tust.2011.11.004.

Li C, Stillborg B. Analytical models for rock bolts. Int J Rock Mech Min Sci 2000;36:1013–29.

Li CC. Principles of rockbolting design. J Rock Mech Geotech Eng 2017;9:396–414. https://doi.org/10.1016/j.jrmge.2017.04.002.

Li CC, Kristjansson G, Høien AH. Critical embedment length and bond strength of fully encapsulated rebar rockbolts. Tunn Undergr Sp Technol 2016;59:16–23. https://doi.org/10.1016/j.tust.2016.06.007.

Li CC, Stjern G, Myrvang A. A review on the performance of conventional and energy-absorbing rockbolts. J Rock Mech Geotech Eng 2014;6:315–27. https://doi.org/10.1016/j.jrmge.2013.12.008.

Li D, Li Y, Chen J, Masoumi H. An analytical model for axial performance of rock bolts under constant confining pressure based on continuously yielding criterion. Tunn Undergr Sp Technol Inc Trenchless Technol Res 2021;113:103955. https://doi.org/10.1016/j.tust.2021.103955.

Li L, Hagan PC, Saydam S, Hebblewhite B, Zhang C. A Laboratory Study of Shear Behaviour of Rockbolts Under Dynamic Loading Based on the Drop Test Using a Double Shear System. Rock Mech Rock Eng 2019;52:3413–29. https://doi.org/10.1007/s00603-019-01776-x.

Liu S-S, Zhao M-H, Li L. Analysis of dynamic broken line model based on experimental data of anchor anti-pullout. Rock Soil Mech 2014;35:3389–95.

Liu X, Yao Z, Xue W, Wang X, Huang X, Li Y. Experimental Study of the Failure Mechanism of the Anchorage Interface under Different Surrounding Rock Strengths and Ambient Temperatures. Adv Civ Eng 2021;2021:1–17. https://doi.org/10.1155/2021/6622418.

Luo J, Haycocks C, Karmis M, Westman E. A critical overview of US rock bolting practices. 5th Int. Symp. Roffbolting Min., 1998, p. 13–34.

Lutz LA. Analysis of stresses in concrete near a reinforcing bar due to bond and transverse cracking. J Proc 1970;67:778–87.

Ma S, Nemcik J, Aziz N. An analytical model of fully grouted rock bolts subjected to tensile load. Constr Build Mater 2013;49:519–26. https://doi.org/10.1016/j.conbuildmat.2013.08.084.

MAPEI. MAPEI Product Catalogue 2020.

Martín LB, Tijani M, Hadj-hassen F. A new analytical solution to the mechanical behaviour of fully grouted rockbolts subjected to pull-out tests. Constr Build Mater 2011;25:749–55. https://doi.org/10.1016/j.conbuildmat.2010.07.011.

McKay KS, Erki MA. Grouted anchorages for aramid fibre reinforced plastic prestressing tendons. Can J Civ Eng 1993;20:1065–1069. https://doi.org/doi:10.1139/l93-137 .

Miller SM, Ward D c. Evaluation of pullout resistance and direct-shear strength of grouted fiberglass cable bolts. Int Jouranl Rock Mech Min Sci 1998;35:400.

Minova. Minova Product Catalogue 2019.

MINOVA, NEWSON S, CAMPOLI A, SYKES A, O'CONNOR D, SMITH N. The MINOVA Guide to Resin-Grouted Rockbolts. Cambridge, UK, Piggott Black Bear: 2006.

Moosavi M, Jafari A, Khosravi A. Bond of cement grouted reinforcing bars under constant radial pressure. Cem Concr Compos 2005;27:103–9. https://doi.org/10.1016/j.cemconcomp.2003.12.002.

Mousavi SS, Dehestani M, Mousavi KK. Bond strength and development length of steel bar in unconfined self-consolidating concrete. Eng Struct 2017;131:587–98. https://doi.org/10.1016/j.engstruct.2016.10.029.

Murata J, Kawai A. Studies on bond strength of deformed bar by pullout test. Concr Libr Japan Soc Civ Eng 1984;1:113–22.

Nie W, Zhao ZY, Guo W, Shang J, Wu C. Bond-slip modeling of a CMC rockbolt element using 2D-DDA method. Tunn Undergr Sp Technol 2019;85:340–53. https://doi.org/10.1016/j.tust.2018.12.025.

Pączkowski P, Puszka A, Gawdzik B. Investigation of Degradation of Composites Based on Unsaturated Polyester Resin and Vinyl Ester Resin. Materials (Basel) 2022;15. https://doi.org/10.3390/ma15041286.

Pierce JC. Pinning up an aqueductr oof. Compress 1953:128–36.

Pinoteau N, Heck J V, Rivillon P, Avenel R, Pimienta P, Guillet T, et al. Prediction of failure of a cantilever–wall connection using post-installed rebars under thermal loading. Eng Struct 2013;56:1607–19. https://doi.org/10.1016/j.engstruct.2013.07.028.

Rahman GMS, Aftab H, Islam MS, Zobayer M, Mukhlish B, Ali F. Enhanced Physico-mechanical Properties of Polyester Resin Film Using CaCO3 Filler. Fibers Polym 2016;17:59–65. https://doi.org/10.1007/s12221-016-5612-y.

Rastegarmanesh A, Mirzaghorbanali A, McDougall K, Aziz N, Anzanpour S, Nourizadeh H, et al. Axial Response of Resin Encapsulated Cable Bolts in Monotonic and Cyclic Loading. Can Geotech J 2023. https://doi.org/https://doi.org/10.1139/cgj-2022-0379.

Rataj M, Yearby M. Development of roof bolting in Australian coal mining. Support Reinf. Pract. Min., Kalgoorlie, Australia: 1999, p. 425–35.

Ren FF, Yang ZJ, Chen JF, Chen WW. An analytical analysis of the full-range behaviour of grouted rockbolts based on a tri-linear bond-slip model. Constr Build Mater 2010;24:361–70. https://doi.org/10.1016/j.conbuildmat.2009.08.021.

Salcher M, Bertuzzi R. Results of pull tests of rock bolts and cable bolts in

Sydney sandstone and shale. Tunn Undergr Sp Technol 2018;74:60–70. https://doi.org/10.1016/j.tust.2018.01.004.

Sandvik. Pioneering solution for ground control 2016.

Scotford RF. Commercial literature. 1960.

Scott JJ. Friction rock stabilizer impact upon anchor design and ground control practices. Rock bolting theory Appl. Undergr. Constr., Rotterdam: Balkema; 1983, p. 407–18.

Shi H, Song L, Zhang H, Chen W, Lin H, Li D, et al. Experimental and numerical studies on progressive debonding of grouted rock bolts. Int J Min Sci Technol 2022;32:63–74. https://doi.org/10.1016/j.ijmst.2021.10.002.

Shrivastava AK, Rao KS. Physical Modeling of Shear Behavior of Infilled Rock Joints Under CNL and CNS Boundary Conditions. Rock Mech Rock Eng 2018;51:101–18. https://doi.org/10.1007/s00603-017-1318-8.

Signer SP. Field verification of load transfer mechanics of fully grouted roof bolts. United States. Bureau of Mines: 1990.

Singer SP, Cox D, Johnston J. A method for the selection of rock support based on bolt loading measurements. 1997.

Stillborg B. Professional users handbook for rock bolting. ClausthalZellerfeld: Trans Tech Publications; 1994.

Talobre J. La statique du boulon d‘ancrage dans les travaux au rocher. Construction 1957:439–45.

Tepfers R. Cracking of concrete cover along anchored deformed reinforcing bars. Mag Concr Res 1979;31.

Teymen A, Kılıç A. Effect of grout strength on the stress distribution (tensile) of fully-grouted rockbolts. Tunn Undergr Sp Technol 2018;77:280–7. https://doi.org/10.1016/j.tust.2018.04.022.

Thenevin I, Blanco-martín L, Hadj-hassen F, Schleifer J, Lubosik Z, Wrana A. Laboratory pull-out tests on fully grouted rock bolts and cable bolts : Results and lessons learned. J Rock Mech Geotech Eng 2017;9. https://doi.org/10.1016/j.jrmge.2017.04.005.

Thomas E, Seeling CH, Perz F, Hansen MV. Control of roof and prevention of accidents from falls of rock and coal. Bur Mines 1948;7471.

Thompson AG, Villaescusa E, Windsor CR. Ground Support Terminology and Classification: An Update. Geotech Geol Eng 2012;30:553–80. https://doi.org/10.1007/s10706-012-9495-4.

Vandermaat D. Stress corrosion cracking of rockbolts: a laboratory based approach utilising a controlled mine envrionment. University of New South Wales,

2014. https://doi.org/https://doi.org/10.26190/unsworks/17350.

Vlachopoulos N, Cruz D, Forbes B. Utilizing a novel fiber optic technology to capture the axial responses of fully grouted rock bolts. J Rock Mech Geotech Eng 2018;10:222–35. https://doi.org/10.1016/j.jrmge.2017.11.007.

Wang M, Hu Y, Jiang C, Wang Y, Liu D, Tong J. Mechanical Characteristics of Cement-Based Grouting Material in High-Geothermal Tunnel. Mater 2020;13. https://doi.org/10.3390/ma13071572.

Wang S, Hagan PC, Cao C. Rockbolting. Adv. Rock-Support Geotech. Eng., 2016, p. 61–149.

Wang W, Pan Y, Xiao Y. Synergistic resin anchoring technology of rebar bolts in coal mine roadways. Int J Rock Mech Min Sci 2022;151:105034. https://doi.org/10.1016/j.ijrmms.2022.105034.

Wee S, Kang S, Hai K, Yang E. Experimental and analytical investigation on bond-slip behaviour of deformed bars embedded in engineered cementitious composites. Constr Build Mater 2016;127:494–503. https://doi.org/10.1016/j.conbuildmat.2016.10.036.

Weigel WW. Channel irons for roof control. Eng Min J 1943;144:70–2.

Windsor CR. Rock reinforcement systems. Int J Rock Mech Min Sci 1997;34:919–51.

Witt R, Cizek E. Effect of Filler Particle Size on Resins. Ind Eng Chem 1954;46:1635–9.

Wu S, Lamei H, Chen H, Crosky A, Hagan P, Saydam S. Mineralogically influenced stress corrosion cracking of rockbolts and cable bolts in underground mines. Int J Rock Mech Min Sci 2019;119:109–16. https://doi.org/10.1016/j.ijrmms.2019.04.011.

Xue-gui S, Xian-jie D, Hong-hu Y, Ben-kui L. Research of the thermal stability of structure of resin anchoring material based on 3D CT. Int J Adhes Adhes 2016;68:161–8. https://doi.org/10.1016/j.ijadhadh.2016.03.005.

Yazici S, Kaiser PK. Bond strength of grouted cable bolts. Int J Rock Mech Min Sci Geomech Abstr 1992;29:279–92.

Yi W, Wang M, Zhao S, Tong J, Liu C. The effect of rock hardness and integrity on the failure mechanism of mortar bolt composite structure in a jointed rock mass. Eng Fail Anal 2023;143:106831. https://doi.org/10.1016/j.engfailanal.2022.106831.

Yilmaz S, Özen MA, Yardim Y. Tensile behavior of post-installed chemical anchors embedded to low strength concrete. Constr Build Mater 2013;47:861–6. https://doi.org/10.1016/j.conbuildmat.2013.05.032.

Yokota Y, Zhao Z, Nie W, Date K, Iwano K, Okada Y. Experimental and Numerical Study on the Interface Behaviour Between the Rock Bolt and Bond Material.

Rock Mech Rock Eng 2019;52:869–79. https://doi.org/10.1007/s00603-018-1629-4.

Yue Z, Li A, Wang P, Wang P. An analytical analysis for the mechanical performance of fully-grouted rockbolts based on the exponential softening model. Int J Min Sci Technol 2022;32:981–95. https://doi.org/10.1016/j.ijmst.2022.08.005.

Zhang B, Benmorkane B, Ebead UAA. Design and Evaluation of Fiber-Reinforced Polymer Bond-Type Anchorages and Ground Anchors. Int J Geomech 2006;166.

Zhang C, Cui G, Chen X, Zhou H, Deng L. Effects of bolt profile and grout mixture on shearing behaviors of bolt-grout interface. J Rock Mech Geotech Eng 2020;12:242–55. https://doi.org/10.1016/j.jrmge.2019.10.004.

Zhou Y-W, Wu Y-F, Yun Y. Analytical modeling of the bond–slip relationship at FRP-concrete interfaces for adhesively-bonded joints. Compos Part B Eng 2010;41:423–33. https://doi.org/10.1016/j.compositesb.2010.06.004.

APPENDIX A: CONFERENCE PAPERS

AXIAL BEHAVIOUR OF ROCK BOLTS–PART (A) EXPERIMENTAL STUDY

Hadi Nourizadeh[1], Sally Williams[1], Ali Mirzaghorbanali[1], Kevin McDougall[1], Naj Aziz[2] and Mehdi Serati[3]

ABSTRACT: Several experiments were carried out to investigate the effect of curing time and water to grout ratio on the ultimate load capacity of fully grouted rock bolts subject to pulling out loads. For this purpose, various samples were cast with water to grout ratios of 30%, 36% and 40 %. Pull-out tests were conducted on samples with different curing times, ranging from 7 to 28 days. Results indicate that the peak value of the pull out load increased as curing time increased. In contrast, increasing water to grout ratio weakens the pulling out resistance of fully grouted rock bolts.

INTRODUCTION

Fully-grouted rock bolts are widely used to strengthen and support rock walls and tunnels in mining and civil industries (Li, 2017). These reinforcing systems can be designed as temporary or permanent reinforcement to mitigate the risks associated with tunnelling, namely rock falls and structural collapse (Cao, 2012). A typical grouted rock bolt consists of internal and external fixtures such as a ribbed steel bar installed and encapsulated by cementitious grout in a drilled hole. Once grout cures, chemical adhesion, friction and mechanical interlocking provide the bond strength between the grout and bolt (Cao et al., 2016). System debonding may occur at the grout, bolt-grout interface, grout-rock interface or surrounding rocks (Li and Stillborg, 1999). However, failure at the bolt-grout interface is the most common mode according to previous experimental and *in-situ* studies. Rock bolt systems develop forces in response to rock deformation and displacement. Different stresses are acting on rock bolt systems; these include tension, shear, compression and rotation. Figure 1 illustrates six different loading types that can occur on a rock bolt system depending on the geometric properties of joints and the bolt's spatial position relative to the joint. In this figure, rotation was not taken into account, which creates extra complexities (Thompson et al., 2012).

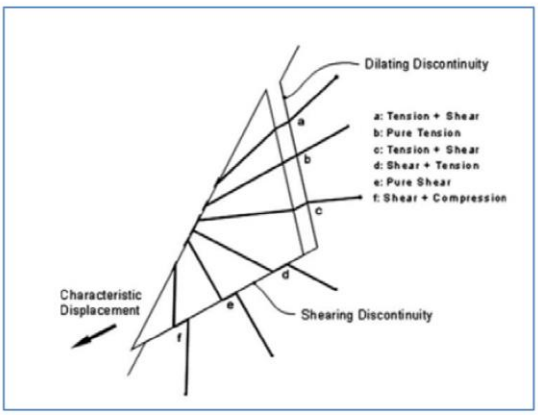

Figure 1: Generic reinforcement system (Thompson et al., 2012)

As illustrated in Figure 2, tensile loads within a rock bolt system occur when a discontinuity dilation displaces a rock mass. Tension is produced between stable and unstable rock regions as shown in Figure 3, thus creating shear loads between the rock-grout interface. The tensile strength of steel, the

[1] *School of Civil Engineering and Surveying, University of Southern Queensland, email:* hadi.norizadeh@usq.edu.au
[2] *School of Civil, Mining and Environmental Engineering, University of Wollongong, email:* naj@uow.edu.au
[3] *School of Civil Engineering, University of Queensland, email:* mehdi.serati@uq.edu.au

AXIAL BEHAVIOUR OF ROCK BOLTS–PART (B) NUMERICAL STUDY

Hadi Nourizadeh[1], Ali Mirzaghorbanali[1], Kevin McDougall[1], Naj Aziz[2] and Mehdi Serati[3]

ABSTRACT: Axial load behaviour of rock bolts was studied using FLAC commercial software in a two-dimensional framework. The numerical model was calibrated using experimental pull out data. Effects of confinement stresses and rock bolt surface roughness on the axial load behaviour were investigated incorporating the calibrated numerical code. Results indicated that the pull out resistance increases with an increase in confinement stresses and surface roughness.

INTRODUCTION

Fully-encapsulated rock bolts are embedded in the borehole using either resin or cementitious grout. This increase the overall stiffness by generating resistances against axial and shear forces. Sliding blocky rocks or movement of bedding planes induce stress in the grout. The induced stresses are then transferred to the reinforcing element, thus, creating interaction between the bolt and surrounding medium. Eventually, this process produces tensile forces in the bolt, preventing further movement of separated blocks and bedding planes.

LITERATURE REVIEW

In fully grouted rock bolts, failure may occur in various modes including rock-grout interface, grout-bolt interface, rock bolt and surface plate. Nemcik et al. (2014) reported that the most common failure mode is the bolt-grout interface. Relaxation in the confinement stress reduces rock bolt anchorage capacity, particularly at the rock-grout interface. Hyett et al. (1992) carried out split-pipe tests using PVC, aluminium and steel pipes to investigate the effects of confinement stress on the bond capacity of grouted cable bolts. They concluded that the axial bearing capacity of cable bolts increases with an increase in confinement stress. In addition, they reported that the failure mechanisms changed as the confinement stress increased. In another study, Hyett et al. (1995) performed several pull-out tests on encapsulated cable bolts incorporating the modified Hoek cell to simulate confinement stresses. It was noted that confining stress affects the ultimate bearing capacity of encapsulated cable bolts. Blanco Martin et al. (2011) carried out a series of pull-out tests to examine the influence of several factors such as confining stress and the bolt's surface profile. The results revealed that confining stress possesses noticeable effects on the anchoring capacity. It was observed that the radial fractures are more pronounced in low values of confining stress. In another study, Nie et al. (2019) reported that the highest bond and residual strength are achieved with high confining stress.

Hawkes and Evans (1951) carried out pull-out tests showing the distribution of shear (bond) stress along the bolt. They concluded that the load distribution follows an exponential function and the peak takes place before any decoupling occurs. Farmer (1975) conducted theoretical and experimental research on the shear stress distribution along resin encapsulated reinforcement elements and concluded that the mobilised shear resistance is an influential factor in the bond resistance. Li and Stillborg (1999) developed an analytical model for fully encapsulated rock bolts by assuming the peak shear stressoccurring a short distance from the loading point, diminishing exponentially to the free end (Figure 1). According to the piecewise function proposed by Li and Stillborg (1999), the shear stress distribution is divided into four sections along fully-grouted rock bolts. These sections include entirely decoupled (A), partially decoupled with a constant bond strength (B), partially decoupled with linearly increasing bond strength (C) and compatible deformation with no decoupling (D) (Figure 2). The proposed model includes some assumptions which may limit the model practicality. Developing a reliable mathematical model to simulate rock bolt bond-stress behaviour is a cumbersome task due to problem complexities. Several tri-linear bond-slip models were presented to simulate the interfacial

[1] *School of Civil Engineering and Surveying, University of Southern Queensland, email:* hadi.norizadeh@usq.edu.au
[2] *School of Civil, Mining and Environmental Engineering, University of Wollongong, email:* naj@uow.edu.au
[3] *School of Civil Engineering, University of Queensland, email:* mehdi.serari@uq.edu.au

FINITE ELEMENT NUMERICAL MODELLING OF ROCK BOLT AXIAL BEHAVIOUR SUBJECT TO DIFFERENT GEOTECHNICAL CONDITIONS

Hadi Nourizadeh[1], Ali Mirzaghorbanali[2], Naj Aziz[3], Kevin McDougall[4], Behshad Shokri Jodeiri[5], Ali Akbar Sahebi[6], Amin Mottalebiyan[7] and Shima Entezam[8]

ABSTRACT: In rock bolting systems, grout acts as a medium to transfer initiated stress from the bolt to stable rock mass, and also to transfer the in-situ stress from surrounding rock to the bolt-grout interface. In this study interaction between the mechanical characteristics of the grout and rock bolt behaviour was investigated in different confining pressure conditions. First, the uniaxial compression strength of the grouts was experimentally determined, and then pull-out tests were carried out on rock bolts encapsulated using the same grouts to quantify the bonding behaviour. Numerical models using ABAQUS explicit finite element code were then applied to further analyse the effects of mechanical properties of the grouts and the confining stress on the behaviour of the rock bolting systems. The compression of the simulated results with the experimental tests showed that the proposed FE models simulate the axial behaviour of rock bolts efficiently. The results of the parametric study indicated that grout mechanical properties and the level of confining stress affect the ultimate bearing capacity of the encapsulated rock bolts and the force-displacement behaviour. The level of damage that occurred at the specimens due to pull-out load is also significantly influenced by these factors.

INTRODUCTION

Rock bolts are widely used in mining and geotechnical engineering and are capable of effectively improving the stability of rock mass, and reducing the rock mass deformation, resulting in improvements in safety, cost and time (Rastegarmanesh et al., 2022). Regardless of the type, rock bolt systems generally develop forces in response to rock deformation and displacement. Fully-grouted rock bolt installation is considered the most common type of rock bolt in mining and civil engineering. Once a fully-grouted rock bolt is installed and rock mass starts to displace, the bolt interacts with the grouted materials and surrounding rock mass and load is transferred from unstable rocks to the intact rock (Nourizadeh et al., 2021). Rock bolts restrain rock movement along a discontinuity and control the rock deformation along the grouted length. When a fully-grouted bolt is subjected to a tensile force, a part of axial stress distributes at the bolt-grout interface, the grout, the grout-rock interface and the rock. The failure can occur in the bolt, at the bolt-grout interface, at the grout, at the grout-rock interface, and inside the rock depending on the type, magnitude, and direction of stress besides the mechanical characteristics of the components. However, the literature concludes that the failure of the fully-grouted rock bolts occurs commonly at the bolt-grout interface. Grout acts as a medium to transfer the stresses from the bolt to the rock mass, and also to transfer the in-situ stress from the rock mass to the reinforcing system (Nourizadeh et al., 2022). Interaction between the mechanical characteristics of the components has been well studied in the literature by many scholars who agree with the direct impacts of stronger encapsulation grouts on bolting performance. Aziz et al. (2016) comprehensively studied the effects of grout thickness and borehole diameter.

The interaction between the components in the rock bolting systems subjected to a tensile force is complicated (Nourizadeh et al., 2022). Therefore, the conventional approaches may not be capable of studying this behaviour in detail. On the other hand, computer simulations are powerful tools for dealing with complexity in Engineering problems. Nemcik et al. (2014) developed a numerical model for fully

[1] Centre for Future Materials (CFM), University of Southern Queensland, email: hadi.norizadeh@usq.edu.au,
[2] School of Civil Engineering and Surveying, University of Southern Queensland, email: ali.mirzaghorbanali@usq.edu.au
[3] School of Civil, Mining and Environmental Engineering, University of Wollongong, email: naj@uow.edu.au
[4] School of Civil Engineering and Surveying, University of Southern Queensland, email: kevin.mcdougall@usq.edu.au
[5] Centre for Future Materials (CFM), University of Southern Queensland, email: behshad.jodeirishokri@usq.edu.au,
[6] School of Mining Engineering, Shahid Bahonar University of Kerman, email: ak.sahebi@gmail.com
[7] Centre for Future Materials (CFM), University of Southern Queensland, email: amin.motallebyian@usq.edu.au,
[8] Centre for Future Materials (CFM), University of Southern Queensland, email: jodeirishokriShima.Entezam@usq.edu.au